Université de Montréal

Long-term Solar Variability in a Hybrid Babcock-Leighton Solar Dynamo Model

par

Deniz Ölçek

Département de physique
Faculté des arts et des sciences

Mémoire présenté à la Faculté des études supérieures
en vue de l'obtention du grade de
Maître ès sciences (M.Sc.)
en physique

December 18, 2018

Université de Montréal
Faculté des études supérieures

Ce mémoire intitulé

Long-term Solar Variability in a Hybrid Babcock-Leighton Solar Dynamo Model

présenté par

Deniz Ölçek

a été évalué par un jury composé des personnes suivantes :

Nicole St-Louis, président-rapporteur

Paul Charbonneau, directeur de recherche

Björn Benneke, membre du jury

Mémoire accepté le:
10 Octobre 2018

SOMMAIRE

Le but de cette étude est d'élucider le comportement à long terme du cycle d'activité magnétique solaire, en particulier l'origine physique des épisodes prolongés d'activité fortement réduite ou amplifiée (Grand Minima et Maxima). Les principales questions abordées dans ce mémoire sont les suivantes: Les Grand Minima / Maxima relèvent-ils d'un processus stochastique? Sont-ils associés à des modes dynamo distincts? Est-ce que leur déclenchement peut être représenté par un processus de Poisson? Quels sont les mécanismes physiques à l'origine de ces événements irréguliers? Comment la dynamo sort-elle de ces modes extrêmes? Quel est le mécanisme qui favorise l'aggrégation des Grand Minima? Quel est le mécanisme responsable du changement de parité lors de ces événements extrêmes? Les réponses à ces questions sont recherchées via une approche de modélisation numérique basée sur un modèle hybride de la dynamo solaire Babcock Leighton. Les séries temporelles résultantes de l'activité solaire simulée et les statistiques de Grand Minima et Maxima sont comparées à leurs homologues déduits des reconstructions cosmogéniques de l'activité solaire passée basée sur les radionucléides cosmogéniques. On constate qu'avec différentes combinaisons de valeurs de paramètres dans des intervals raisonables, il est possible de reproduire un comportement solaire à long terme en accord avec les données des radionucléides cosmogéniques.

Mots-clés: Activité Solaire, Dynamo Solaire, Climat Spatial, Grand Minimum / Maximum

SUMMARY

The purpose of this study is to shed some light on the long-term behavior of the solar magnetic activity cycle, in particular the physical origins of the extended episodes of strongly suppressed or enhanced activity (so-called Grand Minima and Maxima). The primary questions that are tackled in this thesis are as follows: Is the occurrence of Grand Minima/Maxima a stochastic process? Are they associated with distinct dynamo modes? Is their triggering due to a Poisson-like processes? What are the physical mechanisms that cause these irregular events? How does the dynamo enter and exit from these extreme modes? What is the underlining mechanism that makes Grand Minima cluster? What is the mechanism which is responsible from parity change during these extreme events? Answers to these questions are sought via a modelling approach based on a hybrid Babcock Leighton solar dynamo model. The resulting simulated solar activity time series and the statistics of Grand Minima and Maxima are compared to their counterparts inferred from reconstructions of the past solar activity based on cosmogenic radionuclides. With different combination parameter values within a reasonable range, it is possible to reproduce solar-like long-term behavior in agreement with radionuclide data.

Keywords: Solar Activity, Solar Dynamo, Space Climate, Grand Minimum/Maximum

CONTENTS

LIST OF TABLES

LIST OF FIGURES

DEDICATION

To those who have dedicated themselves to understanding nature...

ACKNOWLEDGEMENTS

Foremost, I would like to express my deepest gratitude to my supervisor, Paul Charbonneau, for accompanying me with his immense knowledge, patience and encouragement during my journey of returning to astrophysics after all these years. This thesis work would never have been possible without his help and constant support during this period.

I present my sincerest thanks to Kalevi Mursula for his support and for my undergraduate internship at ReSoLVE in Oulu, Finland, which sparked my interest in solar-terrestial physics.

Alexandre Lemerle, to whom I am indebted for all the fruitful discussions, his collaboration and answering my questions with great patience. This thesis wouldn't have been possible without his PhD work.

Ilya Usoskin, and for his inspiring work, for all of his helpful insights and for kindly providing me their cosmogenic isotope data.

Fran Bagenal, for all the inspiration as an outstanding scientist and communicator, and for hosting me at LASP, Colorado.

I would like to thank summer interns, Gabriel Longpré and Florence Boileau for their valuable contributions to this project.

Throughout my time at UdeM, I also benefited immensely from informal discussions with my colleagues at GRPS; François Labonville, Benoit Tremblay, Corinne Simard, Patrice Beadoin, Jean-François Cosette and Melinda Nagy, and other student friends including Tahina Ramiaramanantsoa and Pierre-Marc Landry.

And finally special thanks,

To my friends all around the globe whose names are hard to summarize in these lines.

To my mom, dad and sister, whose love and tremendous support have always been accompanying me in my life journey.

To my partner, Yan, who has been walking beside me along the same challenging and wonderful paths.

Chapter 1

INTRODUCTION

> Following the light of the Sun, I left the Old World.
>
> Christopher Columbus

In Sun-like stars, the convective envelope below the photosphere is where small and large-scale plasma flows are able to self-sustain the global dynamo which is thought to be the origin of all magnetic activity in such stellar objects (Parker, 1955). Hence understanding the solar magnetic cycle by studying the solar dynamo has been one of the central issues in modern solar physics, ever since early sunspot observations revealed this intriguing fairly regular, cyclic behavior of the Sun. The sunspot measurements continue to be used as the most common direct indicator of solar activity. Nevertheless, indirect proxies have been widely utilized to understand mechanisms related to long-term modulations. Although we have 400 years of continuous direct observations and indirect sunspot data reconstructions, the complete picture of mechanisms that are behind this quasi-periodic behavior still remain a puzzle for solar physicists. The first section of this introductory chapter briefly reviews our current knowledge regarding the characteristics of the Sun and its magnetism. §1.2 gives an overview of the various concepts central in the theory of the solar dynamo, mostly focusing on dynamo mechanisms that are being explored in our analysis. §1.3 introduces the long-term solar variability which is at the heart of this work. Finally, basic features of the dynamo model we use in this study are presented. Chapter 2 contains the research article in which our simulation results are being presented and interpreted in detail.

1.1. Characteristics of the Sun

Although it is a seemingly ordinary star of G2V spectral type, destined to take its place among white dwarf stars in the Universe after becoming a red giant in about 5 billion years, our Sun has a vital significance for our extraordinary planet, being the primary source of energy for life, responsible for the regulation of the space climate in the solar system and

space weather. It is also a variable star and this variability is, among other things, observed by the changes in number of sunspots, in the total and spectral solar irradiances (Fig. 1.1), by the varying charged particle flux from the Sun, frequency of eruptive phenomena and by the modulation of high energy galactic cosmic ray intensity (Usoskin, 2017).

Consisting mainly of Hydrogen (74%) and Helium (24%), the interior of the Sun is divided into several regions where different physical mechanisms dominate. The core of the Sun which extends out to about $0.25R_{\odot}$ is the furnace where nuclear fusion reactions take place. The radiative zone transports the thermal energy of the core to about $0.7R_{\odot}$ by radiative diffusion. Exceeding this radius, the density and temperature sufficiently drop to create an increased opacity caused by partial recombination of Helium and Hydrogen. From $0.7R_{\odot}$ to the surface, there lies the turbulent convection zone where the magnetic field responsible for the solar cycle is generated (Fan, 2009). The convection zone is separated from the radiative zone by the tachocline, which is a thin transition zone between the solid rotation of the radiative zone and the differential rotation of the convection zone. It is still a subject of investigation as to what extent the tachocline is essential for magnetic field generation (Strugarek *et al.*, 2016), although this region plays a central role in the regeneration of the large-scale magnetic field of the Sun and solar-like stars (Guerrero *et al.*, 2016).

The Sun rotates every 25 days at the equator and takes progressively longer to rotate at higher latitudes, up to 35 days at the poles. In recent years, the internal profile of the solar differential rotation was pinned down by helioseismology with good accuracy down to about $0.5R_{\odot}$. Measurements of the meridional flow can also be made by various modern techniques including direct Doppler imaging, local helioseismology, and feature tracking (Hathaway and Upton, 2014). The poleward component of this flow residing at the surface is observed to be about 20 m/s and, in the convection zone where the density is much higher, the return flow toward the equator is found to be moving at a much slower speed (around 1 to 2 m/s) carrying material from the mid-latitudes (Fig. 1.2). The rate of meridional circulation is similar to that of the sunspot activity with the rising and falling of sunspots, i.e. the solar cycle period is set primarily by the circulation time of the meridional flow (Charbonneau, 2010).

1.1.1. Solar Magnetic Cycle

The Sun shows surface magnetic activity on various scales and magnitudes varying across its surface. Its polar field is 5–10 G (0.0005–0.001 T), whereas the field is typically 3,000 G (0.3 T) in sunspots and 10–100 G (0.001–0.01 T) in solar prominences (Williams, 2013). The magnetic field also varies in time. The quasi-periodic 11-year solar cycle is the most prominent variation in which the number and size of sunspots rises and falls over time, and it is very central to solar physics.

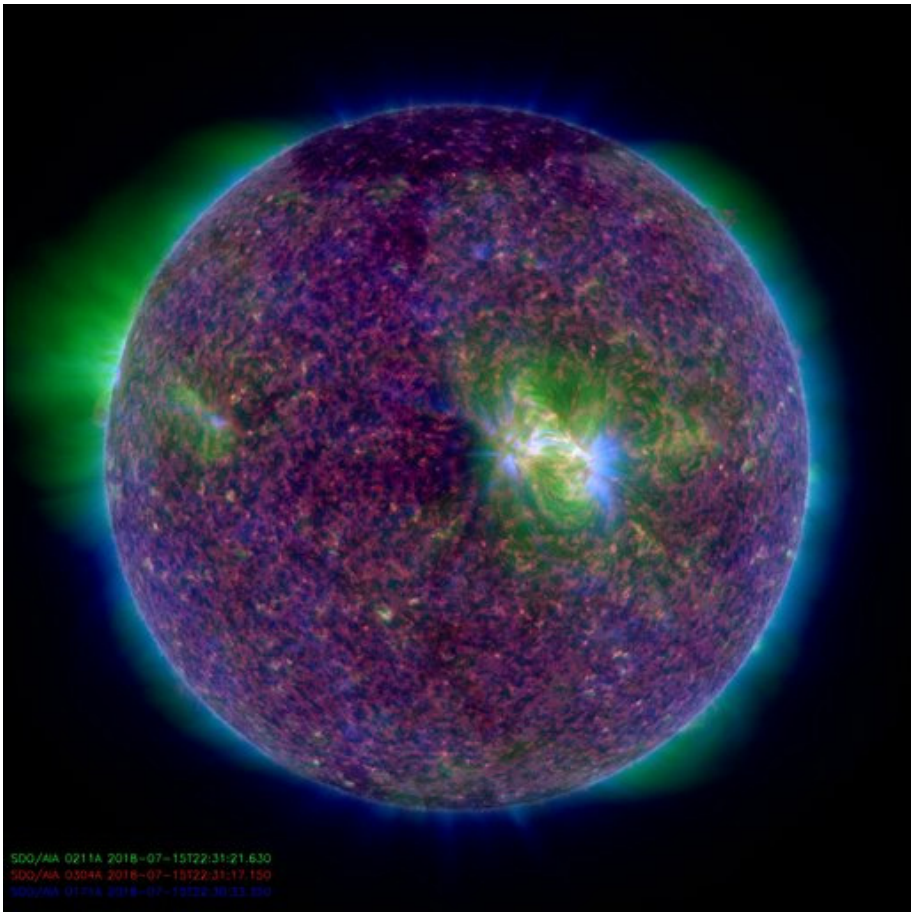

FIG. 1.1. This image of the Sun combines three images with different emission temperatures. Here red, green and dark blue show respectively the 304Å emission (50,000K) by He II in the chromosphere, the 211Å emission (2,000,000K) by Fe XIV in the corona and the 171Å emission (6,000K) by Fe IX in the corona (Source: https://sdo.gsfc.nasa.gov/data/).

The Sun's magnetic field is understood to be generated by a combination of magneto-hydrodynamical inductive processes taking place primarily in the solar convection zone. It was Hale (1919) who first measured the Zeeman splitting in the spectra of sunspots, made a connection between magnetic fields and sunspots, and found out that the sunspot cycle period is about 22 years, covering two polar reversals of the solar magnetic dipole field. Hale's famous polarity laws also established the existence of a well-organized magnetic flux system in the solar interior as the source of sunspots (Fig. 1.3); the indicators of magnetic activity.

Sunspots (Fig. 1.3), visible as dark patches on the Sun's photosphere, are slightly cooler (3,800 K) than the photosphere (5,777 K). Consequently, they look darker as the regions of the photosphere around them are relatively brighter and hotter. They correspond to concentrated magnetic fields where the convective transport of heat is inhibited from the solar interior to the surface. At a typical solar minimum, few sunspots are visible, and occasionally none can be seen at all. As the solar cycle progresses towards its maximum,

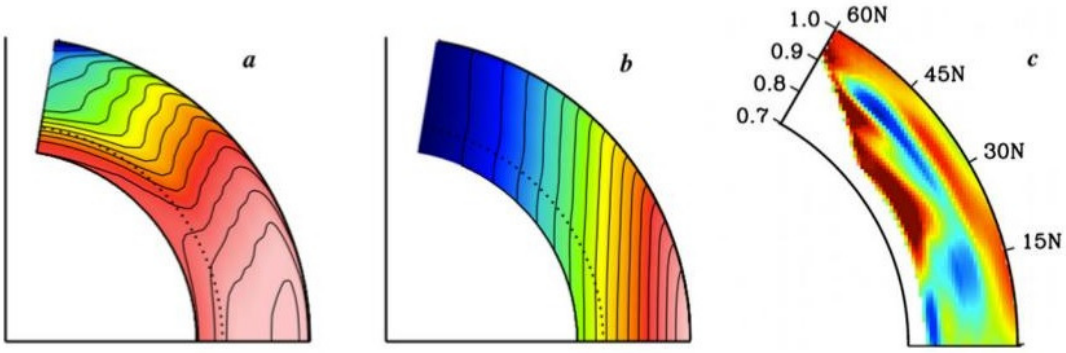

FIG. 1.2. Profiles of solar differential rotation and meridional circulation deduced from helioseismology as shown in Fig. 6 in Karak *et al.* (2015). Frames (a) and (b) show the angular velocity and the specific angular momentum increasing linearly from blue to pink, with ranges of (a) 300–460 nHz and (b) 0–1.4 $\mathrm{Mm^2 s^{-1}}$. They are based on global helioseismic RLS inversions of GONG data from 1996 (Howe *et al.*, 2000; Schou *et al.*, 2002). (c) Mean colatitudinal velocity v_θ in the northern hemisphere inferred from time-distance helioseismic inversions of SDO/HMI data from 2010–2012 (Zhao *et al.*, 2013). Red and blue areas indicate poleward and equatorward flow respectively with a saturation level for the color table of ± 15 m $\mathrm{s^{-1}}$.

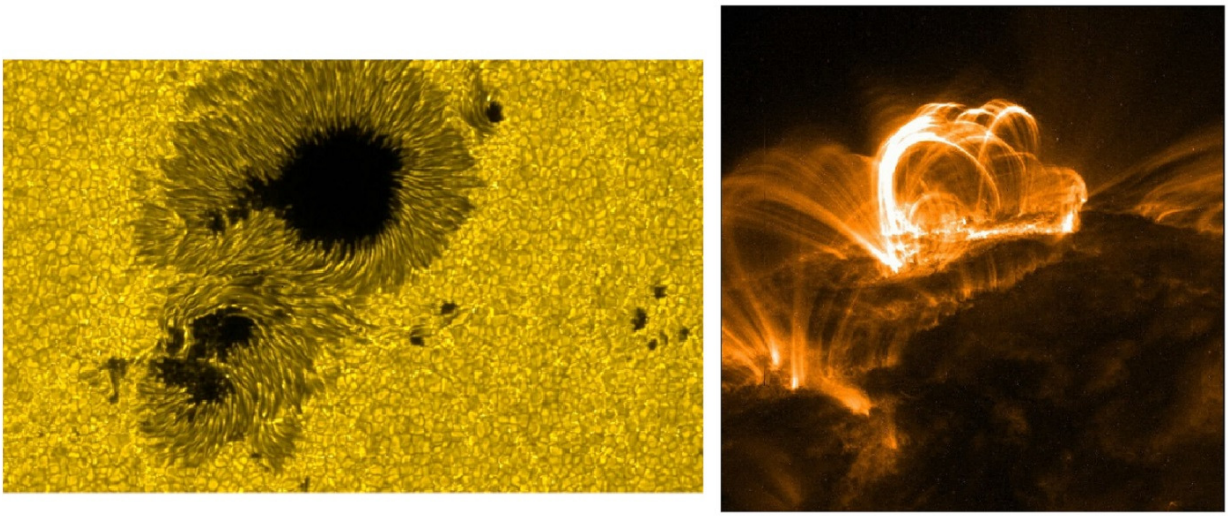

FIG. 1.3. Features of sunspots. *Left*: Sunspots have two parts: the darkest part which is called the central umbra, where the magnetic field is approximately vertical to the Sun's surface and the surrounding lighter area (penumbra), with a more inclined magnetic field. *Right*: Coronal loops observed in UV wavelength by TRACE. They are resulted from twisted magnetic flux rising through the solar interior to the surface, populating both active and quite regions on the photosphere. Source: NASA.

sunspots tend to form closer to the solar equator, a phenomenon known as Spörer's law. The largest sunspots can be tens of thousands of kilometers across (Solov'ev and Kirichek, 2014).

Detailed observations of sunspots have been carried out since the beginning of the 1800s and show that sunspots do not appear periodically at random locations over the surface of the Sun but are concentrated in two latitude bands on either side of the equator as shown in the well-known butterfly diagram (Figures 1.4 and 1.5). Sunspots are widely recognized to be tracers of the internal magnetic field, although there is a number of other solar activity indicators that also vary in relation with the sunspots including the 10.7 cm radio flux, the total solar irradiance, flares, coronal mass ejections, geomagnetic activity, galactic cosmic ray fluxes, and radioisotopes in tree rings and ice cores (Hathaway, 2015).

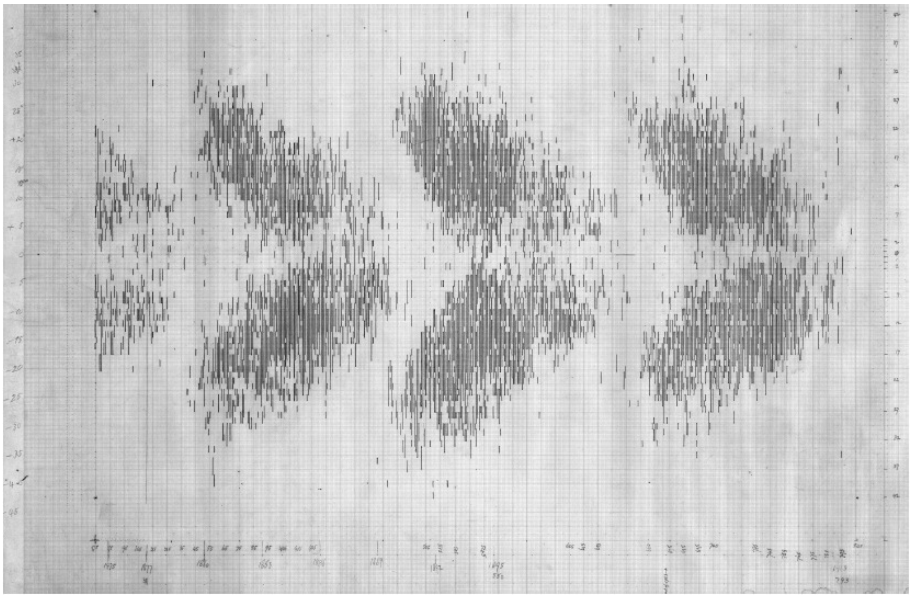

FIG. 1.4. Time-latitude butterfly diagram drawn by Annie S.D. Maunder and E. Walter Maunder. The longitude-averaged sunspot data goes from 1875 to 1913, covering solar cycles 11 (partially) through 14. The horizontal axis shows the time whereas the vertical one is for the latitude, with equator being in the middle. Each small black vertical segment covers the latitude range of sunspot pairs on a given day. Source: Annie Maunder, a Pioneer of Solar Astronomy, High Altitude Observatory web page: https://www2.hao.ucar.edu/news/2018-jun/annie-maunder-pioneer-solar-astronomy.

The periodic behavior of the solar magnetic variability is described with the 22-year sunspot cycle, demonstrating polar reversals every 11 years - a phenomenon known as the Hale cycle. This cyclic behavior originates from an oscillatory exchange of energy between toroidal and poloidal solar magnetic fields. At solar-cycle maximum, the external poloidal dipolar magnetic field is near its minimum strength, but an internal toroidal dipolar field, generated through differential rotation within the tachocline, is near its maximum strength. During this period, magnetic buoyancy within the convective zone forces the emergence of toroidal magnetic field lines through the photospher which emerge as pairs of sunspots that are approximately aligned in the East–West direction, with a small tilt angle obeying

Joy's Law. The two members of each pair also carry opposite magnetic polarities. Their disintegration during the declining phase of the solar cycle builds up the poloidal field for the next cycle. As sunpots start to diminish both in number and in intensity, the internal toroidal field reduces to its minimum strength while the poloidal field peaks to its maximum strength. Sunspots are restricted to latitudinal bands approximately between $-30°$ and $30°$. They emerge as pairs with opposite polarity closer and closer to the equator throughout a cycle, peaking in coverage at about $\pm 15°$ of latitude (Hathaway, 2015).

Sunspots typically appear in groups embedded in larger, topologically complex, magnetically bipolar regions, whose local magnetic polarity they share in most cases. The bipolar regions are also roughly oriented in the East–West direction (the direction of solar rotation) and their polarities obey the same set of polarity rules. Their member sunspots maintain the same magnetic orientation in each hemisphere during an 11-year activity cycle, having the opposite magnetic orientation in the Northern and Southern hemispheres. Furthermore, the magnetic orientation of the bipolar regions reverses from one cycle to the next. As a consequence of these rules, the pattern of magnetic orientations repeats itself with a period of two activity cycles having polarity reversal from one cycle to the other, i.e. the magnetic cycle of the Sun has a duration of about 22 years (Solanki *et al.*, 2004). Another systematic property of bipolar regions is their deviation from a precise East–West orientation: on both hemispheres, the more Westward located polarity (leading with respect to the direction of rotation) is nearer the equator than the following polarity. On average, the corresponding tilt angle with respect to the East–West direction, γ, is proportional to the mean heliographic latitude, λ, of the bipolar region: $\gamma = 0.5\lambda$ (Joy's law). Larger bipolar regions obey the polarity rules and Joy's law more strictly than smaller regions (without sunspots), which are probably more strongly affected by disturbances and deformation of the underlying magnetic structure by convective motions (Dasi-Espuig *et al.*, 2010; McClintock and Norton, 2013).

With the rise of the next 11-year sunspot cycle, differential rotation converts magnetic energy back from the poloidal to the toroidal field, but with a polarity that is opposite to the previous cycle. This process carries on perpetually, and each 11-year sunspot cycle leads to a change in the overall polarity of the Sun's large-scale magnetic field. The magnetic field observed at the solar surface, a small part of which continues beyond the solar corona and permeates inter-planetary space, is produced by a dynamo process operating in the solar interior (Solanki *et al.*, 2004; Hood and Hughes, 2011; Charbonneau, 2013). The field emerging at the surface in the form of bipolar regions embracing wide ranges of size and magnetic flux is a partial manifestation of what is going on in the interior. The solar cycle is magnetic in nature and is generated by magnetohydrodynamical (MHD) processes within the Sun. §1.4 discusses the relevant MHD mechanisms and solar dynamo models.

While the study of solar activity has been the primary issue in the Solar Astrophysics community, the solar cycle also inspired some researchers to search for similar cyclic behaviors

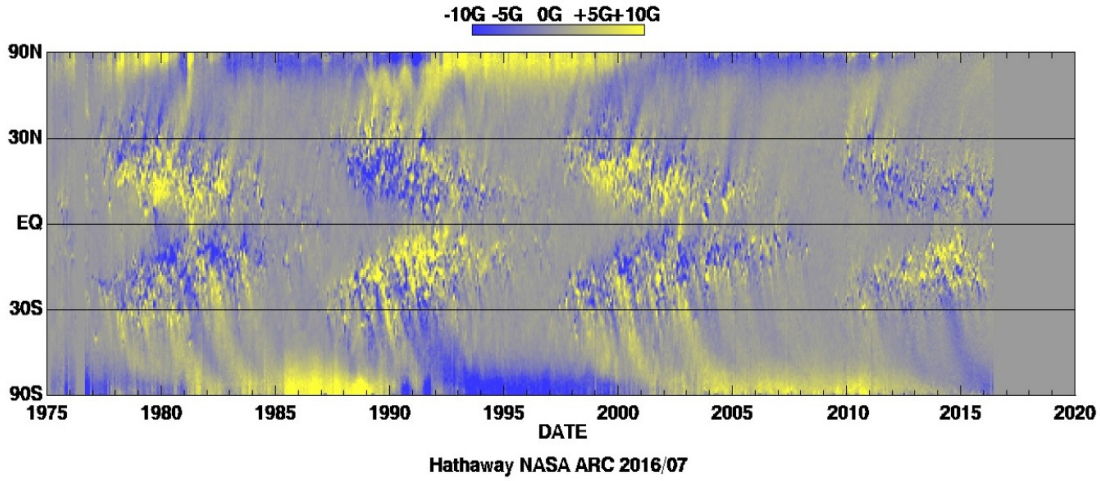

FIG. 1.5. A synoptic magnetogram showing the longitudinally-averaged solar radial field on the surface as a function of time and latitude. The blue parts (yellow) represent the entering (exiting) field lines on the surface of the Sun. Compared to Fig.1.4, this figure provides more information concerning the surface magnetic field including polarity reversals. http://solarscience.msfc.nasa.gov/images/magbfly.jpg

in other main-sequence stars, especially those with solar-like masses. Ca H & K emissions from singly-ionized calcium in the lower chromosphere due to magnetic heating is a proven proxy for magnetic flux in the Sun and in solar analogs, and shows that the Sun is not the only star with a periodic magnetic cycle (Egeland *et al.*, 2017) (see Fig. 1.6).

Besides the 22-year Hale cycle covering polarity reversals, the spectral analysis of different data sets hint to the existence of few other long-term cycles such as the Gleissberg cycle (80-100yrs) (Beer, Tobias, and Weiss, 1998; Usoskin *et al.*, 2016b; Beer, Tobias, and Weiss, 2018). We will also have a closer look at these solar quasi-periodicities in the following section.

1.2. Reconstruction of the past solar activity with cosmogenic isotopes

The Sun's magnetic activity and the associated changes in its extended atmosphere evolve on time scales that range from minutes to billions of years. Both the instrumental direct records and the much longer interval of paleoclimate records are important in understanding short and long-term solar behavior as geochronology methods allow the quantification of environmental, climatic and solar variability over time.

There are a variety of proxies of solar activity that are based on direct measurements. Besides the most well-known sunspot number series, measurements of solar irradiance, aurora occurrences, etc. are also direct solar proxies. They are usually more reliable for the recent times, having a temporal resolutions of weeks to years. However, as systematic solar

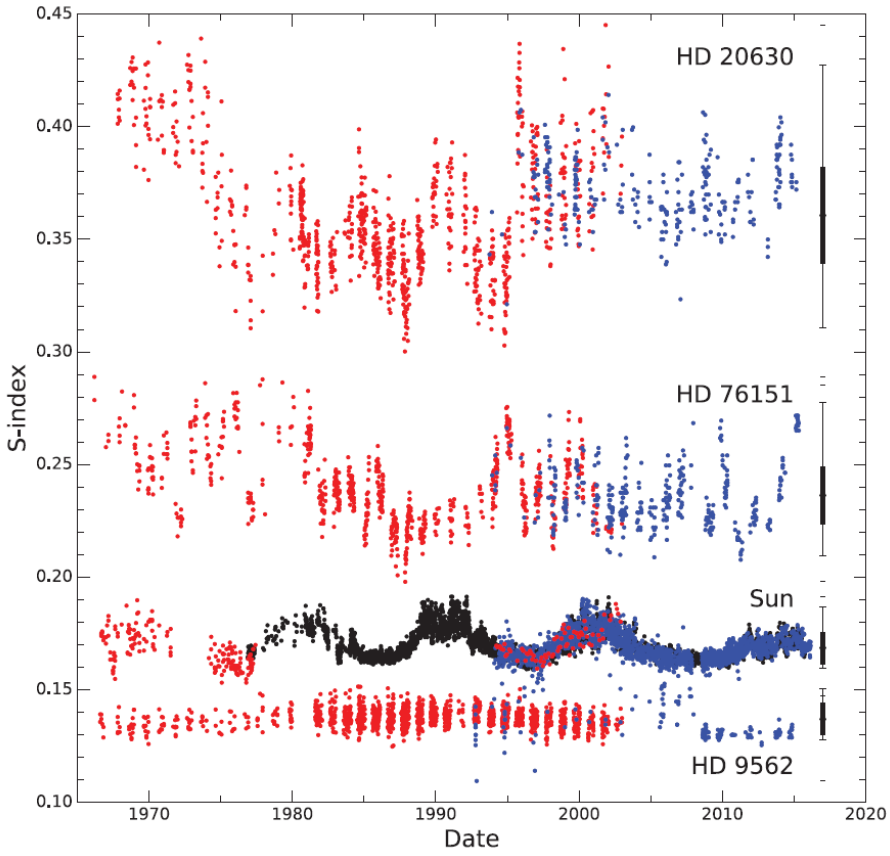

FIG. 1.6. Calibrated composite MWO (red) + SSS (blue) time series for the Sun and three solar analogs as shown in Fig.4.5 in Egeland (2017). This figure illustrates the range of mean values, amplitudes, and patterns of variability in samples studied by Egeland (2017). The Sun is an approximately regular, low amplitude variable star compared to HD 76151 and HD 20630 whose variability is significantly more complicated than that of the Sun, which can be reasonably well described by a mean amplitude and local minimum/maximum. Also, notice that HD 9562 appears to have a few clear low-activity phases resembling the Maunder Minimum similar to the Sun.

observations are only limited to the past four centuries or so, researchers studying the Sun and Heliosphere felt the necessity for different, indirect solar proxies to acquire information about the Sun's distant past and its long-term patterns. Dating techniques based on radionuclides imprinted with information from the heliosphere came up as a highly promising way, although with their own systematic difficulties.

Basically, the indirect proxies are the parameters which can be measured nowadays but present different effects of solar magnetic activity in the past. They can be viewed as the signatures of terrestial effects induced by variable solar-magnetic activity, that is stored in natural archives. Essentially, these effects can be divided in two: nuclear (like used in cosmogenic isotopes) or chemical (nitrate method), both caused by high energy cosmic rays

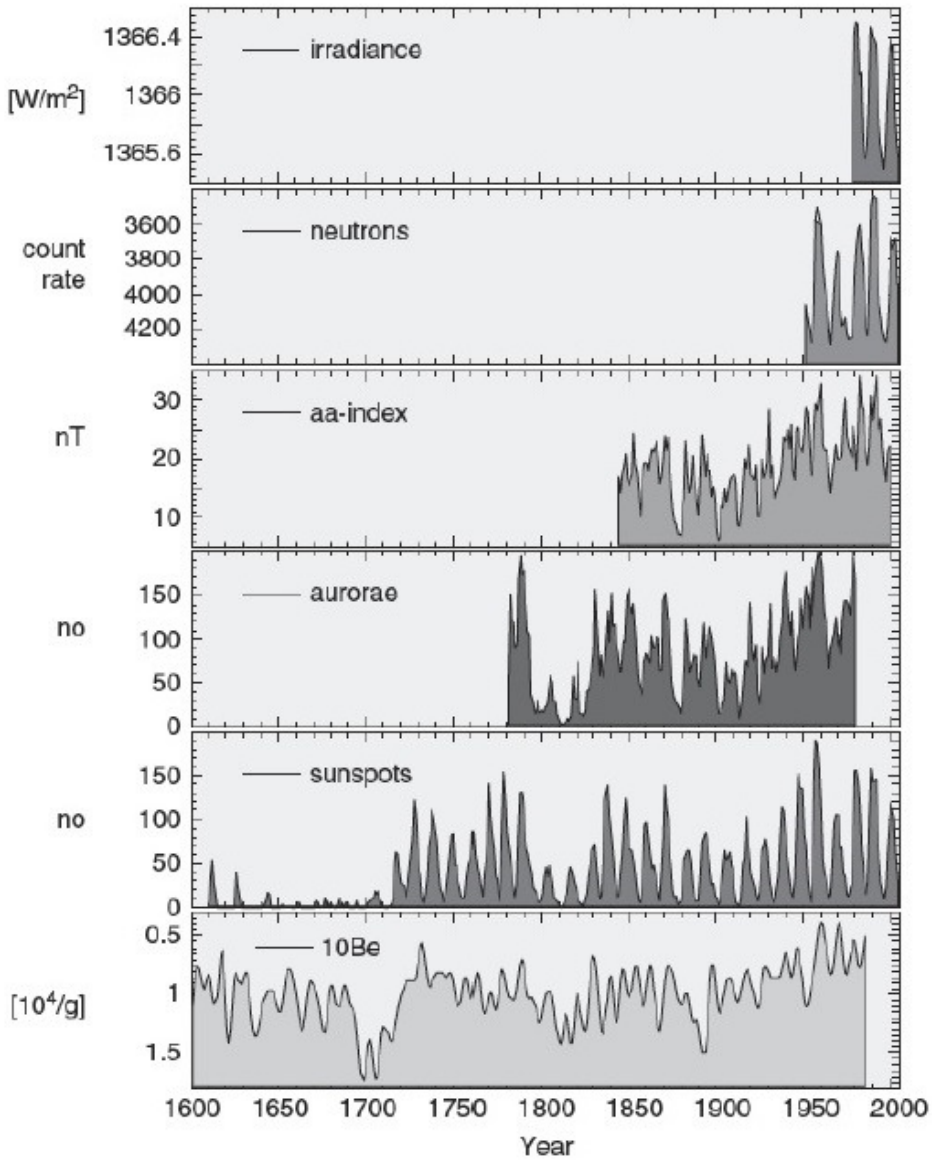

FIG. 1.7. Comparison of solar activity time series deduced from various direct and indirect proxies. This is reproduction of Fig. 11.10 of Schrijver and Siscoe (2010), /p.319/. All proxies show some common features. ^{10}Be is the only one that has the potential to be extended over 10,000 years.

entering in the earth's atmosphere (Usoskin, 2017). Here, our focus will be on the nuclear effects and the reconstruction method with cosmogenic isotopes ^{10}Be and ^{14}C which are the two commonly used radionuclides in solar studies.

Cosmogenic nuclides such as ^{3}H, ^{10}Be, ^{14}C, ^{26}Al and ^{36}Cl are due to the bombardment of the upper few kilometres of the Earth's atmosphere and surface by cosmic rays, with the maximum production being in the upper troposphere/stratosphere. ^{10}Be and ^{14}C production rates are the main regular precursors of solar activity on long-term scales but cannot resolve the details of individual solar cycles. An important advantage of the cosmogenic data is

that primary archiving is done naturally in a similar manner throughout the ages and these archives are measured nowadays in labs using modern techniques such as Accelerator Mass Spectrometry (AMS).

^{14}C is measured in independently-dated tree rings and participates in the complex carbon cycle, which doesn't include spatial and short-term variability of cosmogenic isotope production. For the relatively stable climate of the Holocene, it provides a useful tool for studying past solar activity, but for the glacial and deglaciation epochs, is limited due to drastic climate and ocean ventilation changes. Additionally, it cannot be used after the end of the nineteenth century because of the extensive burning of fossil fuels diluting the atmospheric $^{(14)}CO_2$ concentration with respect to the preindustrial epoch (the Suess effect) and atmospheric nuclear tests which nearly doubled the radiocarbon concentration (Usoskin, 2017).

The other solar activity proxy ^{10}Be is measured in stratified polar ice cores in Greenland and Antarctica (see, e.g. Beer *et al.*, 1990; Raisbeck *et al.*, 1990; Yiou *et al.*, 1997; Berggren *et al.*, 2009) but the details of its atmospheric transport lacks a reliable quantitative model that can relate the measured isotope concentration in ice to the atmospheric production, 3D atmospheric-circulation models are currently being developed for more accurate reconstructions (Usoskin, 2017).

The ^{10}Be and ^{14}C data show the presence of an eleven year cycle that is anti-correlated with solar activity. A close analysis of the data shows many other remarkable features (Beer, Tobias, and Weiss, 1998; Beer, 2000; Wagner *et al.*, 2001). For instance, these reconstructions revealed that the Maunder Minimum is not an isolated event and that other such minima in solar activity appear in the records. These suppressed activity epochs in data stretch back about 11,000 years (Wagner *et al.*, 2001) and reoccur with a mean period of approximately 200 years (Usoskin, 2017). These reconstructions also demonstrate that the solar dynamo went through several Grand Maxima in the past. There are several other solar proxies as shown in Fig. 1.7 that allow us to trace the solar magnetic variability, but none of them can be stretched as far in the past as cosmogenic isotope data.

Although the temporal resolution of this method can distinguish the individual cycles (see Fig.1.7) for about the last 500 years, it degrades as we go further in the past. This data also offers a limited amount of events covering the Holocene epoch ($\sim$ 11,000 years). Nevertheless, the analysis still has some statistical significance and it does give important clues about long-term solar variability and the occurrences of these extreme epochs such as they tend to cluster, or whether Grand Minimum can be followed by a Grand Maximum or vice versa. Another significant result from the analysis of the ^{10}Be record during the Maunder Minimum is the persistence of cyclic behaviour (Beer, Tobias, and Weiss, 1998; Poluianov, Usoskin, and Kovaltsov, 2014). This would seem to indicate that a cyclic magnetic variability continues to operate throughout this period of reduced activity, even if sunspots

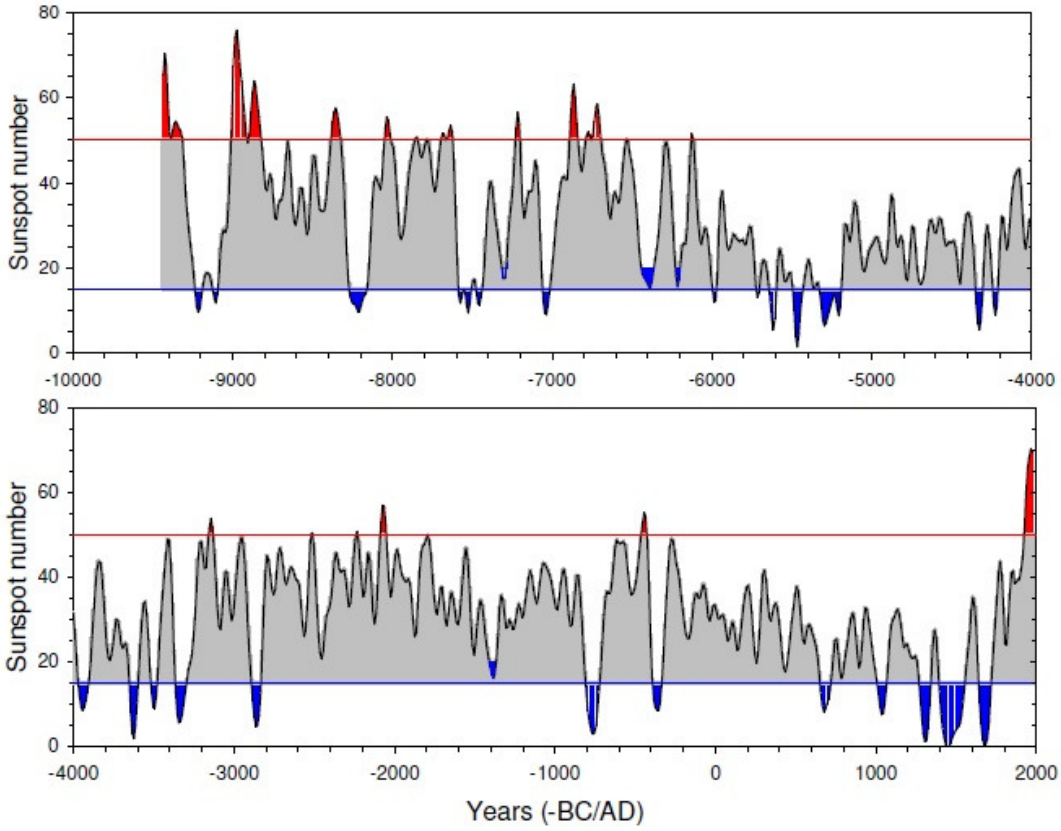

FIG. 1.8. Reconstructed sunspot activity (decadal means smoothed with a 1-2-2-2-1 trapezoidal filter) throughout the Holocene as shown in Fig. 17 in Usoskin (2008). This time series is reconstructed from ^{14}C by Usoskin, Solanki, and Kovaltsov (2007) using geomagnetic data in Yang, Odah, and Shaw (2000). Blue and red areas denote Grand Minima and Maxima, respectively.

were largely not visible at the solar surface. The analysis of the ^{14}C record, which stretches back approximately 11,000 years in Fig. 1.8, provides supporting evidence for modulation of the regular activity. This data clearly shows recurrent Grand Minima/Maxima.

Now, we will examine these radio nuclides closely, to have a better sense of how they carry information about the past solar activity.

1.2.1. Production, transport and deposition of ^{10}Be and ^{14}C

As briefly mentioned above, high energy cosmic rays entering the Earth's atmosphere are responsible for the production of cosmogenic radionuclides. The crucial link here between these cosmic rays and the solar activity is that the cosmic ray flux is modulated by the solar magnetic field via the solar wind and the frozen-in solar magnetic field during their heliospheric trajectory. The intensity of modulation depends on solar activity and therefore, cosmic ray flux and the ensuing cosmogenic isotope production depends on solar activity.

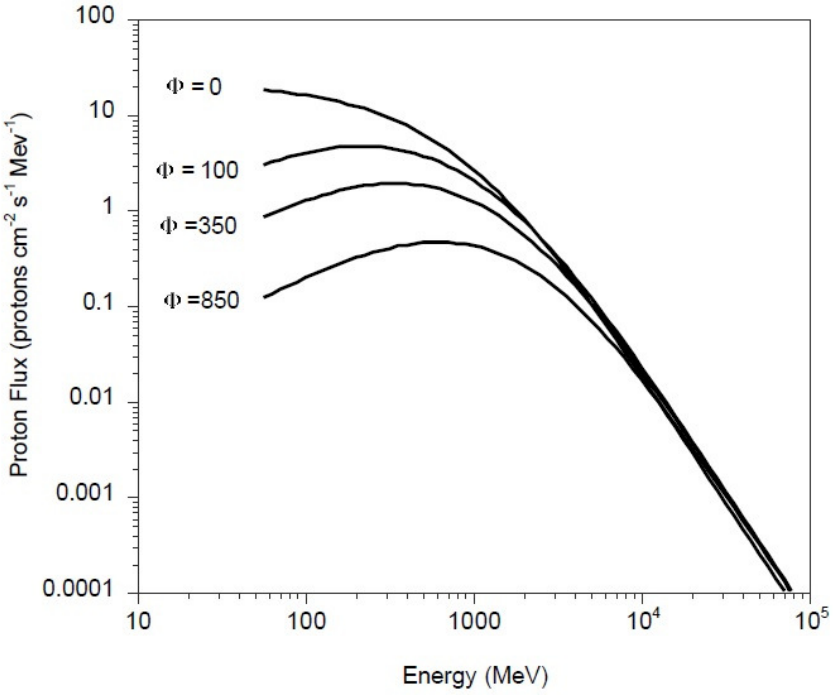

FIG. 1.9. Energy spectrum of the primary cosmic ray proton flux at the top of the atmosphere as a function of the solar modulation parameter Φ. $\Phi = 0$ MeV corresponds to a completely inactive Sun (i.e. if there was no solar magnetic activity), $\Phi = 850$ MeV to a rather active one (Fig. 1 in Beer (2000)).

These high energy rays modulated by the heliosphere cause nuclear spallation reactions as they enter the atmosphere, leading to the production of these isotopes.

Cosmogenic radionuclei are produced continuously by the interaction of cosmic ray particles with the atmosphere. The primary galactic cosmic rays consist of protons (87%), Helium nuclei (12%), and heavier elements (1%). Fig. 1.9 demonstrates the effect of solar modulation on the energy spectrum of primary protons. Modulation of the differential energy spectrum of galactic cosmic rays by solar activity takes place within a radius of about 100 AU around the Sun. During active times, increased number of coronal mass ejections cause large distortions in the interplanetary magnetic field, which in turn result in enhanced scatter of galactic cosmic rays away from the inner parts of the heliosphere. Consequently, the net flux reaching the top of the atmosphere is reduced especially at the low energy end of the spectrum. This process has been parametrized using the solar activity parameter Φ. A value of $\Phi = 0$ MeV corresponds to no solar modulation (i.e. quiet Sun) and refers the estimated interstellar spectrum, while $\Phi = 850$ MeV corresponds to a rather active Sun (Beer, 2000) (see Fig. 1.9).

^{10}Be, is produced as a result of nuclear fission spallation of atmospheric N and O during the cosmic ray-induced atmospheric cascade. The production is defined mostly by the multiplicity of the nucleic components, which increases with the energy of primary cosmic

rays, although there exist a small contribution from photo-nuclear reactions. Maximum production occurs at an altitude of 10-15 km and most of the global ^{10}Be is produced in the stratosphere (55-70%) and the rest in the troposphere. Useful for long-term studies of solar activities because its half-life is around 1.5×10^6 years, it is often measured in stratified ice cores (Muscheler and Heikkilä, 2011; Beer, 2000; Usoskin, 2017).

^{14}C is more unstable with its half-life of about 5730 years. It is widely used for paleoclimatology, quaternary geology, archeology etc. The present day radiocarbon calibration curve, based on a dendrochronological scale, uninterruptedly covers the whole Holocene (from the present back to 50,000BP) and provides another solid quantitative basis for studying solar activity variations on the multi-millennial timescale (Beer, 2000).

Soon after their production, these radionuclides get attached to atmospheric aerosols and hence follow their fate. After complicated transport and mixing in the atmosphere, the cosmogenic isotopes are stored in the natural archives such as polar ice, trees, marine sediments etc. This process is also affected by changes in the geomagnetic field and climate. After residing approximately 2 years in the atmosphere, ^{10}Be is deposited at Earth's surface including in ice caps and ice cores (Beer, 2000). ^{14}C is stored in tree rings after about 30 years in the atmosphere (Stuiver, 1994), reaching the lower troposphere by rain and snow (Usoskin, 2017).

^{10}Be produced in the troposphere is mostly deposited locally, in the polar regions, while stratosphere ^{10}Be can be partly or completely mixed (Beer, Tobias, and Weiss, 2018). In addition, because of the seasonal (usually Spring) intrusion of stratospheric air into the troposphere at mid-latitudes, there is an additional contribution of stratospheric ^{10}Be. Therefore, the measured ^{10}Be concentration (flux) in polar ice is modulated not only by production but also by climate/precipitation effects. However, comparisons between Greenland and Antarctica ^{10}Be series, and between ^{10}Be and ^{14}C data suggest that the Beryllium data mostly depicts production variations (solar signal) on top of which some meteorological effects can be superposed (Beer, 2000; Usoskin, 2017; Beer, Tobias, and Weiss, 2018).

Upon production, cosmogenic radiocarbon gets rapidly oxidized to carbon dioxide and participate in the carbon cycle of interrelated systems, carried between atmosphere,biosphere and ocean. Due its long residence time in the atmosphere, ^{14}C becomes locally mixed with the other atmospheric compounds and involved in an exchange with the upper level layer of the ocean. The measured ^{14}C change over time comes from the biosphere (trees), which receives radiocarbon from the atmosphere. Therefore, the processes involved are quite complicated. However, using the carbon cycle model and assuming that all its parameters are constant in time, the production rate can be evaluated from the measured ^{14}C data. This model is well validated for the Holocene epoch as there is no indication for a considerable oceanic change or other natural variability of the carbon cycle. However, during the last glaciation and deglaciation there were dramatic changes in the carbon cycle, especially due to ocean

ventilation. Apart from this, the lack of independent information about the carbon cycle parameters hinders qualitative estimation of solar activity from ^{14}C before the Holocene epoch (Beer, McCracken, and von Steiger, 2012). Additionally, ^{14}C data cannot be easily used for the last century, primarily because of the extensive burning of fossil fuels. This situation is also known as the Suess effect. The extensively produced greenhouse gas CO_2 dilutes the atmospheric $^{(14)}CO_2$ concentration with respect to the pre-industrial epoch. For this reason, the measured ^{14}C cannot be straightforwardly translated into the production rate and after the late 19th century, a special correction is needed as fossil fuel burning adds about an order of magnitude to the amplitude of the 11-year cycle. Moreover, this correction has a spatial and temporal dependence due to the fact that the use of fossil fuels is highly nonuniform around the globe while the cosmogenic production of ^{14}C is roughly homogeneous (Usoskin, 2017).

In summary, the production rate of cosmogenic isotopes can vary as it is affected by different factors such as variations of the cosmic-ray flux on a geological timescale due to the changing galactic background, the slowly changing geomagnetic field and modulation of cosmic rays in the heliosphere by solar magnetic activity. All slow changes in cosmogenic isotope data are ascribed to climatic changes and geomagnetic variations, while short-term fluctuations are believed to be of solar origin. Variations of the second type make past solar activity reconstructions possible.

1.2.2. Physical basis of the reconstruction method

The key concept that enters the solar activity reconstructions via cosmogenic nuclide records is the solar modulation potential Φ, i.e. the measure of fluctuations in the open solar magnetic field which carries information regarding the changes on the photospheric magnetic field and cycle amplitude. The information imprinted in cosmogenic isotopes via modulated galactic cosmic rays (GCR) helps us understand the long-term behaviour of the solar magnetic field over the Holocene epoch. As simple as it sounds, the reconstruction must step all the way from the open solar flux to sunspot number; this is a complex endeavour that entails elaborate physical models that takes different phenomena affecting the information stored in the natural archives into consideration.

The process starts with GCRs approaching the vicinity of the Solar system. The flux of these highly energetic, fully ionized nuclei is considered roughly constant. Before entering in Earth's atmosphere and magnetic field, they go through a complicated transport in the heliosphere, and their path and energy are modulated by the open solar flux. Fig. 1.10 shows the most striking feature in GCR modulation, i.e. its 11-year cycle, which is in inverse relation to the solar cycle, with a delay ranging from a month to two years with respect to the sunspots. The short-term fluctuations driven by interplanetary transients caused by solar eruptive events can also be observed (Usoskin, 2017).

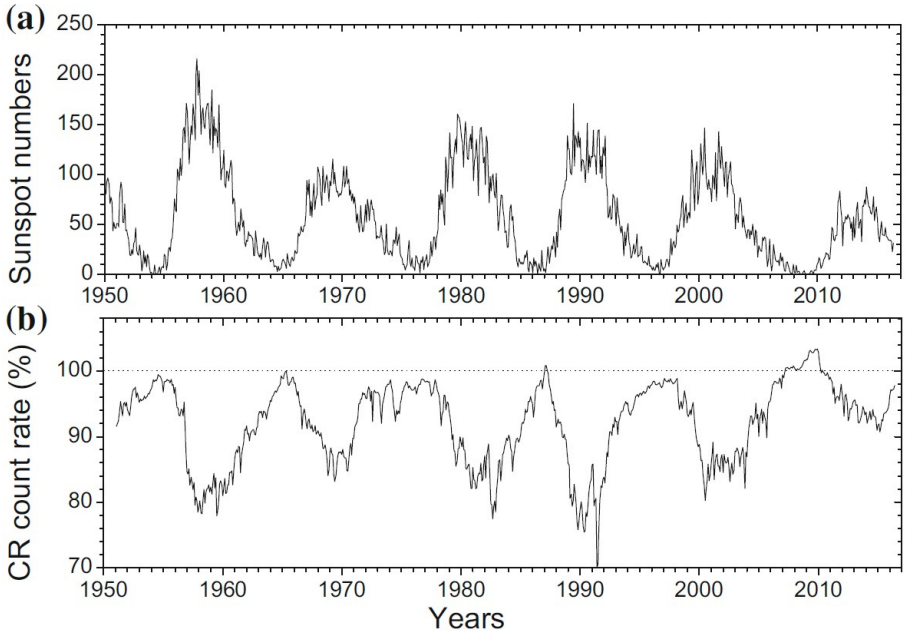

FIG. 1.10. Inverse correlation between cosmic rays and sunspot activity (Fig. 4 in Usoskin (2017)).

After entering in Earth's atmosphere, energetic GCR particles lead to an atmospheric cascade. They suffer from ionization energy losses in the upper layers and gradually decelerate while colliding with nuclei in the atmosphere, producing primary and secondary particles as a result of nuclear interactions (Beer, 2000). As reviewed in Usoskin (2017), computation of isotope production is straightforward, provided a model of the atmospheric cascade is available. Cosmogenic isotopes are a by-product of the hadronic branch of the cascade triggered by the modulated GCR flux. Therefore, in order to evaluate the GCR flux from the cosmogenic isotope data, it is essential to compute the physics of cascade development via Monte Carlo numerical methods.

Geomagnetic shielding is another important aspect of the cosmogenic radioisotope method. Radiocarbon is globally mixed in the atmosphere before deposition and its production is heavily affected by fluctuations in the geomagnetic dipole moment (Beer, 2000; Usoskin, 2017; Beer, Tobias, and Weiss, 2018). The information that these radionuclides carry on solar variability is also affected by the geomagnetic field. Hence before analyzing the data, changes in the geomagnetic field should be carefully subtracted. Diligent spectral analysis is well known to be able to pull out well-defined frequencies from chaotic time-series considering geomagnetic variability (see, e.g. Tobias, Weiss, and Kirk, 1995).

Climatic variability may also lead to some modulation, but it is inconclusive on whether changes in climate could produce comparable effects in both ice core and tree ring data. In any case, these indirect proxy data provide strong support for the hypothesis that the solar dynamo cycle is modulated, with expected terrestrial effects that are quite diverse for these

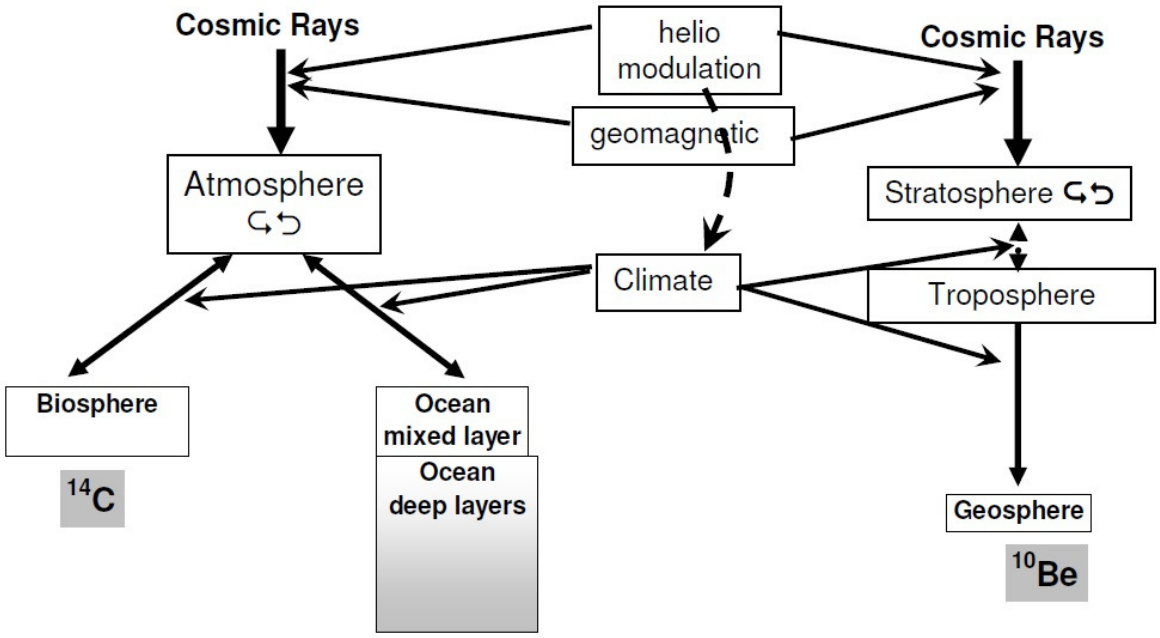

FIG. 1.11. Diagram showing the processes involved in the formation and deposition of cosmogenic isotopes used as indirect solar proxies (Fig. 7 in Usoskin (2017)).

isotopes. Comparing them can help in separating solar and climatic effects (Tobias, 2002; Beer, 2000). Fig. 1.11 summarizes all the elements playing a role in this process.

Due to a wide range of methods and results of solar-activity reconstruction, it is crucially important to verify them. The major source of errors in solar activity reconstructions is related to uncertainties that are responsible for the variations in the paleomagnetic data. These errors are much less significant for the last millenium but increasingly start to effect the statistics for the earlier times (Beer, 2000; Usoskin, 2017).

The validity of models used during reconstructions have been confirmed by independent data on measurements of ^{44}Ti stony meteorites. The reconstruction essentially depends on the temporal changes of the geomagnetic dipole field as well as on the modulation potential Φ (Usoskin *et al.*, 2006) (see also Fig.1.9). To refine the reconstructions, a deeper understanding of the effects of symmetry and morphology of the field on the solar wind is needed (Beer, Tobias, and Weiss, 2018).

1.3. Solar Activity Over Multi-Millennia

As reviewed in the previous sections, despite its common characteristics carried through over time, the solar cycle can drastically vary from one cycle to another both in amplitude and duration. The early records of sunspots indicate that the Sun went through a period of inactivity in the late 17th century (between 1645-1715) covering multiple solar cycles.

This long quiet period is known as the Maunder Minimum (MM) and the lack of sunspots during this epoch is well documented in a variety of data sets covering different naked-eye sunspot observations, the telescopic solar observations, auroral sightings at high latitudes and cosmogenic radionuclide data (Usoskin *et al.*, 2015; Poluianov, Usoskin, and Kovaltsov, 2014; Miyahara *et al.*, 2006; Ribes and Nesme-Ribes, 1993). This well-known and still puzzling period of solar inactivity also corresponds to the final, deeper phase of a climatic period called the "Little Ice Age" on Earth. The MM is considered an example of occasionally occurring Grand Minima (Miyahara *et al.*, 2006) and there is strong evidence from cosmogenic isotope data that the Sun has gone through similar periods of inactivity in the more distant past. Another, more recent but less dramatic example for such an epoch is the Dalton Minimum (DM) at the turn of the 19th century, which is another period of reduced solar activity covering 3 magnetic cycles.

As another example of an extreme feature of solar variability, there are also highly enhanced activity periods namely Grand Maximum. Grand Maxima occur when several solar cycles exhibit greater cycle amplitude than the average level for decades or even centuries. Solar cycles still occur during these grand solar maximum periods but the intensity of those cycles is much greater. The only Grand Maximum observed during the telescopic era is the Modern Maximum which began with Solar Cycle 15 in 1914, reached a maximum in Cycle 19 during the late 1950s and, came to an end in Cycle 23 in 2000 as Cycle 24 is recorded as a very low-activity cycle.

Fig. 1.12 demonstrates one most recent solar activity time series reconstructed from ^{14}C data (presented in Usoskin *et al.* (2016b)), covering the last 9,000 years. This sunspot series was prepared with the new reconstruction of the geomagnetic dipole field moment, GMAG.9k. Usoskin *et al.* (2016b) identified 20 Grand Minima and 14 Grand Maxima, most of which were listed in previous studies as well (see, e.g. Usoskin, Solanki, and Kovaltsov, 2007; Inceoglu *et al.*, 2015) and showed that the Grand Minima and Maxima occurred intermittently, with clustering near highs and lows of the Hallstatt cycle ($\simeq$ 2,400 years). The threshold cycle amplitude values determined for Grand Minima and Grand Maxima are in principle based on sunspot distribution histograms as shown in Fig. 1.13. Here, the two ends of the histogram exceeding the normal distribution fit indicate the sunspot threshold values.

1.3.1. Grand Minima

A Grand Minimum is a distinct type of period when the solar magnetic activity is significantly reduced. Grand Minima are thought to correspond to a special state of the dynamo (Sokoloff and Nesme-Ribes, 1994; Miyahara *et al.*, 2006; Moss *et al.*, 2008; Käpylä *et al.*, 2016) and these special periods challenge the solar-dynamo theory, as there is no agreement on how they occur and which mechanisms exactly affect their duration and the frequency of their occurrences.

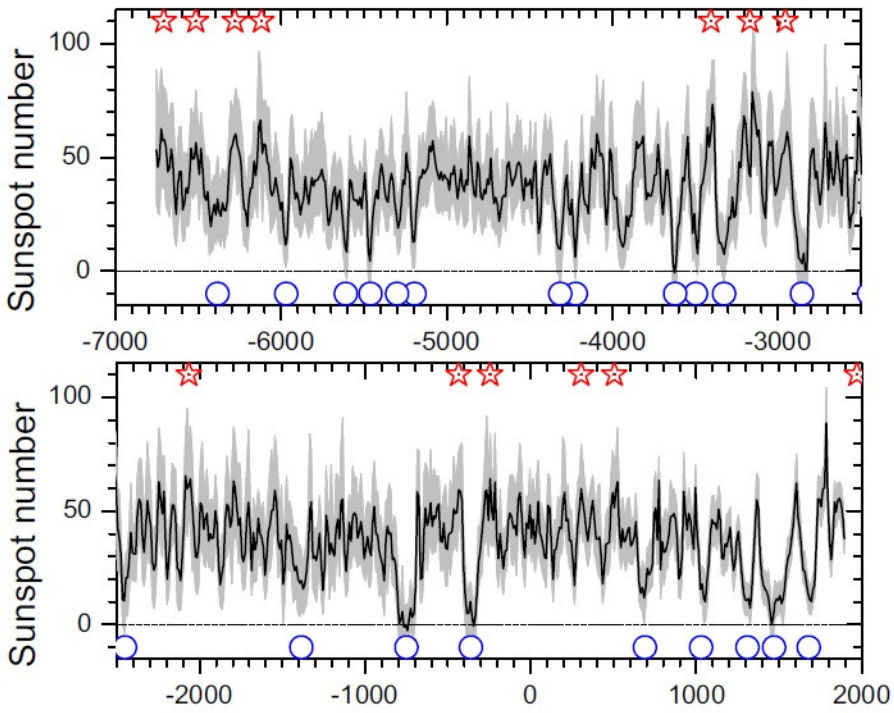

FIG. 1.12. Sunspot activity (decadal means, smoothed with a 1-2-2-2-1 trapezoidal filter) throughout the Holocene, reconstructed from ^{14}C as shown in Fig. 20 in Usoskin (2017)). Blue and red symbols denote Grand Minima and Maxima, respectively.

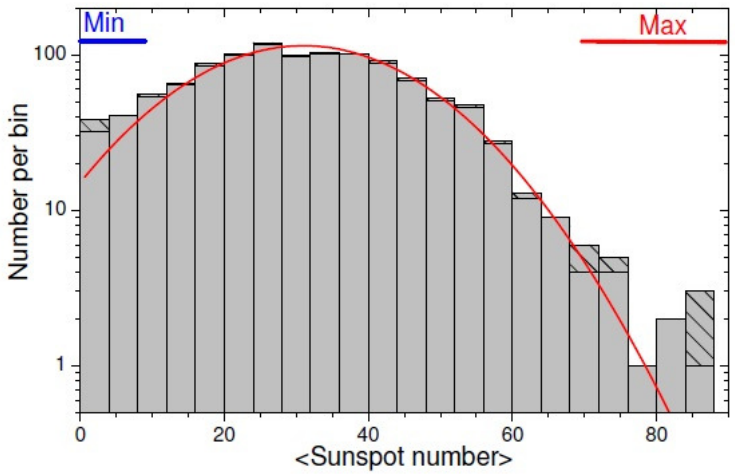

FIG. 1.13. Histogram of sunspot-numbers for the series shown in Fig. 1.8. Hatched areas correspond to directly-observed sunspots after 1610. The curve represents the best fit normal distribution (Fig. 5 in Usoskin, Solanki, and Kovaltsov (2007)).

The presence of Grand Minima in the solar activity on long-term scales has been shown multiple times by different studies (e.g. Solanki *et al.*, 2004; Usoskin, Solanki, and Kovaltsov,

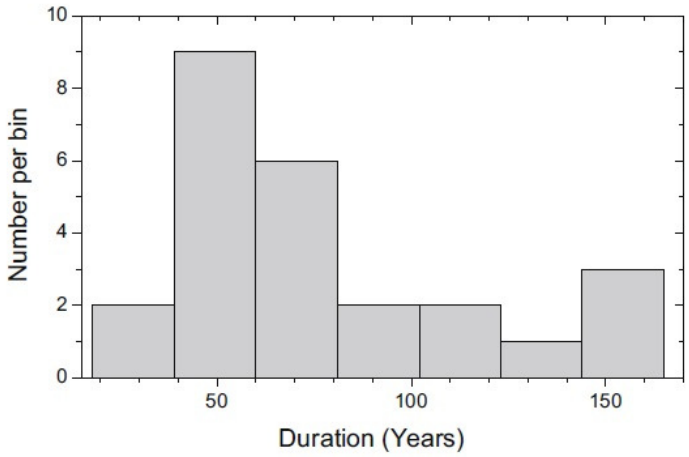

FIG. 1.14. The duration histogram of Grand Minima prepared with the time-series shown in Fig. 1.12. The distribution shows a hint of a bimodal structure, which would indicate two classes of Grand Minimum (Fig. 22 in Usoskin (2017)).

2007; Steinhilber *et al.*, 2012; Inceoglu *et al.*, 2015), using the radioisotope data of ^{14}C in tree rings and ^{10}Be in ice cores.

These studies agree that the duration distribution of Grand Minimum has a bimodal structure indicating two classes of Grand Minimum as shown in Fig. 1.14: either of a short (30–90 years) duration similar to the Maunder minimum, or a rather long one (>100 years), similar to the Spörer minimum, in agreement with earlier conclusions (Stuiver and Braziunas, 1989). The mean duration varies between 70-80 year depending on studies. Furthermore, the nature of the occurrence of such events according to waiting time distribution (WTD) analysis (see Fig. 1.15) hints that Grand Minima occur randomly, independent from each other, as the WTD seems to better fit to an exponential distribution (Usoskin, Solanki, and Kovaltsov, 2007; Usoskin, 2008, 2017). However, the number of samples in the radionuclide data is not sufficient for more robust statistics.

A Grand Minimum, when interpreted as an epoch of radical reduction of the solar cycle amplitude, can be reproduced even using relatively simple solar dynamo models that involve differential rotation and the helicity of convective flows as drivers for the dynamo waves responsible for the cyclic activity, including nonlinearities (see, e.g. Brandenburg *et al.*, 1989; Jennings and Weiss, 1991; Olemskoy and Kitchatinov, 2013). The dynamo model which is used in this study (introduced in §1.7 and §2.2) is one such model that is capable of mimicking such epochs. It is usually much harder to reproduce Grand Minimum-like events with full MHD simulations. Nevertheless, there are a few models that succeeded at generating such solar-like long-term variations (see, e.g. Augustson *et al.*, 2015). There is a rich literature, full of attempts to explain Grand Minimum as an unusual behavior of the solar dynamo/cycle (see, e.g. Moss *et al.*, 2008; Charbonneau, 2010; Karak and Choudhuri,

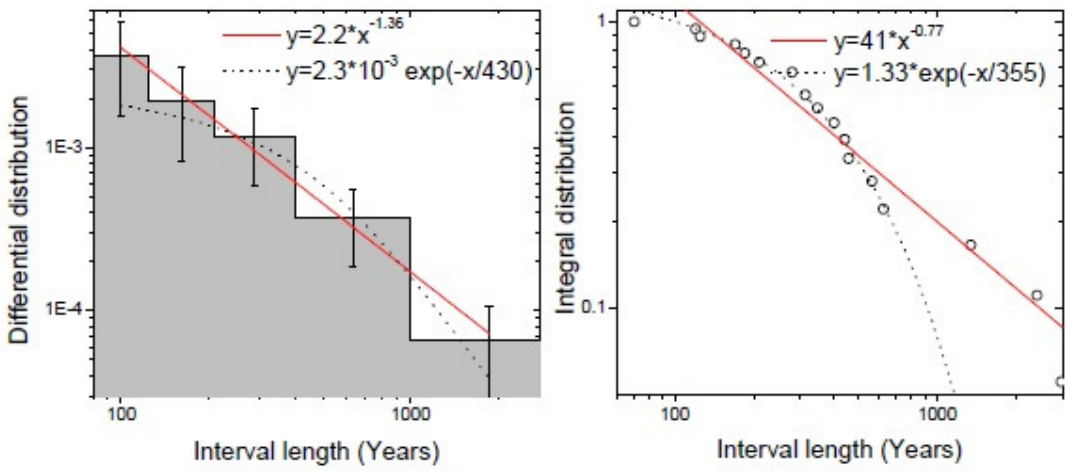

FIG. 1.15. Probability density (left panel) and cumulative (right panel) distribution of the waiting time between two subsequent Grand Minima for the series shown in Fig. 1.8. The histogram (left) and circles (right) represent the observed distribution, while solid and dotted lines demonstrate best fit power law and exponential approximations, respectively (Fig. 6 in Usoskin, Solanki, and Kovaltsov (2007)).

2011; Choudhuri and Karak, 2012; Olemskoy, Choudhuri, and Kitchatinov, 2013; Hazra, Passos, and Nandy, 2014), which we will look into in §1.6.

Now we shall get to know the most famous one, the Maunder Minimum more closely.

1.3.1.1. *The Maunder Minimum*

One known example of a quiescent period in the telescopic era is doubtlessly the Maunder Minimum (MM) during which the solar activity as recorded in sunspot data is at least of an order of magnitude lower than that present during normal solar cycles. Despite severe dearth of sunspots, the Maunder minimum (MM) cannot however be considered as an epoch with total absence of sunspots (Ribes and Nesme-Ribes, 1993), as the sunspot number becomes relatively large towards the end of it (1698-1712; observed by La Hire) (Usoskin *et al.*, 2015). Fig. 1.16 demonstrates the increasing number of sunspots and the strong hemispheric asymmetry during the second half of MM.

According to Poluianov, Usoskin, and Kovaltsov (2014), the cycle amplitude measured in the cosmogenic isotope ^{10}Be during the Maunder Minimum is comparable to that during the recent epoch of high solar activity. The partial absence of the cyclic sunspot activity gives an intuitive expectation that such suppressed activity would culminate in much smaller variations in cosmogenic isotope data. Time series and wavelet analysis (Frick *et al.*, 1997; Beer, Tobias, and Weiss, 1998; Poluianov, Usoskin, and Kovaltsov, 2014) confirms the presence of cyclic behavior of solar activity during the second half of the Maunder Minimum

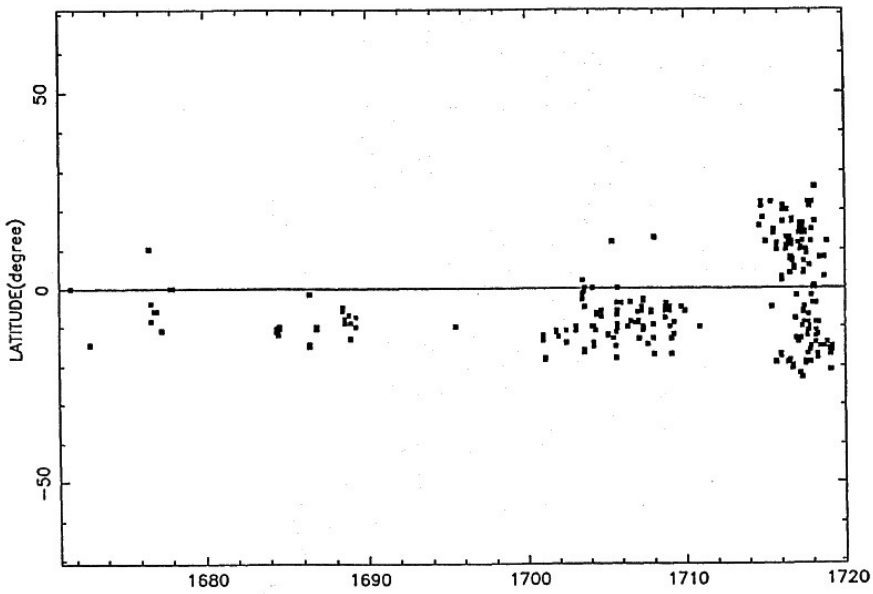

FIG. 1.16. Butterfly diagram for sunspots showing the hemispheric asymmetry during the second half of the Maunder Minimum (Ribes and Nesme-Ribes, 1993).

with a slight change in cycle length exceeding the nominal 11-year value. This increase of the cycle length is thought to be due to the phase shift between the activity before and after the Maunder minimum (Sokoloff and Nesme-Ribes, 1994). It is harder to resolve the cycle period in ^{14}C data, as radiocarbon takes part in the global carbon cycle, which leads to significant attenuation and phase shift of the 11-year cycle signal in the measured ^{14}C (Bard *et al.*, 1997). As a result of this attenuation, individual cycles can hardly be resolved in ^{14}C data, even for the recent times covering the Maunder Minimum. On the other hand, ^{10}Be data provides a much clearer idea about the cyclic behavior although it gets harder to resolve the timescales for the distant past in the deeper end of an ice core compressed by the bulk of ice-mass above it.

For the MM, the Schwabe cycles were determined (Fligge, Solanki, and Beer, 1999) with the amplitude being comparable to that of recent high cycles (Beer, Tobias, and Weiss, 1998; Berggren *et al.*, 2009). It is also demonstrated that the 11-year cycle in the ^{10}Be data may be out of phase with sunspot numbers (Usoskin, Mursula, and Kovaltsov, 2001), contrary to the normal anti-phase relation, although the reason is still to be clarified. Owens, Usoskin, and Lockwood (2012) and Wang and Sheeley (2013) claim that it might be due to the changing role of different mechanisms acting during the formation of the heliospheric magnetic flux. In any case, it has been shown that, modulated GCRs in the heliosphere may exhibit a normal 11-year cycle via the cosmogenic-isotope proxy (as shown inFig. 1.17) even when the Sun itself shows hardly any sunspot cycle (Poluianov, Usoskin, and Kovaltsov, 2014).

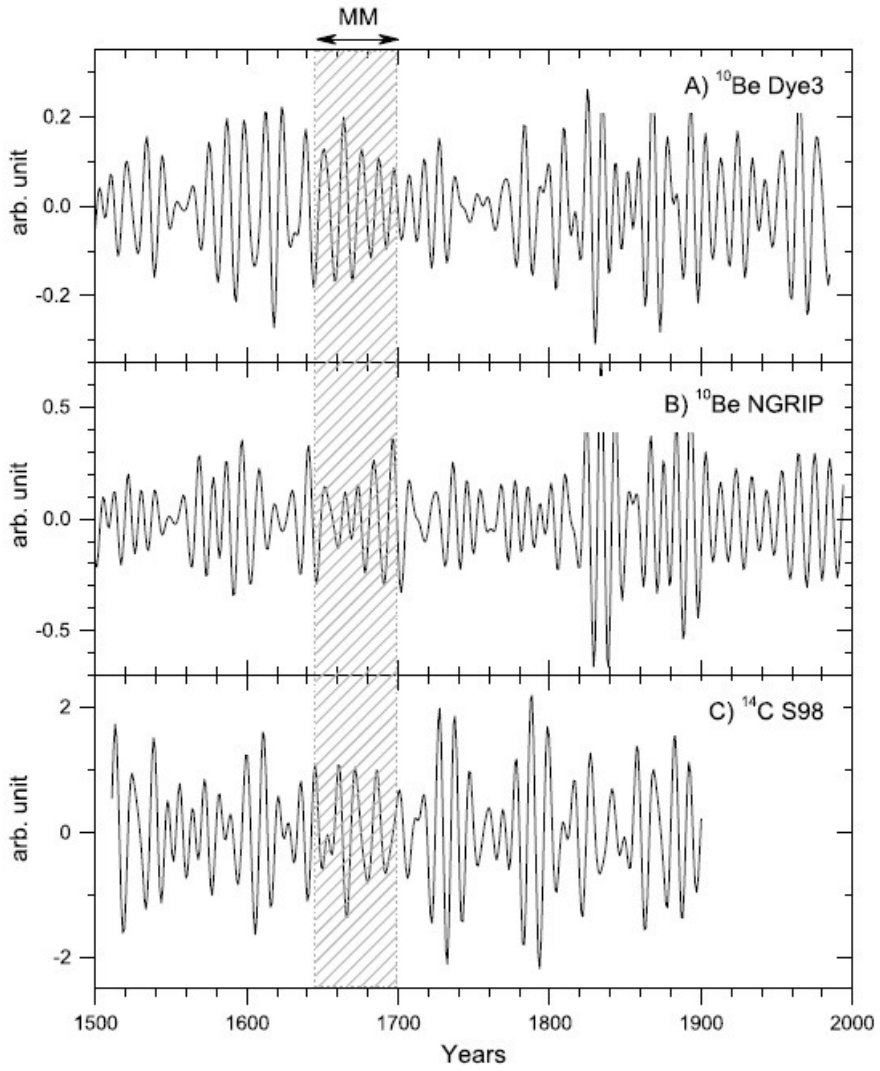

FIG. 1.17. Band-pass filtered (8 – 15 years FFT band-pass filter with rectangular window) of cosmogenic ^{10}Be measured in the Greenland Dye-3 (A), NGRIP ice cores (B) and raw ^{14}C data (C) shown in Fig. 2 in Poluianov, Usoskin, and Kovaltsov (2014). The vertical hatched area denotes the Maunder Minimum. This data shows that the amplitude of the cycles is comparable to that during the regular cycles, hence MM was not a period of complete inactivity.

Another striking feature of the MM is that, the solar magnetic activity depicts asymmetric behavior as the Sun emerged from this Grand Minimum, with sunspots only appearing in the northern solar hemisphere for a couple of solar cycles (Ribes and Nesme-Ribes, 1993; Sokoloff and Nesme-Ribes, 1994) as observations of sunspots in the late 17th century also indicate. After these two cycles, the Sun appeared to recuperate its dipolar symmetry and Hale's polarity laws is recovered (Watari, 1996). There is a clear distinction between the last cycle of the MM and the first cycle after the MM observed in the symmetry properties

of the hemispheric sunspot distribution on the photosphere as shown in Fig. 1.16. The butterfly diagram of this epoch (Ribes and Nesme-Ribes, 1993) shows an activity wave in the south hemisphere and it becomes approximately symmetric with respect to the solar equator in the last cycle once again. The recovery from a dramatic N-S asymmetry is usually considered as the end of the Maunder minimum. A dynamo interpretation of this asymmetry is possible (Sokoloff and Nesme-Ribes, 1994). During the last cycle of the Maunder minimum, the dynamo wave propagates through the Southern hemisphere only, while the dynamo waves becomes roughly N-S symmetric after the end of the minimum. The magnetic field configuration at the end of the Maunder minimum can be considered as being almost equally constituted by dipolar and quadrupolar dynamo components. Dynamo waves propagating in one (randomly, Northern) hemisphere were obtained in the numerical simulations of Jennings and Weiss (1991), while a general idea about the link between Grand Minima and North-South asymmetry of dynamo solutions was suggested by Brandenburg *et al.* (1989). We will elaborate more on hemispheric asymmetry and dipolar and quadrupolar dynamo components related to our dynamo solutions on §1.5 where the parity issue is examined.

All these findings regarding the MM coincide with the fact that low sunspot activity does not necessarily imply strong heliospheric fields and that the relation between solar activity and cosmogenic isotope production is nonlinear.

1.3.2. Grand Maxima

Grand Maxima are known as transient epochs of peculiarly high magnetic activity. Nevertheless, the definition of Grand Maximum is not as robust as the definition of Grand Minimum and is more sensitive to other parameters such as geomagnetic field data or overall normalization (Usoskin *et al.*, 2016a). The one prominent example of this sort of event is the Modern Maximum (1940-2009 approximately), accidentally coinciding with the space era. The existence of the Modern Maximum is confirmed with its various, precise and detailed in-situ and remote observation of the Sun, interplanetary medium and geosphere (Clette *et al.*, 2014; Usoskin, 2017).

In Clette *et al.* (2014), the strong anti-correlation between the number of spotless days over each sunspot cycle minimum and the amplitude of the adjoining cycles (as shown in Fig. 1.18) is presented as an indicator of the uniqueness of the Modern Grand Maximum on the centennial time scale, as the uninterrupted series of low spotless day counts (less than 400 days) during the last 6 cycles stands out. Fig. 1.19 (blue dashed line) also demonstrates the trend that leads to a higher activity epoch. The reality of the Modern Grand Maximum was also independently confirmed by Zięba and Nieckarz (2014) who have shown, by studying active versus passive (spotless) days that cycles 17-23 were more active, compared to cycles 8-15. Although uncertainties in sunspot numbers during the 18th and 19th centuries (see discussion in §1.2.1) make it a bit unclear on the centennial time scale, data on cosmogenic

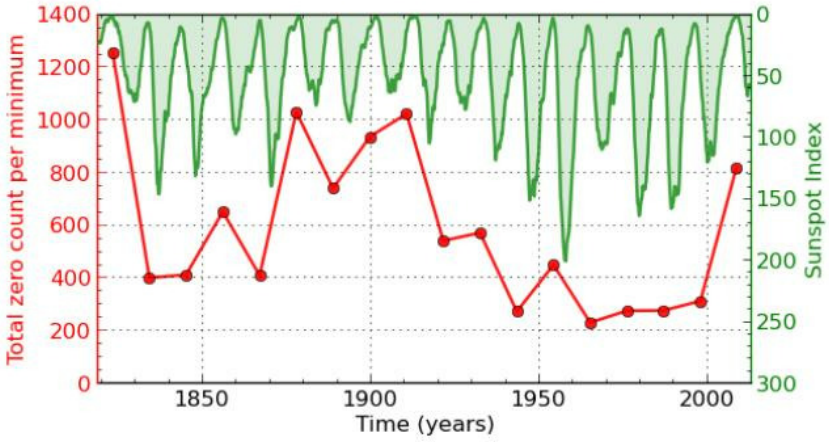

FIG. 1.18. Cycle-to-cycle variation of the total number of spotless days from cycle 6 to 24, for which daily sunspot numbers are available (red curve). The SN series is over-plotted with a reversed scale to highlight the strong anti-correlation between this indicator and the amplitude of the solar cycle. The count for the cycle 23-24 minimum is similar to the late 19th century. The first value for the cycle 5-6 minimum (Dalton minimum) is much larger (Fig. 64 in Clette *et al.* (2014)).

isotopes (Usoskin, Mursula, and Kovaltsov, 2003; Solanki *et al.*, 2004; Inceoglu *et al.*, 2015) imply that such high activity episodes occur quite seldom. However, as it seems, after the very weak solar minimum in 2008-2009 (see, e.g. Gibson, Zhao, and Fisk, 2011), solar activity returns to its normal moderate level in cycle 24. Thus, the high activity episode known as the Modern Grand Maximum is over.

Keeping all the systematic uncertainties related to the reconstructions via cosmogenic isotopes in mind, a total of 23 Grand Maxima have been identified with a total duration of around 1400 years clustering near highs of the Hallstatt cycle. According to these estimations, the Sun spends around 9-12% of its time in a hyperactive state (Usoskin *et al.*, 2016b). The distribution of the waiting time between consecutive Grand Maxima points at a deviation from exponential law (Usoskin, 2017) and most of the reconstructed Grand Maxima (about 70%) are not longer than 50 years (Barnard *et al.*, 2011). Note, that the Modern Grand Maximum is over now and we are living in an epoch of moderate or even weak solar activity. There are few dynamo models proposed for the Grand Maximum as well (see,e.g. Kitchatinov and Olemskoy, 2016). It is still a subject of investigation whether Grand Maxima correspond to a special state of solar dynamo or rather to a tail of the regular mode (Usoskin, 2017).

1.3.3. Quasi-periodicities and characteristic times

Previous studies have applied Fourier analysis to both the ^{10}Be and ^{14}C records in order to pick out various periodicities (Beer, 2000; McCracken, 2013). Reconstructions based on

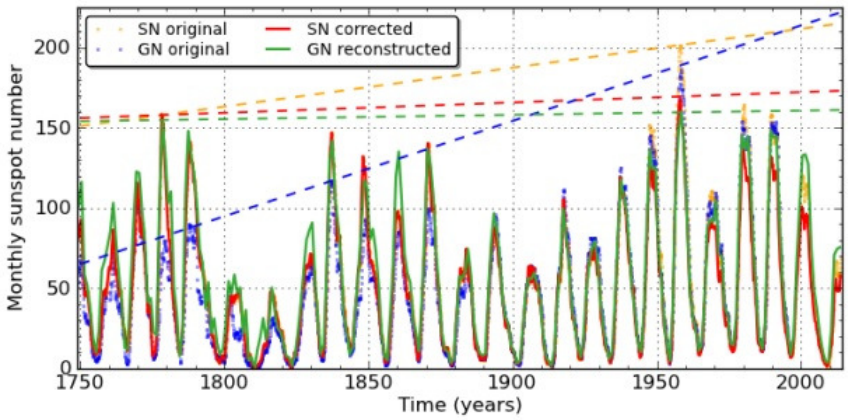

FIG. 1.19. Comparison of the original and corrected/recalibrated SN and GN series over the entire interval 1749 - 2013, showing the limited difference in maximum cycle amplitudes between the 20th century and previous centuries after the new corrections. In order to better visualize the trends, dashed lines connect the highest maxima of the 18th and 20th century, for each series of the corresponding color (Fig. 63 in Clette *et al.* (2014)).

cosmogenic radio nuclides as well as direct observations of solar magnetic activity, argue that the solar dynamo has operated similarly to the present day for at least the past 10,000 yrs. The persistence of the 87-yr Gleissberg cycle throughout supermodulation events suggests that the Hale and Schwabe cycles continue independently of the modulational mechanism for activity. We further analyze the behaviour of the solar activity during the Spörer and Maunder Minima. Such Grand Minima recur with the characteristic de Vries period of approximately 210 yr but their incidence is modulated by the Hallstatt cycle with a characteristic period of around 2,400 yr (Usoskin *et al.*, 2016b; Beer, Tobias, and Weiss, 2018).

TAB. 1. I. Table listing a summary of important solar quasi-periodicities and their duration.

Quasi-periodicity	Cycle duration (yr)	Reference
Schwabe	~ 11	(Hale, 1919)
Hale	~ 22	(Hale, 1919)
Gleissberg	60-120	(Gleissberg, 1939)
De Vries/Suess	~ 210	(Suess, 1980)
Hallstatt	~ 2400	(Vasiliev and Dergachev, 2002)

The origins of the quasi-periodicities shown in Table 1. I, especially long-term ones are not yet well-understood.

1.4. Modelling the Solar Dynamo

Solar-type stars build magnetic fields by tapping the energy of magnetized fluid motions and the sustainment of their large-scale magnetic fields is maintained by a dynamo mechanism. In rotating stars like the Sun, convection transports energy and momentum producing shearing flows and circular bulk motions to sustain the magnetic energy. In the meantime, dissipative forces continuously diffuse the field while the dynamo action regenerates it. In other words, the evolution of stellar magnetic fields is an interplay between the resistive decay and hydrodynamical induction of the magnetic field (Charbonneau, 2010, 2013). Hence, it is crucially important to model the solar magnetic cycle that cyclically alternates magnetic polarities about every 11 years as a magnetohydrodynamical process.

Nevertheless, as the post-telescopic observations and cosmogenic isotope data suggest, the solar magnetic cycle is far from being strictly cyclic, depicting short and long-term variabilities. Short-term variability includes the 154-day periodicity, quasi-biennial variations, and double-peaked maxima, whereas long-term variability refer to Grand Minimum and Grand Maximum events, the Gleissberg cycle, etc.(Hathaway, 2015). This variable nature of the Sun challenges the dynamo theories in multiple ways. Here, we will summarize the fundamentals of the solar dynamo processes drawing from multitude of excellent reviews including Solanki *et al.* (2004); Charbonneau (2010) and Cameron and Schüssler (2017), as well as the main physical mechanisms behind dynamo action and mainstream solar dynamo theories. Although there is a rich variety of solar dynamo models combining physical mechanisms supported by observations, our primary focus will be solar cycle models based on flux transport and active region decay, as the model we use in this study belongs to this class. Before looking into this specific kind of dynamo model, let's begin with the essential ingredients of solar/stellar dynamo modelling.

1.4.1. Basic concepts

Nowadays it is widely accepted that a magnetohydrodynamic dynamo is indeed responsible for generating and maintaining the magnetic field of the Sun in the solar convection zone and neighboring layers, converting the existing toroidal field to poloidal field and vice versa. There are several, credible pieces of the puzzle which aim to explain different processes in the dynamo loop. Yet, the details of how this dynamo operates still remain ill-understood and there is no strong consensus unifying different propositions (Charbonneau, 2013).

The underlining principle behind dynamo action, first pointed by Sir Joseph Larmor in 1919 (Cameron, 2016) is the inductive action of fluid motions coupled with differential rotation. His idea was widely recognized as one of a few possible explanations for the origin of this magnetic field, thus opening the path to contemporary solar cycle modelling. Alfvén's development of magnetohydrodynamics (MHD) in 1942 provided us with a concrete physical

theory to expand on Larmor's idea. Larmor's suggestion also fitted nicely with Hale's polarity laws, in that the inferred equatorial antisymmetry of the solar internal toroidal fields is precisely what one would expect from the shearing of a large-scale poloidal magnetic field by an axisymmetric and equatorially symmetric differential rotation pervading the solar interior.

According to MHD theory, we can treat the plasma as a electrically conducting fluid and use Ohm's Law to combine Maxwell's equations into a single MHD induction equation, for non-relativistic, quasi-neutral plasmas in which the length scales of interest are much larger than collisional mean-free-path of electrons and the electron/ion gyration radius:

$$\frac{\partial \mathbf{B}}{\partial t} = \nabla \times (\mathbf{u} \times \mathbf{B} - \eta \nabla \times \mathbf{B}) \tag{1.4.1}$$

where $\eta = c^2/4\pi\sigma_e$ is the magnetic diffusivity (σ_e being the electrical conductivity), and with the magnetic field being still subject to the divergence-free condition $\nabla \cdot \mathbf{B} = 0$. An evolution equation for the flow field $\mathbf{u}$ must also be provided. If we develop the outside curl and use vector identities, eq. 1.4.1 gives:

$$\left(\frac{\partial}{\partial t} + \mathbf{u} \cdot \nabla\right)\mathbf{B} = (\mathbf{B} \cdot \nabla)\mathbf{u} - \mathbf{B}(\nabla \cdot \mathbf{u}) + \eta \nabla^2 \mathbf{B} \tag{1.4.2}$$

where the term on the left is the advection of the magnetic field by the flow $\mathbf{u}$, on the right the first term is the amplification of the field by shear, the second term is the amplification of the field by compression and the last term is the dissipation of the field through diffusion. Differential rotation can amplify the field via the shear term $(\mathbf{B} \cdot \nabla)\mathbf{u}$. This shearing effect of differential rotation is also known as the Ω-effect. Eq. 1.4.2 well summarizes the inductive and dissipative terms that play crucial roles in the sustainment of the large-scale magnetic fields.

The MHD induction equation (eq. 1.4.1) is the basis for Parker's axisymmetric kinematic dynamo model in which plasma flows can generate toroidal ($\hat{\phi}$ direction) and poloidal ($\hat{r}, \hat{\theta}$ plane) fields (Parker, 1955). Parker showed that, with the induction equation, it is possible to generate a toroidal field with a purely poloidal field acted upon by rotational shearing. However, in order to close the dynamo loop, another mechanism must transform the toroidal field back to a poloidal field. Parker's solution to this problem was a process through which updrafts/downdrafts acquire cyclonicity via the action of the Coriolis force, i.e. frozen-in $\mathbf{B}$ acquires a twist, leading to a non-axisymmetric flow necessary to circumvent the anti-dynamo theorem of Cowling (1933) and generate a poloidal field to produce a global cycle. Parker's dynamo equations also provide wave-like solutions, which features the propagation of dynamo action. His groundbreaking idea was quickly followed by the development of mean-field electrodynamics, which rapidly settled as the theoretical base for solar dynamo modeling.

We know from the sunspot butterfly diagram, Hale's polarity law, the shape of the solar corona at and around solar activity minimum and synoptic magnetograms that, the large-scale solar magnetic field can be approximated as axisymmetric about the Sun's rotation axis, as well as antisymmetric about the equatorial plane. Given these circumstances we can express the large-scale field as the sum of a toroidal component in the longitudinal direction and a poloidal component in the latitudinal direction, the latter being expressed in terms of a toroidal vector potential (Charbonneau, 2010). Hence, the most general axisymmetric magnetic field can be written in spherical polar coordinates (r, θ, ϕ) as:

$$\mathbf{B}(r, \theta, \phi) = \nabla \times A(r, \theta, \phi)\boldsymbol{e_\phi} + B(r, \theta, \phi)\boldsymbol{e_\phi} \tag{1.4.3}$$

The decomposition expressed in eq. 1.4.3 satisfies the solenoidal constraint $\nabla \cdot \mathbf{B} = 0$. Inserting these into the MHD induction equation (eq. 1.4.1) produces two (coupled) evolution equations for A and B, the latter simply given by the ϕ-component of eq. (1.4.1), and the former, under the Coulomb gauge $\nabla \cdot \mathbf{A} = 0$, by

$$\frac{\partial(A\boldsymbol{e_\phi})}{\partial t} + (\mathbf{u} \cdot \nabla)(A\boldsymbol{e_\phi}) = \eta\nabla^2(A\boldsymbol{e_\phi}) \tag{1.4.4}$$

But what are the physical mechanisms that generate each of these magnetic field components from the another?

1.4.2. Dynamo models of the Solar cycle

A dynamo mechanism operating in the lower part of the solar convection zone is generally considered to be the source of the Sun's magnetic field. Most current models place the dynamo at the interface between the convection zone and the radiative core, a layer marked by convective overshooting and a strong radial shear in the Sun's differential rotation (Solanki *et al.*, 2004). As pointed earlier, currently there is no standard model for the solar dynamo. Basically, a proposed model needs to respect key observational constraints while embodying plausible mechanisms for the regeneration of poloidal and toroidal magnetic field components. Hence, we need to divide magnetic field regeneration mechanisms in two, considering the conversion from pre-existing toroidal to poloidal and from poloidal to toroidal components.

The toroidal field residing in the solar convection zone is revealed to be the source of sunspot groups by the systematic observations of the solar surface (Hale, 1919). This East-West oriented field is generated by shearing of a preceding poloidal field by the differential rotation of the Sun (Babcock and Babcock, 1955). The poloidal field in question is a dipole field aligned with the rotation axis in stellar/terrestial objects. Once the toroidal field is generated, the poloidal field is reproduced from the toroidal field by the turbulent flows and/or magnetic buoyancy upwelling in the convection zone, closing the second half of a dynamo cycle. This interaction and co-action between the toroidal and poloidal components

of the solar magnetic field leads to a 22-year magnetic cycle and an 11-year cycle of sunspot activity (Cameron and Schüssler, 2017). Therefore, physical mechanisms which lead to the generation of a toroidal field from a pre-existing poloidal component $P \Rightarrow T$, and a poloidal field from a pre-existing toroidal component $T \Rightarrow P$ must be taken into consideration during modelling. Furthermore, the solar poloidal magnetic component flips polarity near sunspot cycle maximum (as seen in the magnetogram shown in Fig. 1.5), when internal toroidal field T is thought to have its peak value, whereas the poloidal component P peaks at time of sunspot minimum. This cyclic regeneration of the Sun's full large-scale field can thus be thought of as a temporal sequence from $P(+) \Rightarrow T(-) \Rightarrow P(-) \Rightarrow T(+) \Rightarrow P(+) \Rightarrow ...$, where the $+$ and $-$ refer to the signs of the poloidal and toroidal components, as established observationally (Solanki *et al.*, 2004; Charbonneau, 2010).

While $P \Rightarrow T$ conversion is explained with a rotational shearing mechanism, there exist various candidates proposed for the $T \Rightarrow P$ conversion. Some noteworthy examples are cyclonic convection (Parker, 1955) and the surface decay of bipolar magnetic regions (Babcock, 1961), now known as the Babcock-Leighton (BL) mechanism. After the development of Helioseismology, there have been other attempts to explain $T \Rightarrow P$ mechanism such as helical waves along thin magnetic flux tubes (Schmitt, 1987; Ossendrijver, 2000), and shear instabilities in the tachocline (Dikpati and Gilman, 2001a). The common point of all these cases is that the frozen-in magnetic field threading inductive plasma flows becomes twisted through the effect of the Coriolis force, and rotational influence is enforced on the inductive flows, which overcome Cowling's anti-dynamo theorem by breaking the axisymmetry of the field (Charbonneau, 2013).

Ultimately, understanding the operation of the solar dynamo giving rise to such a magnetic cycle is connected to unravelling how differential rotation, turbulent convection, and meridional flows co-function. Helioseismological observations bring new constraints on differential rotation and meridional flows covering almost the entire CZ (see Fig.1.2). Hence, the quest for modelling the solar dynamo is challenged by the lack of measurements of the solar interior and in order to generate credible models, it is essential to have some constraints on the deep, internal magnetic fields as well.

From the existing observational constraints so far, we know that a reliable model should reproduce the basic features of the solar cycle such as: cyclic polarity reversals with around an 11-year half-period, the equatorward migration of the sunspot-generating deep toroidal field and its inferred strength, the poleward migration of the diffuse surface field, the observed phase lag between poloidal and toroidal components, the polar field strength, observed antisymmetric parity and the predominantly negative (positive) magnetic helicity in the Northern (Southern) solar hemisphere. As the complexity level of a model increases, it may also exhibit more sophisticated features like phase locking, the Waldmeier Rule (anticorrelation rule between cycle amplitude and duration), the Gnevyshev–Ohl Rule (alternation

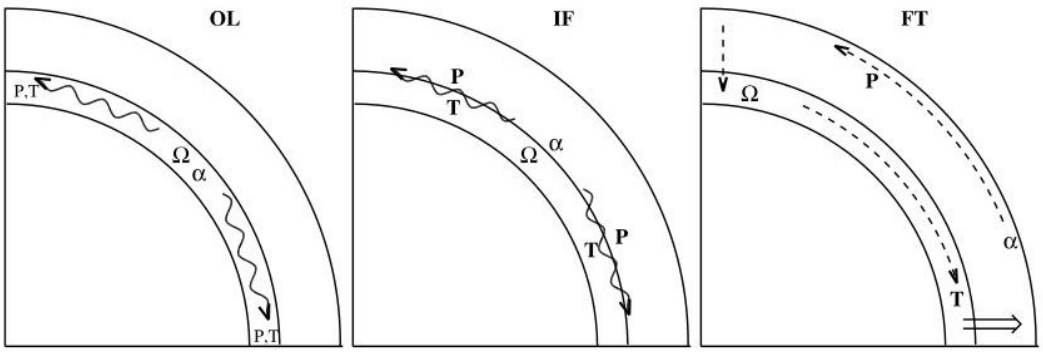

FIG. 1.20. Illustration showing where α and Ω effects reside in different classes of dynamo models. From left to right, an overshootlayer dynamo, an interface dynamo and a flux transport dynamo are demonstrated in the form of quadrants from a meridional cut, in Fig. 9 of Solanki, Inhester, and Schüssler (2006).

of higher-than-average and lower-than-average cycle amplitudes) and occasional epochs of suppressed amplitude and of high-level activity over many cycles a.k.a. Grand Minima and Grand Maxima (Charbonneau, 2010).

Despite its many virtues, conventional $\alpha\Omega$-dynamo operating in the bulk of the convection zone has difficulties in reproducing the latitudinal migration of the sunspot zone since the radial rotational shear is much smaller than the latitudinal shear in the convection zone and dynamo waves propagate along isolines of angular velocity (Yoshimura, 1975; Kitchatinov, 2002; Brandenburg, 2005). Moreover, in such models, Parker's turbulent α-effect of cyclonic convection, cannot act efficiently upon such strong fields. Some of the various possible models for overcoming these problems can be classified into the following three types as summarized in Solanki, Inhester, and Schüssler (2006) (for detailed reviews, see Ossendrijver (2005); Rüdiger and Hollerbach (2004); Schüssler and Schmitt (2004)):

- overshoot layer dynamos: the α-effect is restricted to the overshoot region, when turbulence is weaker,
- interface dynamos: the Ω-effect is dominant in the overshoot region while a typical α-effect operates in the convection zone and strong magnetic fields build up only in underlying convectively stable layers, the coupling element of both regions being magnetic diffusion,
- flux transport dynamos: the radial transport of magnetic flux into the overshoot layer and the latitudinal migration of the magnetic field are dominated by advection by a large-scale meridional flow.

The basic ingredients of these three classes of models are illustrated in Fig. 1.20. Perhaps the most studied cases of flux transport dynamos are the Babcock-Leighton dynamo models

(Wang and Sheeley, 1991; Dikpati *et al.*, 2005; Charbonneau, 2010), based on the principle mechanism suggested by Babcock (1961) and Leighton (1969), in their early models of the solar cycle. The key idea in these models is the regeneration of the large scale dipole field via the decay of bipolar active regions. The meridional field from the azimuthal field component is thought to originate from the twist enforced by the Coriolis force on azimuthal flux tubes rising through the upper layers of the convection zone. The apparent indicator of this twisting effect is the latitudinal tilt of active regions at the photosphere. While the radial shearing in the tachocline governs the Ω-effect, it is hypothesized that the generated poloidal field is transported by a large-scale meridional circulation in the convective envelope, a combination of the observed polewards surface flow and a conjectured equatorwards subsurface return flow (Choudhuri, Schussler, and Dikpati, 1995; Dikpati and Charbonneau, 1999; Nandy and Choudhuri, 2001; Solanki, Inhester, and Schüssler, 2006).

The flux transport by a meridional flow idea has been integrated in some models of overshoot-layer dynamos (see Dikpati and Gilman, 2001a) and interface dynamos (see Dikpati *et al.*, 2005) as well. We will not heavily examine each of the cases listed above, but instead will have a more general look at the advection-dominated dynamos with Babcock–Leighton (BL) mechanism for regeneration of a poloidal magnetic field, originally proposed by Choudhuri, Schussler, and Dikpati (1995) and Durney (1995).

1.4.2.1. *The Kinematic Approach*

There are basically two possible approaches to the solar dynamo problem; one of which is via direct numerical simulations (DNS) in which all the MHD equations are solved numerically, the other being the kinematic approach, in which the velocity field is specified from the beginning and one solves only eq. 1.4.1 for the evolution of the large-scale magnetic field.

In general, DNS considers the Lorentz forces associated with the growing magnetic field which basically acts on the inductive flows once they get stronger and gain dynamical significance. This results in the decrease of the exponential growth characterizing supercritical linear solutions and even it makes the growth stop, opposing the driving fluid motions (Charbonneau, 2013). This phenomenon is called the backreaction of the Lorentz Force and models that take this physical effect into consideration, uses the dynamical approach.

On the other hand, as physically relevant as it is, adding this effect to a model can be complicated. Indeed in that case the Reynolds stresses powering the large-scale flows in the solar convective envelope should then also be modelled (Charbonneau, 2013), and obviously numerical simulations with the dynamic approach use more computation time. Therefore, some simplification without eliminating the central mechanisms responsible for sustaining the cyclic dynamo behavior can be beneficial to focus on the effects of certain mechanisms while dealing with relatively less parameters.

This is where the kinematic approach comes in, which implies a major simplification of the MHD equations. Basically, in this approach, the flow (velocity) field $\mathbf{u}$ is specified *a priori*, hence the only equation left to be solved during computation is the induction equation (eq. 1.4.1) which becomes truly linear in B (Charbonneau, 2013). Helioseismological observations (Thompson *et al.*, 1996) have provided us with new measurements of differential rotation throughout the interior, and the meridional circulation in the outer half of the solar convection zone with good precision. These measurements revealed that the kinematic approximation is still a good working assumption at least for the differential rotation part of the mean flow $\mathbf{u}$, given the low amplitude of observed torsional oscillations in the convective envelope and the lack of significant cycle-related changes in the internal solar differential rotation (Charbonneau, 2010).

The model used in this study embraces the kinematic approach, which uses steady parametrized large-scale flow fields compatible with surface and helioseismology observations (see §1.7).

1.4.2.2. *Mean-field theory*

The mean-field theory is based on the idea that, under certain conditions, small-scale turbulence in the solar convective zone can produce large-scale magnetic fields. The dynamo models based on this principle remain among the prevalent scenarios to explain dynamo action in the solar/stellar interiors. The key building block on which mean field theory rests is the two scale approach, which consists in a decomposition of the field variables into mean and fluctuating parts (Charbonneau, 2013). This was first achieved by Steenbeck and Krause (1966), who reformulated Parker's idea by decomposing the fields and flows into average ($\langle\mathbf{B}\rangle; \langle\mathbf{u}\rangle$) and fluctuating ($\mathbf{B}'; \mathbf{u}'$) components. These two-component fields and flows are inserted into the induction equation eq. (1.4.1) and averaged in such a way that $\langle\mathbf{B}'\rangle$ and $\langle\mathbf{u}'\rangle$ vanish, leaving the following new form:

$$\frac{\partial \mathbf{B}}{\partial t} = \nabla \times (\langle\mathbf{u}\rangle \times \langle\mathbf{B}\rangle + \langle\mathbf{u}' \times \mathbf{B}'\rangle - \eta \nabla \times \mathbf{B}) \tag{1.4.5}$$

where the turbulent electromotive force $\langle\mathbf{u}' \times \mathbf{B}'\rangle$ is expressed through a truncated series expansion in terms of the large-scale magnetic field:

$$\langle\mathbf{u}' \times \mathbf{B}'\rangle \equiv \alpha\langle\mathbf{B}\rangle + \beta\nabla \times \mathbf{B}, \tag{1.4.6}$$

thus achieving closure. The essential toroidal-to-poloidal process is contained in the α tensor, where Parker's helical twisting mechanism can be expressed in a tensorial form. The Ω-effect contained in β plays the role of an enchanced "turbulent diffusivity". The simplest and most commonly used implementation of kinematic mean-field dynamo models reduces

these tensors to scalar quantities under near-homogeneous and near-isotropic conditions.In an axisymmetric formulation, eq. (1.4.1) can be decomposed into two parts: eq. (1.4.1) concerning the time evolution of the purely toroidal magnetic field B and the poloidal vector magnetic potential A. Transforming those expressions into a non-dimensional form reveals three dimensionless numbers which govern the axisymmetric mean-field dynamo models:

$$C_\alpha = \frac{\alpha_{LS} R_\odot}{\eta_t}, \tag{1.4.7}$$

$$C_\Omega = \frac{\Omega_0 R_\odot^2}{\eta_t}, \tag{1.4.8}$$

$$R_m = \frac{u_0 R}{\eta_t} \tag{1.4.9}$$

where C_α and C_Ω are the dynamo numbers. In the context of large-scale astrophysical magnetic fields, the importance of the α mechanism in eq. (1.4.7) is immediately evident as it acts as an inductive mechanism and makes it possible to drive a mean current parallel to the mean toroidal field, which, in turn will regenerate a poloidal field thereby closing the dynamo loop. The third term, R_m, is a dimensionless magnetic Reynolds number, which measures how effective the advection due to meridional circulation is in the transport of A and B components in meridional planes compared to diffusion (Charbonneau, 2013).

For simplicity of notation, we continue to use η for the total magnetic diffusivity, retaining the possibility of variation with depth and with the understanding that within the convective envelope this now includes the (dominant) contribution from the β term of the mean-field theory.

1.4.2.3. *Solar Flux Transport dynamos (FTD)*

After the first attempts of combining flux emergence and surface transport (Wang and Sheeley, 1991), helioseismology revealed new constraints on the internal structure of the velocity field, i.e., the large-scale, axisymmetric meridional flow and the differential rotation revealed by Thompson *et al.* (2003), which led to the idea of the flux-transport dynamo (Wang, Nash, and Sheeley, 1989; Choudhuri, Schussler, and Dikpati, 1995; Dikpati and Charbonneau, 1999; Küker, Rüdiger, and Schultz, 2001; Hotta and Yokoyama, 2010). This scenario was developed to successfully explain some features of the solar activity such as the equatorward migration of sunspots and the poleward migration of the surface field (Hotta and Yokoyama, 2010).

Flux transports model of the solar cycle are commonly constructed by solving eq. (1.4.3) and decomposing it in a set of coupled partial differential equations for the magnetic field's axisymmetric toroidal and poloidal components. One key component of such dynamos is the

meridional circulation, which is thought to manifest itself in turbulent, stratified rotating convection due to an imbalance between Reynolds stresses and buoyancy forces (Charbonneau, 2010). Assuming that there are no source terms exterior to the domain boundaries, we consider the inductive action of a steady, axisymmetric flow on an axisymmetric magnetic field on large spatial scales. We write the mean velocity field in the following form:

$$\mathbf{u} = \Omega(r,\theta) r \sin\theta \boldsymbol{e_\phi} + \Big[u_r(r,\theta)\boldsymbol{e_r} + u_\theta(r,\theta)\boldsymbol{e_\theta} \Big], \tag{1.4.10}$$

where $\Omega(r,\theta)$ is the angular, differential velocity and $[u_r(r,\theta)\boldsymbol{e_r} + u_\theta(r,\theta)\boldsymbol{e_\theta}]$ is the velocity of the meridional circulation $\mathbf{u}_m$. Substituting eq. 1.4.3 and eq. 1.4.10 in eq. 1.4.1 we obtain two equations describing the time evolution of poloidal and toroidal components of the magnetic field:

$$\frac{\partial A_\phi}{\partial t} = -\frac{1}{\varpi}(\mathbf{u}_m \cdot \nabla)(\varpi A_\phi) + \eta\left(\nabla^2 - \frac{1}{\varpi^2}\right) A_\phi, \tag{1.4.11}$$

$$\frac{\partial B_\phi}{\partial t} = -\varpi(\mathbf{u}_P \cdot \nabla)\left(\frac{B_\phi}{\varpi}\right) + \eta\left(\nabla^2 - \frac{1}{\varpi^2}\right) B_\phi + \varpi(\nabla \times (A\boldsymbol{e_\phi})) \cdot \nabla\Omega + \frac{1}{\varpi}\frac{\partial \varpi B}{\partial r}\frac{\partial \eta}{\partial r} - B\nabla\cdot\mathbf{u}_m. \tag{1.4.12}$$

where $\varpi = r\sin\theta$ and the terms including $\mathbf{u}_m$ (with its components u_r and u_θ) correspond to advective flow by the meridional circulation. Although equations (1.4.11) – (1.4.12) lack the necessary source terms that sustain the large-scale magnetic field, they lay the basis of an $\alpha\Omega$ dynamo model with flux transport and summarize how toroidal and poloidal fields feed each other and sustain the continuity of the dynamo loop. The third $\nabla\Omega$ term on the the right hand side, however, is a source term, in that it can lead to the growth of B as long as A does not decay away.

Meridional circulation is one of the fundamental dynamo ingredients (see Fig. 1.24) which has an essential role in transporting the magnetic flux generated. The poleward flow at the surface neighboring the active region belts has been measured helioseismically down to $r/R_\odot = 0.85$ and obeying mass conservation, an equatorward return flow is logically required. The cycle period of the dynamo loop is determined by the flow velocity of this meridional plasma-field movement to a great extend (Karak *et al.*, 2015).

For a dynamo model to be classified as a flux transport dynamo, the equatorward propagation speed of the deep-seated toroidal field needs to be comparable to the propagation speed of the dynamo wave, where the circulation-dominated magnetic field transport leads. In this case, the cycle period is primarily determined by the circulation's turnover time as it is not heavily affected by the value of the turbulent diffusivity.

On the other hand, if the circulation speed is low, it can lead to a Doppler shift in the dynamo wave, creating a small change in the cycle period (Charbonneau, 2013). Re-assessing sunspot records within the context of FTD models have a potential to provide more insight into cycle properties such as amplitude and cycle variation, and extreme events like Grand Minima (Karak *et al.*, 2015), which mold long-term solar variability.

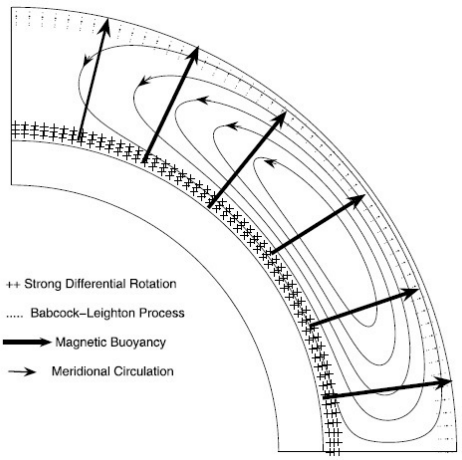

FIG. 1.21. A cartoon explaining how the flux transport dynamo works. The diagram shows a single meridional quadrant, with the rotation axis coinciding with the left boundary and the meridional flow confined to the convection zone and upper tachocline (Fig. 1 in Choudhuri (2015)).

1.4.2.4. *Babcock-Leighton Mechanism (BL)*

Babcock-Leighton dynamos are characterized by the generation of a poloidal field through the decay and dispersal of tilted bipolar active regions (sunspots), which agrees best with the surface observations and by the generation of a toroidal field through the observed differential rotation (see Fig.1.22 and 1.23).

It all started with Babcock (1961) proposing a scenario describing the cyclic behavior of the solar dynamo in terms of a consistent physical approach based on bipolar active regions. In this scenario, the existing poloidal magnetic field represented by the global dipole is twisted by differential rotation resulting in loops of azimuthal field rising due to magnetic buoyancy and eventually tilted sunspot groups and bipolar magnetic regions (BMRs) with the leading sunspots closer to the equator than the following sunspots as they break through the surface. The tilting angle is observed to increase with latitude. BMR tilts go through a preferential cancellation of leading-polarity magnetic flux across the equator, leaving a net polarity flux on each hemisphere, eventually spreading over the hemisphere and migrating poleward. This phenomenon leads to the reversal of the global dipole field which in turn becomes the source of the (reversed) toroidal field of the next activity cycle, thus leading to a 22-year magnetic cycle. The mathematical form of Babcock's idea is eventually developed by Leighton (1969) as two coupled partial differential equations (both in time and latitude), representing the toroidal and poloidal components of the azimuthally averaged (axisymmetric) magnetic field. Additionally, in terms of a diffusion model, Leighton (1969) included

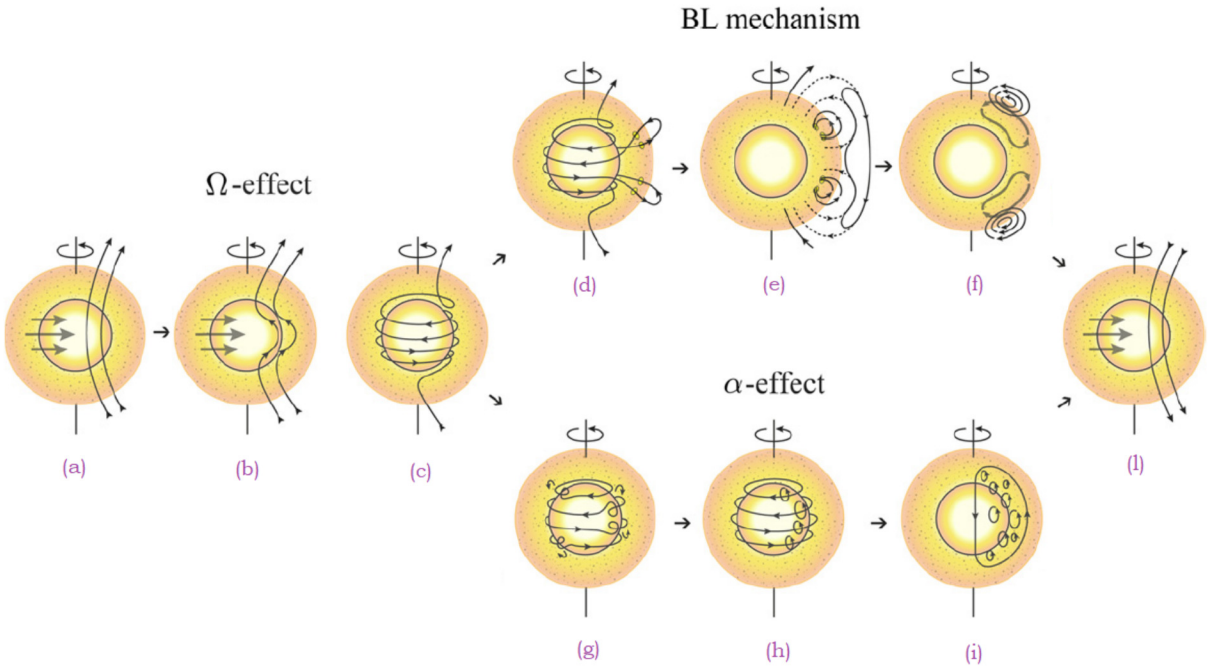

FIG. 1.22. A diagram explaining the solar flux-transport dynamo processes. For the regeneration of a toroidal field, two alternative mechanisms, the BL mechanism and a small-scale α-effect are being introduced as adapted from Fig. 1 in Sanchez, Fournier, and Aubert (2014). (a,b,c) illustrate the generation of the toroidal component from a large-scale poloidal field, where the toroidal field is produced by the shearing of the poloidal field by the solar differential rotation near the convection zone bottom. Then, when the toroidal field strength is strong enough, buoyant loops rise to the surface being twisted as they rise and form sunspots. (d,e,f) shows the BL mechanism where additional flux emerges and spreads in latitude and longitude from decaying spots. And finally, the meridional flow carries the surface magnetic flux poleward, causing polar fields to reverse. Alternatively, the BL mechanism illustrated in (d,e,f) may be replaced by the turbulent α-effect, shown in (g,h,i), acting on the toroidal field at the base of the convection zone. While many models are based on either one of these mechanisms for the $T \Rightarrow P$ conversion, some models (like the one used in this study) rely on both mechanisms.

radial shear to the differential rotation, treating the transport of surface magnetic flux by supergranular flows (Cameron and Schüssler, 2016).

Observations support the hypothesis that the reversal of the polar surface field takes place through the poleward transport and accumulation of poloidal flux originating from tilted BMRs. It is yet to be discovered whether this is an active component, or a passive side-effect of the regenerative cycle of the solar magnetic field (Charbonneau, 2005). In the recent versions of the BL model, a meridional circulation in the convective envelope is usually added to bring this surface poloidal field down to the base of the convection zone, to the thin

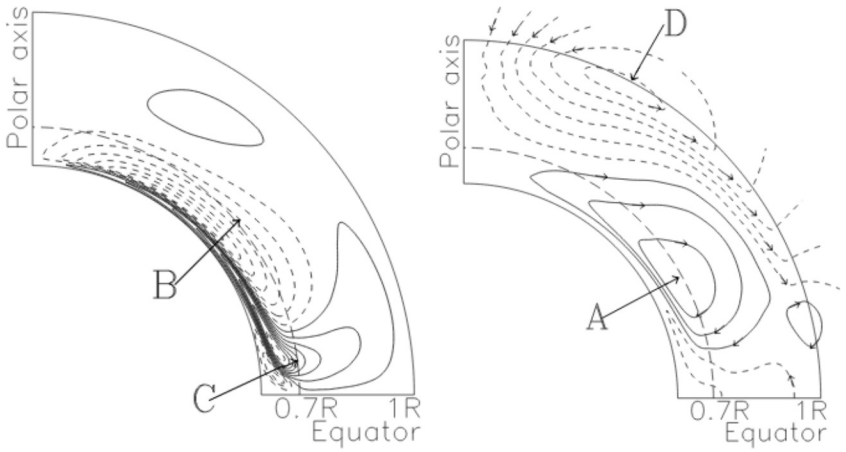

FIG. 1.23. Snapshot of the toroidal field (left) and poloidal field (right) plotted in a meridional quadrant as in Fig. 8 in Charbonneau and Dikpati (2000), showing the large-scale evolution of the magnetic field in a Babcock-Leighton type dynamo model.

rotational shear layer called the tachocline where field amplification and storage is thought to take place in solar-like dynamos (Wang and Sheeley, 1991; Durney, 1995; Dikpati and Charbonneau, 1999; Nandy and Choudhuri, 2002; Guerrero and Muñoz, 2004). The bottom row (BL mechanism) of Fig.1.22 demonstrates this case where solar flux-transport dynamo processes as in the BL mechanism merged with an internal meridional circulation.

What makes the BL mechanism stand out as a plausible explanation is that it can be directly observed operating at the photosphere, and it is far better constrained than any other mechanism proposed. Particularly, the distribution of tilt angles of BMRs with respect to the East-West direction, is well estimated from white light (Howard, 1991; Dasi-Espuig *et al.*, 2010) and magnetographic observations (Wang, Nash, and Sheeley, 1989). Recently, new constraints on the operation of the solar dynamo and the validity of the BL scenario have become available. The polar fields at activity minimum are shown to be a good proxy to estimate the strength of the following solar cycle (Wang and Sheeley, 2009; Svalgaard, Cliver, and Kamide, 2005; Muñoz-Jaramillo, Balmaceda, and DeLuca, 2013). This idea became more formally recognized when Cameron and Schüssler (2015) demonstrated that the net toroidal flux in one solar hemisphere generated by differential rotation is determined by the emerged magnetic flux at the solar surface. They also concluded that the latitudinal differential rotation is the dominant generator of net toroidal flux, whereas the shear layer near the surface (Thompson *et al.*, 1996; Barekat, Schou, and Gizon, 2014) plays only a minor role.

Another important study by Cameron and Schüssler (2016) was to amalyze the observed properties of the sunspot butterfly diagrams to understand the effect of turbulent magnetic diffusivity on the toroidal field in the convection zone. They found the turbulent diffusivity

to be in the range 150 – 450 $\mathrm{km^2 s^{-1}}$, placing the solar dynamo in the 'high-diffusivity' regime. Together with the inference of a high turbulent diffusivity, all these relevant observational results obtained since 1969, concerning the poleward meridional flow at the surface and the measurement of the differential rotation in the convection zone by helioseismology, provide us with constraints to build more realistic dynamo models of the solar cycle.

1.5. Parity

The solar global field has a distinct parity with a dominantly dipolar configuration, i.e., antisymmetric about the equator. Polar fields almost always have different signs between hemispheres, even though they show a weak, but significant North–South asymmetry in phase and amplitude, which may be due to the inhomogeneous formation of magnetically complex sunspot groups (Roy, 1977). In this regard, parity is also a measure of hemispheric asymmetry, both in the poloidal and toroidal components of the large-scale field. As illustrated in Fig. 1.24, for instance, the antisymmetric mode or the odd-parity ($P = -1$) for the toroidal field (B_ϕ) refers to a dipole whereas the even-parity ($P = 1$) is associated with a quadrupolar mode where B_ϕ is symmetric about the equator. Analysis of sunspot cycle data by Hathaway *et al.* (1996) puts forward that the solar hemispheres are magnetically coupled in a particular parity mode, which is nearly always antisymmetric for the toroidal field, as described by Hale's polarity law.

Additionally, another interesting feature of the sunspot data as shown in Fig. 1.16 is that the distribution of sunspots when exiting from the Maunder Minimum is asymmetric through the hemispheres, largely accumulated in the Southern Hemisphere for about three magnetic cycles. As the Sun comes of out this period, the large-scale solar magnetic field becomes dominantly dipolar once again. Here, the modulation is thought to be linked with changes in parity (symmetry) (Ribes and Nesme-Ribes, 1993).

One focus of investigation has been to try to understand how dynamo processes lead to a particular parity mode in the Sun and the results from different solar dynamo models differ in details. Some studies have suggested that the α-effect around the base of the convection zone leads to the production of the large-scale dipolar magnetic field, pointing out that circulation dominated solar dynamo models with the BL mechanism for producing the poloidal field near the surface may not give the observed magnetic configuration with the expected parity (see Dikpati and Gilman, 2001b; Bonanno *et al.*, 2002). In their circulation dominated models, Dikpati and Gilman (2001b) as well as Bonanno *et al.* (2002) solved the dynamo equations in the full sphere and concluded that an α-effect mimicking the BL mechanism concentrated near the solar surface excites a quadrupolar mode in which the toroidal field is symmetric across the equator, which is being the opposite of what is observed. Only when the α-effect is placed near the bottom of the CZ, is a dipolar parity established, in agreement with the observations.

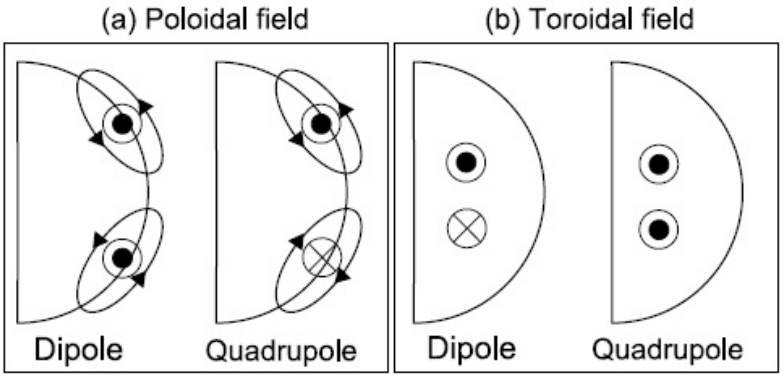

FIG. 1.24. Illustration of the different parity configurations from Fig. 1 of Hotta and Yokoyama (2010). Panel (a) shows the poloidal fields (line) for a dipole and a quadrupole field and the corresponding vector potentials. Panel (b) shows the toroidal field for a dipole and a quadrupole.

However, Chatterjee, Nandy, and Choudhuri (2004) do not agree with this conclusion as they demonstrated that the dipolar parity is the preferred parity if the diffusivity of the poloidal component is sufficiently high in circulation dominated BL models, even when the helical effect is concentrated near the solar surface. Hence the exact necessity of the α-effect in producing the solar dipole field is still inconclusive. The parity of the stellar global magnetic field seems to depend on which field component (toroidal or poloidal), is more coupled by the turbulent diffusivity between the hemispheres and further systematic parameter studies are needed to understand the parity issue (Hotta and Yokoyama, 2010).

Our simulation results agree with those of Chatterjee, Nandy, and Choudhuri (2004),who generated a solar-like dipolar magnetic configuration with BL mechanism operating near the surface. However, the secondary source term - the turbulent α-effect close to the base of the convection zone $(0.70 - 0.85 R_\odot)$ by itself produces only a quadrupolar or symmetric toroidal field with no active regions, in other words no dipolar field. §2.4.2 elaborates on the parity issue and how these two dynamo mechanisms with different parities interact during Grand Minima/Maxima.

1.6. Grand Minima Scenarios

One of the unsolved pieces of the solar dynamo puzzle is the occurrence of Grand Minima whose existence poses a challenge to the solar dynamo modelling (§1.4). There is a rich literature on the subject including a variety of hypothesis, with none being completely satisfactory. Yet, there are a few leading ideas that can roughly be categorized in two classes.

One plausible explanation for Grand Minima is the modulation of the cycle amplitude in an extreme way by the dynamo mechanisms generating the cycle. Scenarios based on amplitude modulation involve nonlinear magnetic back-reaction of the Lorentz force on the

plasma flows, which causes amplitude variations on timescales longer than the main cycle period (see, e.g. Tobias, 1997; Pipin, 1999; Küker, Arlt, and Rüdiger, 1999; Moss and Brooke, 2000). In such non-kinematic models including this backreaction, the regular cyclic behavior continues, but the cycle amplitude periodically falls below the threshold necessary for the formation of the strong toroidal magnetic flux ropes that will rise through the convective envelope to produce sunspots at the surface (Charbonneau, Blais-Laurier, and St-Jean, 2004). This scenario is also thought to arise due to the interaction between two co-existing dynamo modes of opposite parity with respect to the equatorial plane (Sokoloff and Nesme-Ribes, 1994; Tobias, 1997; Beer, Tobias, and Weiss, 1998; Charbonneau, 2005).

The second type of scenarios in which this backreaction of the Lorentz force is not taken into account is based on intermittency, i.e. a transition between a regular cycle and unusually supressed epoch with a magnetic field too weak for sunspot formation (Charbonneau, Blais-Laurier, and St-Jean, 2004). Alternation between these two distinct states happens irregularly and can be the result of stochasticities inherent to the dynamo model or by external random noise (Platt, Spiegel, and Tresser, 1993). Intermittent behavior has been seen in various solar dynamo models (see, e.g. Schmitt, Schuessler, and Ferriz-Mas, 1996; Moss and Brooke, 2000; Ossendrijver, 2000; Charbonneau, 2001; Ossendrijver and Covas, 2003).

The different models demonstrate that solutions can display both types of modulation in different parameter regimes and with the existing data, it is still not possible to make a clear distinction between these two types of explanations. Reconstructions made with cosmogenic isotope records across the Maunder Minimum (Beer, Tobias, and Weiss, 1998; Poluianov, Usoskin, and Kovaltsov, 2014) demonstrate sustained cyclic activity (see Fig. 1.17) that could be explained by amplitude modulation. From another point of view, the observed random occurence of Grand Minima and the variability of their durations are the features more easily reproduced in intermittency-based models. The distinction is expected to become clearer once the nonlinear relationship between sunspot formation and the total strength of the dynamo-generated internal magnetic field is better understood.

Another essential aspect to consider in modelling Grand Minima is whether the dynamo model is self-exited or not. An $\alpha\Omega$ dynamo model is self-excited, while a model based on the BL mechanism or flux tube instabilities for poloidal field regeneration is not. The crucial difference is that in a non-self-excited model, if the primary dynamo cannot sustain itself at very low magnetic field strengths, a secondary inductive mechanism must be implemented to restart it again, which is the case for the model used in this study. Many solar cycle models, whether self-excited or not, achieve the production of long-term variability, including Grand Minima and Maxima, through forced stochastic fluctuations of the dynamo source terms. Additionally, in proper parameter intervals, the distribution of Grand Minima duration and

waiting times constructed from simulation outputs are in approximate agreement with radioisotope records, showing exponential behavior with a memoryless, random trigger. Here follows several dynamo model cases categorized by their specific behaviors.

In self-excited nonlinear solar dynamo models without a lower operating threshold on the field strength/sunspot formation (see, e.g. Passos and Lopes, 2012; Cameron and Schüssler, 2017), amplification remains possible even if the magnetic field falls to very low levels. A stochastic forcing (e.g. by the turbulent electromotive force) can push the dynamo solution into the subcritical regime and later back into the supercritical regime. This type of amplitude modulation scenario is called *on-off intermittency* (Platt, Spiegel, and Tresser, 1993). It offers a simple explanation for Grand Minima but the operation of the dynamo must be maintained close to the critical regime all the time. An example of this type is the stochastically-forced, 2D kinematic axisymmetric mean field-like dynamo model of Kitchatinov and Olemskoy (2012) that runs in the mildly supercritical regime, so that Grand Minima occurs through on-off intermittency. This model also includes a non-local surface source term capturing the BL mechanism without adapting a lower field strength threshold on its poloidal source term. For similar cases, see also Ossendrijver and Hoyng (1996); Moss *et al.* (2008); Usoskin, Sokoloff, and Moss (2009).

In the case of non-self-excited nonlinear dynamo models of the solar cycle in which source terms are subjected to a lower operating threshold on the magnetic field regeneration (e.g. BL-type models), a different and more dynamical intemittency scenario known as *in-out intermittency* is at play. Here the criticality threshold is defined with a bifurcation point and the cycle amplitude is characterized by a finite basin of attraction (Devaney, 1989; Charbonneau, 2013). In such a scenario, initial solutions starting above or below the limits of the basin converge to $\mathbf{B} = 0$, causing the cyclic activity to shut down. The recovery from this situation necessitates another inductive term that can bring the dynamo back to its operation regime. The desired situation can be achieved by magnetic noise or a turbulent α-effect. The kinematic 2D mean-field-like model of Passos *et al.* (2014) is an example of this sort using the BL mechanism for poloidal field reproduction, a solar-like differential rotation, a quadrupolar meridional flow and a turbulent α-effect to boost the primary dynamo in the absence of the BL source term (see, also Choudhuri and Karak, 2012; Olemskoy and Kitchatinov, 2013).

There is also a non-kinematic version of self-excited dynamos which includes nonlinear magnetic backreaction on large-scale flows during the regeneration of the poloidal component from an existing toroidal field. This mechanism is characterized by the magnetic Prandtl number which characterizes the ratio of momentum diffusivity (viscosity) and magnetic diffusivity. In the low Prandtl number regime, such models can produce extreme amplitude modulation such as those characterizing Grand Minima and Maxima. There is a variety of

models falling under this category (see, e.g. Pipin, 1999; Kitchatinov *et al.*, 1999; Brooke, Moss, and Phillips, 2002; Bushby, 2006).

Finally, there are higher-level, 3D global magnetohydrodynamical simulations of turbulent convection zone and dynamo action embodying many dynamo mechanisms and their joint operation is capable of reproducing both extreme amplitude modulation and intermittency (see, e.g. Augustson *et al.*, 2015; Käpylä *et al.*, 2016).

Among the different types presented above, our model (Lemerle and Charbonneau, 2017) can be categorized as a kinematic non-self-excited dynamo model sharing similarities with Passos *et al.* (2014). The initial condition is a dipole and it is the preferred solution, although the parity is free to evolve in the simulations. Therefore, we would except to observe an in-out type intermittent behavior. However, stochastic and deterministic effects due to nonlinear coupling of two dynamo mechanisms in the kinematic model also leads to surprising effects that are discussed more in depth in the paper presented in Chapter 2 (Ölçek et al. 2018, submitted).

1.7. The 2X2D Hybrid Babcock-Leighton Solar Dynamo Model

The Lemerle and Charbonneau (2017) model from which we started is actually made up of two sub-simulations and it is calibrated using real magnetographic data for activity cycle 21. It is called 2×2D because it is based on the coupling of a surface flux transport (SFT) simulation with a mean-field-like interior dynamo model. In other words, it couples a two-dimensional simulation on a spherical surface, to a two-dimensional simulation on a meridional plane, each simulation providing the source term required by the other. As summarized in Lemerle and Charbonneau (2017), the numerical implementation proposed for carrying out this BL scheme is in principle straightforward:

1. New bipolar magnetic regions are continuously injected into the STF (see Fig. 1.25) at times, latitudes and longitudes. Fluxes and polarity are generated at the solar surface through a (probabilistic) flux emergence algorithm based on the strength and spatial distribution of the deep-seated magnetic fields in the FTD.
2. The surface transport equation is solved on the solar spherical surface and generates the expected cancellation, decay, transport and specific features typically observed in surface magnetograms.
3. The flux transport dynamo equation is solved in the meridional plane, using the evolving results of the surface simulation as a time-dependent upper boundary condition on the poloidal field. Shearing by differential rotation eventually builds up strong toroidal magnetic fields deep in the convection zone;
4. The dynamo loop is closed by allowing this deep-seated magnetic structure to generate the emergences and returns back to the beginning of this sequence.

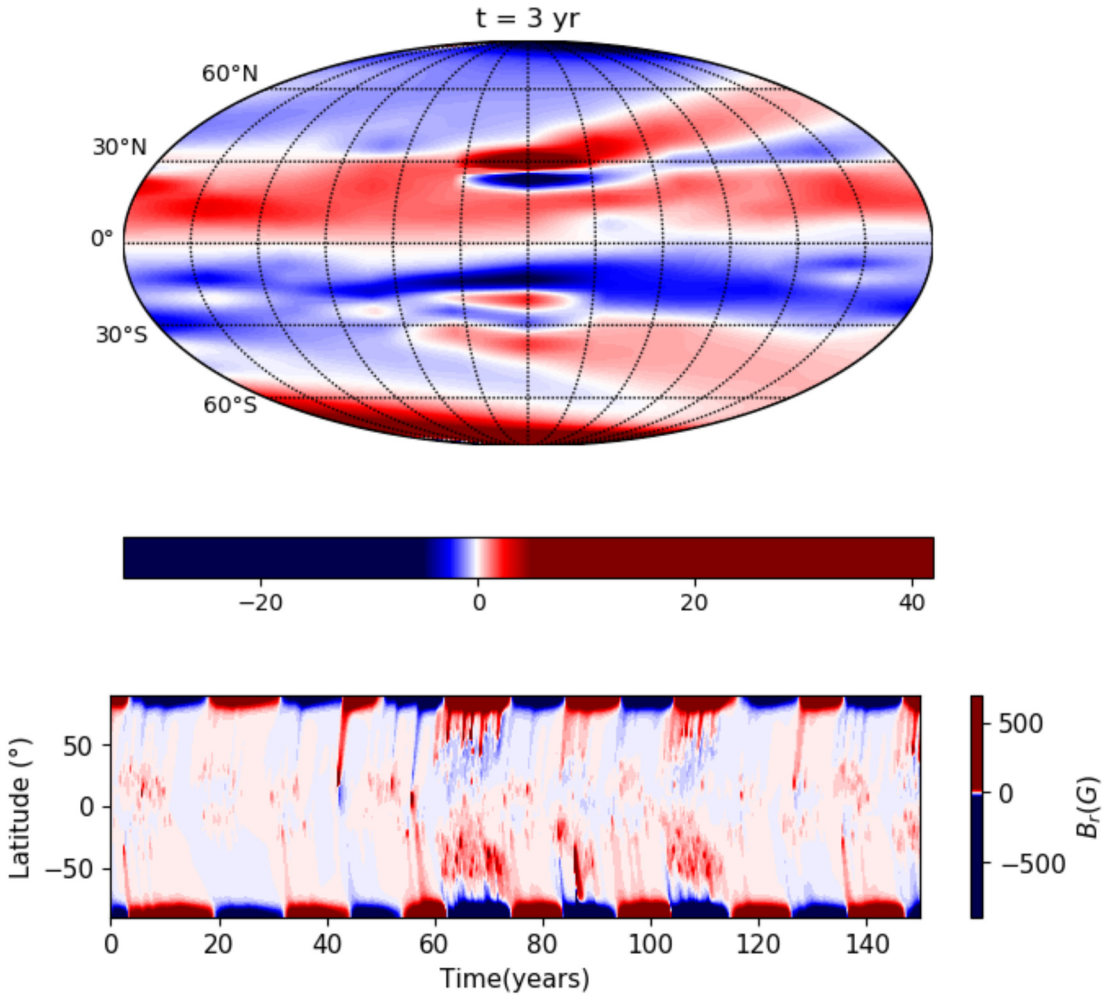

FIG. 1.25. *Top*: Mollweide projection of the radial field on the photophere generated by SFT (Lemerle and Charbonneau, 2017) at t = 3 years. *Bottom*: Evolution of the surface radial field for 1000 years $K = 0.35$, $\alpha_0 = -12$ cm s^{-1}, $B_0 = 200$ G, $B_Q = 150$ G, $\eta_c = 10^8$ cm^{2}s^{-1}, $\eta_t = 10^{12}$ cm^{2}s^{-1}. Note the good hemispheric synchronicity in the polar field reversal and variability in the cycle length.

The characteristics of the model, which makes it an excellent tool to study long-term solar variability as well as to make short-term predictions, are that it is extremely well-constrained with the observations (calibrated with cycle 21 data), it has short and secular fluctuation patterns agreeing with the observations and the dipole strength in each new cycle arises naturally. Furthermore, it runs much faster compared to a kinematic 3D model, such as that of Miesch and Dikpati (2014).

The model also includes the following effects to achieve the solar-like pattern:

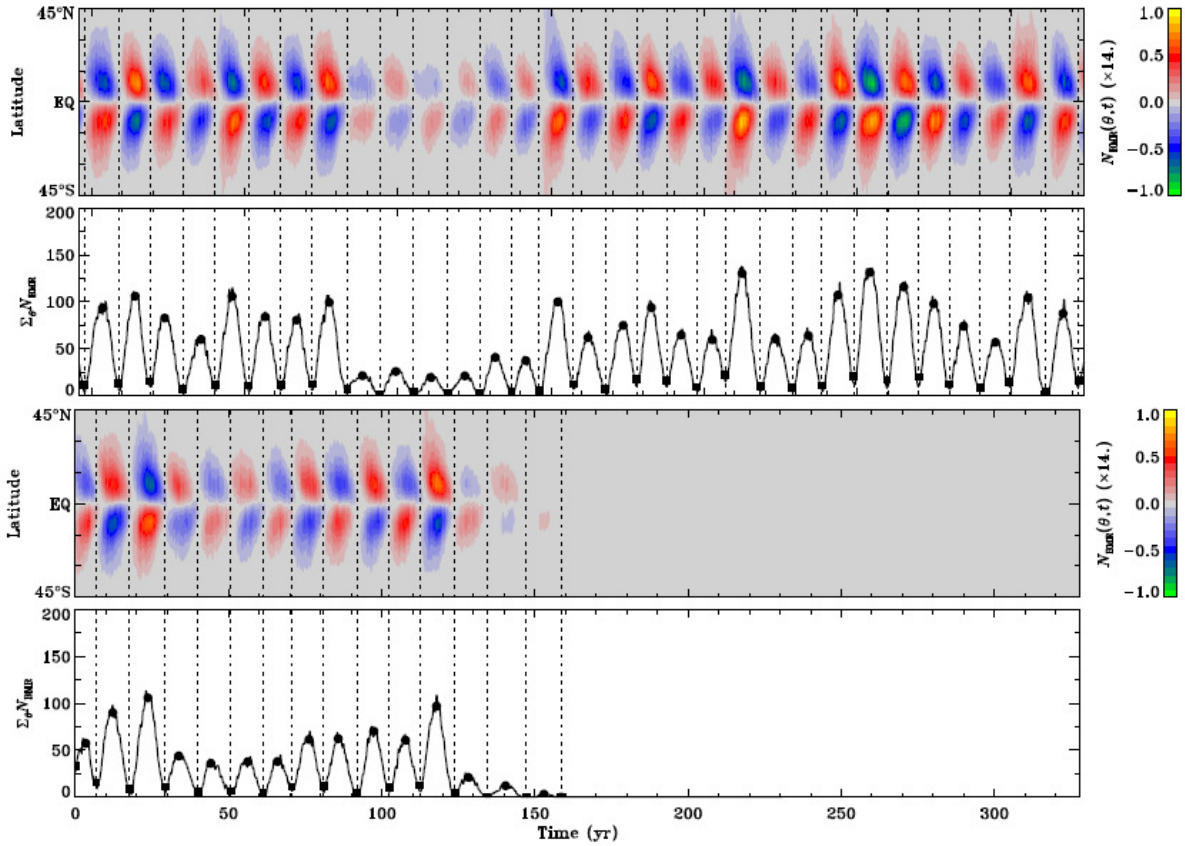

FIG. 1.26. Time-latitude butterfly diagram and pseuso sunspot number as a function of time. This is a simulation result from the original version of the model with the BL mechanism depicting a Dalton-like Grand Minimum in the first two rows. After a while, the dynamo action does not sustain and dies off as shown in the last two rows (Fig. 10 in Lemerle and Charbonneau (2017)).

1. turbulent diffusion at the surface and in the convection zone,
2. poleward meridional flow at the surface and an equatorward return flow transporting the toroidal flux,
3. latitudinal differential rotation and the near-surface layer of radial rotational shear and
4. flux emergence in the form of tilted bipolar magnetic regions treated as a source term for the radial surface field.

Besides these principal features of the original model, we also needed an additional source to elevate the magnetic energy when it is too low for the BL mechanism to operate. This additional inductive mechanism is chosen to be the most likely candidate used in such cases: the turbulent α-effect. Any other source of small-scale magnetic perturbation may do the job. Fig. 1.26 demonstrate the behavior of the model without this secondary effect and how the dynamo can go into a grand minimum state without coming out of it. This situation,

which is examined in detail in Nagy *et al.* (2017), occurs due to the stochastic nature of emergences in the model.

It has been pointed that if the BL mechanism is the sole inductive source of the poloidal magnetic field, then an secondary mechanism is required to pull the dynamo out of a Grand Minimum phase. There is a vast literature with representative models demonstrating the viability of these proposed "kickstart" processes (Charbonneau, 2001; Charbonneau, Blais-Laurier, and St-Jean, 2004; Choudhuri, Schussler, and Dikpati, 1995; Choudhuri and Karak, 2012; Karak *et al.*, 2015; Kitchatinov and Olemskoy, 2013; Passos *et al.*, 2014; Sanchez, Fournier, and Aubert, 2014). These different source terms are usually chosen in different strengths and spatial localizations and with some level of fine tuning to achieve a solar-like cycle period and to trigger Grand Minima at the observed frequency that is required (Karak *et al.*, 2015; Passos *et al.*, 2014).

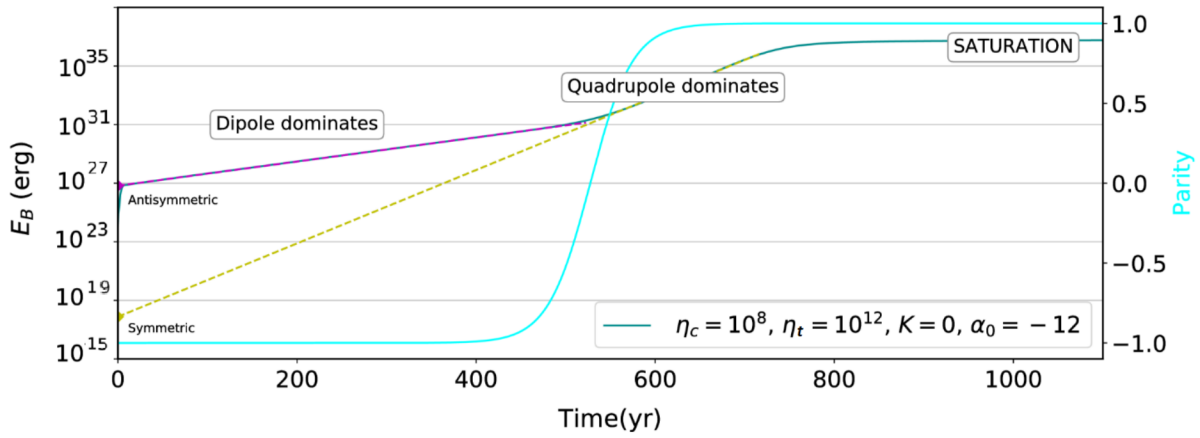

FIG. 1.27. Growth of the α-dynamo. Once the dynamo is saturated, it has only a quadrupolar component despite the initial dipole field. Parameters are fixed at $\alpha_0 = -12$ cm s^{-1}, with $K = 0$, $B_0 = 200$ G, $B_Q = 150$ G, $\eta_c = 10^8$ cm^{2}s^{-1}, $\eta_t = 10^{12}$ cm^{2}s^{-1}.

The small-scale α-effect mechanism used in this study is an alternative mechanism proposed to explain the production of a poloidal magnetic field from an existing toroidal field. It is based on the link between the small scale turbulence and the mean magnetic field. Both, the BL mechanism and the α-effect include a twisting action on the magnetic field. However, while BL mechanism is based on the Coriolis force acting on buoyantly-rising large-scale magnetic flux tubes, the turbulent α-effect occurs due to cyclonic updraft/downdraft imparting small-scale twists on large-scale $\mathbf{B}$. The term described in eq. 1.7.1 represents the electromotive force by the small-scale fluctuating components of the field and the flow, capturing this effect. It is possible to re-express this term as described below in an analytic *ad hoc* form,

$$\alpha(r,\theta;B) = \frac{\alpha_0}{1+(B/B_0)^2} f(r,\theta) \tag{1.7.1}$$

where α_0 is the amplification parameter of the α-effect, B_0 is the threshold value for the magnetic toroidal field and the f function expresses other dependencies to r and B_ϕ. This remains an extreme oversimplification of the complex interaction between the flow and the field that is known to characterize MHD turbulence, but it is widely used in solar dynamo modelling (Charbonneau, 2010). Therefore, this effect is integrated into the model and it will be elaborated more upon in §2.2.2. We present an in-depth analysis to explore the effects of different values of α_0 as well as other parameters influencing the behavior of the model one by one in the Annex.

1.8. Presentation of the Study

A research article is currently in draft form for the purpose of presenting the analysis results throughout this Master's project and we anticipate to submit the paper to the international research Journal *Solar Physics* in September, 2018. An advanced draft of this paper is included as Chapter 2 of this thesis. As the first author of the article, I performed all the analysis and produced all the figures presented and performed and developed most of the analysis codes. My research director Paul Charbonneau, who is the second author of this paper, made major contributions to the text and provided guidance and insights on all the analysis conducted. The article is being written by two of us. The third author Alexandre Lemerle is the principle creator of the Babcock-Leighton model used in this study and provided assistance in the addition of the turbulent α-effect. Gabriel Longpré and Florence Boileau, undergraduate summer interns, are included as co-authors of this paper as they conducted a "proof-of-concept" exploratory calculations in the summer of 2016 under the supervision of Paul Charbonneau. Throughout this study, after modifying the spatial zone of the α-dynamo, I conducted a thorough exploration of the model parameter space, performed a large set of very long simulations and analyzed their outputs in order to understand the physical underpinning and statistics of Grand Minima/Maxima produced by the model. Some additional results of this thesis work are also presented in the Annex to this thesis.

Results from this project have been presented in various workshops and conferences in Solar Astrophysics and Space Physics research: the Canadian Solar Workshop 2017 at Station de Biologie des Laurentides (QC), Solar Heliospheric and Interplanetary Environment (SHINE) Conference 2017 in St-Saveur (QC), NASA Heliophysics Summer School 2017 in

Boulder (CO, USA), Scientific Committee on Solar-Terrestrial Physics (SCOSTEP) Conference 2018 in Toronto (ON), SHINE 2018 in Orlando (FL, USA) as well as at Laboratory for Atmospheric and Space Physics (LASP) in Boulder (CO, USA) as an invited speaker.

Chapter 2

GRAND ACTIVITY MINIMA AND MAXIMA THROUGH DUAL DYNAMOS

Deniz Ölçek[1], Paul Charbonneau[1], Alexandre Lemerle[2],
Gabriel Longpré[1], Florence Boileau[1]

2.1. ABSTRACT

Reconstructions of past solar activity based on cosmogenic radioisotopes have reavealed that the Sun spends a significant fraction ($\sim 20\,\%$) of its time in aperiodically recurring states of so-called Grand Minima or Grand Maxima, namely epochs of strongly supressed and markedly above-average levels of magnetic activity, respectively. The physical origin of these episodes is not yet understood. In this paper we present a dual dynamo model of the solar cycle, combining a dominant dynamo based on differential rotation shear and surface decay of bipolar active regions, and a weak, deep-seated turbulent dynamo. The resulting dynamo simulations are found to exhibit the equivalent of observed Grand Minima and Maxima. By adjusting the magnitude and saturation level of the secondary turbulent dynamo, we can reproduce well the duration and waiting time distributions of Grand Minima and Maxima inferred from the cosmogenic isotope record. The exit from Grand Minima episodes is typically characterized by strong hemispheric asymetries, in agreement with sunspot observations during the 1645–1715 Maunder Minimum. In these simulations, Grand Maxima can be unambiguously identified as a distinct dual-dynamo state resulting from constructive interference between the two dynamos mechanisms operating within the simulation. This interaction leads to the autonomous production of long quasiperiodicities in the millenial range, commensurate with the Halstatt cycle. Such quasiperiodic modulation, readily produced through dynamical backreaction on large-scale flows in non-kinematic dynamo models, is quite uncommon in a purely kinematic solar cycle model such as the one developed herein.

[1]Département de Physique, Université de Montréal, C.P. 6128, Succ. A, Montréal, Québec, Canada.
[2]Collège de Bois-de-Boulogne, 10555 av. Bois-de-Boulogne, Montréal, QC, H4N 1L4.

We argue that these long periodicities are set by the long diffusion time of the magnetic field accumulating in the stable layers underlying the turbulent convection zone.

2.2. Introduction

Governing space climate in the heliosphere and structuring the Earth's upper atmospheric layer and magnetosphere, the Sun is a magnetically active star showing cyclic magnetic activity with a primary quasi-periodicity of approximately 11 years. The 400-years sunspot record reveals that the activity cycle is far from being strictly periodic and that it exhibits long-term fluctuations (Hathaway, 2009) on decadal to at least centennial timescales. This long term variability includes multi-decadal episodes of very low activity, during which sunspots vanish almost completely, such as the 1645-1715 Maunder Minimum (Eddy, 1976; Ribes and Nesme-Ribes, 1993), as well as sustained period of markedly above-average activity, such as the 1940-2000 Modern Maximum (Usoskin, 2013).

The cosmogenic isotopes such as ^{10}Be in ice cores and ^{14}C in tree rings allow to investigate long-term solar variability much farther into the past (Beer *et al.*, 1990; Usoskin, Solanki, and Kovaltsov, 2007; Knudsen *et al.*, 2009; Steinhilber *et al.*, 2012; Usoskin *et al.*, 2016b). These radioactive isotopes are being produced through spallation reactions triggered by the entry of energetic cosmic rays in the Earth's atmosphere. The cosmic ray flux at Earth's orbit, in turn, is modulated by the strength of the heliospheric magnetic field. Hence the production rates of these isotopes show a strong inverse correlation with solar activity (Usoskin, 2017). Solar activity reconstructions based on radioisotope data (e.g. Solanki *et al.*, 2004; Usoskin, Solanki, and Kovaltsov, 2007) shows that the Sun went through several Maunder Minimum-like and Modern Maximum-like episodes throughout the Holocene epoch.

Different data sets and analysis suggest the existence of two types of Grand Minima, the *short* Maunder-like Minima, and the *long* Spörer-like Minima, spanning over a century. Overall, the Sun spends between 17% and 27% of its time in a Grand Minimum state, and between 8% and 22% time in a Grand Maximum state (see Usoskin, Solanki, and Kovaltsov, 2007; Inceoglu *et al.*, 2015; Usoskin *et al.*, 2016b). Analyses of waiting time distribution (WTD) between Grand Minima/maxima have so far remained inconclusive, with both exponential and power-law WTD providing equally acceptable fits to the various data sets; the former being indicative of a stationary memoryless random process (e.g. Usoskin, Solanki, and Kovaltsov, 2007), while the latter would imply a physical process with long-term "memory" (Usoskin *et al.*, 2014; Inceoglu *et al.*, 2015). These analyses unfortunately have limited statistical significance, due to the small number of Grand Minima and maxima events present in the extant cosmogenic isotope record (see Usoskin, Solanki, and Kovaltsov, 2007; Usoskin, 2017; Vecchio *et al.*, 2017). Such reconstructions nonetheless provide important information regarding the mode of operation of the solar dynamo.

Broadly speaking, dynamo-based explanations of Grand Minima can be subdivided into two main classes: extreme amplitude modulation and intermittency. Under the amplitude modulation scenarios, the same cycle operates continuously, but with large modulation of the internal field strength unfolding on timescales longer than the primary cycle. Whenever the internal field strength falls below the threshold required for the generation and destabilization of magnetic flux ropes, sunspot production ceases and a Grand Minimum ensues. Support for this interpretation can be found in residual cyclic activity observed in the ^{10}Be record during the Maunder Minimum (Beer, Tobias, and Weiss, 1998; Ribes and Nesme-Ribes, 1993). Intermittency refers to nonlinearly or stochastically-driven transition between distinct dynamo regimes, with at least one being characterized by internal magnetic field strength too low to generate sunspots. Support for this class of explanations comes primarily from the observed lack of characteristic timescales in the duration and inter-event waiting times of Grand Minima and Maxima. Not surprisingly perhaps, over the years many different Grand Minima/Maxima scenario have been proposed based on (relatively) simple mean-field like dynamo models (see §4 in Charbonneau, 2010, and references therein); (Pipin and Kosovichev, 2011; Passos *et al.*, 2014; Karak *et al.*, 2015). Grand-Minima-like events have also been observed in a few global magnetohydrodynamical simulations of convection and dynamo action (e.g. Augustson *et al.*, 2015; Käpylä *et al.*, 2016).

Recent modelling work carried out in the context of Babcock-Leighton dynamo models suggests that the primary source of cycle fluctuations is associated with the scatter in tilt angles of bipolar magnetic regions (BMRs), which directly translates into variability of the surface dipole moment building up in the descending phase of sunspot cycles (e.g. Svalgaard, Cliver, and Kamide, 2005; Cameron *et al.*, 2010; Yeates and Muñoz-Jaramillo, 2013; Jiang *et al.*, 2014; Nagy *et al.*, 2017). This idea finds strong support in the good precursor potential of the surface dipole at solar minimum (see Petrovay, 2010, and references therein), and in the observed impact of large active regions with extreme properties on the evolution of surface magnetism (Wang and Sheeley, 1991; Yeates, Baker, and van Driel-Gesztelyi, 2015; Cameron and Schüssler, 2017).

In this paper, we use the recently-developed hybrid 2x2D BL solar cycle model of Lemerle and Charbonneau (2017) to investigate the circumstances under which fluctuations in emerging active region properties, including but not limited to tilt angle variability, can reproduce the duration and frequency of Grand Minima and Maxima inferred from the cosmogenic isotope record. The lower operating threshold of Babcock-Leighton dynamos, associated with a minimal internal magnetic field strength required to generate BMR emergences, requires the introduction of a secondary inductive mechanism to "kickstart" the dynamo once fallen into an extended Grand Minimum. Towards this end, we introduce a turbulent α-effect in the lower reaches of the convective envelope, as described in §2. The resulting hybrid dynamo succeeds in producing solar-like Grand Minima, as exemplified by the case study presented

in §3, in which we also examine the statistical characterization of durations and inter-event waiting time distributions for Grand Minima and Maxima. One interested feature of this hybrid model is the intermittent production of epochs of elevated magnetic energy and sunspot emergences, which we can identify as Grand Maxima in the simulation, associated with a distinct mode of dual dynamo operation. We briefly summarize in §5 results from a large set of similar simulations aimed at examining the dependence of Grand Minima/Maxima characteristics on parameters of the model. We conclude in §6 by summarizing our most salient results, followed by a critical discussion of their relevance to our understanding of long timescale variations in the magnetic activity of the real Sun.

2.3. A hybrid solar dynamo model

2.3.1. A 2X2D Babcock-Leighton dynamo

In this section, we first describe the principal elements of the solar cycle model of Lemerle and Charbonneau (2017, hereafter LC17), on which the foregoing simulations are based (see also Lemerle, Charbonneau, and Carignan-Dugas, 2015). The model is a kinematic mean-field-like dynamo relying on differential rotation shear to generate the large-scale toroidal magnetic component, and on the surface decay of bipolar magnetic regions (the so-called Babcock-Leighton mechanism) to regenerate the poloidal large-scale magnetic component. The Babcock-Leighton mechanism is observed to operate at the solar surface, and is often argued to be the primary mechanism driving the reversal of the solar dipole (Charbonneau, 2010; Karak and Cameron, 2016; Cameron and Schüssler, 2012).

The solar interior and photospheric plasma is non-relativistic and collision-dominated. Therefore, inductive effects of flows at large spatial scales are expected to be well-described by the single-fluid magnetohydrodynamical induction equation:

$$\frac{\partial \mathbf{B}}{\partial t} = \nabla \times (\mathbf{u} \times \mathbf{B} - \eta \nabla \times \mathbf{B}), \tag{2.3.1}$$

with η being the net magnetic diffusivity, including contributions from unresolved scales of fluid motions, in the present case granulation, supergranulation, and more generally small-scale turbulent flows associated with thermally-driven convection. The large-scale flow $\mathbf{u}$ is considered given and steady, and only includes contributions from differential rotation and large-scale meridional flows.

Formulated in spherical polar coordinates (r,θ,ϕ), the originality of the LC17 model lies in solving concurrently two coupled geometrically simplified forms of eq. (2.3.1), each in two spatial dimensions. The first is a 2D flux transport dynamo (FTD) model (see, e.g. Dikpati and Charbonneau, 1999; Karak *et al.*, 2015) for the temporal evolution of an axisymmetric ($\partial/\partial\phi \equiv 0$) magnetic field described by a toroidal component $B(r,\theta,t)\hat{\mathbf{e}}_\phi$, and a

toroidal vector potential $A(r,\theta,t)\hat{\mathbf{e}}_\phi$, the latter defining the poloidal component via $\nabla\times(A\hat{\mathbf{e}}_\phi)$. Equation (2.3.1) then separates into

$$\frac{\partial A_\phi}{\partial t} = -\frac{1}{\varpi}(\mathbf{u}_P\cdot\nabla)(\varpi A_\phi) + \eta\left(\nabla^2 - \frac{1}{\varpi^2}\right)A_\phi, \tag{2.3.2}$$

$$\frac{\partial B_\phi}{\partial t} = -\varpi(\mathbf{u}_P\cdot\nabla)\left(\frac{B_\phi}{\varpi}\right) + \eta\left(\nabla^2 - \frac{1}{\varpi^2}\right)B_\phi + \varpi(\nabla\times(A\hat{\mathbf{e}}_\phi))\nabla\Omega + \frac{1}{\varpi}\frac{\partial\varpi B}{\partial r}\frac{\partial\eta}{\partial r} - B\nabla\cdot\mathbf{u}_P. \tag{2.3.3}$$

The second component is a conventional surface flux transport (STF) model (see also Wang, Lean, and Sheeley, 2002; Baumann *et al.*, 2004; Lemerle, Charbonneau, and Carignan-Dugas, 2015; Whitbread *et al.*, 2017), in which the large-scale non-axisymmetric surface radial magnetic component $B_R(\theta,\phi,t)$ evolves in response to advective transport by (axisymmetric) surface differential rotation and meridional fluid motions, diffusive transport by supergranular diffusion, and with the emergence of bipolar active regions acting as a source ($S_{\rm BMR}$):

$$\begin{aligned}\frac{\partial B_R}{\partial t} = &-\frac{1}{Rsin\theta}\frac{\partial}{\partial\theta}\left[u_\theta(R,\theta)B_R\sin\theta\right] - \Omega(R,\theta)\frac{\partial B_R}{\partial\phi}\\ &+\frac{\eta_R}{R^2}\left[\frac{1}{\sin\theta}\frac{\partial}{\partial\theta}\left(\sin\theta\frac{\partial B_R}{\partial\theta}\right) + \frac{1}{\sin^2\theta}\frac{\partial^2 B_R}{\partial\phi^2}\right] - \frac{1}{\tau_R} + S_{\rm BMR}(\theta,\phi,t).\end{aligned} \tag{2.3.4}$$

In this expression $S_{\rm BMR}$ is a surface flux source term associated with the emergence of individual bipolar magnetic regions. The full dynamo model is constructed by coupling these FTD and STF modules; at a given time step, integrating the azimuthal average of the STF-generated $B_R(\theta,\phi,t)$ yields a surface latitudinal distribution of vector potential $A(R,\theta,t)$ providing a time-evolving upper boundary condition on A in the FTD model. This boundary condition effectively acts as a source term on the RHS of eq. (2.3.2). The internal distribution of magnetic fields in the FTD module at a given time step, in turn, is used to construct an "emergence function" giving the probability of triggering a BMR emergence in the STF module at that time step. A constant scaling factor (denoted K in what follows) establishing the slope of the linear relationship between emergence probability and emergence function value, acts as the dynamo number for the model. Properties of emerging BMRs (magnetic flux, pole separation, tilt with respect to the E-W line, etc) are randomly drawn from statistical distributions constructed from magnetographic observations spanning cycle 21 (see Appendix in Lemerle, Charbonneau, and Carignan-Dugas, 2015, for details).

Two nonlinearities are included in the model, both inspired by calculations of the stability, rise and emergence of magnetic flux ropes under the thin flux tube approximation (see D'Silva

and Howard, 1993; Caligari, Moreno-Insertis, and Schussler, 1995; Fan, 2009). The first is a lower threshold on the emergence function, below which the emergence probability vanishes. The second is a reduction, with increasing internal magnetic field strength, of the tilt angle between the line segment joining the two poles of the BMR and the E-W direction (as embodied in Joy's Law. See, e.g. McClintock and Norton, 2013). The latter is the only amplitude-limiting nonlinearity built into the model, and is parametrized by the algebraic expression:

$$\gamma(\theta; B) = \gamma_0(\theta) \frac{1}{1 + (B/B_q)^2} \ , \tag{2.3.5}$$

where γ is the tilt angle and the $B_q = 500$ G sets the (diffuse) field strength at which reduction of the tilt sets in. See §4.2 in LC17 for further details. Critical in what follows, the lower threshold on the emergence function implies that the dynamo is not self-excited; should the internal field strength fall below this threshold for whatever reason, emergence of BMRs ceases, and then so does regeneration of the poloidal component, thus breaking the dynamo loop.

As detailed in LC17, the full coupled model involves 18 adjustable parameters, which were formally optimized to yield the optimal fit to the observed spatiotemporal distribution of BMR emergences in cycle 21. The resulting best-fit model reproduces many features of the observed solar cycle, including some that were not used to constrain the optimization, notably the observed latitudinal variation of the surface meridional flow, as well as the good correlation between the surface dipole at the end of cycle n, and the peak amplitude of (pseudo-)sunspot number time series of cycle $n + 1$.

Running the LC17 model under its optimal parameter settings reveals a behavior that is quite interesting in the context of Grand Minima events; every once in a while, the emergence algorithm will inject in the simulation a high flux BMR with peculiar tilt angles, either disobeying Joy's law (trailing pole closer to equator than leading pole), or even, in more extreme cases, so-called anti-Hale polarity patterns, i.e., an ordering of polarity opposite to that normally characterizing BMR emerging in a given hemisphere and cycle. These events are rare, but have the potential to derail the build-up of the surface dipole (Nagy *et al.*, 2017), the *sine qua non* condition for the production of the subsequent cycle. Such "rogue" BMRs are also observed occasionally on the Sun and it has been demonstrated that a strong BMR emergence with atypical properties can affect strongly the amplitude of the next cycle and lead to episodes of unusually low/high activity (see Wang and Sheeley, 1991; Yeates, Baker, and van Driel-Gesztelyi, 2015; Cameron and Schüssler, 2012).

Figure 2.1 shows a representative example of such an event where the dynamo completely shuts off, for a reference run using the optimal parameter values established in LC17, with dynamo number $K = 0.48$. The top panel shows a time-latitude diagram of the zonally-averaged surface radial magnetic component (color scale), on which are superposed a few

isocontours of BMR emergence density. The bottom panel shows the corresponding time series of the unsigned surface dipole moment (black) and pseudo sunspot number (blue; hereafter abbreviated PSSN), defined here as the monthly averaged number of emergences to yield a measure similar in magnitude to the usual international sunspot number. Here

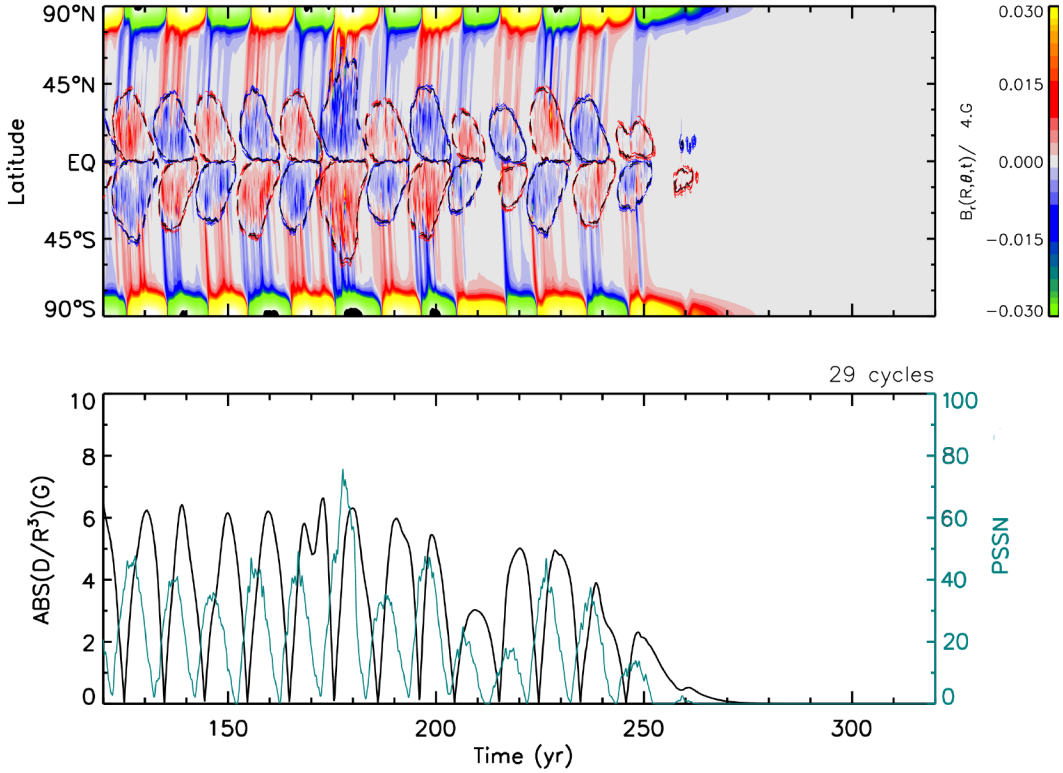

FIG. 2.1. Time-latitude diagram of the surface radial field (top) with superimposed isocontours of emergent BMR density (top), and time series of pseudo-sunspot number and absolute value of the dipole moment (bottom), in a representative run of the LC17 model with dynamo number $K = 0.48$. Here the dynamo shuts off at $t \simeq 260\,\mathrm{yr}$ following an unfavorable sequence of emergences in the preceding sunspot cycle.

the dynamo shuts off at $t \simeq 260\,\mathrm{yr}$ following an unfavorable sequence of emergences in the preceding sunspot cycle (see Nagy *et al.*, 2017), for a detailed analysis of this type of event). If the dipole becomes too weak so that shearing by differential rotation does not succeed in inducing a deep-seated toroidal component exceeding the threshold strength on the emergence function, BMRs no longer emerge, and the dipole then exponentially decays instead of reversing, as is clearly the case here for $t > 260\,\mathrm{yr}$. In order to successfully restart the dynamo in such situations, an additional inductive mechanism is needed to bring the system back above threshold.This idea has been implemented in a number of extant dynamo models characterized by a lower operating threshold, including but not limited to dynamo models relying on the Babcock-Leighton mechanism of poloidal field regeneration

(e.g. Ossendrijver, 2000; Charbonneau, Blais-Laurier, and St-Jean, 2004; Hazra, Passos, and Nandy, 2014; Passos *et al.*, 2014; Sanchez, Fournier, and Aubert, 2014).

2.3.2. Adding a turbulent convective dynamo

The obvious candidate for a self-excited dynamo is turbulent induction associated with cyclonic convection, as embodied in the classical α-effect (Parker, 1955; Krause and Raedler, 1980),(§3 in Charbonneau, 2014, and references therein). This introduces an additional electromotive force (EMF) on the RHS of the induction equation (Eq. 2.3.1), of the form $\langle \mathbf{u}' \times \mathbf{B}' \rangle$, where primes refer to small-scale flow and field fluctuations (unresolved on the scale of $\mathbf{u}$ and $\mathbf{B}$ in Eq. 2.3.1), and the brackets denote averaging over an intermediate scales. For nearly isotropic, nearly homogeneous and weakly nonlinear MHD turbulence, the turbulent EMF can be expanded as

$$\epsilon \equiv \alpha \langle \mathbf{B} \rangle + \beta \nabla \times \mathbf{B} \ , \tag{2.3.6}$$

where β amounts to a turbulent magnetic diffusivity, typically much larger than the microscopic (Ohmic) magnetic diffusivity, and α is the celebrated α-effect of mean-field theory. If rotational shear is assumed to dominate induction of the toroidal large-scale magnetic component (the so-called $\alpha\Omega$ dynamo approximation), then β simply replaces η in eqs. (2.3.2)–(2.3.3), and eq. (2.3.2) picks up a source term on its RHS, of the form $S = \alpha B$. This can evidently lead to an exponential growth of the magnetic field, so it is common practice to introduce an *ad hoc* amplitude-limiting nonlinearity, often in the form of algebraic α-quenching:

$$\alpha(r,\theta;B) = \frac{\alpha_L(r,\theta)}{1+(B/B_0)^2} \ , \tag{2.3.7}$$

where B_0 then sets the field strength at which the α-effect becomes quenched, and the functional $\alpha_L(r,\theta)$ sets the spatial extent of the associated turbulent induction. In what follows we use an α-effect concentrated in the bottom half of the convection zone, as defined by the following spatial dependency:

$$\alpha_L(r,\theta) = \cos\theta \sin\theta \left(\frac{\alpha_0 R_\odot}{\eta_t} \right) \left[1 + \mathrm{erf}\left(\frac{r-r_1}{d_1} \right) \right] \left[1 - \mathrm{erf}\left(\frac{r-r_2}{d_2} \right) \right] \ , \tag{2.3.8}$$

with $r_1 = 0.70 R_\odot$, $r_2 = 0.85 R_\odot$ and $d_1 = d_2 = 0.050 R_\odot$, $\mathrm{erf}(x)$ is the error function, and the coefficient α_0 sets the strength of the α-effect. In the dimensionless form of the governing equations, this becomes subsumed in a secondary dynamo number $C_\alpha = \alpha_0 R/\eta_t$ measuring the strength of turbulent induction versus dissipation, η_t being the turbulent diffusivity value within the convection zone. In what follows we consider negative values of the α-effect in

the Northern Hemisphere, as suggested by analytical estimates and arising in numerical simulations for the lower reaches of the convection zone (§3 in Charbonneau, 2014, and references therein).

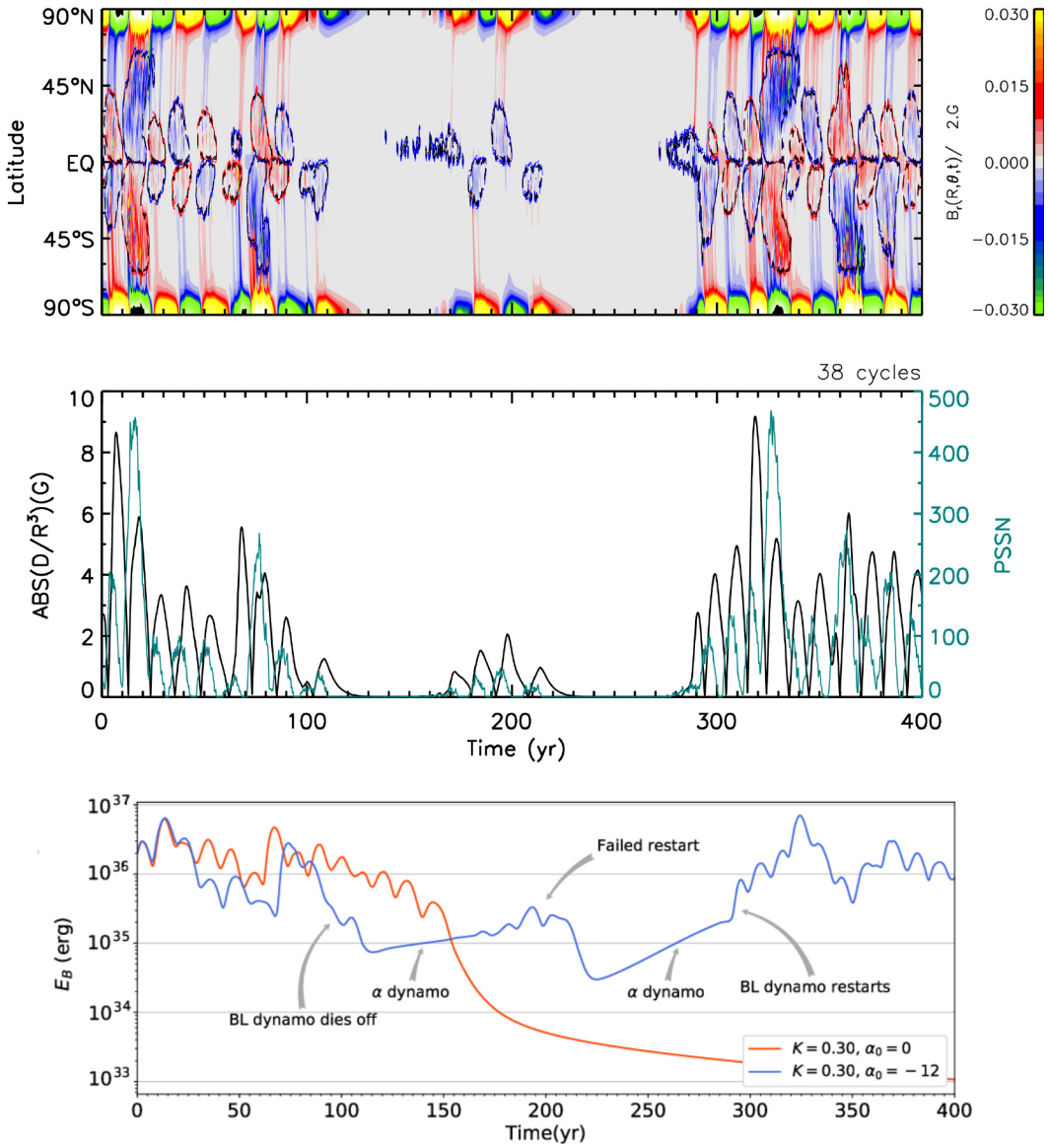

FIG. 2.2. Segment of a representative simulation of the hybrid dynamo including the turbulent α-effect. Parameter values are $K = 0.30$, $\alpha_0 = -12$ cm s^{-1}, $B_0 = 220$ G, $B_Q = 150$ G, $\eta_c = 10^8$ cm^{2}s^{-1}, $\eta_t = 10^{12}$ cm^{2}s^{-1}. The top and middle panels are the equivalent to Fig. 2.1, and the bottom shows the corresponding time series of magnetic energy integrated over the full domain. The primary dynamo shuts down at $t \simeq 100$ yr, but restarts again at $t \simeq 290$ yr after a "failed restart" at $t \simeq 180$ yr (see text).

Figure 2.2 shows a 400 yr segment of a representative run of the LC17 dynamo simulation, with the weak deep-seated turbulent α-effect now operating concurrently with the surface

Babcock-Leighton mechanism. When the latter falls below threshold, here around $t \simeq 100\,\mathrm{yr}$, the cycle soon stops, as on Fig. 2.1; but field induction by the weak turbulent α-effect managed to bring the internal magnetic field back above the operating threshold of the primary (dominant) Babcock-Leighton mechanism, so that "normal" cyclic behavior resumes at $t \simeq 290$ yr, after a "failed restart" at $t \simeq 180$ yr.

Some relatively fine tuning of the strengths and operating thresholds of the two inductive mechanisms is required to achieved the desired effect. If the turbulent α-effect is too strong, it overwhelms the Babcock-Leighton mechanisms and the cyclic behavior is lost. Even for the sample solution displayed on Figure 2.2, it occasionally leads to a surge of mid-latitude activity, for example at $t \simeq 20$ and $320\,\mathrm{yr}$. The effects of these (and other) parameter variations are summarized in §2.6 below.

The bottom panel on Fig. 2.2 displays time series of magnetic energy integrated over the solution domain. The blue curve correspond to the sample solution of the upper panels, while the orange curve shows the behavior of a simulation with the α-effect set to zero, but otherwise identical in its parameter settings. The exponential growth of the magnetic field driven by the α-effect following shutdown of the primary Babcock-Leighton dynamo is readily visible here. Note the two different slopes in the two quiescent intervals separated by the failed restart; in the first, the dipolar mode is excited, while in the second it is the more rapidly growing quadrupolar mode which brings the magnetic field back above threshold. Note also how the simulation with the α-effect undergoes its first shutdown *before* the pure Babcock-Leighton simulation, evidence again that the secondary α-effect dynamo is altering the operation of the primary Babcock-Leighton dynamo, even under "normal" cyclic operation.

Adjustable parameters in the reference LC17 solar cycle model, i.e., without a turbulent α-effect, were formally optimized to minimize the difference between observed and simulated butterfly diagrams. In order to retain the good fit to observations characterizing this reference simulation, our adopted strategy is to (1) retain all optimal values of LC17 for defining parameters of the primary dynamo, allowing variations only within the error bounds resulting from the genetic algorithm-based optimization procedure; and (2) introduce as weak a turbulent α-effect as possible, while strong enough to achieve restart of the primary dynamo.

Acting as the sole poloidal field regeneration mechanism, and for the differential rotation and meridional circulation profile adopted in the LC17 model, the resulting turbulent $\alpha\Omega$ dynamo produces a steady magnetic field peaking at mid-latitudes in the bottom half of the convection zone. In the linear regime the growth rates of the fundamental modes of antisymmetric and symmetric equatorial parity are similar, with the latter dominating in the nonlinearly saturated regime for C_α larger than about 0.28. Fig. 2.3 shows the growth profile of the α-dynamo for various values of α_0 as well as for two different (high and low) core diffusivity values. All simulations are initialized with the same, very weak seed magnetic

field. As expected, the growth rate of α-dynamo is greater when α_0 is larger and η_c is smaller. Hence, the values of these parameters can be expected to affect the duration of Grand Minimum episodes.

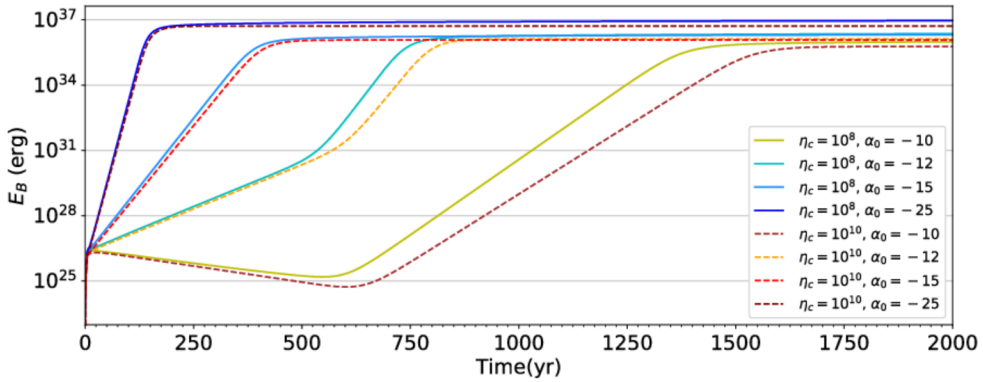

FIG. 2.3. Different solutions of α-dynamo being the sole source term. The BL mechanism is turned off in order to investigate the relationship between the parameter α_0 and η_c, while other parameters are kept fixed ($K = 0.30$, $B_0 = 200$ G, $B_Q = 150$ G, $\eta_t = 10^{12}$ cm^{2}s^{-1}). The effect of core diffusivity over the growth rate of the α-dynamo is explored within a range previously tested for the model in Lemerle and Charbonneau (2017). The growth α-dynamo is slightly higher when η_c is smaller.

Moreover, because symmetric equatorial parity is the preferred mode in most of the dynamo number range considered in what follows, the operation of this secondary turbulent dynamo will introduce departures from the pure antisymmetric parity characterizing the original Babcock-Leighton refenence dynamo solution of LC17. In order to quantify such departures we introduce a measure of equatorial parity P, defined as

$$P = \frac{B_q^2 - B_d^2}{B_q^2 + B_d^2} \,, \tag{2.3.9}$$

where

$$B_q = \frac{B_N + B_S}{2(B_N + B_S)} \,, \tag{2.3.10}$$

$$B_d = \frac{B_N - B_S}{2(B_N + B_S)} \,. \tag{2.3.11}$$

The quantities B_N and B_S refer to the toroidal magnetic component extracted at latitudes $\pm 30°$ at the base of the connection zone ($r/R_\odot = 0.7$). Under these definitions B_q and B_p become measures of the relative magnitudes of even (quadrupole-like) and odd (dipole-like) contributions to the magnetic field. The parameter P is restricted to the range $[-1,1]$, with

$P = -1$ refering to a purely equatorially antisymmetric magnetic configuration, whereas $P = +1$ indicates a purely symmetric configuration.

2.4. Case study: Distinct dynamo modes in a solar-like solution

With the α-effect now included as an additional inductive source, the LC17 model can now reproduce a wide variery of dynamo behaviors, some including Grand Minima and/or Grand Maxima, and others markedly non-solar. We first present and analyze in detail a simulation with parameter values yielding patterns of Grand Maxima and Minima similar to observational inferences based on cosmogenic radioisotopes. The defining parameter values are identical to that of the reference solar solution presented in LC17, with the sole exception of the (turbulent) envelope diffusivity η_t, for which a slightly reduced value is used, but still well within the confidence interval returned by the optimization procedure. We extended this simulation to 50,000 years, amounting to nearly 5000 activity cycles, in the course of which occurred of order 10^2 Grand Minima and almost as many Grand Maxima. This "case study" simulation is the focal point of this section, with the impact of parameter variations on model behavior summarized afterwards in §2.6.

Fig. 2.4 shows a smoothed pseudo-sunspot number time series for this 50,000 years case study simulation. In order to facilitate comparison with reconstructions based on cosmogenic radioisotopes (e.g. Usoskin, Solanki, and Kovaltsov, 2007; Gleissberg, 1944; Mursula and Ulich, 1998), we process our simulation data in a similar manner in order to extract secular variations. A 10-yr cadence time series is first generated by constructing a modulation envelope from cycle maxima, which is then interpolated on a fixed 10-yr step temporal grid. A trapezoidal 1-2-2-2-1 smoothing filter is then applied to this time series, the result being plotted as a solid line on Fig. 2.4. This smoothing will lead to a slight reduction in the measured durations of Grand Minima. In some cases, such as on Fig. 2.2 two closely-spaced Grand Minima separated by a brief "failed restart" will emerge as a single Grand Minimum. The smoothing also precludes the reliable identification of Grand Minima or Maxima of duration inferior to 30 years.

Again in a manner similar to the analysis of the radioisotope record, we construct on Fig. 2.5 the histogram of decadal PSSN values, and fit it with a Gaussian (dashed line). Usoskin, Solanki, and Kovaltsov (2007); Usoskin (2017) construct an equivalent histogram from their radioisotope-based activity reconstruction, and choose the lower and upper points of departure from Gaussian behavior as setting the two thresholds defining their Grand Minima and Maxima. We follow this approach here, setting our lower threshold defining Grand Minima

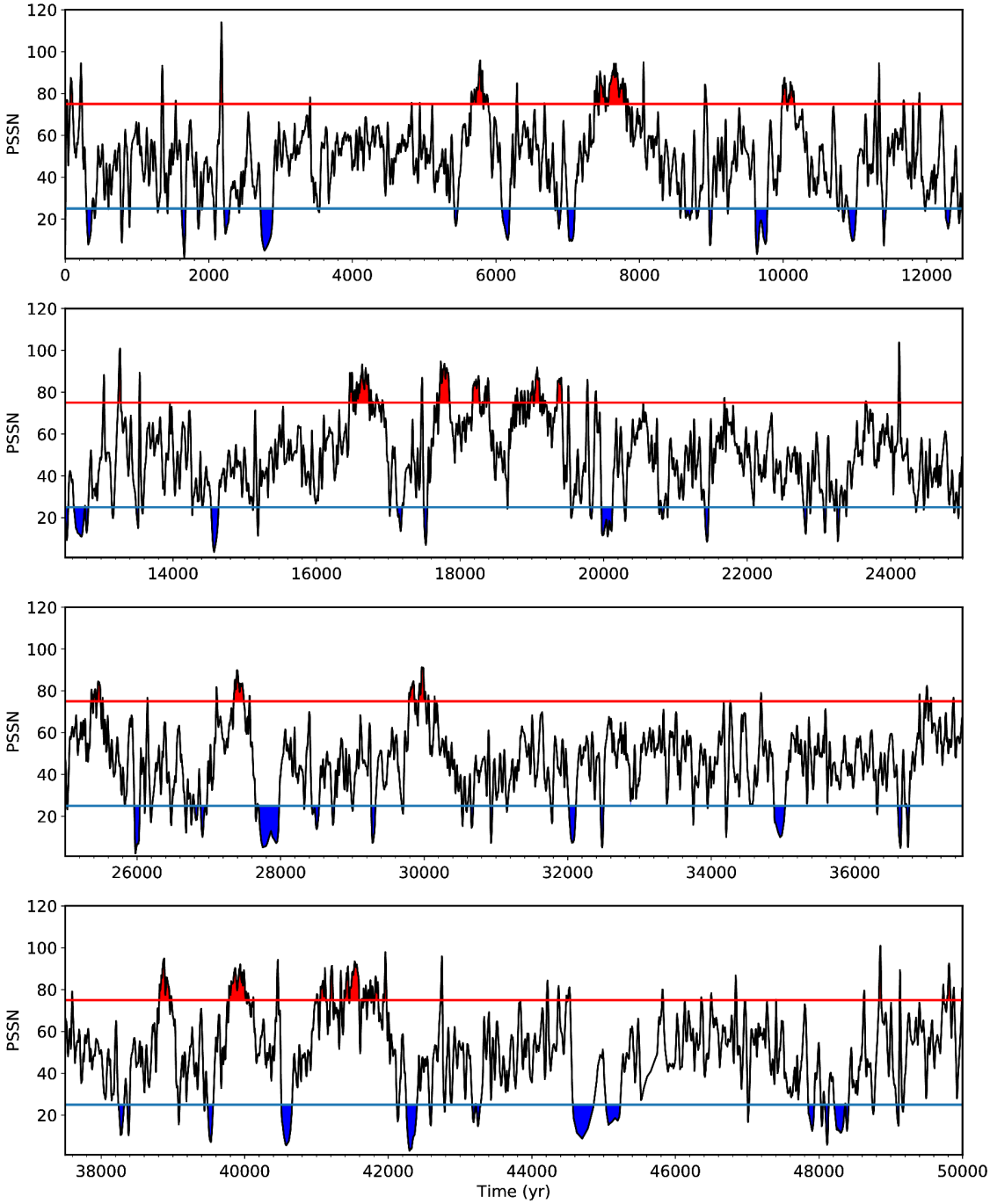

FIG. 2.4. Smoothed pseudo sunspot number time series spanning 50,000 years, for a solution with $K = 0.32$, $\alpha_0 = -12$ cm s^{-1}, $B_0 = 210$ G, $B_Q = 120$ G, $\eta_c = 10^8$ cm^{2}s^{-1}, $\eta_t = 10^{11.8}$ cm^{2}s^{-1}). Starting from monthly PSSN values, a modulation envelope is first constructed from cycle maxima and resampled on a decadal cadence, and the resulting series smoothed with a trapezoidal 1-2-2-2-1 filter. Blue and red areas denote Grand Minima and Maxima, respectively. For ease of comparison, this plot was purposefully formatted to resemble the reconstructed activity plot inferred from the cosmogenic radioisotope record, as displayed in Fig. 3 of Usoskin, Solanki, and Kovaltsov (2007).

at a smoothed PSSN value of 25. Our upper threshold defining Grand Maxima is set at a value of 75, which still lies in the region of acceptable Gaussian fit on Fig. 2.5. As discussed further below, Grand Maxima show up unambiguously in our simulations as a mode of elevated magnetic energy, mixed parity, and frequent mid-latitude BMR emergences. These time spans of these events turn out to be well delineated by a smoothed PSSN threshold of about 75. In view of our smoothing procedure, we only retain as Grand Minima/Maxima episodes during which the smoothed PSSN remains below 25 or above 75 for three consecutive cycles. These threshold values are indicated by blue and red horizontal lines on the various panels of Fig. 2.4.

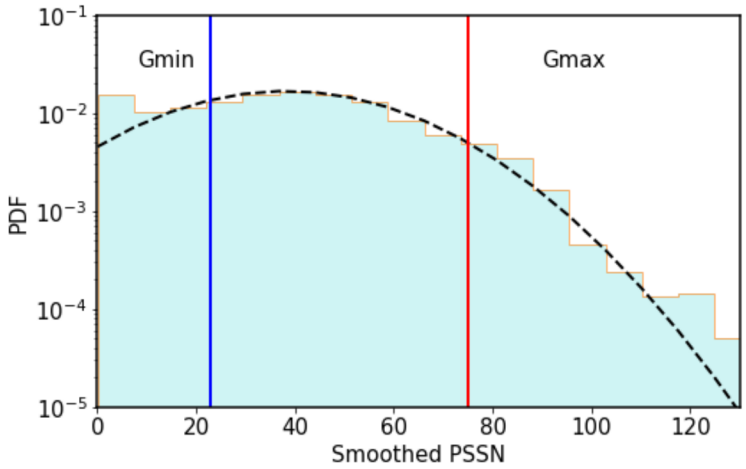

FIG. 2.5. Histogram for sunspot-number distribution for the series in Fig. 2.4. The curve represent the best fit normal distribution while vertical lines correspond to the threshold values used to define Grand Minima and Grand Maxima on Fig. 2.4.

2.4.1. Grand Minima and Maxima

In the 50,000 years simulation depicted on Fig. 2.4, we have identified 102 Grand Minima with a total duration of 6900 years approximately, amouting to 13.6% of the simulated time. The corresponding epochs have been colored in blue on the time series of Fig. 2.4. Examination of the surface time-latitude diagrams reveals that in the course of many of these Grand Minima, some BMR emergences sometimes take place, either in the form of failed restarts, as on Fig. 2.2, during which surface dipole buildup and reversal can resume for a few decades, or more irregular emergence patterns still leaving a weak surface dipolar signal, albeit aperiodic. This could be interpreted as residual cyclic activity, as evidenced by the ^{10}Be record throughout the Maunder Minimum (see, e.g. Beer, Tobias, and Weiss, 1998).

The physical mechanims triggering onset and exit of Grand Minima are well identified in our dynamo model. Onset occurs when an unfavorable sequence of BMR emergences derails the buildup of the dipole in the descending phase of a cycle. Most often this involves a single

or a few high-flux BMR emerging with a E-W tilt pattern deviating strongly from Joy's Law (see, Nagy *et al.*, 2017). Recovery to "normal" cyclic behavior takes place through the agency of the deep-seated turbulent α-effect dynamo, as exemplified on Fig. 2.2.

Under our modelling setup and parameter regime, a steady quadrupole is the fastest growing mode for α-effect dynamo. As a consequence, the recovery from Grand Minima begins with the buildup of quadrupolar internal magnetic field (see the fourth panel in Fig. 2.6), transiting to a mixed-parity once the primary Babcock-Leighton dynamo begins to reactivate, and recovering dipolar parity once normal primary dynamo operation has resumed. The two Grand Minima on Figure 2.2 offer an example of this pattern, with emergences starting to occur in the Northern hemisphere for a few decades before the failed restart at $t \simeq 170\,\mathrm{yr}$, and true restart at $t \simeq 290\,\mathrm{yr}$. This stands in qualitative agreement with sunspot observations during the Maunder Minimum (Ribes and Nesme-Ribes, 1993), which are most readily interpreted as resulting from a mixed-parity dynamo state (Sokoloff and Nesme-Ribes, 1994; Usoskin, Mursula, and Kovaltsov, 2000).

Parity modulation is most readily produced in nonlinear dynamo models including the magnetic backreaction on differential rotation where the magnetic field backreacts on the large-scale flow feeding the dynamo and it is a feature of a dynamical dynamo (see, e.g. Tobias, 1997; Beer, Tobias, and Weiss, 1998; Küker, Arlt, and Rüdiger, 1999; Moss and Brooke, 2000; Bushby, 2006). Here, in contrast, it materializes in a purely kinematic regime, from the interaction of two dynamos mechanisms operating under distinct saturation levels.

In this regime of mixed parity, our solar cycle model can also transit to a dual-dynamo state which is the model's equivalent of Grand Maxima. Observationally, Grand Maxima are harder to define than Grand Minima; in the case of the Maunder Grand Minimum, persistent dearth of sunspots is a clear criteria, but for Grand Maxima "markedly above normal levels" is quantitatively more ambiguous (Clette *et al.*, 2014; Usoskin, 2017), the examplar being the Modern Maximum (1940-2009 approximately). The reality of the Modern Maximum, which is the only example directly verifiable with sunspot data, is considered established via detailed observations of the Sun (Gibson, Zhao, and Fisk, 2011; Clette *et al.*, 2014; Zięba and Nieckarz, 2014; Usoskin *et al.*, 2016a). Cosmogenic isotope data also reveals enhanced activity during this period, as well as the existence of other similar events throughout the Holocene (Usoskin, Mursula, and Kovaltsov, 2003; Solanki *et al.*, 2004; Inceoglu *et al.*, 2015).

Observationally, it remains unclear whether Grand Maxima correspond to a special state of the solar dynamo, or rather to the upper amplitude of regular cyclic activity (Usoskin, 2017). In contrast, in our simulations Grand Maxima can be identified unambiguously on the basis of the internal magnetic field configurations. This is detailed on Figure 2.6, which closes in on a 300 yr segment of the case study simulation of §2.4, including a short Grand Minimum followed, upon exit, by the onset of a Grand Maximum. During Grand Maxima, the turbulent α-effect dynamo operates at elevated levels, almost on par with the

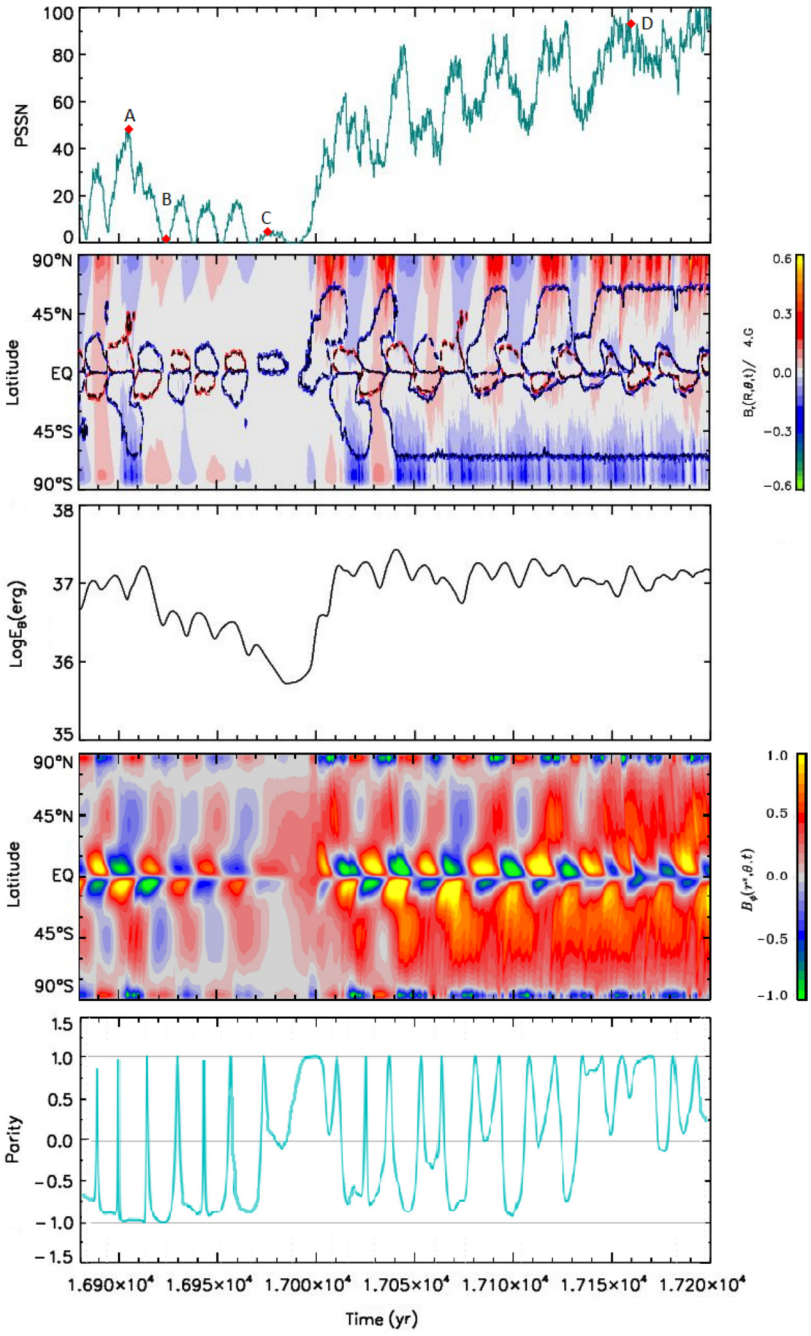

FIG. 2.6. *From top to bottom*: PSSN timeseries with times labeled (A),(B),(C),(D) corresponding respectively to epochs of primary cycle maximum, minimum, a Grand Minimum and a Grand Maximum; the second panel is a time-latitude diagram of the zonally-averaged surface radial field, with superimposed isocontours of BMR emergence density; the third a time series of total magnetic energy; the fourth a time-latitude diagram of the axisymmetric toroidal field at r=0.7R; and the bottom panel shows a time series of solution parity P, as defined in eq. (2.3.9), values of -1 $(+1)$ corresponding to dipole-like (quadrupole-like) magnetic configurations. This segment is extracted from our case study simulation in Fig. 2.4 and shows a "normal" dynamo behavior, a short Grand Minimum, followed by a Grand Maximum state (see text).

primary Babcock-Leighton dynamo. This leads to the build up of a steady, equatorially symmetric internal toroidal field at the base of the convection zone (fourth panel from top), which, in turn, generates a steady stream of BMR emergences at mid-latitudes, so that elevated PSSN counts are sustained even in the minimum phase of the primary dynamo (see top panel). This represents a discrepancy between our simulation and the Modern Maximum, during which the real sunspot number reached values close to zero between successive activity cycles.

Comparison of this Figure (and other similar Grand Maximum episodes) with the corresponding time interval on Figure 2.4 indicates that they are well-delineated by a smoothed PSSN count of about 75. The corresponding threshold value is indicated by the red vertical line segment on the smoothed PSSN histogram of Figure 2.5. Based on this criterion, 84 Grand Maxima can be identified in the 50,000 yr simulation of Fig. 2.4, with a total duration of around 5250 yr; the simulation thus spends around 10.2% of its time in an elevated active state.

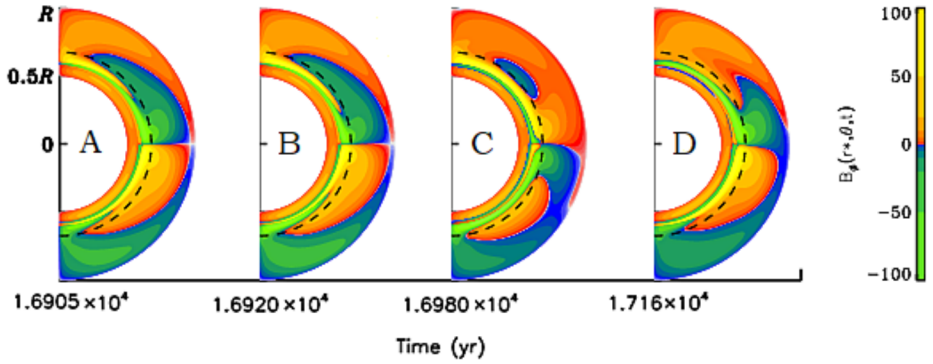

FIG. 2.7. Meridional plane snapshots of the interior axisymmetric toroidal magnetic field component at epochs labeled A, B, C, and D on the top panel of Fig. 2.6. These correspond to a maximum (A) and minimum (B) of the primary cycle during normal cyclic operation, the end of a short Grand Minimum (C), and a Grand Maximum (D). The later two snapshots show marked departure from equatorially antisymmetric parity (see text).

Fig. 2.7 illustrates the internal toroidal field distribution plotted in the meridional plane, for the four epochs labeled A through D on Figure 2.6. Snapshots A and B are respectively at a maximum and minimum phase of the primary cycle during "normal" cyclic activity. Snapshot C is at extracted during the brief Grand Minimum spanning here three cycles. Snapshot D is extracted near the peak of the Grand Maximum episode that follows recovery from the short Grand Minimum. The internal toroidal field is almost perfectly equatorially antisymmetric in snapshots A and B, as expected if the primary Babcock-Leighton dynamo dominates. Snapshot C shows significantly weaker fields, as well as a significant departure from pure antisymmetric parity. This departure is more pronounced, and the field strength

much larger, during the Grand Maximum episode from which snapshot D is extracted. This mixed parity dual-dynamo mode results here from a form of constructive interference between the primary Babcock-Leighton dynamo, and the deep-seated turbulent dynamo.

2.5. Statistical properties of Grand Mimima and Maxima

Having established criteria allowing the identification of Grand Minima and Maxima in our simulations, we can now turn to their statistical properties. The mean duration of a Grand Minimum in the "case study" simulation is 67.57 years, quite close to the mean duration of 80 years extracted from activity timeseries reconstructed from cosmogenic isotope data (Usoskin, Solanki, and Kovaltsov, 2007). Additionally, the recent analysis presented in Usoskin *et al.* (2016b) indicates that 2-3 Grand Minima occur every 1000 years, similar to the occurence frequency measured in our simulation.

Figure 2.8 shows frequency distributions of Grand Minima and Maxima, as extracted from our case study simulation. Even with a 50,000 yr simulation with 102 Grand Minima, the distributions remains irregular. We do note a hint of possible bimodality in the distribution of Grand Minima durations, with a few Grand Minima lasting a few centuries and a more numerous population of Grand Minima lasting under one century. Note also that the 30-60 yr bin is by far the most populated.

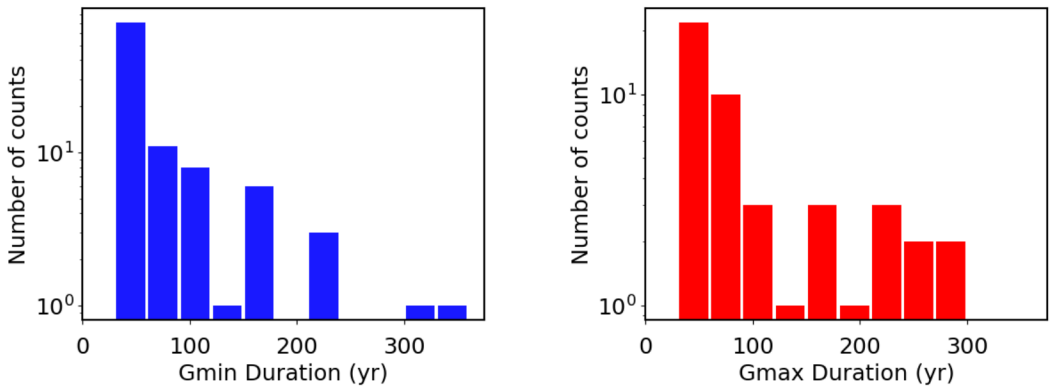

Fig. 2.8. Grand Minima and maxima duration histograms constructed with 102 Grand Minima and 84 Grand Maxima in the time series shown in Fig. 2.4.

Grand Maxima appear to have a more regular distribution, falling more smoothly from decades to centuries, but again the relatively small number of events (84) yields a sparsely populated historam. Examination of Figure 2.4 also reveals that Grand Minima are about as likely to be eventually followed by a Grand Maximum than by another Grand Minimum; the extended Grand Maximum immediately following the short Grand Minimum on Figure 2.6 is not at all the rule this respect.

2.5.1. Waiting Time Distributions (WTD)

The waiting time is defined as the time elapsed between two consecutive events. The probability distribution of the waiting times for Grand Minima and Maxima are shown on Figure 2.9. A stationary memoriless random (Poisson) process is expected to lead to an exponential WTD, while departure from such a distribution may indicate non-stationary or memory-bearing stochastic processes (Wheatland, 2000, 2003; Lepreti, Carbone, and Veltri, 2001; Usoskin, Solanki, and Kovaltsov, 2007; Solanki *et al.*, 2004; Clauset, Shalizi, and Newman, 2009; Inceoglu, Arlt, and Rempel, 2017). In particular, power-law WTDs are usually indicative of scale-free temporal correlations. The black solid lines on Figure 2.9 are least-squares fits to an exponential form, while the red line on the right panel is a power-law fit. All histogram bins were used in these fits, the point being simply to ascertain the general form of the two WTDs. Here an exponential fit yields an acceptable representation of the Grand Minima WTD, while for the Grand Maxima WTD a power-law form yield a somewhat better fit, although from a strictly statistical point of view an exponential form cannot be ruled out. Also statistically marginal but still noteworthy is the markedly elevated count in the first bin of the Grand Minima WTD (note that the vertical axis is logarithmic), a possible indication of mild clustering of events. These various properties are all qualitatively similar with those charaterizing the corresponding distributions inferred from cosmogenic isotope data (Usoskin, Solanki, and Kovaltsov, 2007).

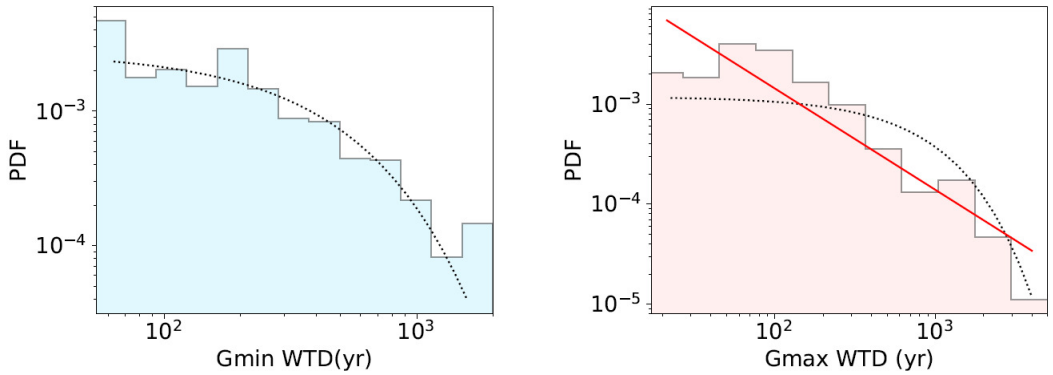

FIG. 2.9. Probability density functions of waiting time distributions (WTD) of Grand Minima (left) and Grand Maxima (right).

In our basic dynamo model, Grand Minima are triggered by one or more "rogue" active region with high magnetic fluxes and tilts departing strongly from Joy's Law (Wang and Sheeley, 1991; Yeates, Baker, and van Driel-Gesztelyi, 2015; Nagy *et al.*, 2017). Tilts are ascribed to each emerging BMR by random draws from a stationary empirical distributions built from cycle 21 magnetographic data (see Lemerle, Charbonneau, and Carignan-Dugas, 2015, Appendix, for details). Under these conditions an exponential WTD is in fact expected. Exit from Grand Minima is a deterministic process, as it is set by the growth rate of the

secondary turbulent dynamo, as well as the overall internal magnetic field distribution at the time of onset. Event-to-event variations in the internal field distribution is ultimately responsible for the relatively wide spread of Grand Minima durations characterizing our simulations.

The non-exponential form of the Grand Maxima WTD is compatible with the idea that the latter result from a mechanism that is not completely stochastic. We identified Grand Maxima as resulting from a form of constructive interference between the primary dynamo and the secondary turbulent dynamo. Changes in the internal distribution of magnetic fields, in particularly at and below the base of the convection presumably driven by stochastic effects, allow comparatively stronger quenching of the Babcock-Leighton mechanism, with the inductive induction of the α-effect then becoming comparable, yielding a true dual-dynamo. Support for this interpretation is found in the internal magnetic field distribution (Figure 2.7), as well as in the varying equatorial parity in going from normal cyclic activity to Grand Maxima state (Figure 2.6, bottom panel).

2.5.2. Quasi-Periodicity Analysis

Visual examination of Fig. 2.4 suggests that Grand Minima and Maxima do not recur periodically, and that a Grand Minimum need not be necessarily followed by a Grand Maximum, and vice-versa. Nonetheless the presence of long periodicities or quasi-periodicities cannot be ruled out on such a purely visual basis.

Figure 2.10 presents a Morlet wavelet analysis of the 50,000 yr smoothed PSSN time series of Figure 2.4, performed using the WAIPY package (Calim Costa 2013). The right frame shows a standard Fourier spectrum, as well as the Morlet spectrum resulting from time integration of the Wavelet power distribution. Because the time series results from 1-2-2-2-1 smoothing of a series of decadal sampling, the primary 11-yr half-cycle is not expected to show up with significant amplitude in these various spectra. The most striking pattern in the Wavelet power distribution is observed in the period range of 1000–3000 years, where intermittently recurring power structures are clearly visible, adding up to statistically significant peaks in the time-integrated power spectra on the right.

With the existence of a recurring quasi-periodicity in the 1000-3000 yr range thus established, a closer examination of Figure 2.4 reveals a tendency for groups of 3-4 extended Grand Maxima to cluster with a commensurate spacing of 1000-3000 years, these clusters being separated by some 8000 years. This longer recurrence period corresponds, again roughly, to the power structure at the longest periods accessible to the wavelet analysis of Fig. 2.10, but a much longer simulation is required to firmly establish its quasi-period. This clustering of Grand Maxima is consistent with the non-exponential form of their waiting time distribution (viz. Fig. 2.9). There is again qualitative similarity with the cosmogenic radioitosope

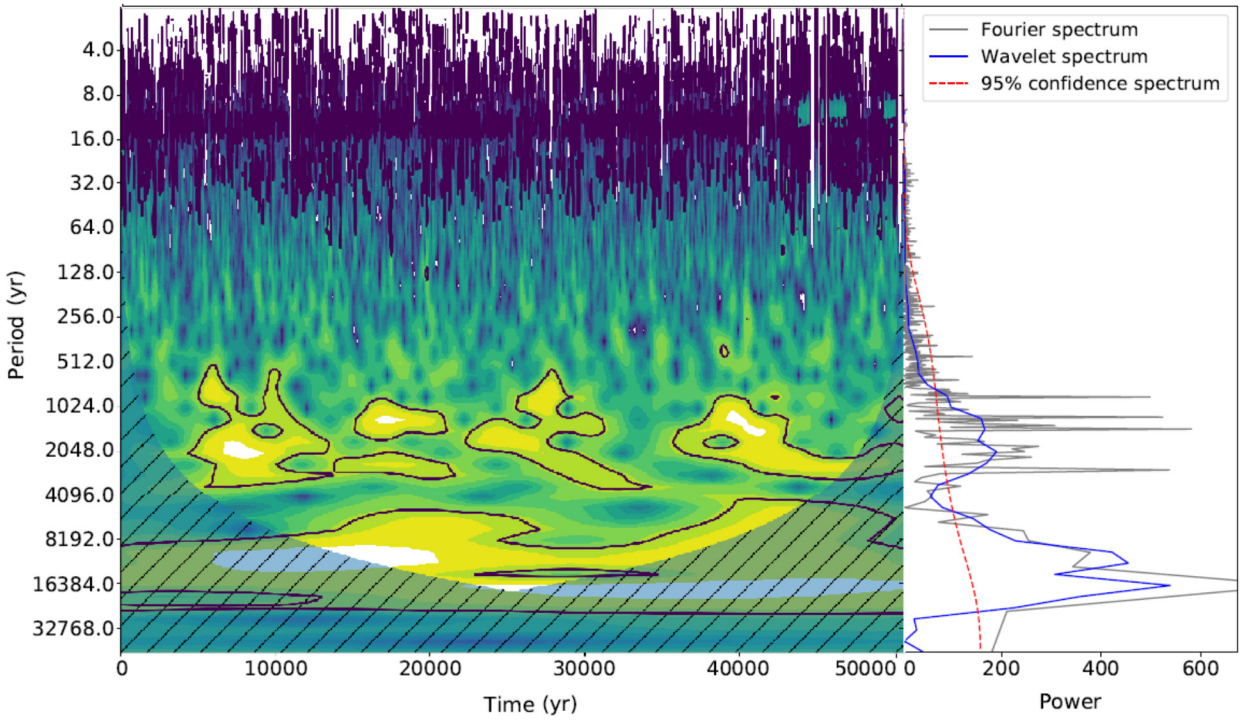

FIG. 2.10. *Left*: Morlet wavelet spectrum of the smoothed PSSN time series of Figure 2.4. *Right*: Global wavelet spectrum showing both Morlet(blue), Fourier(grey) power spectra and %95 significance level(red) for the Morlet wavelet spectrum. Note the irregular waxing and waning of powering the 1000-3000 yr period range. The hatched area is not statistically significant. The right panel shows the time-integrated Morlet spectrum (in blue) with the 95% confidence level indicated by the red dashed line, along with a standard Fourier spectrum (in gray).

reconstructions of Usoskin *et al.* (2016b), who offer evidence that Grand Minima and Maxima occur aperiodically, but with a tendency for clustering respectively near lows and highs of the Hallstatt cycle (2300–2400 yr period range). However, in contrast to these reconstructions, we find no hints of Gleissberg-like periodicity (80–100 yr) in the wavelet transform or Fourier spectra.

The only millenial timescale present within our solar cycle model is associated with magnetic diffusion in the layers underlying the convection zone within which the bulk of the dynamo action is taking place. The best-fit reference model of LC17 is characterized by a contrast of magnetic diffusivity of 4 orders of magnitude between the bottom of the domain $\eta_c = 10^8\,\mathrm{cm^2\,s^{-1}}$, and its "convection zone", where convective turbulence is taken to generate a much stronger net diffusivity, $\eta_t = 10^{11.8}\,\mathrm{cm^2\,s^{-1}}$, for the "case study" simulation presented here. Examination of the dynamo solution reveals the buildup of intense magnetic fields immediately beneath the convection zone, concentrated in a region of radial extent $r/R_\odot \simeq 0.05$ (see Fig. 2.7). An estimate for the magnetic dissipation time of such a structure is

$\tau = (0.05\,R_\odot)^2/\eta_c \simeq 3900\,\mathrm{yr}$. One can conjecture that the buildup of this layer is triggered by a cycle of particularly high amplitude, again resulting from stochasticity in MBR emergences, pushing the system in the dual dynamo state persisting for a time of the order of the diffusive decay time for the participating deep-seated magnetic layer. Support for this conjecture is found in the fact that the power peaks at long periods in the wavelength transform shifts to shorter periods as the core diffusivity is increased to $\eta_c = 10^9\,\mathrm{cm^2\,s^{-1}}$, and vanish as as η_c exceeds $10^{10}\,\mathrm{cm^2\,s^{-1}}$.

2.6. Parameter Dependencies

The "case study" solution discussed in the preceding section was selected among a vast number of simulations computed under different parameter regimes. The parameter being varied, and their ranges of variations, are listed in Table 2. I. The first is the one free parameter of the LC17 model, namely the dynamo number controlling the rate of BMR emergences as a function of the internal magnetic field strength. The following three are structural parameters of the basic LC17 model, and were only varied within the range allowed by the optimization procedure. The last two characterize the strength and saturation field strength for the turbulent α-effect. We have also explored varying the spatial distribution for the α-effect, including a Northern Hemisphere positive α-effect distributed throughout the convection zone. For the (limited) range of such solutions explored, non-solar behavior invariably materializes in these cases.

The effects of changes in these parameter on the occurrence and characteristics of Grand Minima and Maxima can be summarized as follows:

- As the primary dynamo number K increases, the primary dynamo spends more time in "normal" cyclic operation, and the number of Grand Minima decreases. The BL-dynamo operates at a high energy level and the frequency of Grand Maxima increases.
- At low K, the dynamo produces Grand Minima more frequently, operates at a low energy level and Grand Maxima become very rare.
- The parameter α_0 sets the overall magnitude of the alpha effect. Close to its critical value($\alpha_{crit} \simeq -9$ cm s^{-1}), turbulent induction cannot offset magnetic dissipation,

Tab. 2. I. Parametrized variables in the model.

Parameters	Physical meaning	Tested Interval	Values in LC17
K	primary dynamo number	[0.15, 1.20]	-
B_Q	threshold field for tilt quenching (G)	[100, 500]	-
$\log(\eta_c)$	diffusivity in the core($\mathrm{cm^2 s^{-1}}$)	[7, 11]	$8.0\pm^{2.4}_{1.0}$
$\log(\eta_t)$	envelope turbulent diffusivity($\mathrm{cm^2 s^{-1}}$)	[11.0, 13.0]	$12.0\pm^{0.2}_{0.4}$
B_0	threshold toroidal field (G)	[100, 1000]	-
α_0	secondary dynamo number(cm s^{-1})	[-25, -9]	-

and the BL dynamo never restarts once it stops. Running significantly above critical allows restart, but above $\simeq -25$ the turbulent dynamo dominates, and non-solar behavior typically ensues.

- The parameter B_0 is the toroidal magnetic field strength at which quenching of the turbulent α-effect becomes important. The adopted algebraic quenching formula (2.3.7) is entirely *ad hoc*. The key is to pick a value low enough that normal operation of the primary Babcock-Leighton dynamo strongly quenches the α-effect, but still high enough to allow the α-effect to amplify the magnetic field back above the emergence threshold of the Babcock-Leighton dynamo. This desired behavior materializes only in a fairly restricted range of quenching field strengths, otherwise non-solar behavior again ensues. Within this range, lowering the threshold B_0 lowers the overall magnetic energy during "normal" cyclic operation, and Grand Minima become longer. On the other hand, increasing B_0 leads to shorter and more frequent Grand Minima.
- Increasing the core diffusivity η_c decreases the efficiency of the deep-seated α-effect dynamo, and leads to longer quiescent episodes around the model's critical operation level when K is between 0.25 and 0.35.

2.7. Discussion and Conclusion

In this paper we have described the addition of a turbulent electromotive force, in the form of the mean-field α-effect, into the kinematic 2×2D Babcock-Leighton solar cycle model of Lemerle and Charbonneau (2017). This addition was motivated by the need to "jumpstart" the Babcock-Leighton dynamo after the internal magnetic field falls below the field strength threshold allowing the formation and emergence of bipolar magnetic regions. In the resulting dual dynamo model, stochastic fluctuations in properties of emerging bipolar magnetic regions can trigger extended periods of strongly reduced activity, the model's equivalent of Grand Minima, recovery to normal cyclic behavior being driven by the α-effect. We also showed that interaction between the deep-seated, weak turbulent dynamo and the surface Babcock-Leighton mechanism can generate a hybrid dynamo mode characterized by extended periods of markedly above-average activity, which become the model's equivalent of Grand Maxima.

The many adjustable parameters in the Lemerle and Charbonneau (2017) models were formally optimized to match the sunspot butterfly diagram, and these optimal values were retained in most simulations reported upon in this paper. Two new parameters were introduced to control the behavior of the turbulent α-effect: a dynamo number measuring its strength, and a quenching field strength determining its saturation level. This secondary dynamo number is set as low as possible so as to avoid perturbing the normal operation of the primary Babcock-Leighton dynamo, the idea being that the secondary turbulent dynamo

makes a significant inductive contribution only when its Babcock-Leighton counterparts falls below threshold. Straightforward as this may sound, it required a relatively fine tuning of the saturation threshold for the α-effect. Nevertheless, after parameter tuning, the resulting dual-dynamo model succeeded in generating irregularly occurring Grand Minima and Maxima, with distributions of durations and inter-event waiting times remarkably similar to the corresponding distributions inferred from the cosmogenic isotope record.

Solar-like long timescale behavior does require here a relatively fine tuning of the parameters defining the strength and quenching of the α-effect. It is quite conceivable that a more robust parameter set could be uncovered by repeating, with all parameters of our dual dynamo model, the formal optimization procedure used in LC17. This being a very computationally-intensive endeavour, we have opted to postpone it to a follow-up investigation, in the course of which a wider variety of spatial distributions for the turbulent α-effect and meridional flow configurations will also be explored.

In the model, Grand Minima are triggered following the emergence of one or more high-flux active regions having unusual tilt angles, derailing the buildup of the surface dipole and leading to the subsequent shutdown of the primary cycle. This phenomenon is investigated in detail in Nagy *et al.* (2017). Because active regions properties are drawn randomly from stationary distributions of values built from observations, the onset of Grand Minima is a truly memoriless random process, leading to an exponential distribution of inter-event waiting time. Recovery from Grand Minima is achieved through the inductive action of the low-amplitude turbulent α-effect, so that the mean duration of Grand Minima is set primarily by the growth rate of the associated dynamo, itself determined by the adopted value for the dynamo number: the higher this value, the shorter the mean duration of Grand Minima. Because the secondary α-effect dynamo generates a steady, equatorially symetric magnetic field in the parameter regime considered here, the exit from Grand Minima is characterized by a mixed parity state, in qualitative agreement with sunspot observations in the second half of the Maunder Minimum (Ribes and Nesme-Ribes, 1993).

Grand Maxima arise in the model as truly distinct a mixed-dynamo state of mixed parity, in which both the deep-seated α-effect and surface Babcock-Leighton contribute more or less equally to the regeneration of the poloidal large-scale magnetic field through a form of constructive interference. Analyses of the simulation results reveal a non-exponential waiting time distribution for such Grand Maxima events, suggesting that deterministic effects operating on long timescales contribute to their temporal recurrence pattern. Detection of spectral power in the 1000–3000 yr range, also recurring in the wavelet transform, supports this idea. In our kinematic model, the only commensurate timescale is associated with magnetic dissipation in the stable, low magnetic diffusivity layer underlying the high diffusivity "convection zone" at the base of which the α-effect is operating. This suggests that the

slow dissipation of magnetic fields sometimes building up in this deep layer sets this long timescale, over which the dominance of the deep-seated turbulent dynamo waxes and wanes.

We are not claiming that the specific hybrid dynamo model described here is a physically accurate representation of the real dynamo processes taking place in the solar interior. However, our model does show that even in the kinematic regime, short-timescale random fluctuations occurring naturally within the Babcock-Leighton mechanism can lead to systematic variations on very long timescales, including solar-like Grand Minima, Grand Maxima, and quasi-periodicities in the millennia range, that resemble at least qualitatively inferred solar behavior. The occurrence of long quasi-periodicities is particularly noteworthy, as this is usually difficult to generate via stochastic driving alone, and is typically ascribed to deterministic nonlinear magnetic backreaction of large-scale flows, particularly differential rotation (see, e.g. Tobias, 1997; Beer, Tobias, and Weiss, 1998; Küker, Arlt, and Rüdiger, 1999; Moss and Brooke, 2000; Bushby, 2006). Our results indicate that interaction between distinct dynamo mechanisms can achieve the same effect, while generating statistical distributions of Grand Minima and Maxima events consistent with solar activity reconstructions based on the cosmogenic isotope record. Introduction of dynamical backreaction on differential rotation is an obvious next step in further development of the model, as the aforecited non-kinematic studies have shown that this can naturally lead to intermediate, Gleissberg-like centennial quasiperiodicities, which our current model does not appear capable of generating.

Acknowledgements: This work was supported by the Discovery Grant Program of Canada's Natural Sciences and Engineering Research Council. Special thanks to Ilya G. Usoskin for kindly providing their most recent reconstructed solar activity time series based on ^{10}Be and ^{14}C cosmogenic radioisotopes.

Chapter 3

CONCLUSION

In this study, the nature and the statistics of Grand Minimum and Maximum events by studying the effects of various physical mechanisms have been explored. With the aid of a kinematic solar dynamo model driven by BL and turbulent α-effect sources the characteristics of long-term solar variability and dynamo processes behind them have been investigated.

3.1. Summary of the results

The first step of this project was to tackle a particular issue, namely the occasional shut down of the dynamo action due to the randomness inherent in the emergence function, characterizing the LC17 model. We demonstrate that a BL dynamo with a lower field threshold on the sunspot formation requires a secondary inductive mechanism. In our case, this boosting mechanism is selected to be turbulent induction, in the form of the α-effect of mean-field electromagnetics (eq.1.7.1). The inclusion of this effect leads to the successful re-start of cyclic activity and makes the exit from a grand minimum state possible. The short and long-term behaviors of the model, which depend on the amplitude of this effect, along with other tested parameters summarized in Table 2. I, are presented in the Annex, showing how different combinations of these parameters can affect the duration and frequency of Grand Minima and Maxima.

While our hybrid model can exhibit a wide variety of behaviors, it does include a parameter regime in which the cyclic behavior is solar-like. This rather low-level, kinematic model is capable of producing many features of the solar magnetic cycle as well as its multi-millenial variations including Grand Minima, Grand Maxima and long-term quasi-periodicities similar to the Sun. There appears to be three modes that the hybrid model can generate upon inclusion of the secondary inductive mechanism modeled via α-effect: (1) Regular cyclic activity during which the model is neither in a Grand Minimum nor a Grand Maximum state but still exhibits short-term fluctuations where the BL dynamo dominates, (2) Grand Minima, during which the BL dynamo shuts off and the α-dynamo starts re-building the magnetic

field for the BL mechanism to pick up once again, (3) Grand Maxima, during which both the BL and α-dynamo contribute to field induction in a constructive manner.

The low-activity mode, i.e. Grand Minimum, is being triggered because of the stochastic nature of the emergence function in the model (Nagy *et al.*, 2017) and the inclusion of the turbulent α-dynamo makes it possible to recover from such epochs. Due to the equatorially symetric magnetic field that the α-dynamo generates during and at the exit of Grand Minima in the model, we observe a mixed-parity, in accordance with sunspot onbservations indicating a strong hemispheric asymmetry during the second half of the Maunder Minimum (Ribes and Nesme-Ribes, 1993).

Grand Maxima in the model occur as a special mode of elevated sunspot number and highly mixed parity in the large-scale internal magnetic field. During these periods, a BL dynamo at the surface and a α-dynamo at the base of the convection zone operate jointly, contributing more or less equally to the reconstruction of the poloidal field on large scales. During their joint operation, there seems to be a regime in which they are able to create enchanced activity phases without one of them taking over.

The model output presented in §2 spends 13.6% of its time in a Grand Minimum and 10.2% in a Grand Maximum state. The occurrence of Grand Minima follows an exponential waiting time distribution, suggesting a memoryless process driven by the stochastic effects (as discussed in §2.2.1). These results agree with ^{10}Be and ^{14}C data. The WTD analysis of Grand Maxima, in contrast, hints for a deterministic effect playing a role in its occurrence, i.e. a memory effect. As the WTD analysis conducted with reconstruction via cosmogenic radionuclides is inconclusive, there is no firm observational conclusion with which to compare our results regarding Grand Maxima in the model. They, however, seem to cluster as the WTD suggests (§2.4.1) and our wavelet analysis (§2.4.3) shows that this clustering is related to long-time scale quasi-periodicities, near the Hallstatt cycle (2,400 yr). This pattern has also been pointed out by Usoskin *et al.* (2016b) in cosmogenic isotope data. The only commensurate timescale in our kinematic dynamo model is related to magnetic dissipation in the stable, low magnetic diffusivity layer below the high diffusivity "convection zone" at the base of which the α-effect is operating. We argue that the slow dissipation of magnetic fields, sometimes building up in this deeper layer sets this long timescale and is thought to lead to these super-secular quasi-periodicities observed in the wavelet analysis. Furthermore, the high-activity periods in the model show a mixed-parity state as a result of short-term variations and the joint operation of two dynamo mechanisms, namely the BL dynamo and the α-effect (§2.4.2).

We conclude that although it may not necessarily be an accurate representation of the real Sun, it is encouraging to see even in the kinematic regime, that short-timescale random fluctuations occurring naturally within the Babcock-Leighton mechanism along with a secondary, symmetric dynamo mechanism can lead to variations on very long timescales,

including solar-like Grand Minima, Grand Maxima, and quasi-periodicities in the millennial range.

3.2. Future work

As a continuation of this work, many paths may be taken. Since it would be more physically realistic to include the backreaction of the Lorentz force on the flows, a non-kinematic version of this 2×2D model might offer interesting results to study the amplitude modulation via this backreacktion mechanism.

Another compelling idea would be to use a multi-cellular meridional flow profile instead of a single cell, as helioseismological measurements hint (Zhao *et al.*, 2013). Although Babcock–Leighton-type solar dynamo models operating with a steady, single-cell meridional circulation in each hemisphere have been successful in reproducing many solar cycle features so far, Helioseismology indicates that this may be an oversimplified picture (Belucz, Dikpati, and Forgács-Dajka, 2015).

Furthermore, the analysis presented in this thesis may be repeated with a fluctuating α-effect to study its impact as a mechanism of stochastic forcing in re-initiating the dynamo action when the magnetic energy is too low to sustain the BMR production. Additionally, a re-optimization of this dual-dynamo model, using the genetic algorithm-based procedure developed by Lemerle, Charbonneau, and Carignan-Dugas (2015) and Lemerle and Charbonneau (2017) with new modifications will be a necessary, complementary step to be performed. This re-optimization step on all the parameters included along with new ones would increase the robustness of the simulation results.

Appendix A

ANNEX

In this Annex, we present additional results from our set of simulation runs. §A.1 is dedicated to the dependencies on the model parameters. Expanding on the summary presented in §2.6, first we examine each of these parameters closely one at a time, then we introduce a catalog of additional simulations (both solar-like and non-solar solutions), representative of the various dynamo behaviors generated by the model. §A.2 includes two very long (50,000 yr) simulation runs showing secular and super-secular variability in the model for comparison with the case presented in §2.4-2.5. It also contains the duration histograms and waiting time distribution analysis of Grand Minima/Maxima in these time series. §A.3 shows samples of typical Grand Minima and Maxima that our hybrid model can generate. Finally, §A.4 includes a few wavelet analysis performed on different time series to explore the effect of varying the core and envelope diffusivities on long-term quasi-periodicities in the model.

A.1. Model Parameter Dependencies

The model parameters whose effects have been explored throughout different simulation runs during this study are summarized in Table A. I. The behavior of the dynamo model has been diverse exhibiting both solar-like and non-solar behavior. The solar-like regime is limited within a relatively wide range of values for each of these parameters.

Tab. A. I. Parametrized variables in the model.

Parameters	Interpretation	Tested Interval	Optimal Values
K	primary dynamo number (dimensionless)	[0.15, 1.20]	-
B_0	threshold toroidal field (G)	[100, 1000]	-
α_0	secondary dynamo number (cm s^{-1})	[-25, -9]	-
B_Q	emergence/tilt quenching threshold field (G)	[100, 500]	-
$\log(\eta_c)$	diffusivity in the core ($cm^2 s^{-1}$)	[7, 11]	$8.0\pm^{2.4}_{1.0}$
$\log(\eta_t)$	envelope turbulent diffusivity ($cm^2 s^{-1}$)	[11.0, 13.0]	$12.0\pm^{0.2}_{0.4}$

In what follows, the effects of certain parameters are presented one by one in terms of their influences on the evolution of the times series generated by the model.

A.1.1. Parameter K

In the model, what links the emergence function and the real number of BMRs produced by the simulation in a linear way is the parameter K, or the primary dynamo number which effectively controls the strength of the BL mechanism. As the addition of a secondary inductive mechanism can raise the average value produced by the emergence function, we had to lower this parameter when we added the α-dynamo.

The K values close to the threshold where the system makes a transition from a subcritical state to a supercritical state, i.e. where an exponential growth starts to take place until the dynamo saturates (Charbonneau, 2010; Lemerle and Charbonneau, 2017), are found to be within the interval [0.30, 0.40] for the dynamo number.

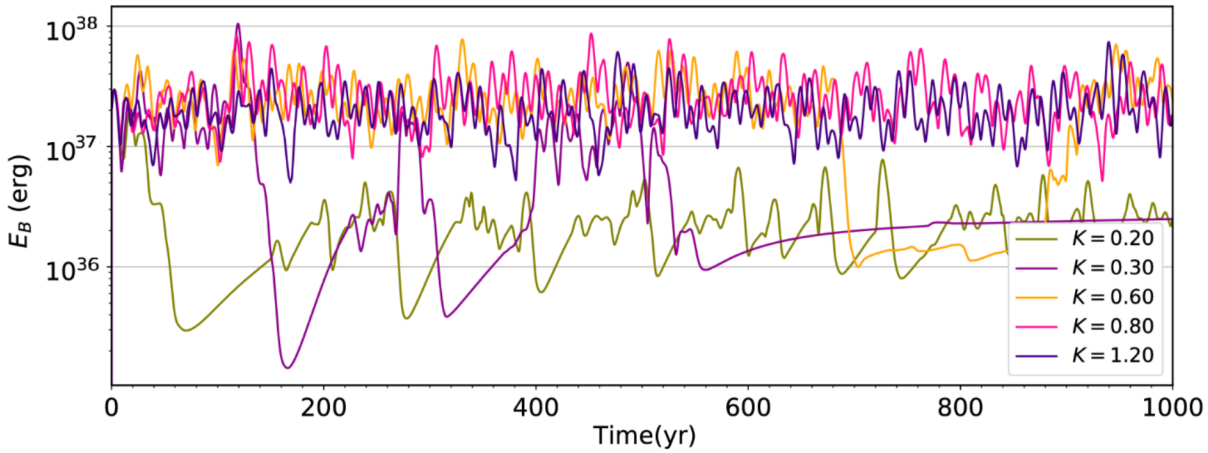

FIG. A.1. Different solutions with K when α_0 is fixed at -13 cm s^{-1} with $B_0 = 200$ G, $B_Q = 150$ G, $\eta_c = 10^8$ cm^{2}s^{-1}, $\eta_t = 10^{12}$ cm^{2}s^{-1}. Increasing K, in general, causes the BL-dynamo to run at a higher energy level and to have fewer or no Grand Minimum while the frequency of Grand Maximum events increases.

In general, as K increases the primary (BL) dynamo spends more time in active phase before entering into a Grand Minimum and the overall number of Grand Minima during the simulation decreases. The BL-dynamo operates at a high energy level and the frequency of Grand Maxima increases. On the other hand, as shown in Fig. A.1, at low K, the dynamo produces short Grand Minimum frequently and operates at low energy level while having occasionally very short Grand Maximum episodes, although this situation also depends on the strength of the α-effect. If both are too weak, then Grand Minima may last longer and there may be no Grand Maximum.

A.1.2. Parameter α_0

The parameter α_0 controls the overall magnitude of the α-effect. Under its critical value ($\alpha \simeq -9$ cm s^{-1}), the α-effect won't be able to offset magnetic dissipation when the BL dynamo stops. Therefore, the higher the α_0 values is above this critical value the more it is guaranteed that the BMRs production restarts after a Grand Minimum-like period when K is also above its critical value. Nevertheless, if it is too high, it will dominate the BL-dynamo and lead to non-solar behaviors. An α-effect negative in the Northern Hemisphere is required to produce solar-like behavior. The positive α_0 values with the same magnitude are observed to have a weaker impact on the BL-dynamo due to a phase offset between the two dynamos.

A.1.3. Steady α-effect at the base of the convection zone

As α_0 increases the primary dynamo spends more time in an active phase before entering into a Grand Minimum and also spends less time in a Grand Minimum while the mean duration of Grand Maxima increases, if the K value is sufficiently high. The amplitude of α_0 has a greater effect on the duration of Grand Maxima when the dynamo runs in the supercritical regime.

If the α_0 value is below -10 cm s^{-1} while keeping the value of K at a supercritical level, the primary dynamo doesn't restart and the α-effect stays ineffective. We estimate that the α_{crit} value is around -9 cm s^{-1}. Above -20 cm s^{-1}, if the K is sufficiently high (> 0.30), the simulation continues to run without having any Grand Minimum. However, if the α-effect is too high compared to K, it takes over and very high latitude emergences tend to appear (see Fig. A.2.

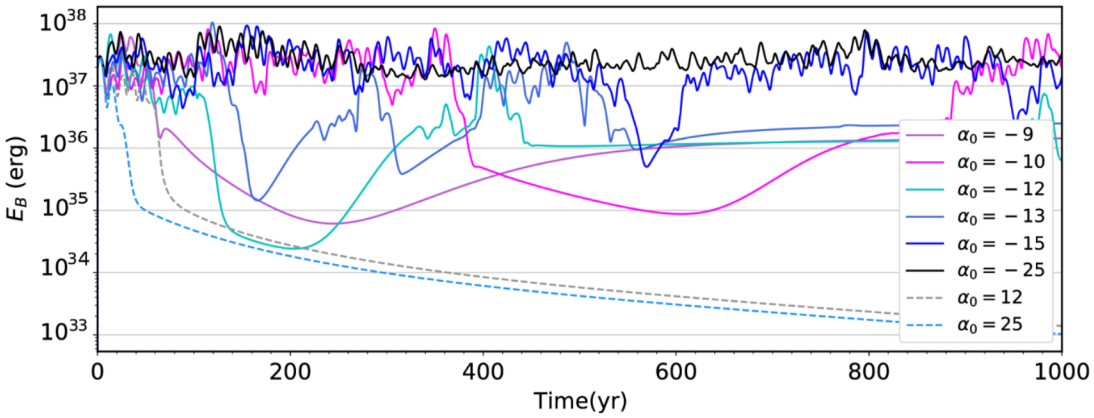

FIG. A.2. Simulation outputs with different α_0 values. Other parameters are fixed at $K = 0.35$ with $B_0 = 200$ G, $B_Q = 150$ G, $\eta_c = 10^8$ cm^{2}s^{-1}, $\eta_t = 10^{12}$ cm^{2}s^{-1}

.

Another feature that the model demonstrates is that, sometimes the BL dynamo goes through failed restarts during a Grand Minimum episode like shown in Fig. A.6, although the α-effect enhances the field strength until a point where the BL mechanism can pick up and generate emergences, but the field strength may not be sufficient to go back to a normal activity level. In these episodes, we observe low activity with a strong hemispheric asymmetry where some emergences are present but only in one hemisphere in an alternating manner as shown in Fig. 2.6 (in §2.3) and polarity oscillates from one hemisphere to the other in each cycle as the BL mechanism tries to restart. This is a different kind of hemispheric asymmetry than observed in the case of the Maunder Minimum in which there were emergences only in the Southern Hemisphere towards the end of this episode.

In summary, if the BMR production stops, without α-effect, the field in both hemispheres will slowly dissipate by diffusion. Hence the inclusion of this effect or a similar turbulent mechanism to re-build the magnetic field is a necessity for exiting from Grand Minimum episodes.

A.1.4. A Spatially wider α-effect

A negative α-effect in the Northern Hemisphere, such as used here, is believed to materialize only in the bottom 2/3 of the convection zone, while retaining the same latitudinal dependency (Charbonneau, 2014). Here the radial extent of this dynamo mechanism is increased by an order of $0.5R_\odot$. Hence, instead of the half bottom part of the convection zone, during this exploration it operates at the 2/3 of it with $r_1 = 0.70R_\odot$, $r_2 = 0.90R_\odot$ and $d_1 = d_2 = 0.050R_\odot$.

This spatial expansion expectedly causes a decrease in α and provides stronger turbulent induction for the same values of α_0. This geometric adjustment leads to shorter Grand Minima and Grand Maxima.

A.1.5. Parameter B_0

The parameter B_0 represents the toroidal magnetic field threshold value above which the α-effect is suppressed. This cut-off is an *ad hoc* dependency to the field's magnitude that shuts down the α-dynamo when the field is strong, that is, when the BL dynamo is running normally. This cut-off prevents the α-dynamo from disturbing the primary dynamo when it operates in a regular regime. If B_0 is too low, then the α-effect will stabilize under the threshold for the production of BMRs, when the BL dynamo is stopped. However, if it is too high, then the α-effect will be very active when the primary dynamo is running. This can also lead to non-solar behaviors.

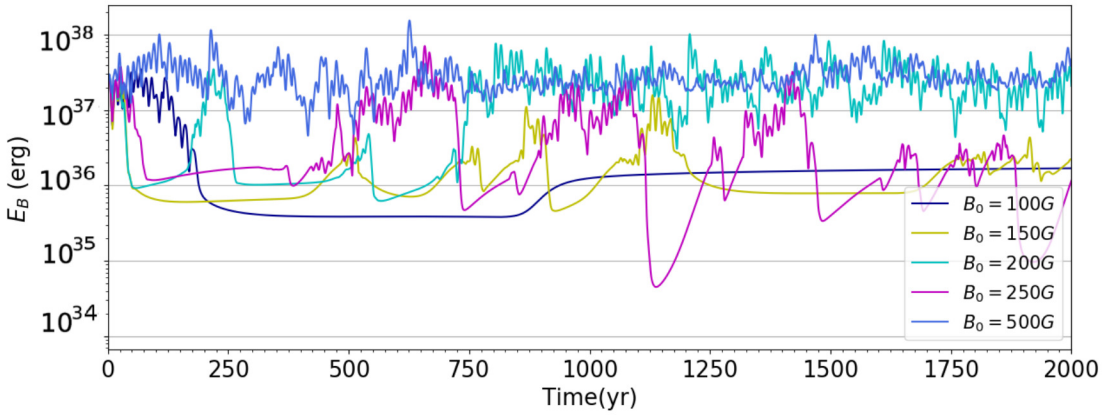

FIG. A.3. Dependence on B_0 while other variables are fixed ($K = 0.30$, $\alpha_0 = -12$ cm s^{-1}, $B_Q = 150$ G, $\eta_c = 10^8$ cm^{2}s^{-1}, $\eta_t = 10^{12}$ cm^{2}s^{-1}). The smaller B_0 gets, the smaller the regular cycle amplitude becomes. Additionally, increasing or decreasing B_0 leads to an increment in the frequency of Grand Minimum episodes.

According to the analysis illustrated in Fig. A.3, lowering the threshold B_0 lowers the overall magnetic energy that the dynamo has during regular cycles and Grand Minima become longer. On the other hand, at high B_0, the simulation produces shorter and more frequent Grand Minima.

A.1.6. Parameter B_Q : Emergence/Tilt Quenching Threshold

As introduced in §2, a mean value for the quenching of the BMR tilt has been introduced in the model in order to replicate the resistance of magnetic tension in strongly magnetized flux tubes against the twisting imparted by the Coriolis force. This provides an amplitude-limiting non-linearity allowing the cycle amplitude to stabilize on the surface in the LC17 model. Here, we explore how this parameter affects the duration of extreme epochs throughout the simulations.

As Fig. A.4 illustrates, increasing the amplitude of B_Q provides us with longer durations for Grand Minimum episodes, whereas decreasing it makes them shorter and more frequent. To find a solar-like regime in which the model acts solar-like on the long-term, for instance having 2-3 Grand Minima per 1000 years with a mean duration of 80 years, coherent with cosmogenic isotope records, moderate levels of tilt quenching are required within the interval [110,250] G.

A.1.7. The role of the core diffusivity

The growth rate of the dynamo is measured only in the presence of the α-effect, by deactivating the primary dynamo, the BL mechanism and by lowering the initial field on the order of 10^{-4} G. Normally the initial field is 8.5 G.

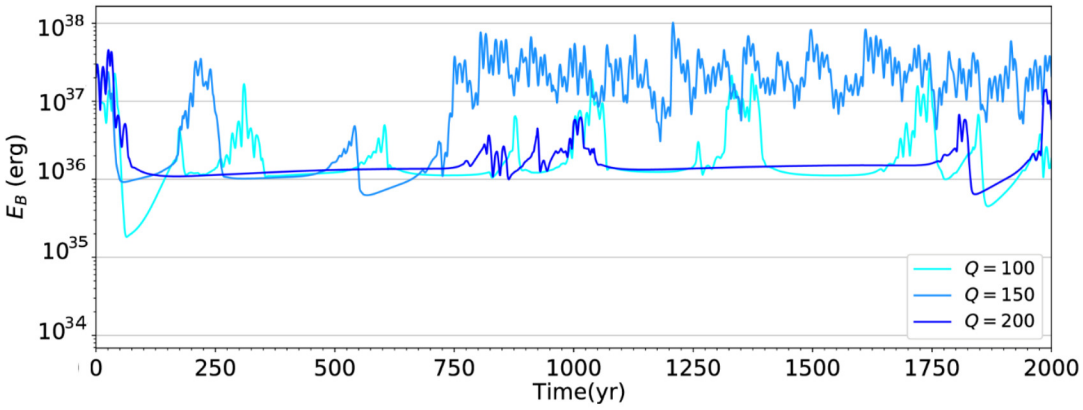

FIG. A.4. Dependence on B_Q while other variables are fixed ($K = 0.30$, $\alpha_0 = -12$ cm s^{-1}, $B_0 = 200$ G, $\eta_c = 10^8$ cm^{2}s^{-1}, $\eta_t = 10^{12}$ cm^{2}s^{-1}). Increasing B_Q provides us with longer duration for Grand Minima episodes, whereas decreasing it makes them shorter and more frequent.

In the model, the net magnetic diffusivity is expressed in the following form:

$$\eta(r) = \eta_c + \frac{\eta_t}{2}\left[1 + \mathrm{erf}\left(\frac{r - R_c}{\delta_c/2}\right)\right], \tag{A.1.1}$$

where η_c is the diffusivity at the stratified core whereas η_t represent the turbulent diffusivity in the bulk of the convection zone with $R_c = 0.7R_\odot$. These parameters are tested within certain intervals and optimal values are estimated for the reference solution of Lemerle and Charbonneau (2017). Here we explore how η_c affects the duration of Grand Minima and Maxima when we increase/decrease it, respecting its tested interval [10^7,10^{11}] cm^{2}s^{-1}. In eq. A.1.1, δ_c/R is the thickness of the transition region between differential and solid rotation, the tachocline, near the base of the convection zone and it is equal to 0.05, fixed by the optimization procedure of LC17.

Increasing η_c, makes the primary dynamo more and more intermittent and even leads to very long quiescent episodes around the model's critical operation level when K is between 0.25 and 0.40, as the growth rate of the α-effect is in inverse relation with the core diffusivity. At this point, lowering α_0 makes the dynamo try to re-start itself more frequently, but the primary dynamo is not sustained and it dies off once again in most of the cases.

Fig. A.5 exhibits how η_c affects the growth rate of the α-effect while α_0 is kept fixed. Thereby, within the tested intervals, we acknowledge that in order to achieve more frequent and shorter Grand Minima, increasing η_c slightly along with adjustments in other parameters may offer more solar-like, long-term behavior in the simulations.

A.1.8. Turbulent diffusivity

In this section, the relationship between η_t in its tested interval $[10^{11},10^{13}]$ $\mathrm{cm^2 s^{-1}}$ and the growth of the α-dynamo is explored.

In Fig. A.5, it is demonstrated that as η_t decreases the α-effect grows faster. This is a natural outcome of a reduced turbulent effect in the envelope. Within its optimized values shown in Table A. I ($12.0\pm^{0.2}_{0.4}$ $\mathrm{cm^2 s^{-1}}$) reducing η_t provides us with shorter Grand Minima and longer Grand Maxima.

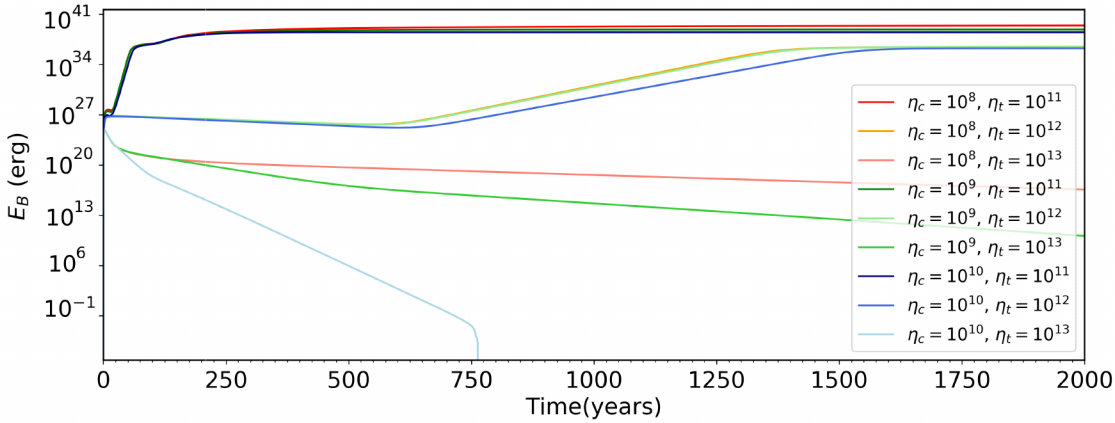

FIG. A.5. The growth of the α-dynamo depending on η_t and η_c while other variables are fixed. The figure illustrates that as either η_t or η_c increases, it affects the growth rate negatively. For the high turbulence and high core diffusivity case, it can even die off (shown in light blue).

A.1.9. Overall Model behavior

Here, various dynamo solutions are presented exploring a wide range of values for each of the parameters introduced earlier, respecting the tested intervals that are determined during the optimization of the model over cycle 21 (Lemerle, Charbonneau, and Carignan-Dugas, 2015; Lemerle and Charbonneau, 2017). All the solutions in this section are presented in the same format. The top panel shows time series of pseudo-sunspot number (PSSN); the second panel demonstrates time series of the radial field on the photosphere; the third panel is for time series of total magnetic energy, and the bottom panel shows time-latitude diagram of axisymmatric toroidal field at the core-envelope interface, $r/R_\odot = 0.7$.

This simulation catalog serves to illustrate the impact of changes in the primary dynamo number K, the secondary dynamo α_0, B_0, B_Q, η_c and η_t on the overall trend manifested in the simulations, respectively.

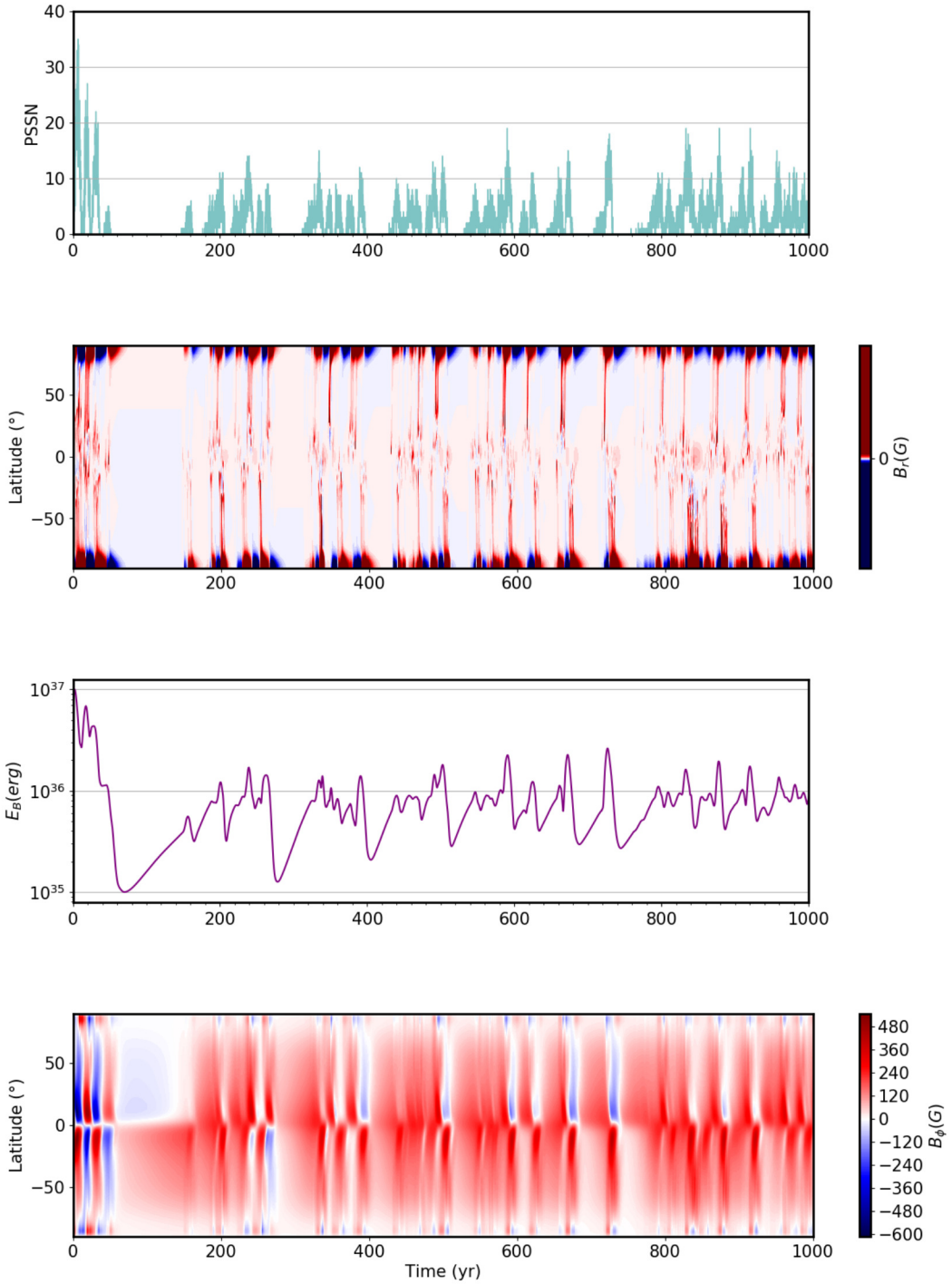

FIG. A.6. *From top to bottom*: PSSN, surface radial field, total magnetic energy, deep-seated toroidal field as a function of time. The BL dynamo number K is too low in this case and the BL dynamo runs in a subcritical regime despite the re-start attempts of the α-dynamo ($K = 0.20$, $\alpha_0 = -13$ cm s^{-1}, $B_0 = 200$ G, $B_Q = 150$ G, $\eta_c = 10^8$ cm^{2}s^{-1}, $\eta_t = 10^{12}$ cm^{2}s^{-1}).

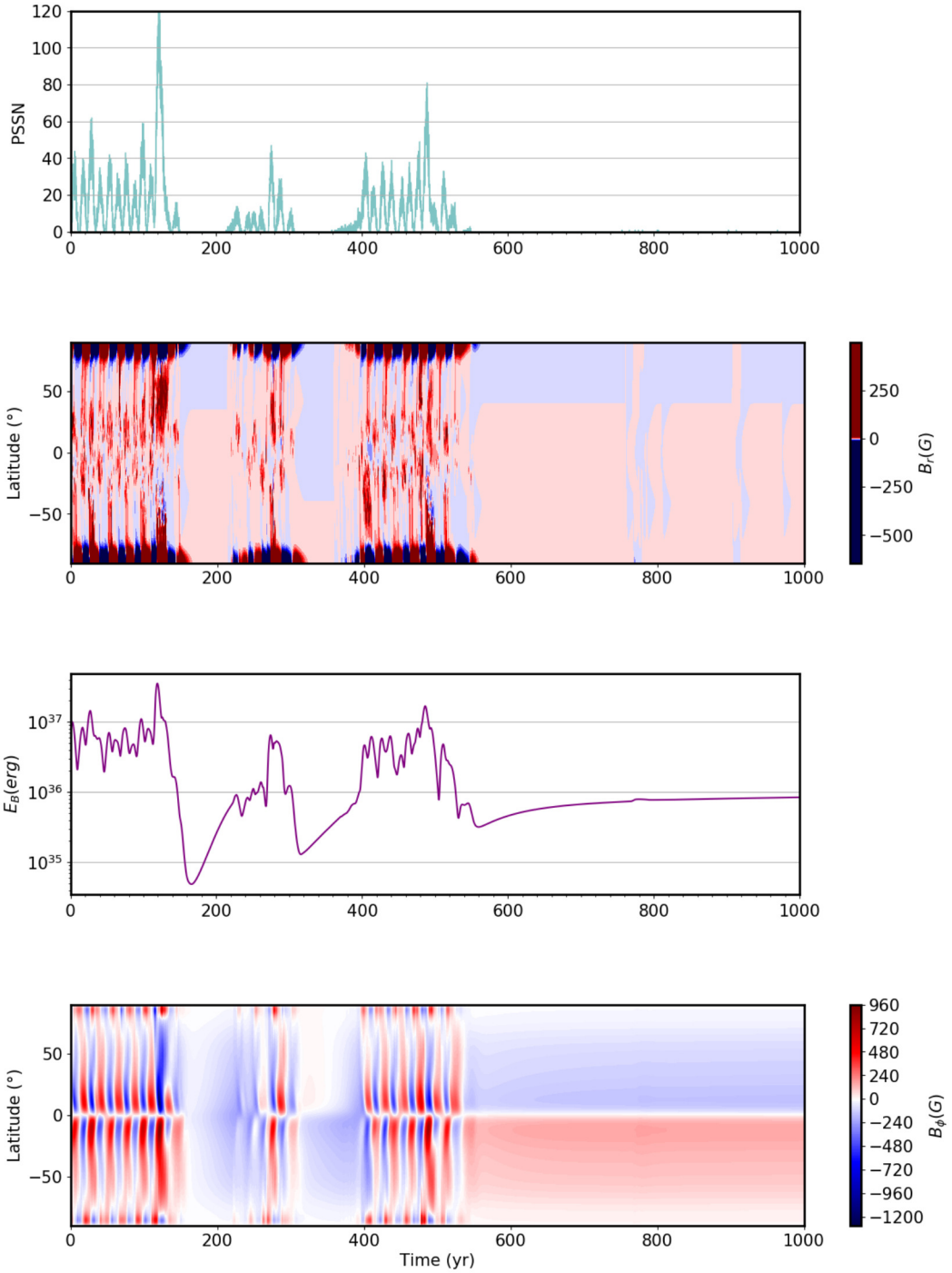

FIG. A.7. *From top to bottom*: PSSN, surface radial field, total magnetic energy, deep-seated toroidal field as a function of time. The BL dynamo number K is higher than its critical and the dynamo runs in a supercritical regime ($K = 0.30$, $\alpha_0 = -13$ cm s^{-1}, $B_0 = 200$ G, $B_Q = 150$ G, $\eta_c = 10^8$ cm^{2}s^{-1}, $\eta_t = 10^{12}$ cm^{2}s^{-1}). This simulation output also includes a Maunder-like Grand Minimum.

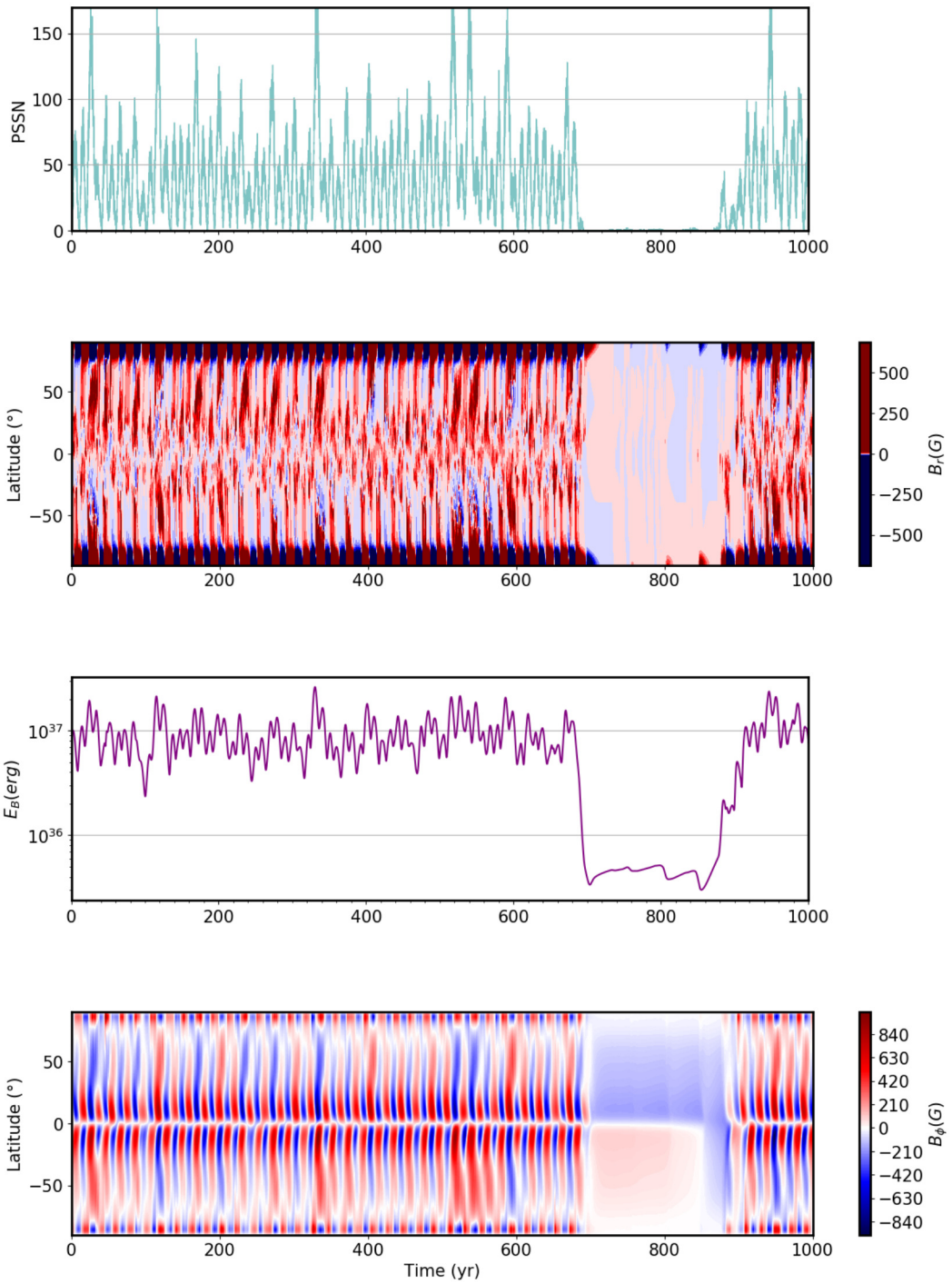

FIG. A.8. *From top to bottom*: PSSN, surface radial field, total magnetic energy, deep-seated toroidal field as a function of time. The BL dynamo number K is higher than its critical and the dynamo runs in a supercritical regime ($K = 0.60$, $\alpha_0 = -13$ cm s^{-1}, $B_0 = 200$ G, $B_Q = 150$ G, $\eta_c = 10^8$ cm^{2}s^{-1}, $\eta_t = 10^{12}$ cm^{2}s^{-1}). This simulation output also includes a Maunder-like Grand Minimum.

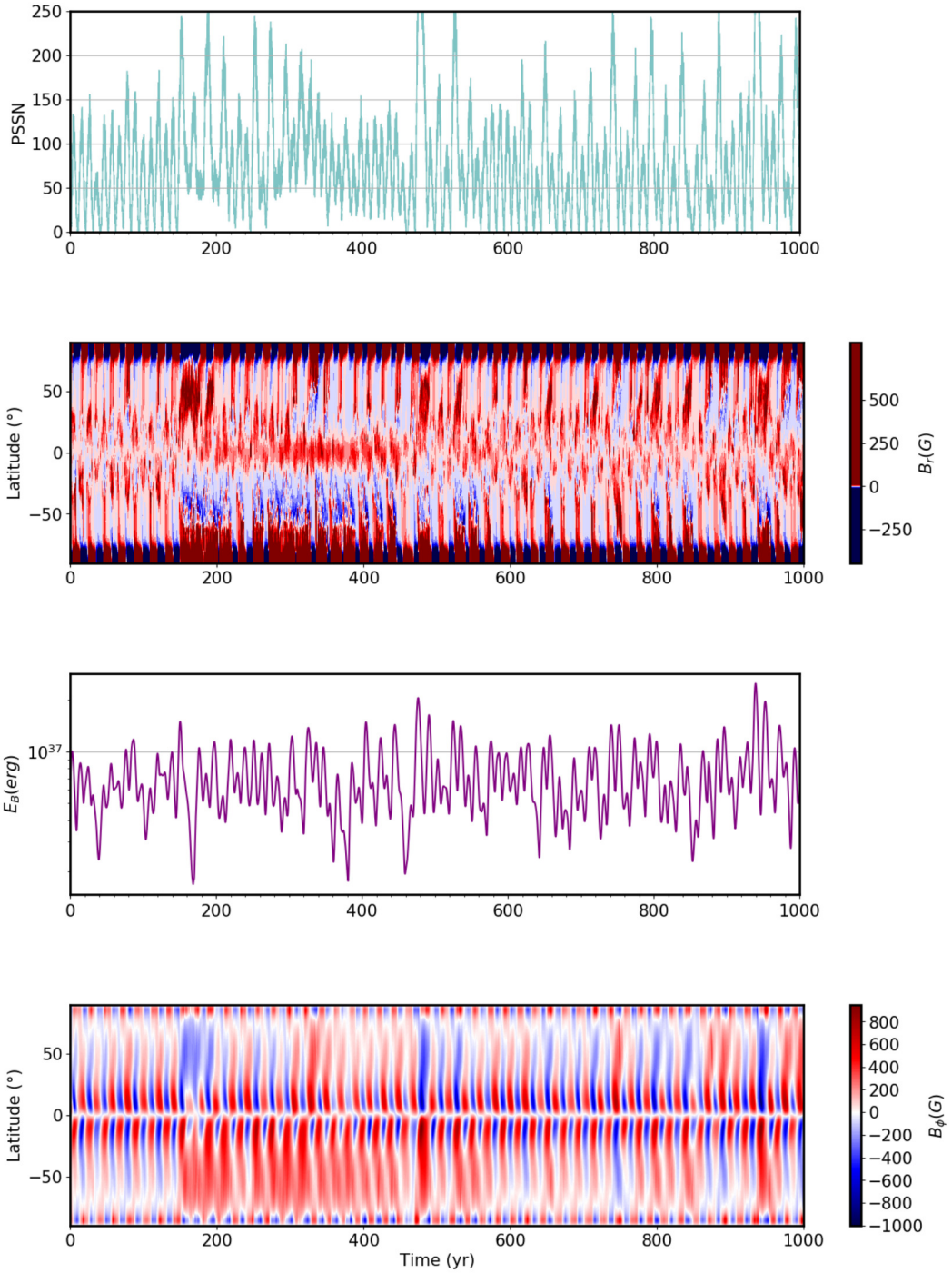

FIG. A.9. *From top to bottom*: PSSN, surface radial field, total magnetic energy, deep-seated toroidal field as a function of time. The BL dynamo number K is much higher than its critical value and the dynamo runs in a supercritical regime ($K = 0.120$, $\alpha_0 = -13$ cm s^{-1}, $B_0 = 200$, $B_Q = 150$ G, $\eta_c = 10^8$ cm^{2}s^{-1}, $\eta_t = 10^{12}$ cm^{2}s^{-1}). Due to the high K value, the dynamo doesn't enter into a Grand Minimum. This simulation output also includes two Grand Maximum events due to strong interference between two induction mechanisms.

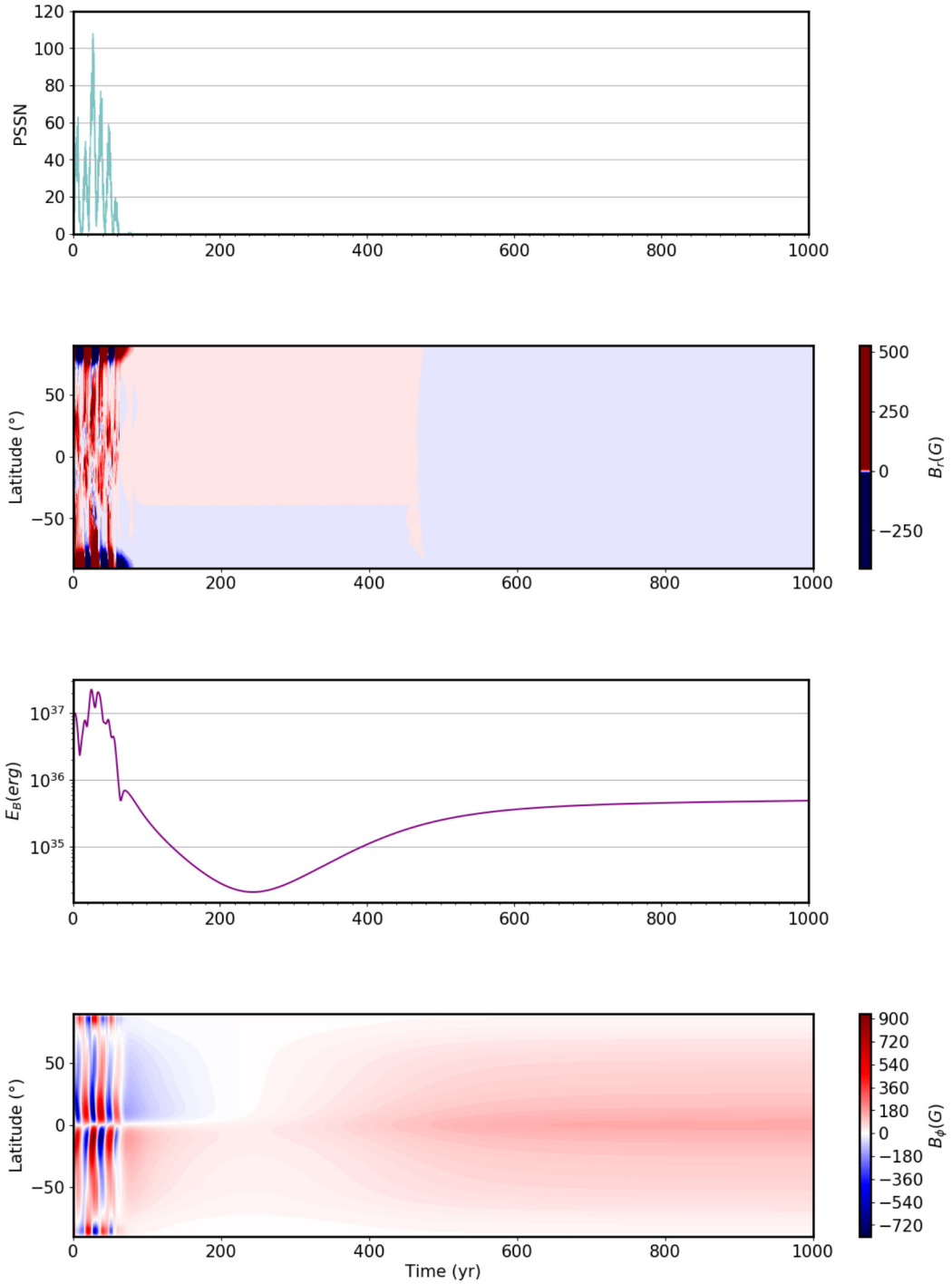

FIG. A.10. *From top to bottom*: PSSN, surface radial field, total magnetic energy, deep-seated toroidal field as a function of time. While the α-effect operates under its critical value, hence it is UNABLE to restart the dynamo action once the primary dynamo shuts down ($K = 0.30$, $\alpha_0 = -9$ cm s^{-1}, $B_0 = 200$ G, $B_Q = 150$ G, $\eta_c = 10^8$ cm^{2}s^{-1}, $\eta_t = 10^{12}$ cm^{2}s^{-1}).

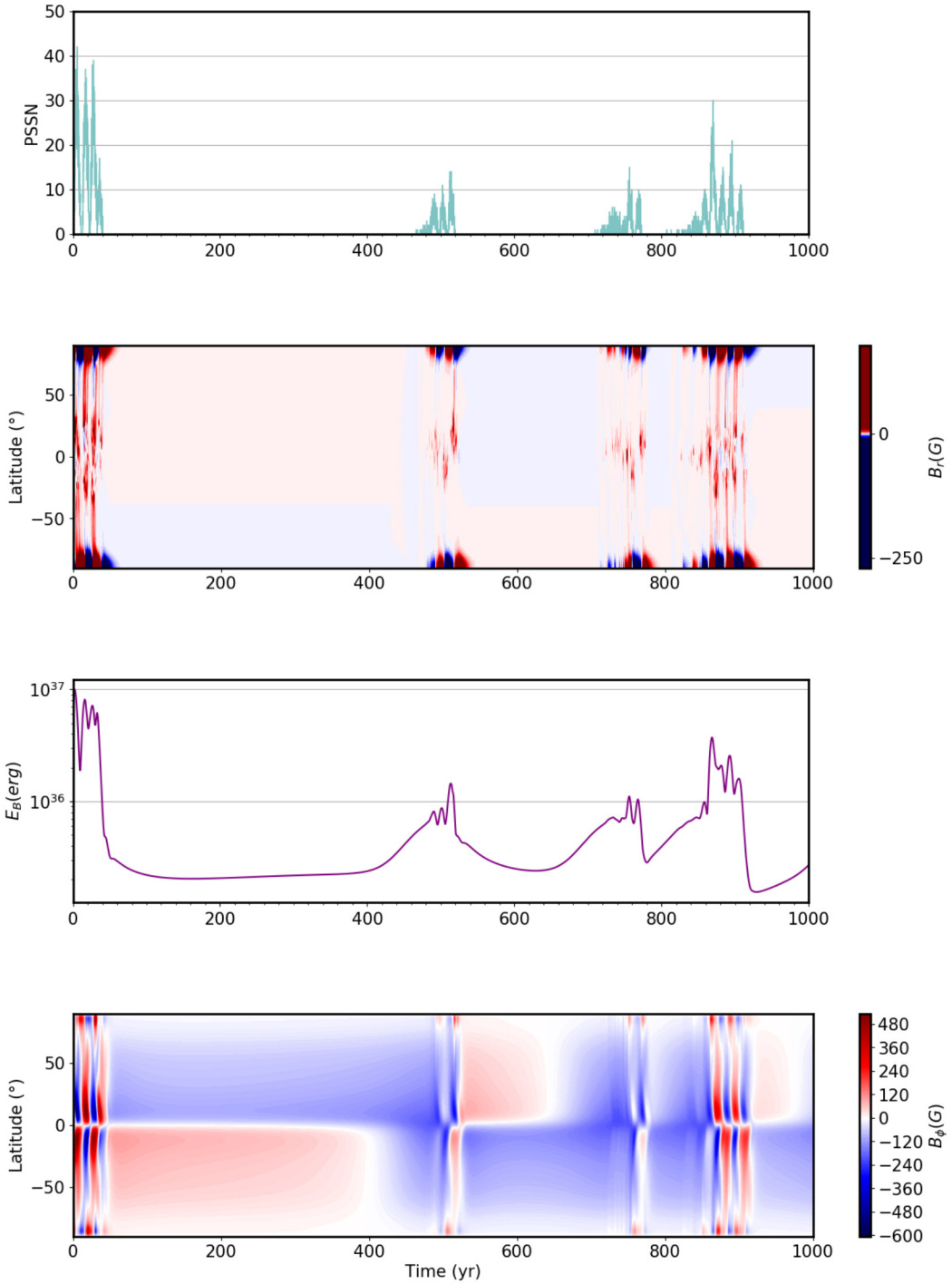

FIG. A.11. *From top to bottom*: PSSN, surface radial field, total magnetic energy, deep-seated toroidal field as a function of time. In this case, the α-effect operates supercriticially, hence it is able to restart the dynamo action once the primary dynamo shuts down but the primary dynamo runs close to a subcritical regime and it shuts down often ($K = 0.30$, $\alpha_0 = -12$ cm s^{-1}, $B_0 = 200$ G, $B_Q = 150$ G, $\eta_c = 10^8$ cm^{2}s^{-1}, $\eta_t = 10^{12}$ cm^{2}s^{-1}). Grand Minima generated by the model are pretty solar-like in terms of their duration, when $-9 < \alpha_0 < -15$ cm s^{-1} and $28 < K < 50$ cm s^{-1} approximately.

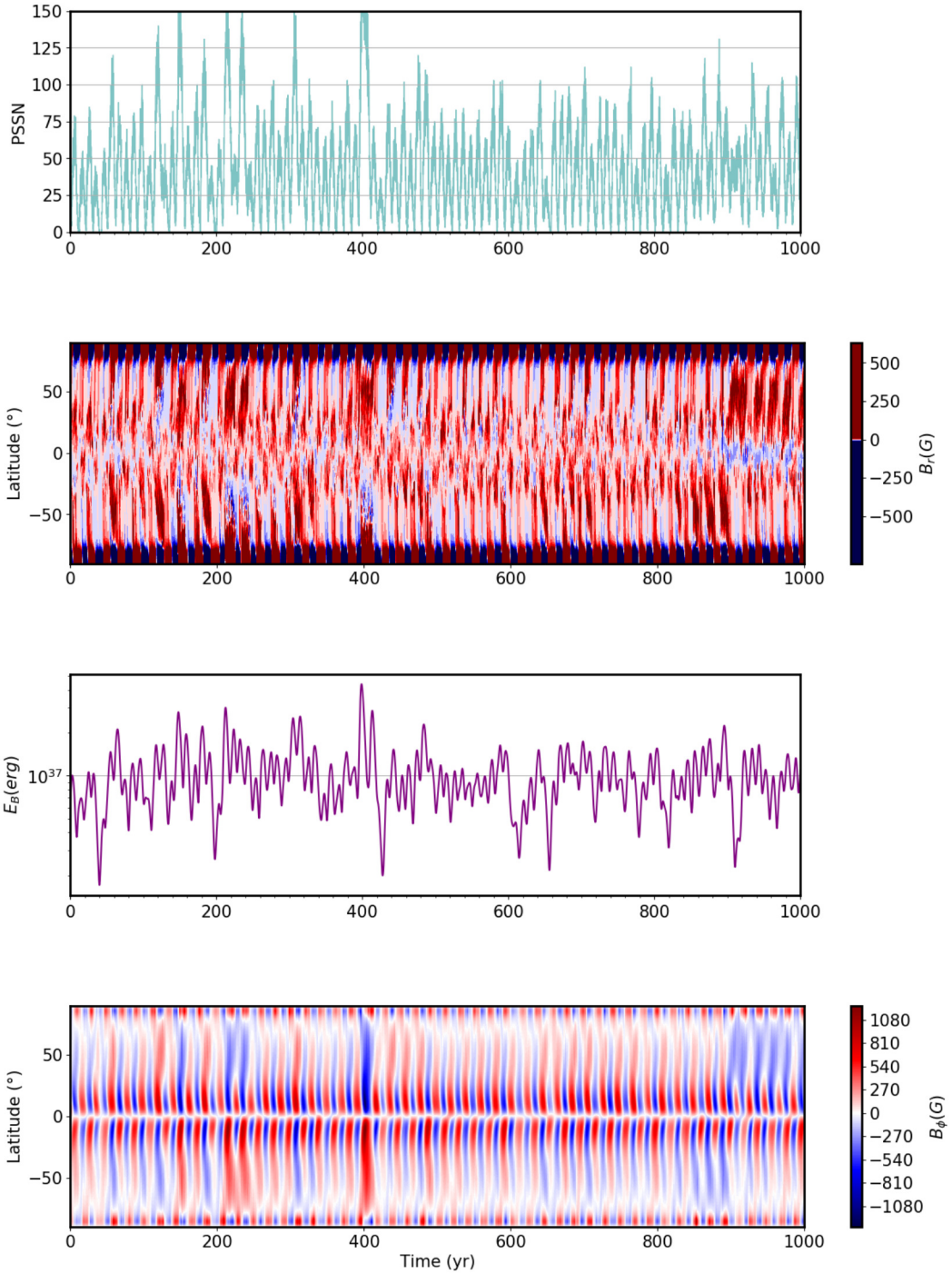

FIG. A.12. *From top to bottom*: PSSN, surface radial field, total magnetic energy, deep-seated toroidal field as a function of time. In this case, both the BL dynamo and α-effect operate supercriticially. The dynamo action doesn't even stop completely ($K = 0.40$, $\alpha_0 = -12$ cm s^{-1}, $B_0 = 200$ G, $B_Q = 150$ G, $\eta_c = 10^8$ cm^{2}s^{-1}, $\eta_t = 10^{12}$ cm^{2}s^{-1}).

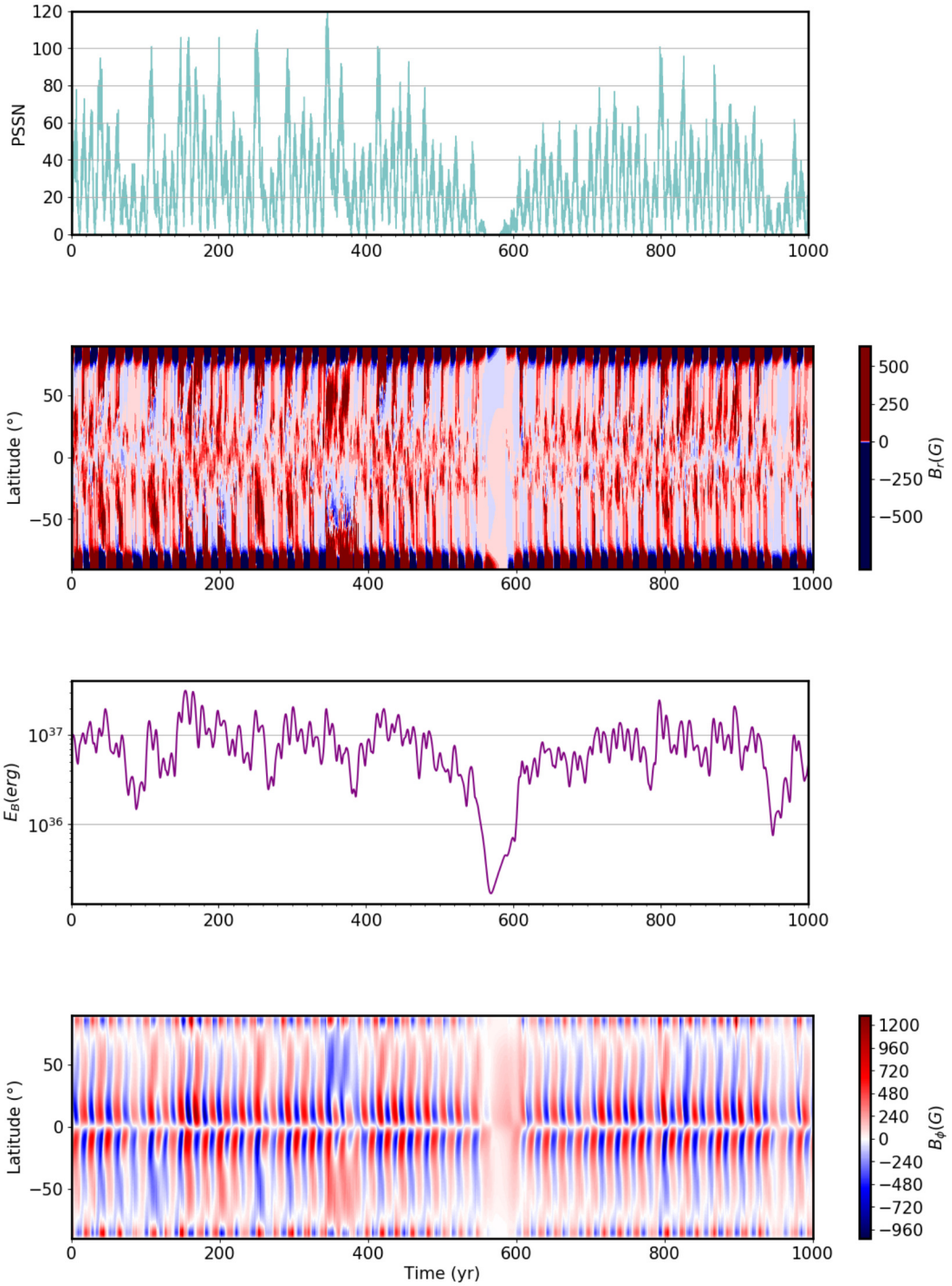

FIG. A.13. *From top to bottom*: PSSN, surface radial field, total magnetic energy, deep-seated toroidal field as a function of time. In this case, the α-effect operates supercriticially, hence it is able to restart the dynamo action once the primary dynamo shuts down ($K = 0.30$, $\alpha_0 = -15$ cm s^{-1}, $B_0 = 200$ G, $B_Q = 150$ G, $\eta_c = 10^8$ cm^{2}s^{-1}, $\eta_t = 10^{12}$ cm^{2}s^{-1}). Grand Minima generated by the model are pretty solar-like in terms of their duration, when $-9 < \alpha_0 < -15$ cm s^{-1} and $28 < K < 50$ cm s^{-1} approximately.

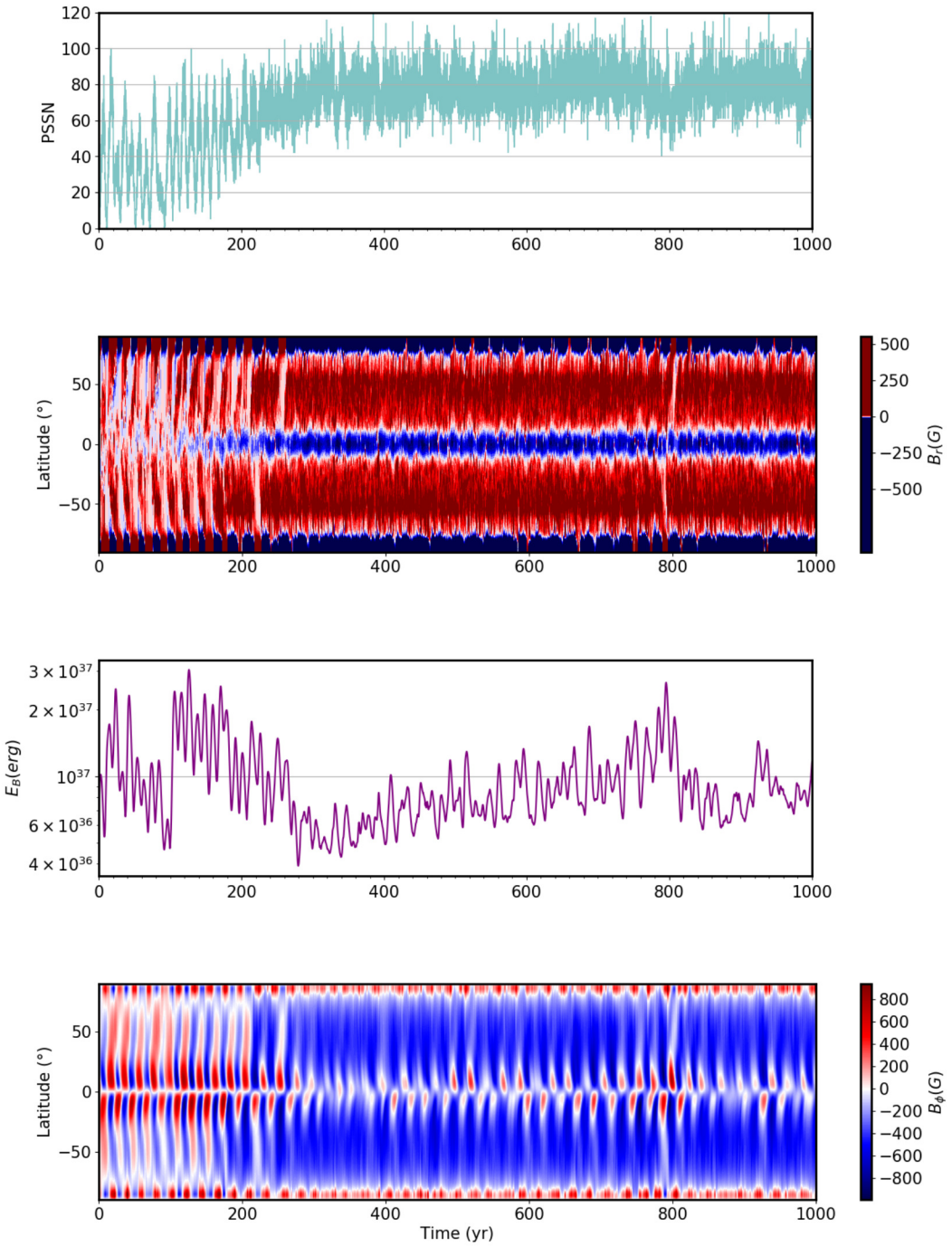

FIG. A.14. *From top to bottom*: PSSN, surface radial field, total magnetic energy, deep-seated toroidal field as a function of time. Here, the α-effect operates supercriticially with a pretty high amplitude. It doesn't allow the primary dynamo to shut down at all. Moreover, it tends to take over keeping the dynamo in a Grand Maximum state and maintaining a dominant quadrupolar field without polarity reversals for a very extended period ($K = 0.30$, $\alpha_0 = -25$ cm s^{-1}, $B_0 = 200$ G, $B_Q = 150$ G, $\eta_c = 10^8$ cm^{2}s^{-1}, $\eta_t = 10^{12}$ cm^{2}s^{-1}).

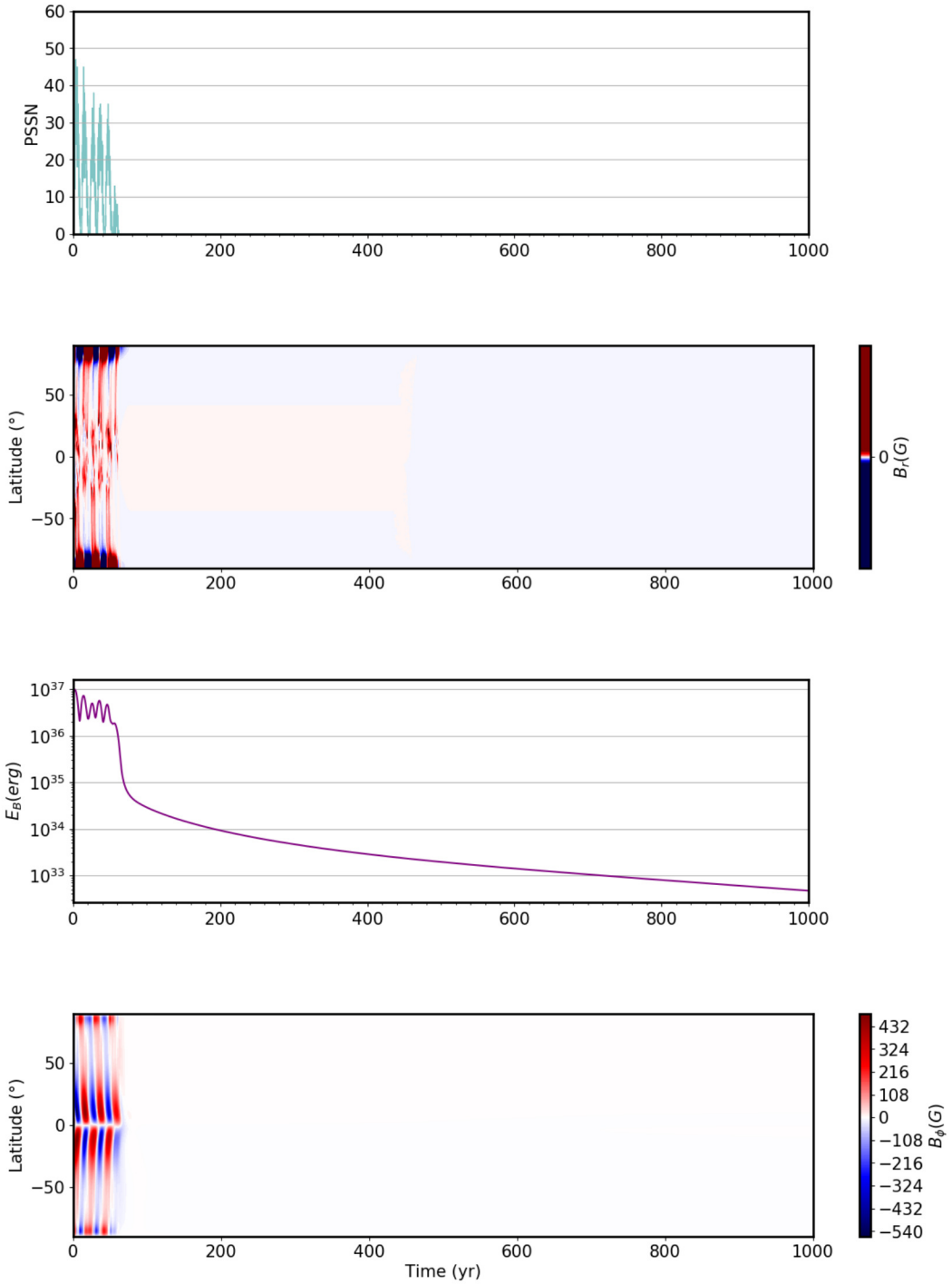

FIG. A.15. *From top to bottom*: PSSN, surface radial field, total magnetic energy, deep-seated toroidal field as a function of time. This case shows that while α_0 has a positive value, it is unable to restart the dynamo action once the primary dynamo shuts down ($K = 0.30$, $\alpha_0 = 12$ cm s^{-1}, $B_0 = 200$ G, $B_Q = 150$ G, $\eta_c = 10^8$ cm^{2}s^{-1}, $\eta_t = 10^{12}$ cm^{2}s^{-1}).

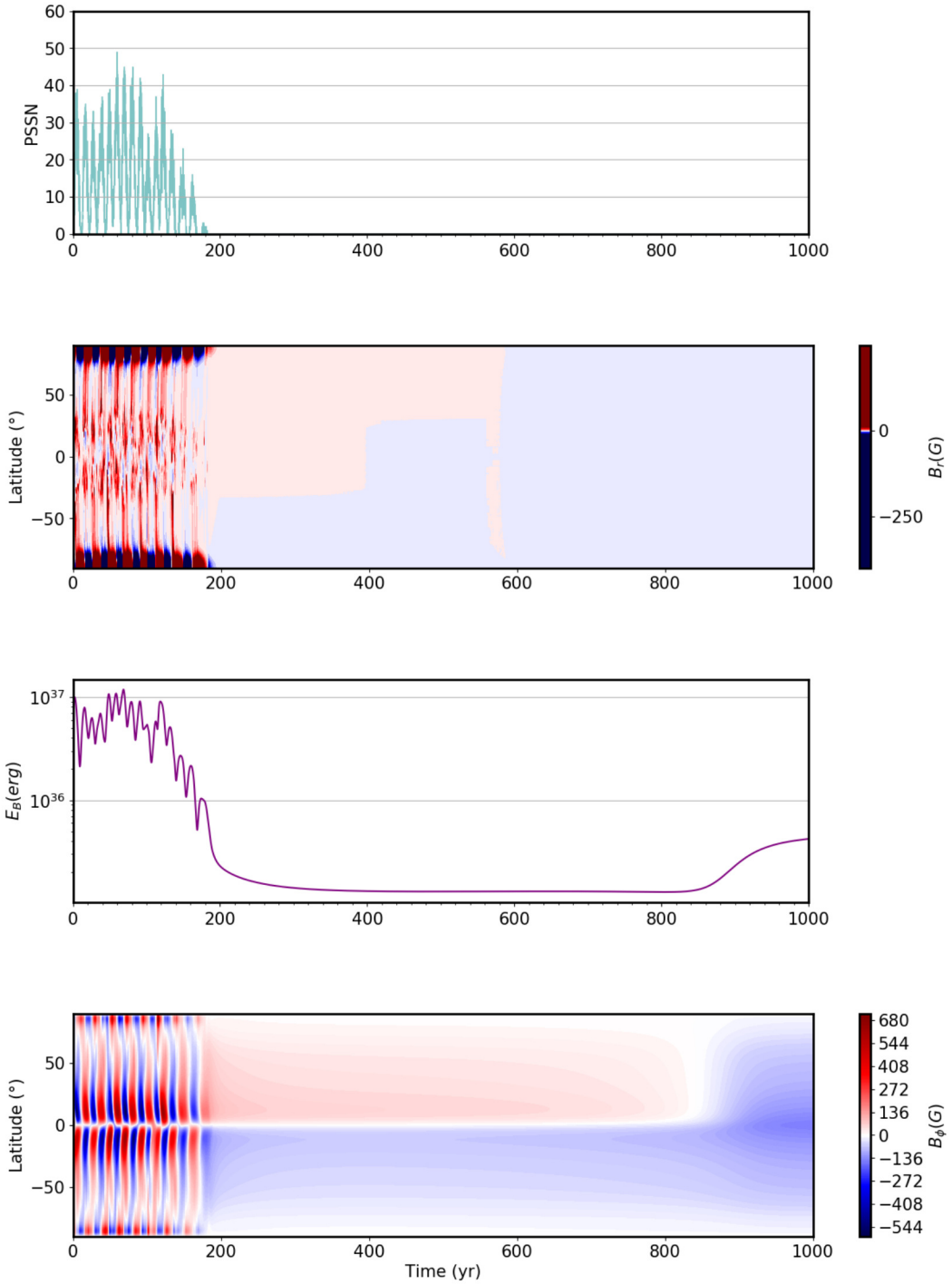

FIG. A.16. *From top to bottom*: PSSN, surface radial field, total magnetic energy, deep-seated toroidal field as a function of time. Here, the threshold field B_0 for the α-effect to kick in is 100G lower than usual and results in very long quiescent epochs. By the end of this simulation the magnetic energy starts to increase again indicating a possible restart ($K = 0.30$, $\alpha_0 = -12$ cm s^{-1}, $B_0 = 100$ G, $B_Q = 150$ G, $\eta_c = 10^8$ cm^{2}s^{-1}, $\eta_t = 10^{12}$ cm^{2}s^{-1}).

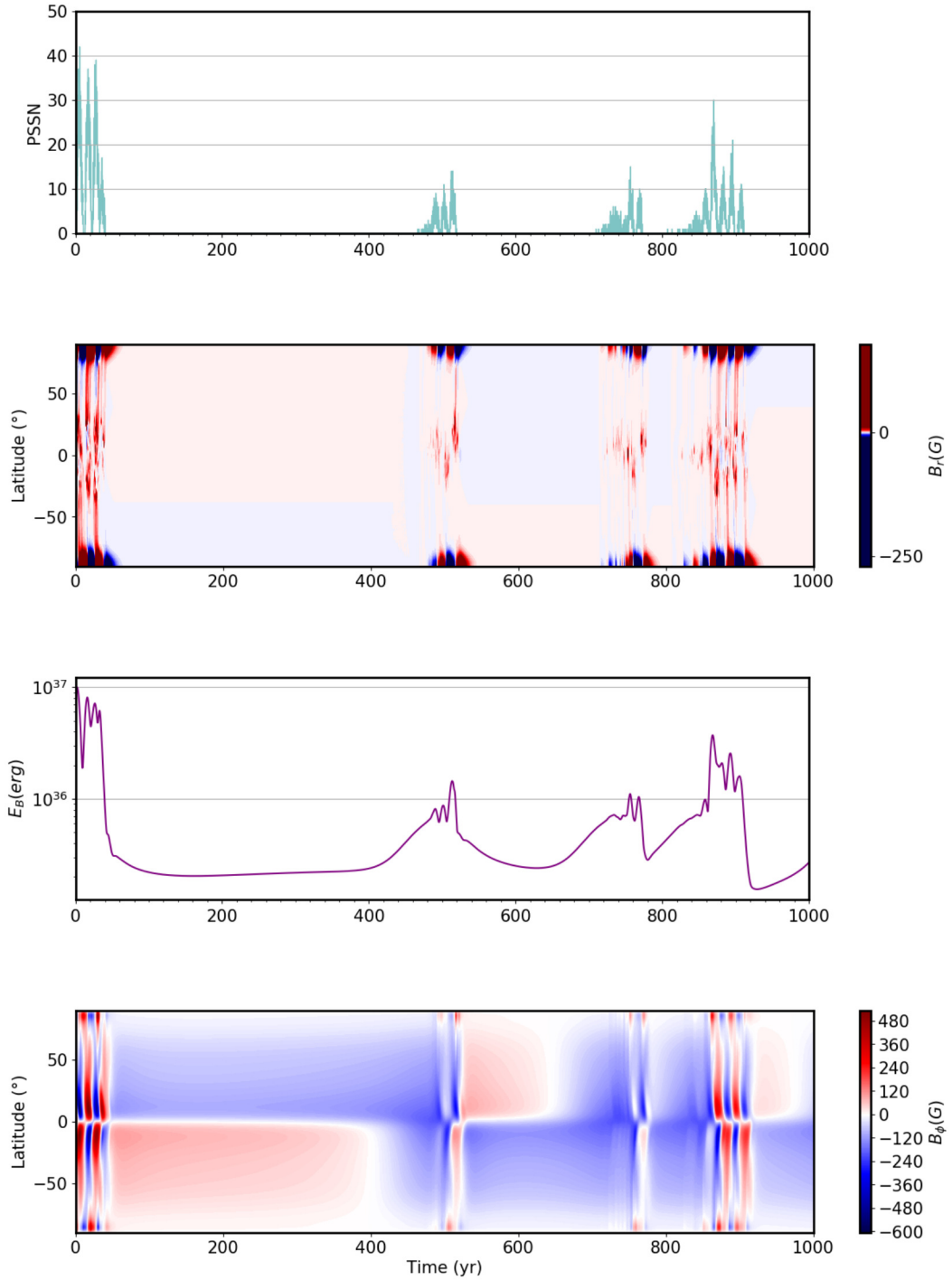

FIG. A.17. *From top to bottom*: PSSN, surface radial field, total magnetic energy, deep-seated toroidal field as a function of time. In this case, the threshold field B_0 for the α-effect to kick in is 50G lower than usual and results in longer quiescent epochs seperated by intermittent restart attempts ($K = 0.30$, $\alpha_0 = -12$ cm s^{-1}, $B_0 = 150$ G, $B_Q = 150$ G, $\eta_c = 10^8$ cm^{2}s^{-1}, $\eta_t = 10^{12}$ cm^{2}s^{-1}).

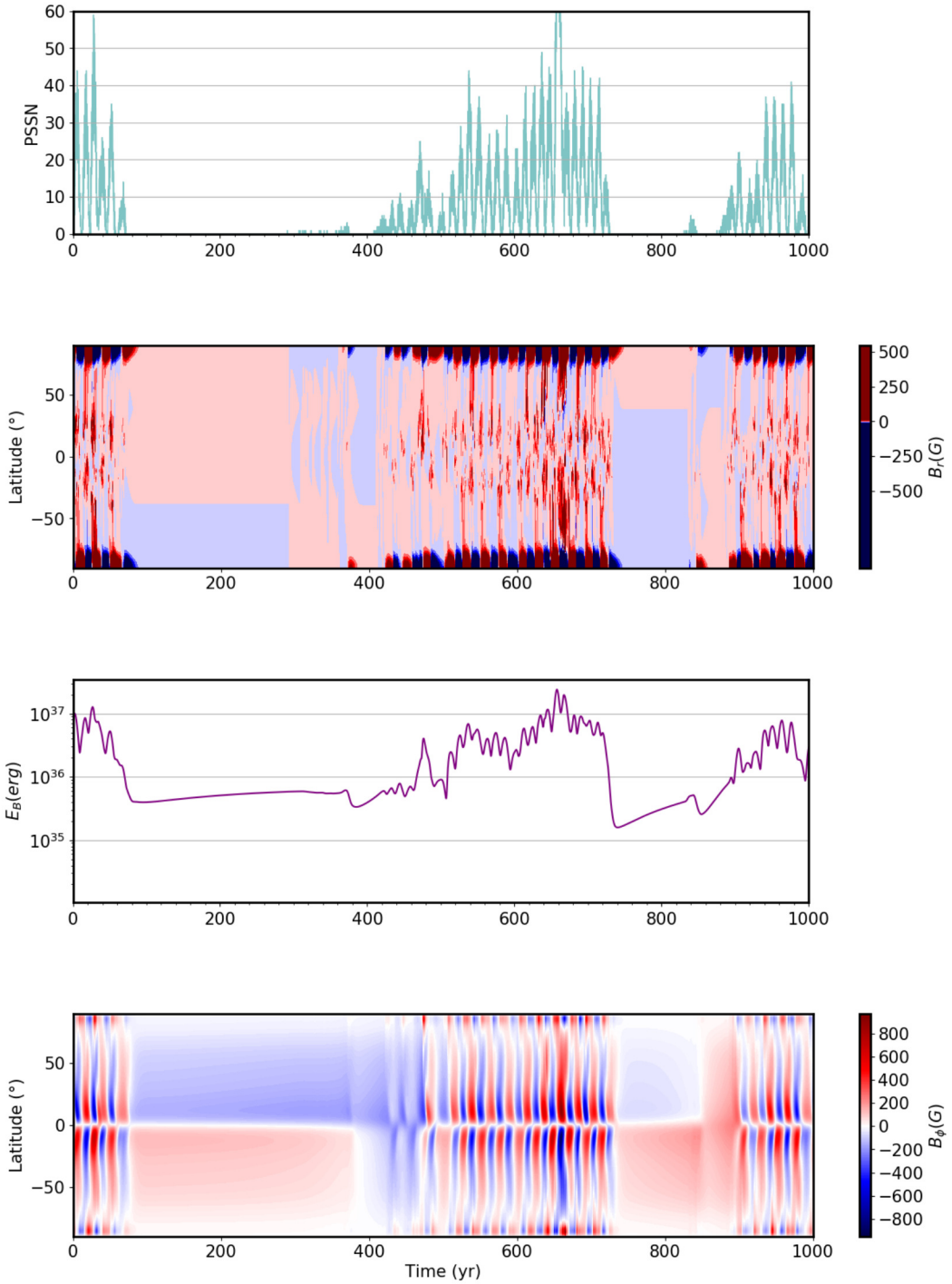

FIG. A.18. *From top to bottom*: PSSN, surface radial field, total magnetic energy, deep-seated toroidal field as a function of time. In this case, the threshold field B_0 for the α-effect to kick in is 50G higher than usual and results in shorter quiescent epochs ($K = 0.30$, $\alpha_0 = -12$ cm s^{-1}, $B_0 = 250$ G, $B_Q = 150$ G, $\eta_c = 10^8$ cm^{2}s^{-1}, $\eta_t = 10^{12}$ cm^{2}s^{-1}).

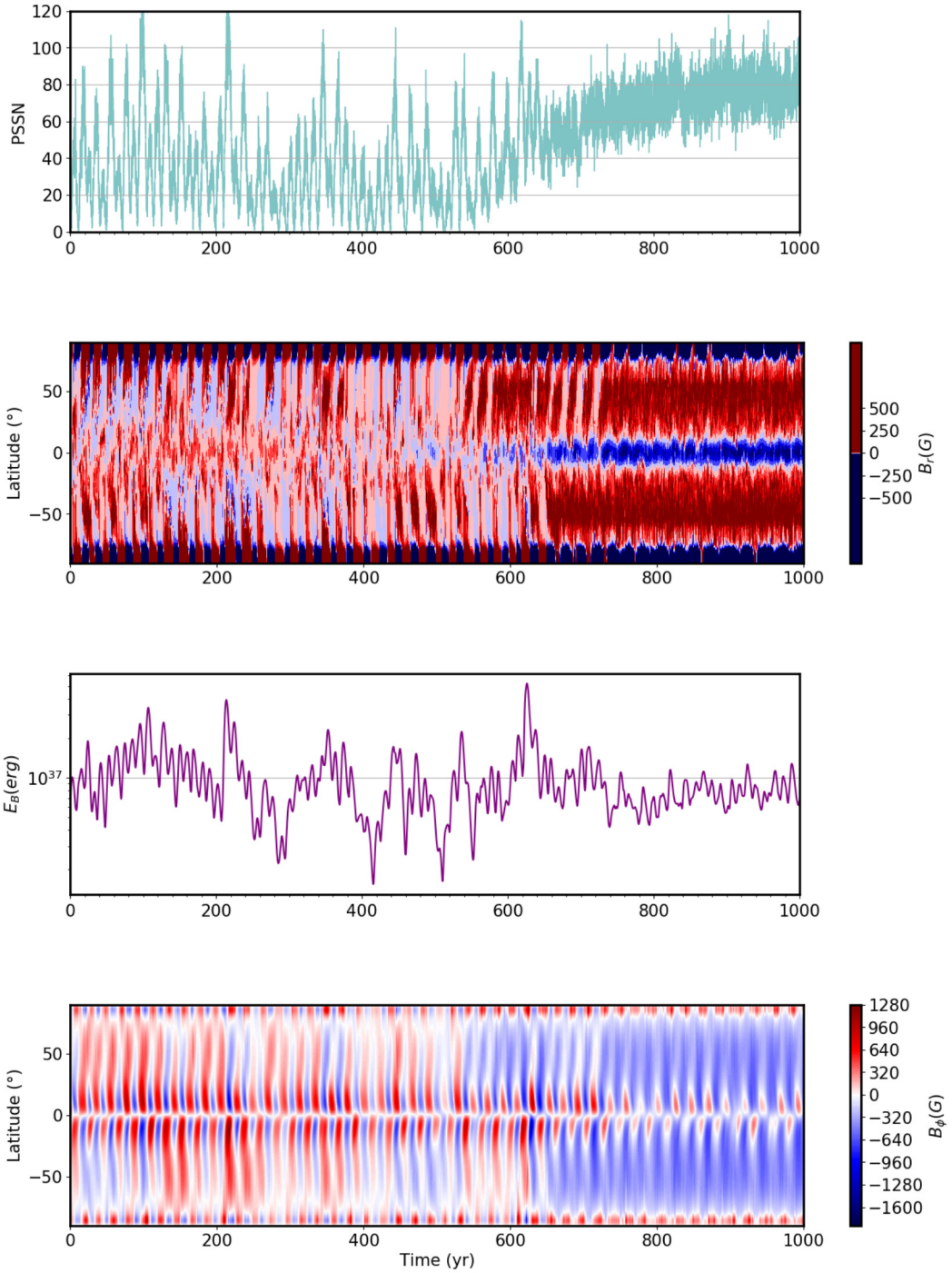

FIG. A.19. *From top to bottom*: PSSN, surface radial field, total magnetic energy, deep-seated toroidal field as a function of time. Here, the threshold field B_0 for the α-effect to kick in is 300G higher than the optimal value and results in shorter quiescent epochs ($K = 0.30$, $\alpha_0 = -12$ cm s^{-1}, $B_0 = 500$ G, $B_Q = 150$ G, $\eta_c = 10^8$ cm^{2}s^{-1}, $\eta_t = 10^{12}$ cm^{2}s^{-1}).

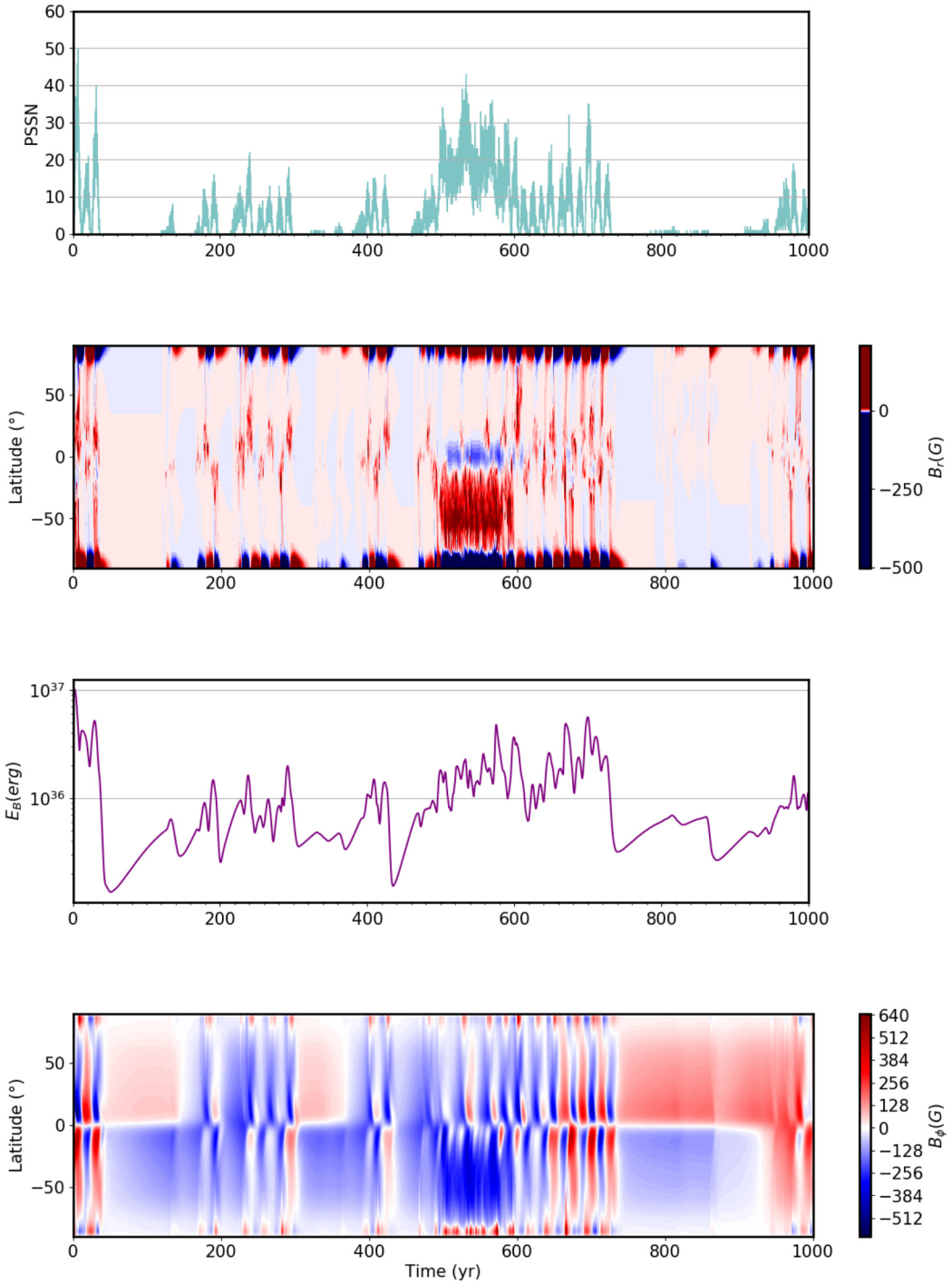

FIG. A.20. *From top to bottom*: PSSN, surface radial field, total magnetic energy, deep-seated toroidal field as a function of time. Here, $B_Q < 150$ G and it makes the dynamo action much more frequently intermittent with many re-start attemps after falling into a Grand Minimum ($K = 0.30$, $\alpha_0 = -12$ cm s^{-1}, $B_0 = 200$ G, $B_Q = 120$ G, $\eta_c = 10^8$ cm^{2}s^{-1}, $\eta_t = 10^{12}$ cm^{2}s^{-1}).

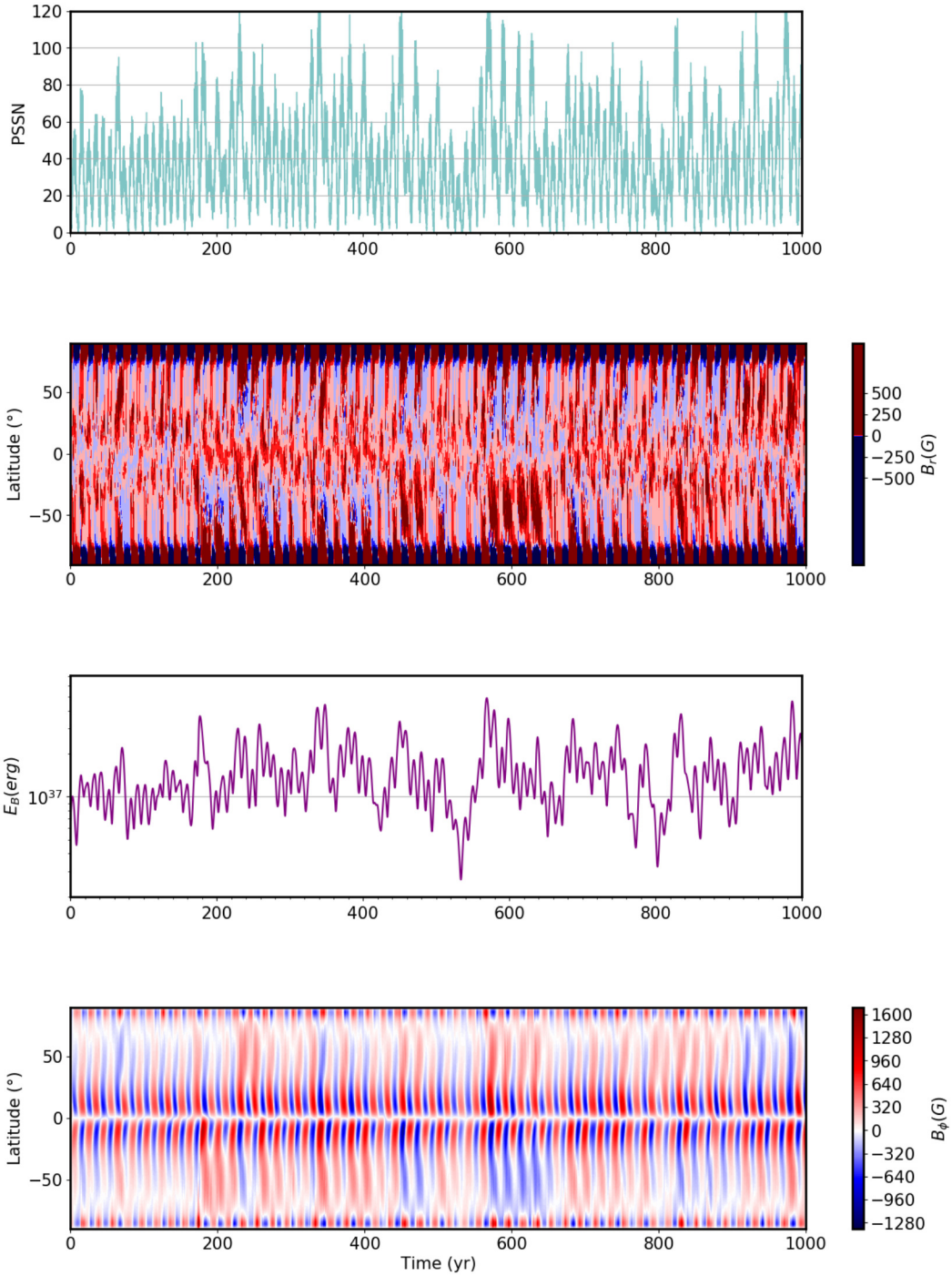

FIG. A.21. *From top to bottom*: PSSN, surface radial field, total magnetic energy, deep-seated toroidal field as a function of time. Here, $B_Q > 150$ G and the dynamo action doesn't completely stop ($K = 0.30$, $\alpha_0 = -12$ cm s^{-1}, $B_0 = 200$ G, $B_Q = 200$ G, $\eta_c = 10^8$ cm^{2}s^{-1}, $\eta_t = 10^{12}$ cm^{2}s^{-1}).

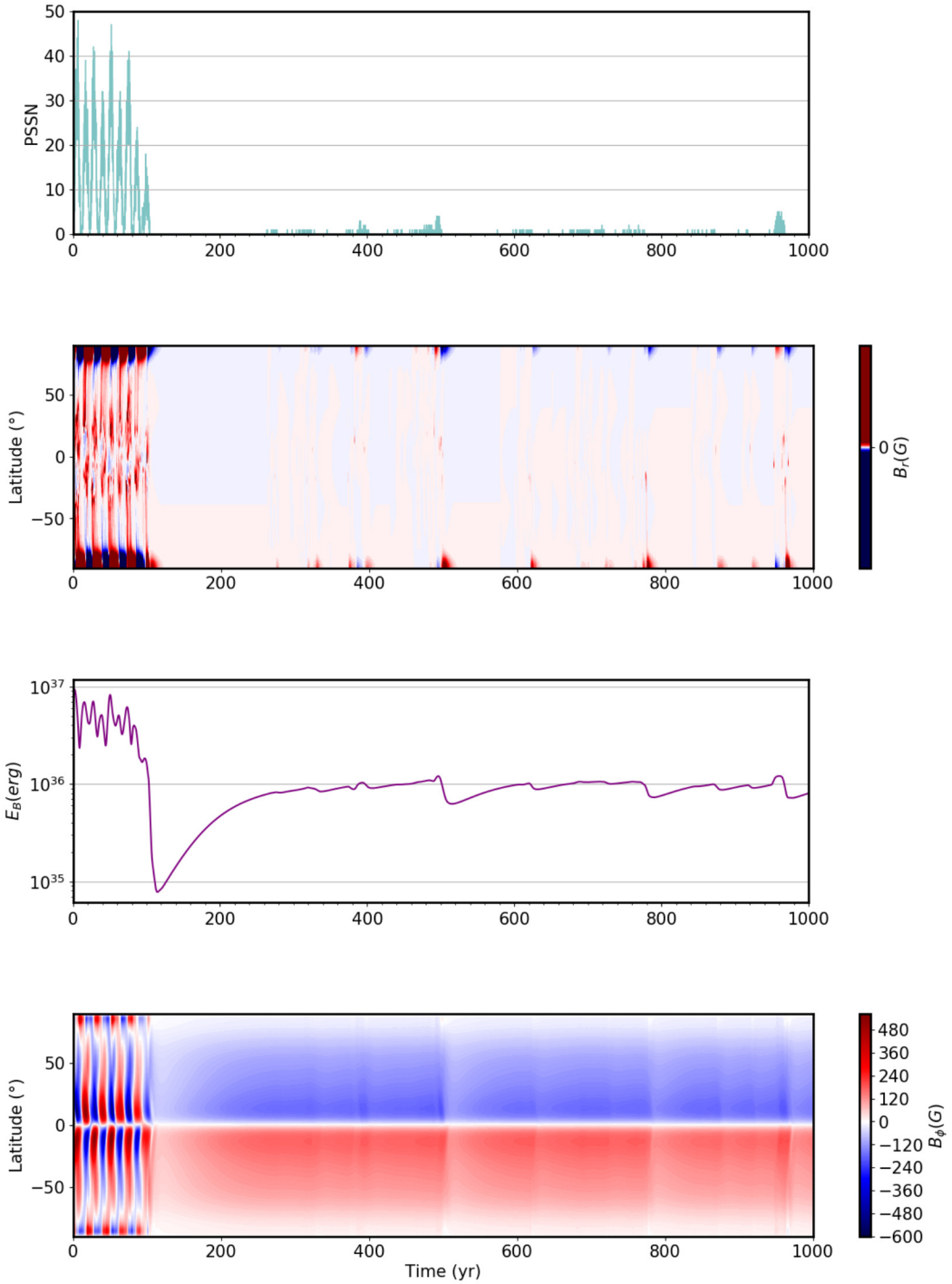

FIG. A.22. *From top to bottom*: PSSN, surface radial field, total magnetic energy, deep-seated toroidal field as a function of time. In this run, η_c is increased by a factor of 10 which resulted in a non solar-like behavior with attempts of recovery. The α dynamo is unable to increase the magnetic energy above the threshold for the BL mechanism to pick up ($K = 0.30$, $\alpha_0 = -12$ cm s^{-1}, $B_0 = 200$ G, $B_Q = 150$ G, $\eta_c = 10^9$ cm^{2}s^{-1}, $\eta_t = 10^{12}$ cm^{2}s^{-1}).

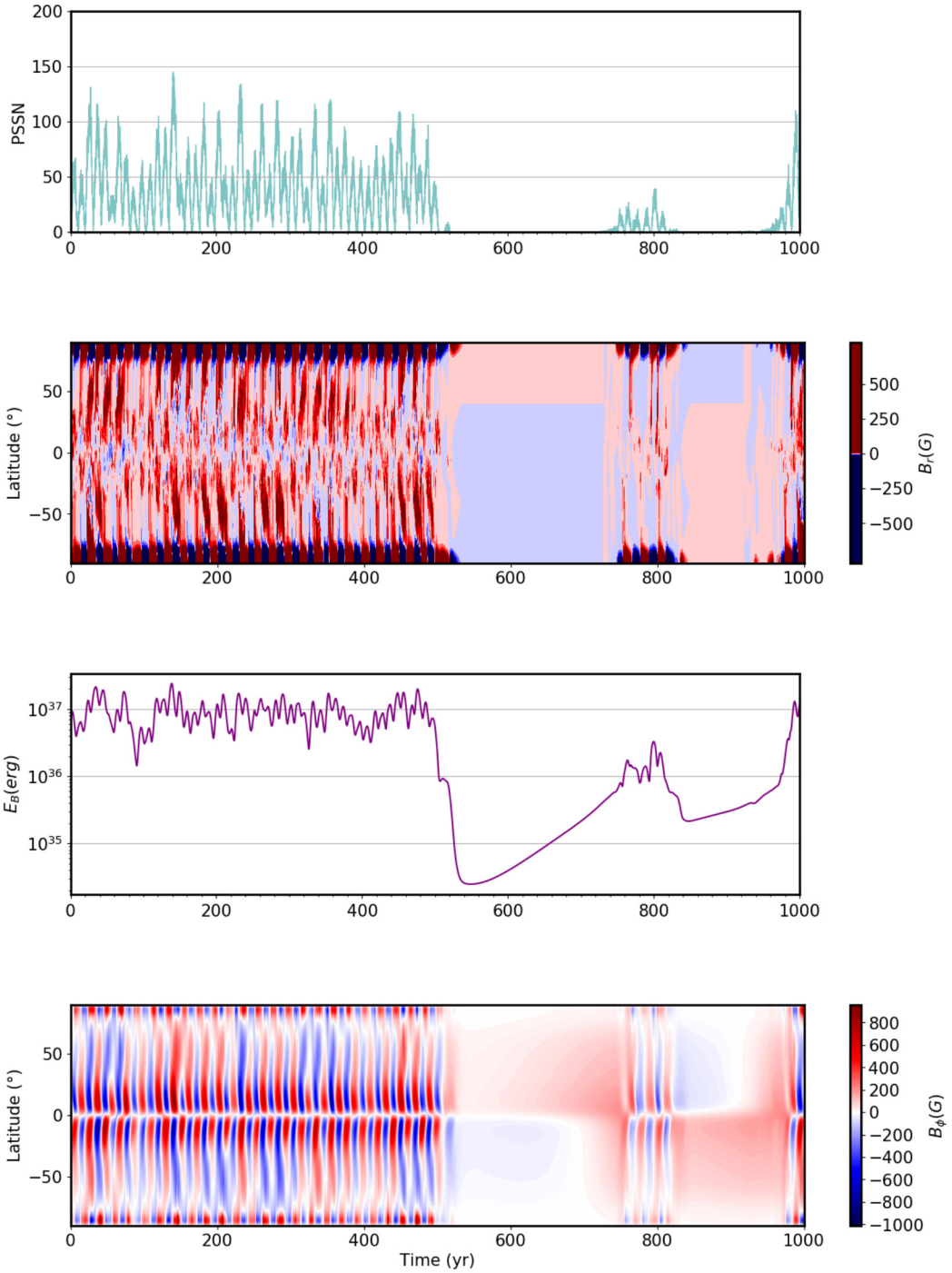

FIG. A.23. *From top to bottom*: PSSN, surface radial field, total magnetic energy, deep-seated toroidal field as a function of time. In this run, η_c is increased by a factor of 10. The α dynamo is able to increase the magnetic energy above the threshold for the BL mechanism to pick up, the primary dynamo number K is also augmented ($K = 0.40$, $\alpha_0 = -12$ cm s^{-1}, $B_0 = 200$ G, $B_Q = 150$ G, $\eta_c = 10^9$ cm^{2}s^{-1}, $\eta_t = 10^{12}$ cm^{2}s^{-1}).

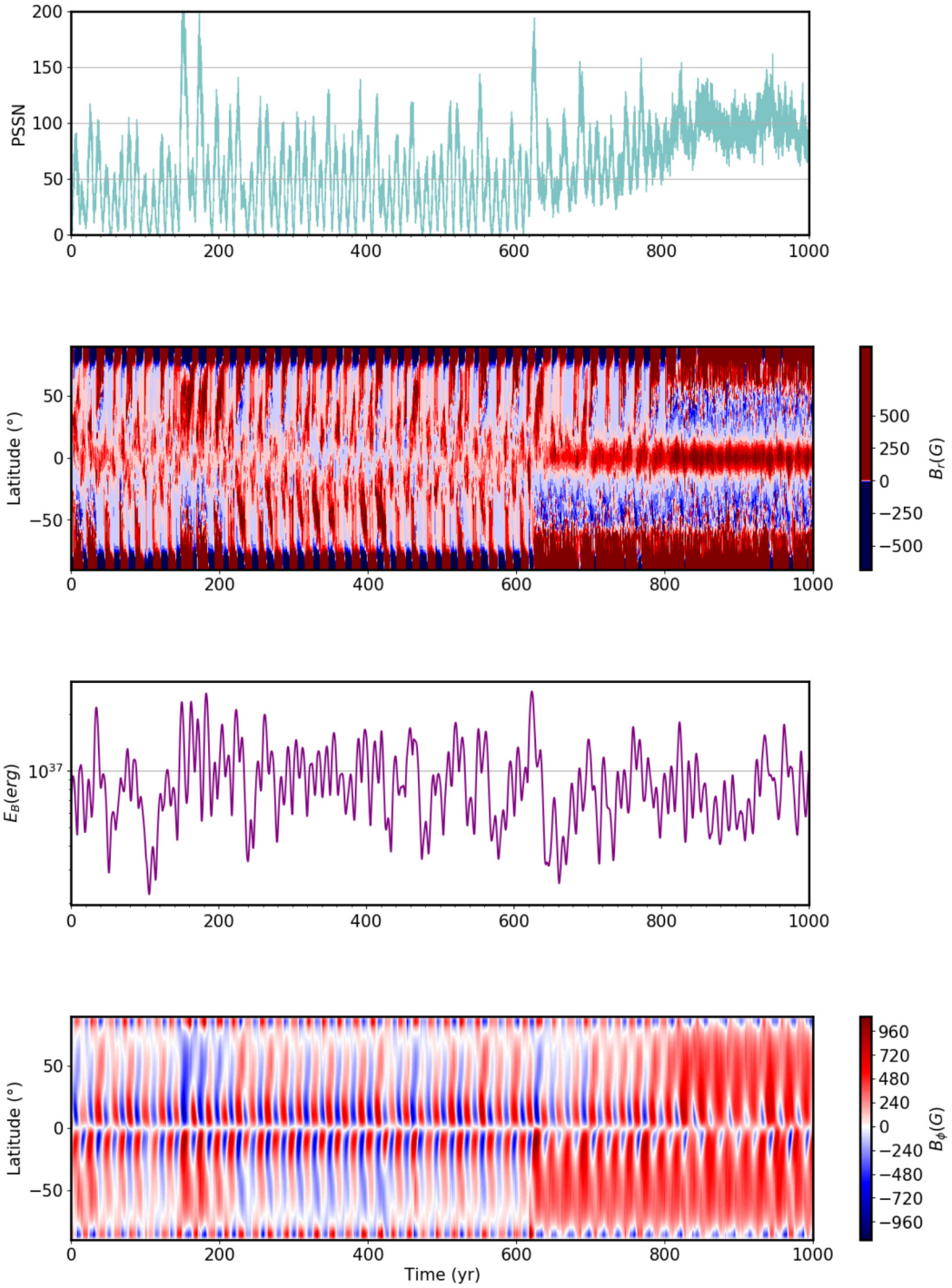

FIG. A.24. *From top to bottom*: PSSN, surface radial field, total magnetic energy, deep-seated toroidal field as a function of time. In this run, η_c is increased by a factor of 10, while K is also augmented. This combination resulted in a non-stop simulation with a Grand Maximum ($K = 0.60$, $\alpha_0 = -16$ cm s^{-1}, $B_0 = 220$ G, $B_Q = 150$ G, $\eta_c = 10^9$ cm^{2}s^{-1}, $\eta_t = 10^{12}$ cm^{2}s^{-1}).

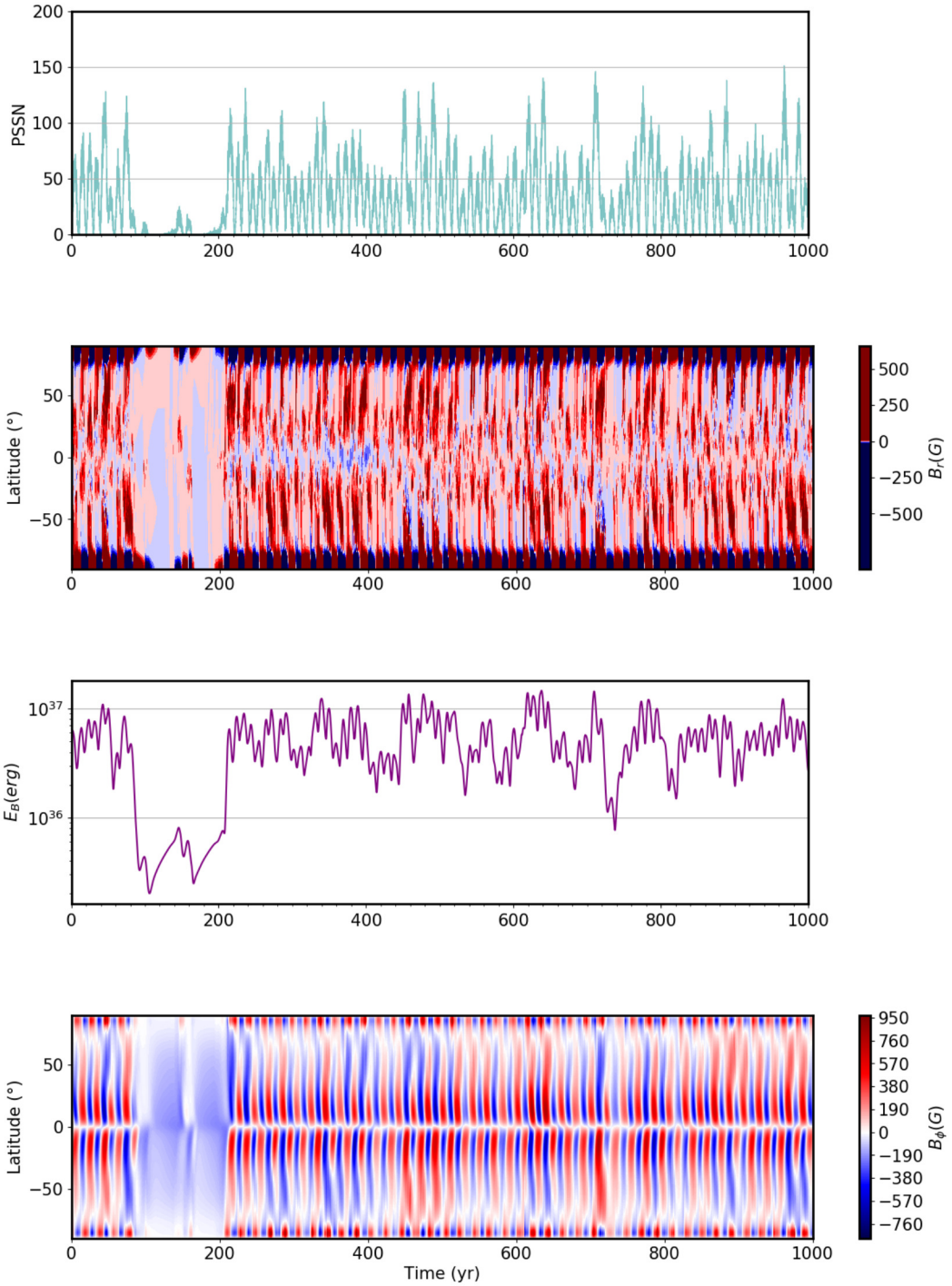

FIG. A.25. *From top to bottom*: PSSN, surface radial field, total magnetic energy, deep-seated toroidal field as a function of time. In this run, η_c is increased by a factor of 20 which leads to a decrease in the mean magnetic energy level compared to the case presented in Fig. A.23 ($K = 0.40$, $\alpha_0 = -12$ cm s^{-1}, $B_0 = 200$ G, $B_Q = 150$ G, $\eta_c = 10^{10}$ cm^{2}s^{-1}, $\eta_t = 10^{12}$ cm^{2}s^{-1}).

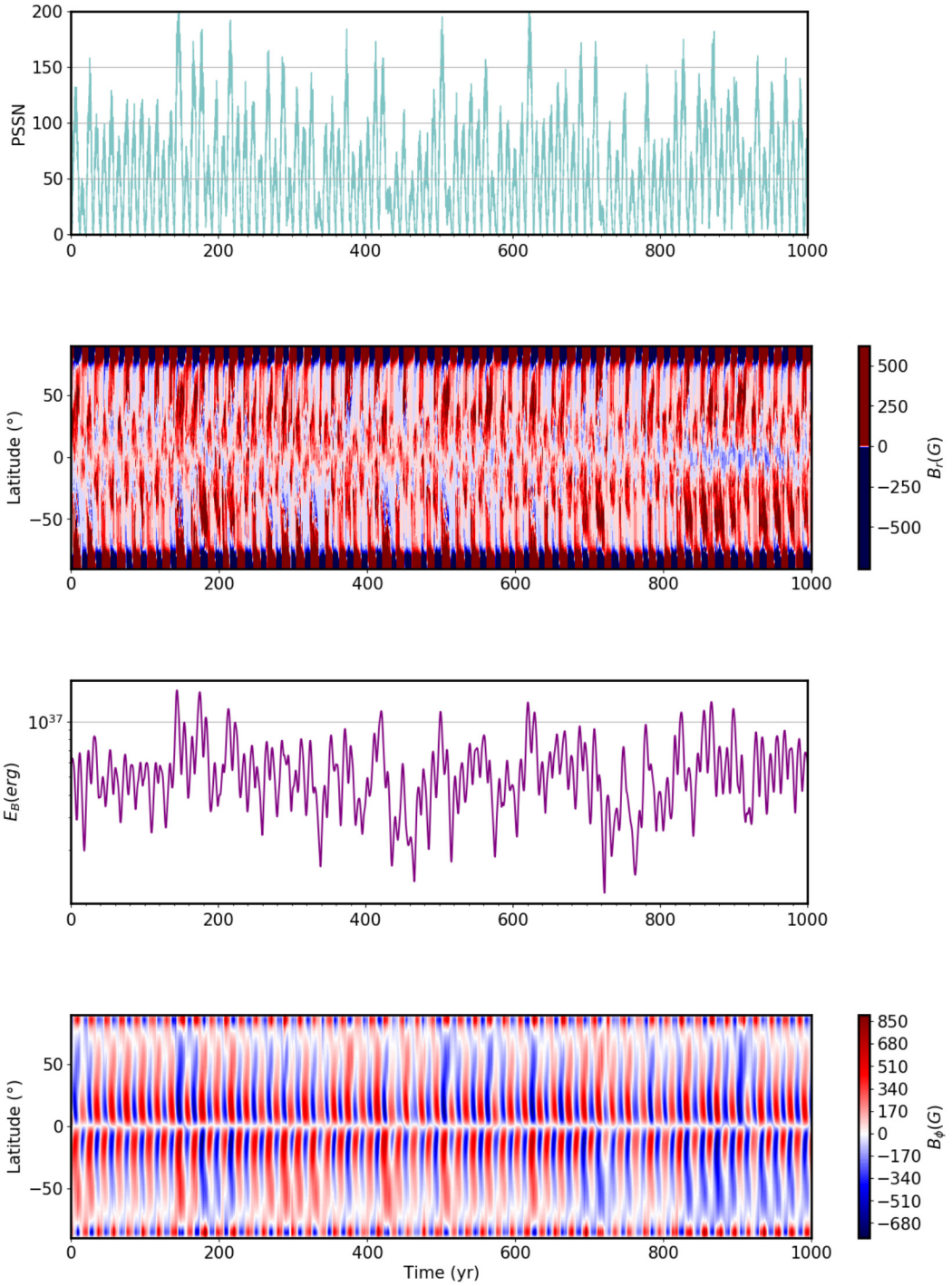

FIG. A.26. *From top to bottom*:PSSN, surface radial field, total magnetic energy, deep-seated toroidal field as a function of time. In this run, η_c is increased by a factor of 20 in Fig. A.25, which leads to a decrease in the mean magnetic energy level. However, since K is relatively higher, there is no Grand Minimum ($K = 0.60$, $\alpha_0 = -12$ cm s^{-1}, $B_0 = 200$ G, $B_Q = 150$ G, $\eta_c = 10^{10}$ cm^{2}s^{-1}, $\eta_t = 10^{12}$ cm^{2}s^{-1}).

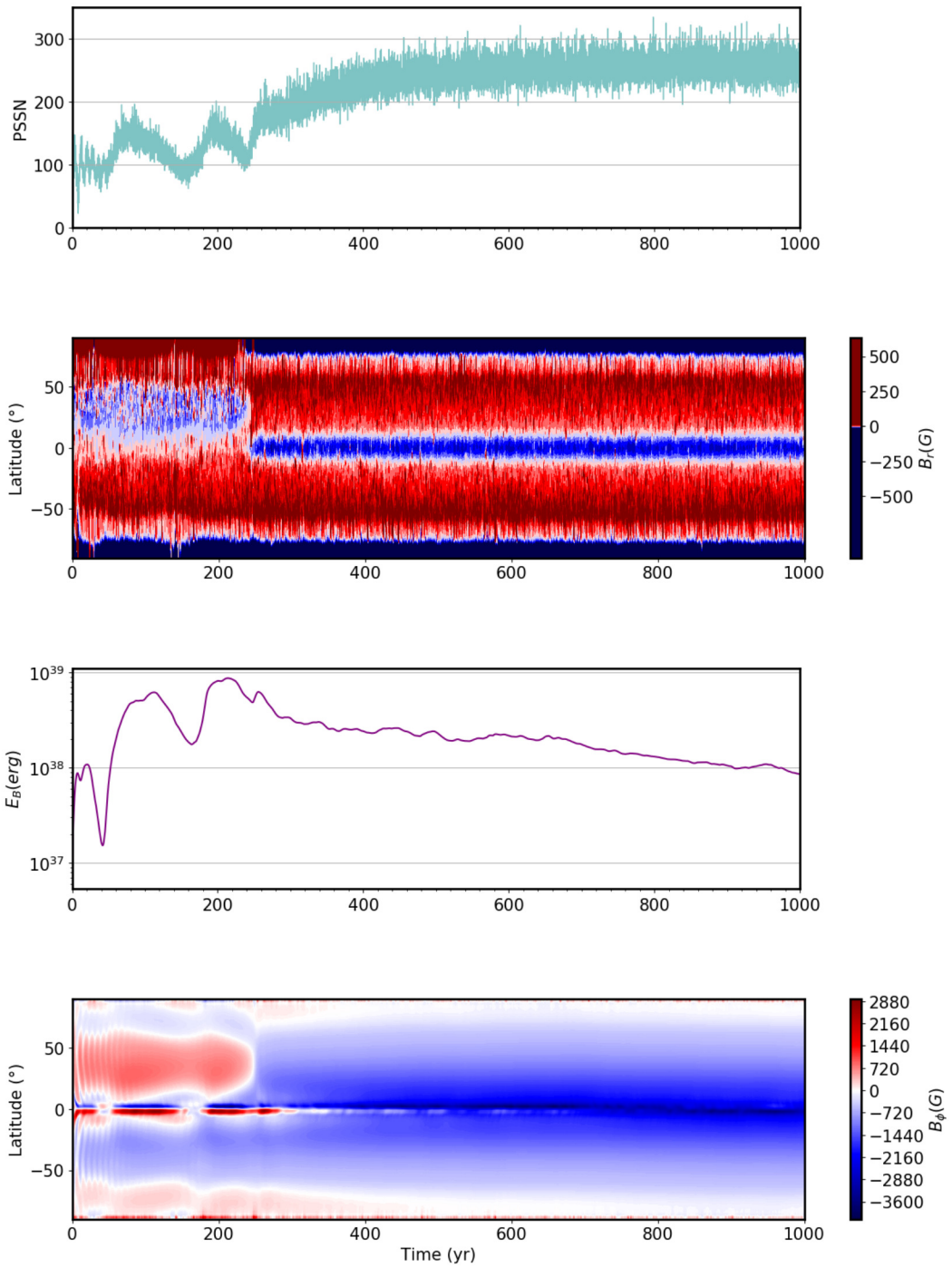

FIG. A.27. *From top to bottom*: PSSN, surface radial field, total magnetic energy, deep-seated toroidal field as a function of time. In this run, η_t is decreased by a factor of 10 which results in dramatic changes in the dynamo's behavior. As the PSSN keeps increasing and comes to a stable level after 300 years, the total magnetic energy dramatically decreases. In the meantime, both the surface radial field and the interior toroidal field become purely quadrupolar ($K = 0.40$, $\alpha_0 = -12$ cm s^{-1}, $B_0 = 200$ G, $B_Q = 150$ G, $\eta_c = 10^8$ cm^{2}s^{-1}, $\eta_t = 10^{11}$ cm^{2}s^{-1}).

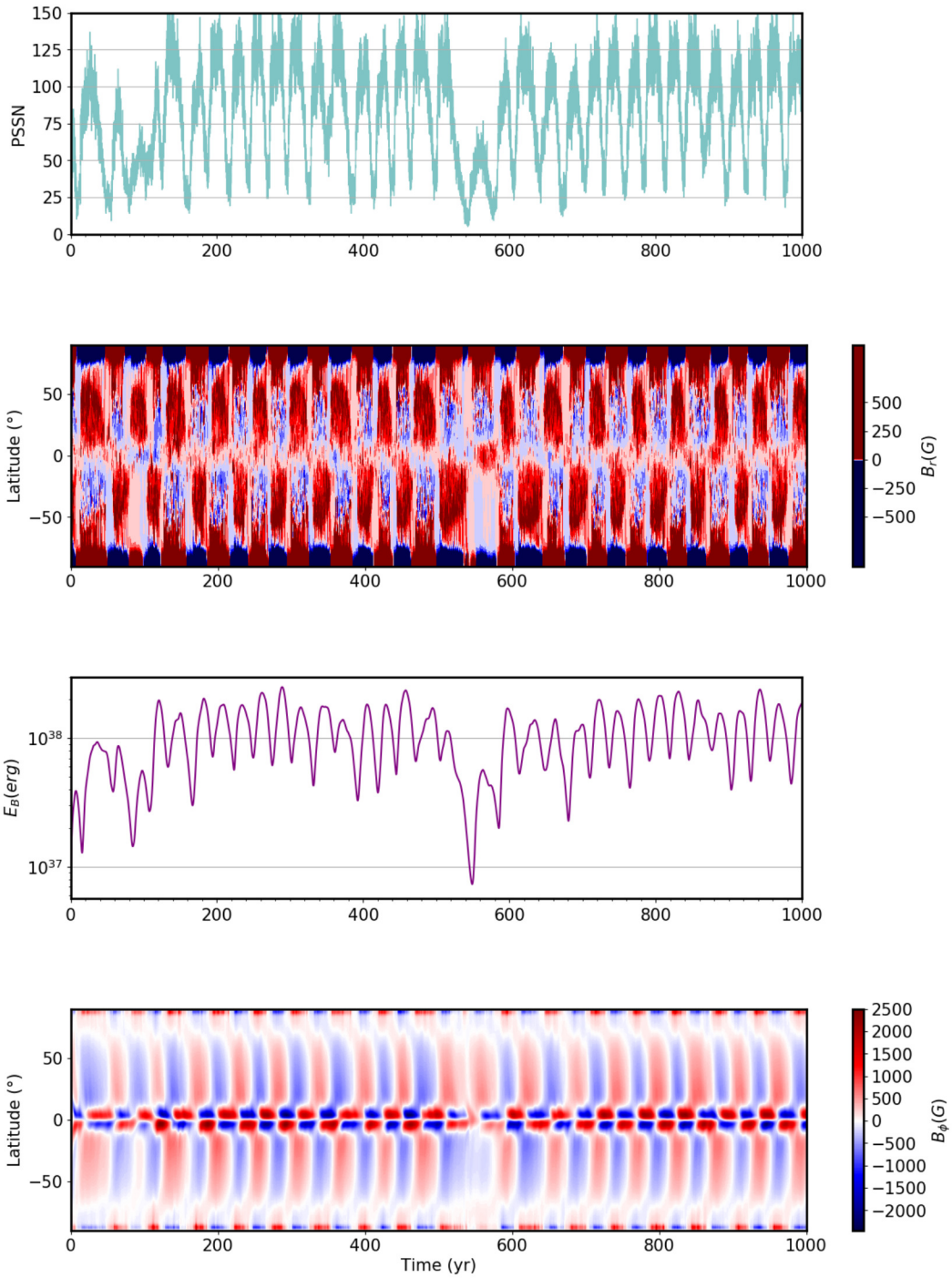

FIG. A.28. *From top to bottom*:PSSN, surface radial field, total magnetic energy, deep-seated toroidal field as a function of time. In this run, η_t is increased by a factor of 5 (but still $< 10^{12} cm^2$) compared to Fig. A.27 and the dynamo action starts to become more solar-like. The interior toroidal field is more confined in lower latitudes and the mean cycle length appears to be a little longer than usual ($K = 0.40$, $\alpha_0 = -12$ cm s^{-1}, $B_0 = 200$ G, $B_Q = 150$ G, $\eta_c = 10^8$ cm^{2}s^{-1}, $\eta_t = 10^{11.5}$ cm^{2}s^{-1}).

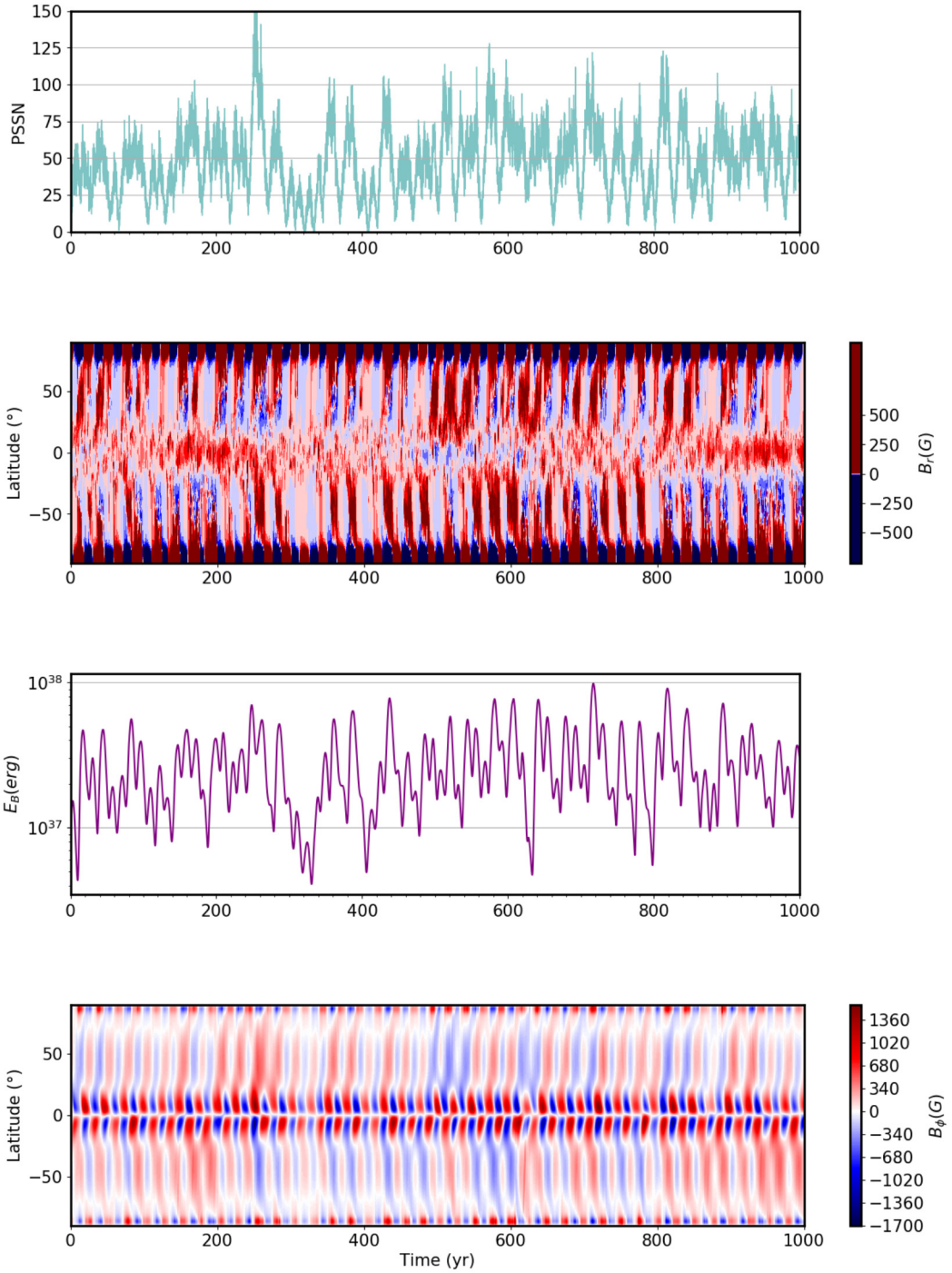

FIG. A.29. *From top to bottom*:PSSN, surface radial field, total magnetic energy, deep-seated toroidal field as a function of time. In this run, η_t is slightly smaller than the reference value (10^{12} cm^{2}s^{-1}). The overall cycle amplitude and the mean magnetic energy are decreased compared to Fig. A.28 ($K = 0.40$, $\alpha_0 = -12$ cm s^{-1}, $B_0 = 200$ G, $B_Q = 150$ G, $\eta_c = 10^8$ cm^{2}s^{-1}, $\eta_t = 10^{11.8}$ cm^{2}s^{-1}).

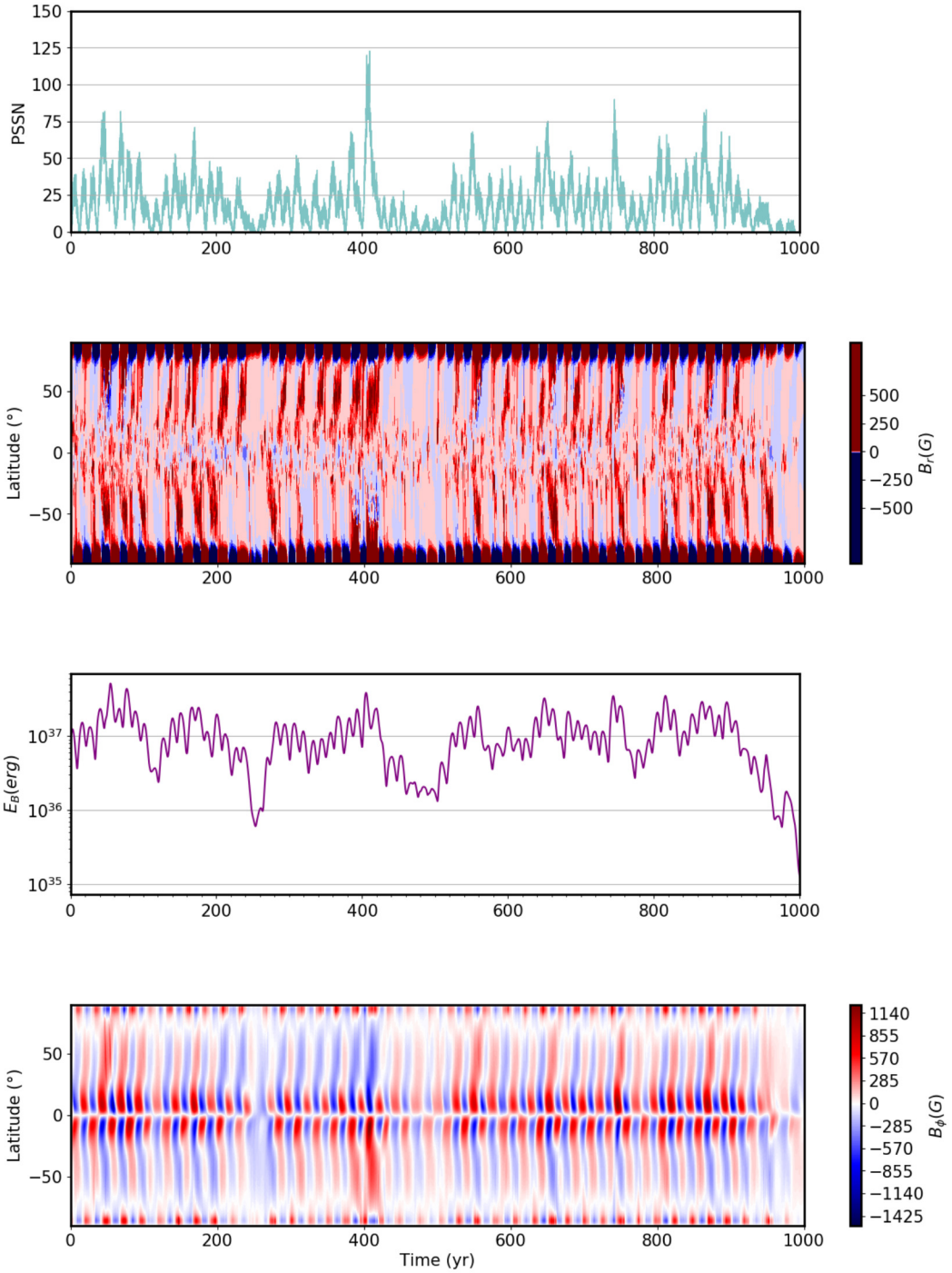

FIG. A.30. *From top to bottom*:PSSN, surface radial field, total magnetic energy, deep-seated toroidal field as a function of time. Here, η_t is slightly smaller than the reference value (10^{12} cm^{2}s^{-1}) but larger then the case in Fig. A.29. Also, K is slightly reduced. Notice how the overall cycle amplitude and the mean magnetic energy decreases compared to Fig. A.29 due to an increase in turbulence. The dynamo enters Grand Minima more frequently and their mean duration is longer ($K = 0.30$, $\alpha_0 = -12$ cm s^{-1}, $B_0 = 200$ G, $B_Q = 150$ G, $\eta_c = 10^8$ cm^{2}s^{-1}, $\eta_t = 10^{11.9}$ cm^{2}s^{-1}).

A.2. Very Long Simulation Runs

Here, two 50,000 yr simulation outputs (other than the one introduced in §2.3) are presented to display the long-term effects that different combinations of parameters provide. In Figs. A.31 and A.34, the threshold PSSN values are chosen according to the procedure followed and described in §2.3. The two cases presented here are far from being solar-like considering the percentage of time the simulations spend in in a Grand Minimum/Maximum state and the mean durations of these epochs. However, the waiting time distributions hint for a memoryless, Poisson-like process for the occurrence of Grand Minima and for some memory effects for the case of Grand Maxima (see Figs.A.33 and A.36).

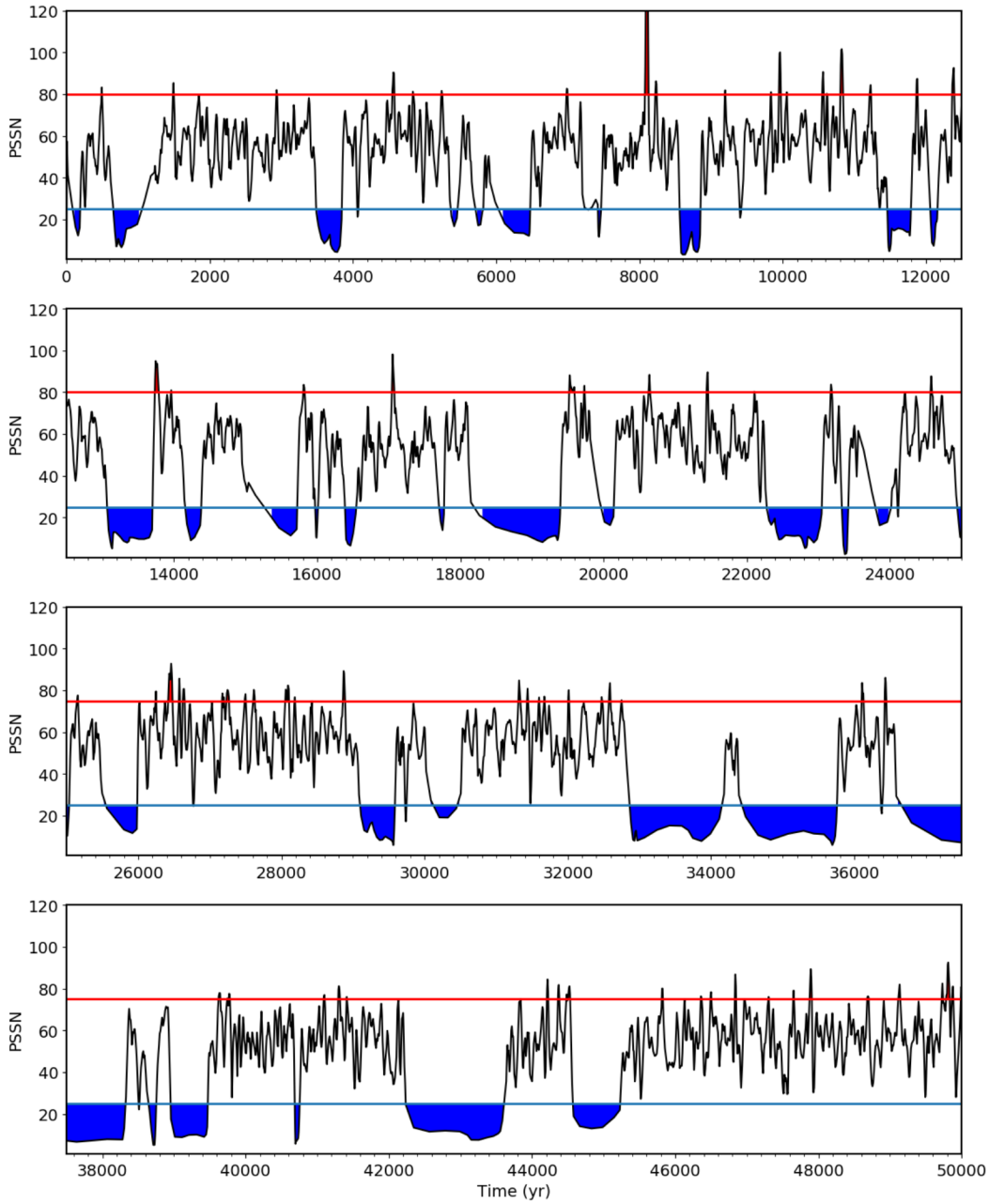

FIG. A.31. In this solution, the mean duration of Grand Minima is often too long and the simulation does not reproduce extended periods of high activity in agreement with cosmogenic isotope records.This simulation spends 40.5 % of its time in a Grand Minimum state and 6.3 % in a Grand Maximum state which is not solar-like ($K = 0.30$,$\alpha_0 = -12$ cm s^{-1}, $B_0 = 200$ G, $B_Q = 150$ G $\eta_c = 10^8$ cm^{2}s^{-1}, $\eta_t = 10^{12}$ cm^{2}s^{-1}).

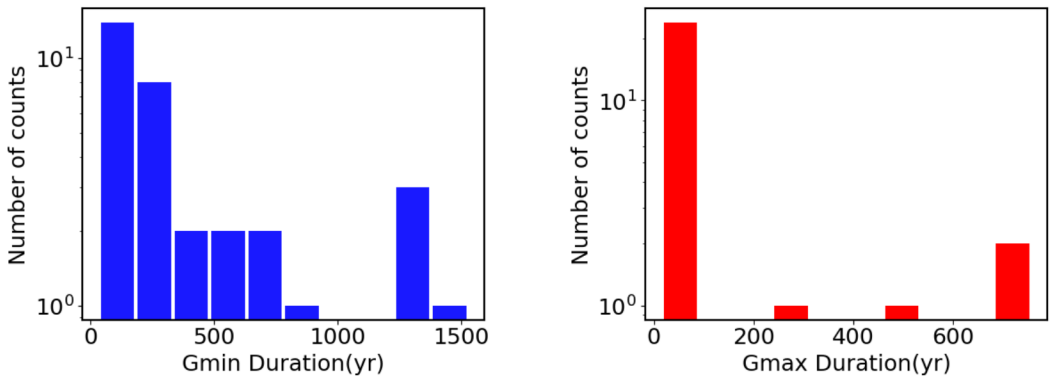

FIG. A.32. Duration histograms for Grand Minima (blue) and Grand Maxima (red) constructed from the time series in Fig. A.31. 73 Grand Minima and 68 Grand Maxima are estimated. The mean durations for Grand Minima and Grand Maxima are 392.7 years and 108.2 years respectively, much longer than the cosmogenic isotope data exhibits ($K = 0.30$,$\alpha_0 = -12$ cm s^{-1}, $B_0 = 200$ G, $B_Q = 150$ G $\eta_c = 10^8$ cm^{2}s^{-1}, $\eta_t = 10^{12}$ cm^{2}s^{-1}).

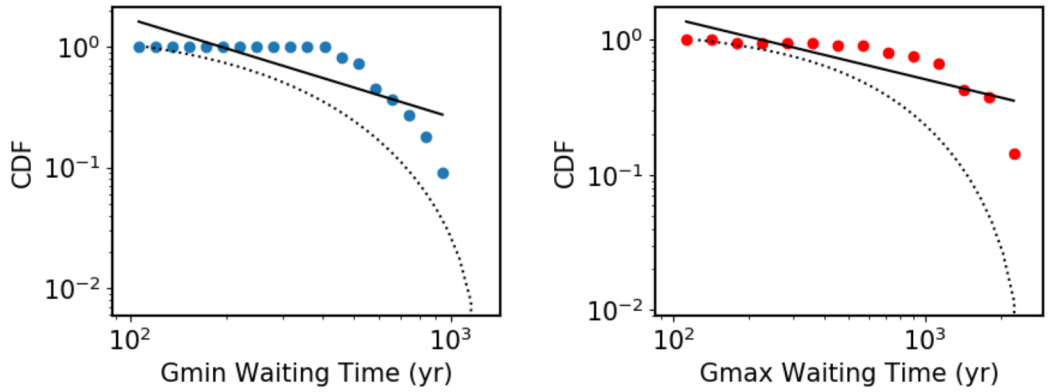

FIG. A.33. Waiting time distributions between two consecutive Grand Minima (right) /Grand Maxima (left) constructed from the time series in Fig. A.31. While the WTD for Grand Minima is in good accordance with an exponential distribution indicating a random process, the WTD for Grand Maxima is better depicted with a power-law, hinting for some memory effects ($K = 0.30$,$\alpha_0 = -12$ cm s^{-1}, $B_0 = 200$ G, $B_Q = 150$ G $\eta_c = 10^8$ cm^{2}s^{-1}, $\eta_t = 10^{12}$ cm^{2}s^{-1}).

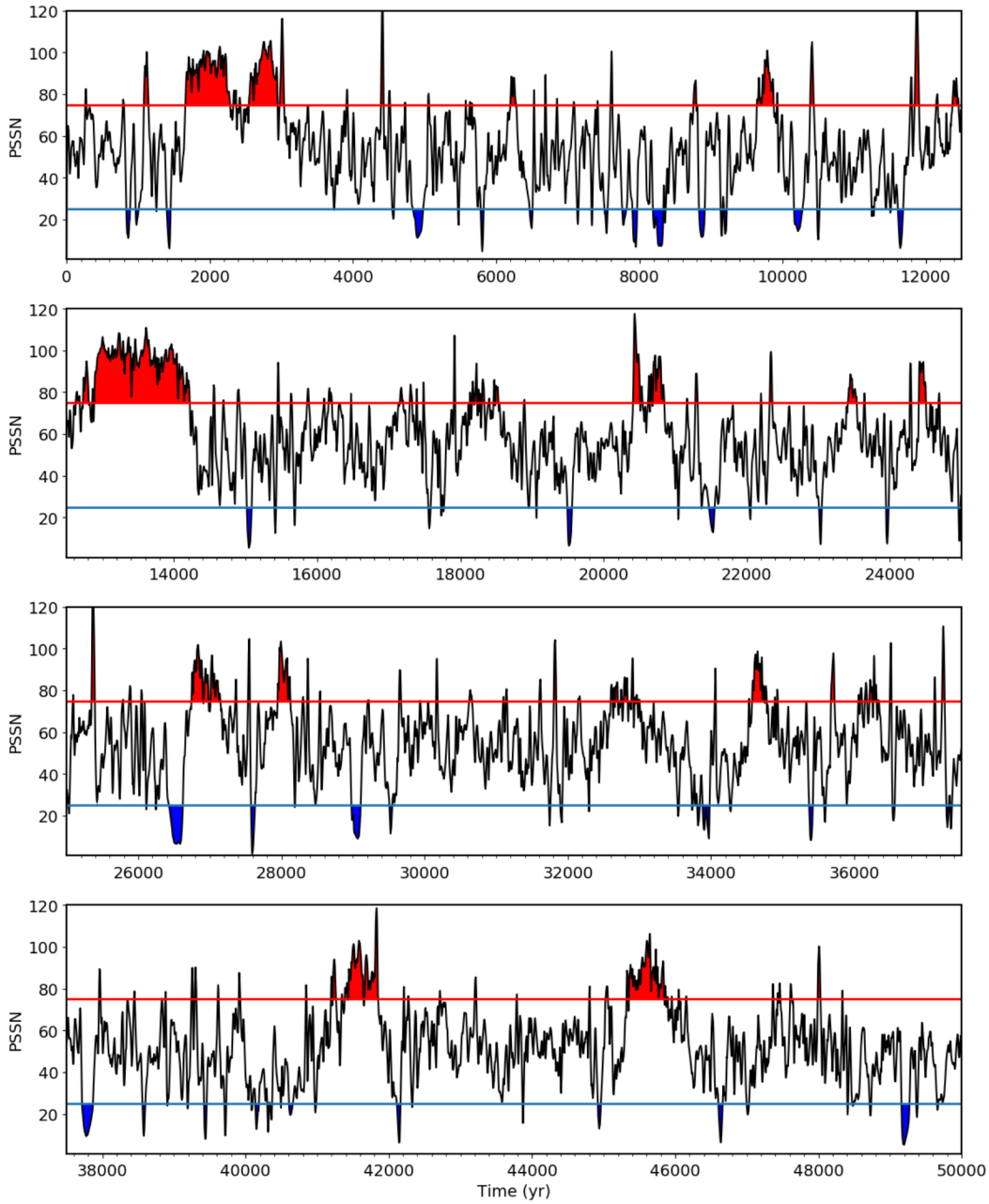

FIG. A.34. In this solution, the mean duration of Grand Minima is often too short. This simulation spends about 8 % of its time in a Grand Minimum state and 48.6 % in a Grand Maximum state which is far from being solar-like. ($K = 0.35$ cm s^{-1}, $\alpha_0 = -12$ cm s^{-1}, $B_0 = 210$ G, $B_Q = 120$ G, $\eta_c = 10^8$ cm^{2}s^{-1}, $\eta_t = 10^{11.8}$ cm^{2}s^{-1}).

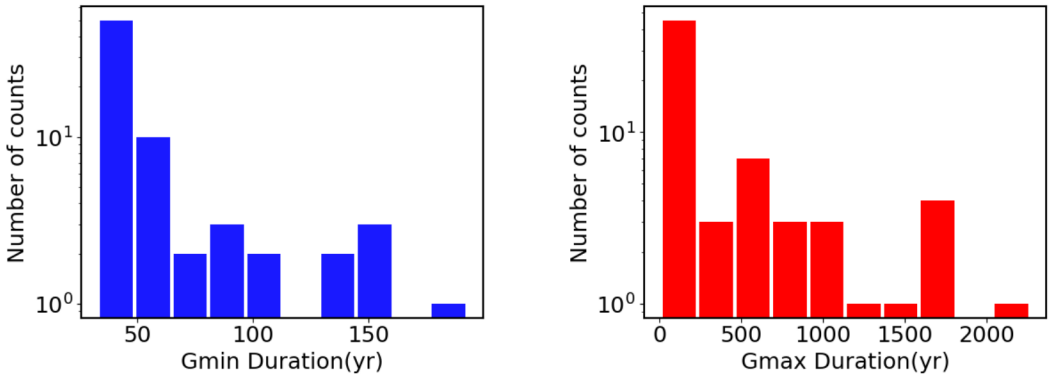

FIG. A.35. Duration histograms for Grand Minima (blue) and Grand Maxima (red) constructed from the time series in Fig. A.34. The mean durations for Grand Minima is 54.5 years, which is shorter than the cosmogenic isotope data shows and Grand Maxima is 357.8 years, much longer than the cosmogenic isotope records tell ($K = 0.35$ cm s^{-1}, $\alpha_0 = -12$ cm s^{-1}, $B_0 = 210$ G, $B_Q = 120$ G, $\eta_c = 10^8$ cm^{2}s^{-1}, $\eta_t = 10^{11.8}$ cm^{2}s^{-1})).

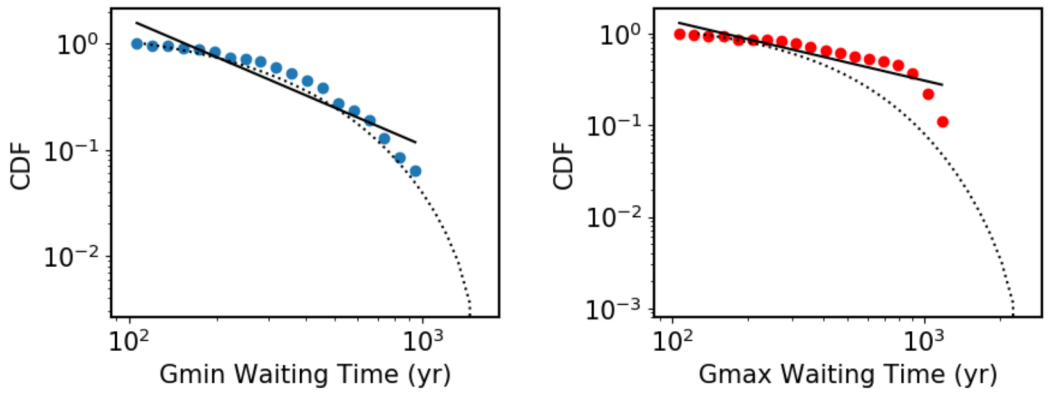

FIG. A.36. Waiting time distributions between two consecutive Grand Minima (right) /Grand Maxima (left) constructed from the time series in Fig. A.34. While the WTD for Grand Minima is in good accordance with an exponential distribution indicating a random process, the WTD for Grand Maxima is better depicted with a power-law hinting for some memory effects ($K = 0.35$ cm s^{-1}, $\alpha_0 = -12$ cm s^{-1}, $B_0 = 210$ G, $B_Q = 120$ G, $\eta_c = 10^8$ cm^{2}s^{-1}, $\eta_t = 10^{11.8}$ cm^{2}s^{-1}).

A.3. Samples of Grand Minimum and Maximum

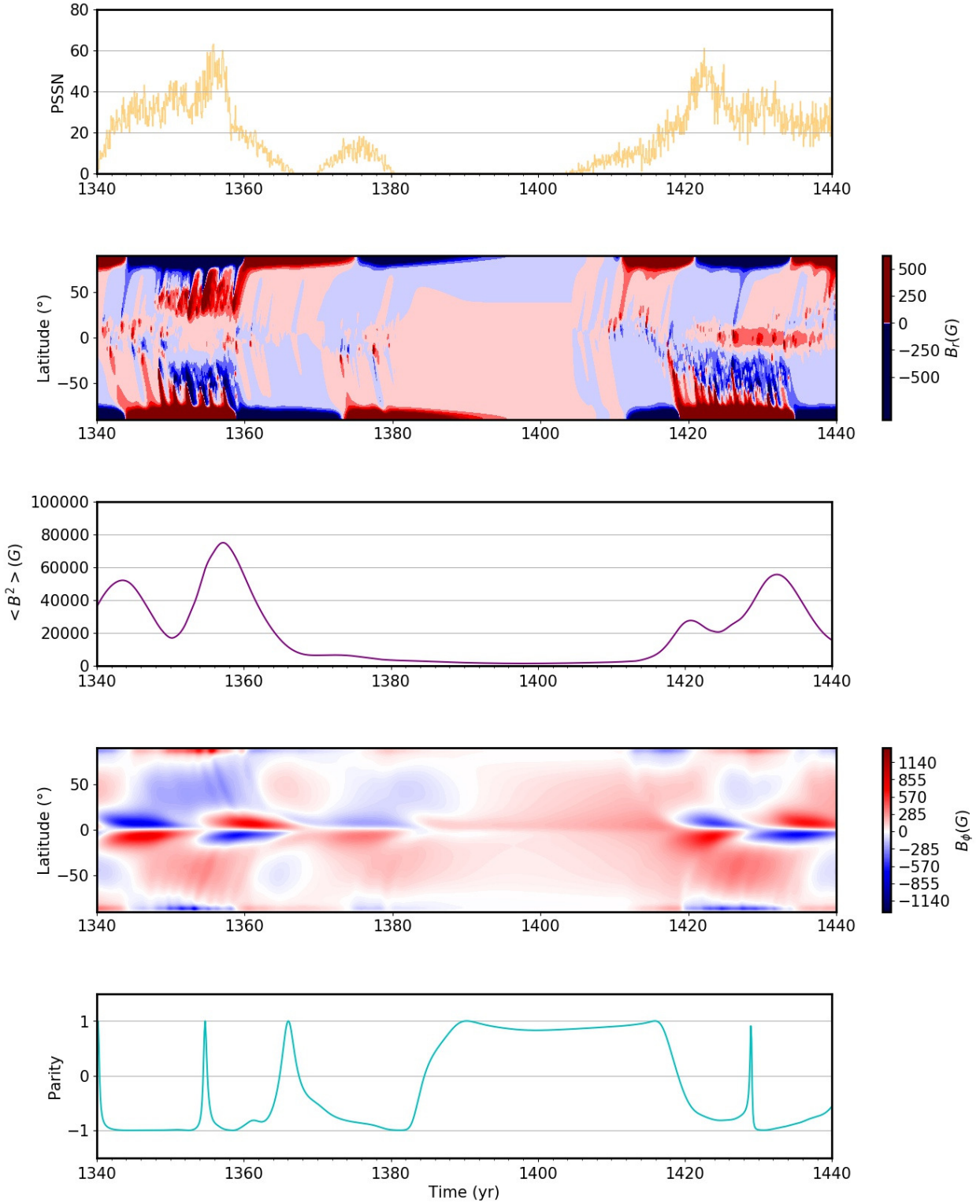

Fig. A.37. A typical Grand Minimum produced by the model, from the time series in §2.3. *From top to bottom*: PSSN, surface radial field, total magnetic energy, deep-seated toroidal field, parity as a function of time. Notice how the surface radial field and interior toroidal field become dominantly quadrupolar as the parity becomes close to 1 throughout the deep-phase of the Grand Minimum ($K = 0.32$, $\alpha_0 = -12$ cm s^{-1}, $B_0 = 210$ G, $B_Q = 120$ G, $\eta_c = 10^8$ cm^{2}s^{-1}, $\eta_t = 10^{11.8}$ cm^{2}s^{-1}).

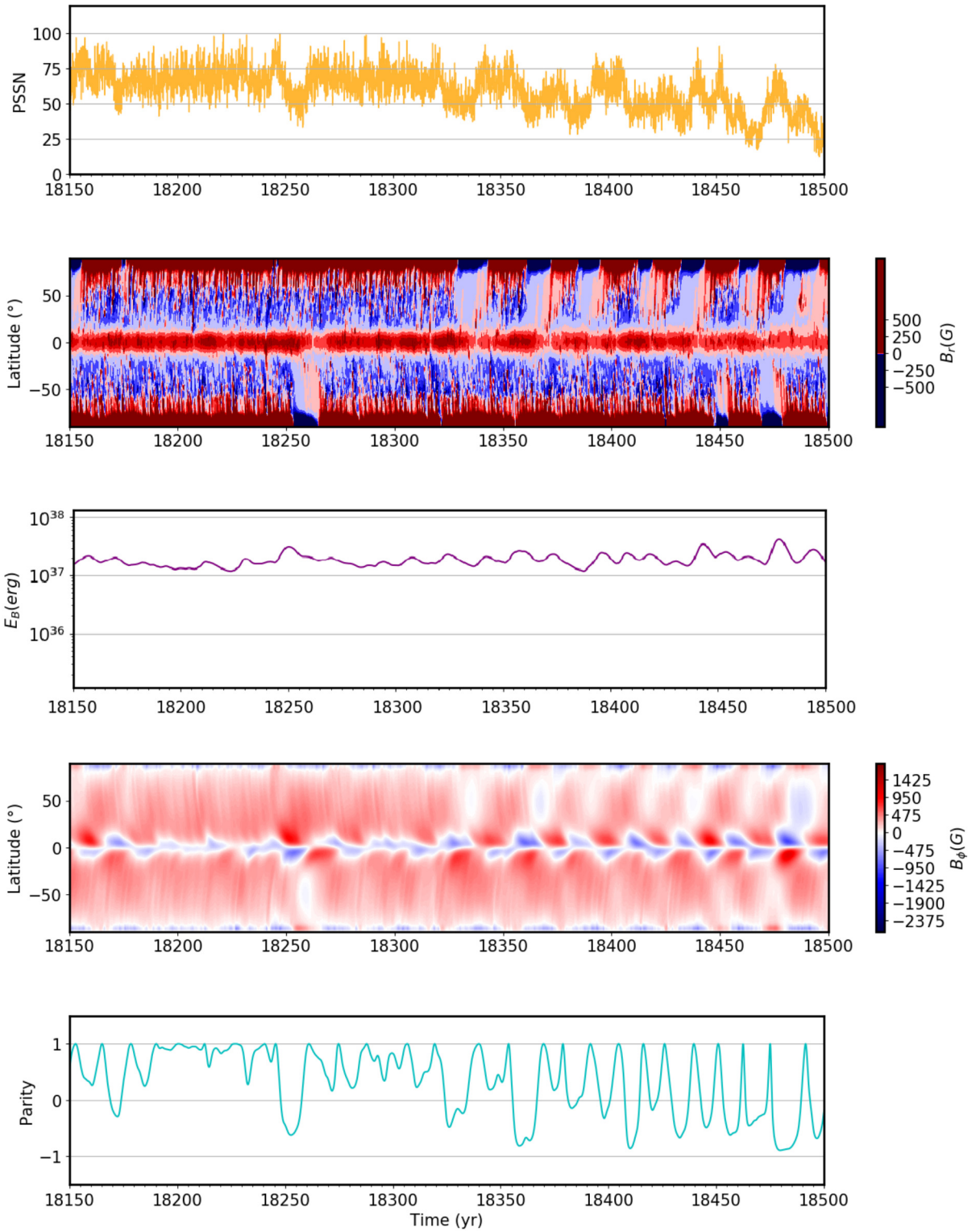

FIG. A.38. A typical Grand Minimum produced by the model, from the time series in §2.3. *From top to bottom*: PSSN, surface radial field, total magnetic energy, deep-seated toroidal field, parity as a function of time. Notice how the surface radial field and interior toroidal field become dominantly quadrupolar as the parity becomes close to 1 for 200 yrs in the first part of the simulation segment and the total magnetic energy is low despite enhanced PSSN ($K = 0.32$, $\alpha_0 = -12$ cm s^{-1}, $B_Q = 120$ G, $B_0 = 210$ G, $\eta_c = 10^8$ cm^{2}s^{-1}, $\eta_t = 10^{11.8}$ cm^{2}s^{-1}).

A.4. Wavelet Analysis

Performing Morlet wavelet analysis and constructing wavelet and Fourier spectra with the help of the WAIPY package, we investigated secular and super-secular quasi-periodicities that the model may be producing. Here are a few more examples complementary to the one presented in Ölçek et al. (2018, submitted).

The composite figures including a period as a function of power and global wavelet spectrum showing both Morlet, Fourier power spectra and 95% significance level for the Morlet wavelet spectrum. While the Morlet analysis gives more precise spatial information, the Fourier analysis offers precision in frequency. In the two cases shown in Figs. A.39 and A.40, all the parameters except the value of α_0 differ from each other. Fig. A.39 demonstrates a case in which η_c has its lowest value and η_c has its largest within the interval that the model is optimized. The result presented in Fig. A.40 is a similar case to the one we closely examined in §2.3 except η_c is augmented one order of magnitude, to test the effect of core diffusivity on long-term quasi-periodicities.

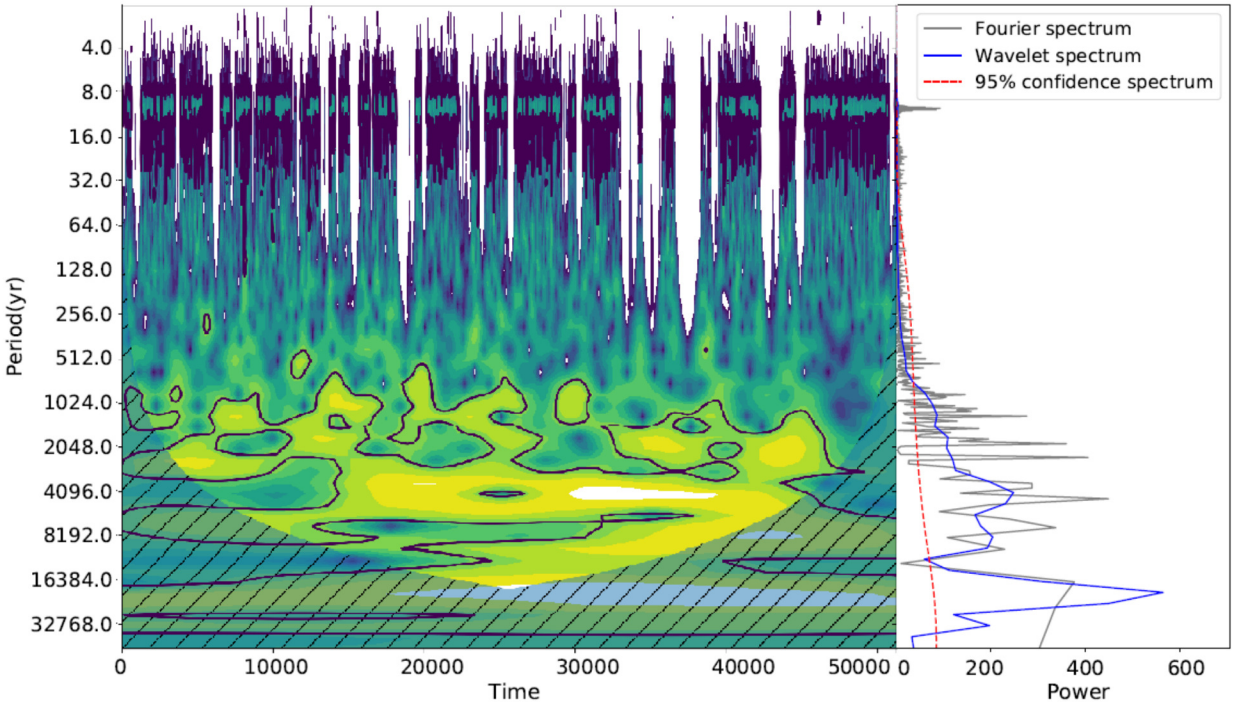

FIG. A.39. *Left*: Period as a function of power. *Right*: Global wavelet spectrum showing both Morlet(blue), Fourier(grey) power spectra and 95% significance level(red) for the Morlet wavelet spectrum. Despite long Grand Minima, the Fourier spectrum (giving precise information in frequency) of this 50,000 yr simulation shows a higher power for the Schwabe cycle compared to the case study in §2.3 ($K = 0.30$, $\alpha_0 = -12$ cm s^{-1}, $B_Q = 150$ G, $B_0 = 200$ G, $\eta_c = 10^8$ cm^{2}s^{-1}, $\eta_t = 10^{12}$ cm^{2}s^{-1}). The peaks in the 1000-4000 yr range hint for super-secular quasi-periodicities.

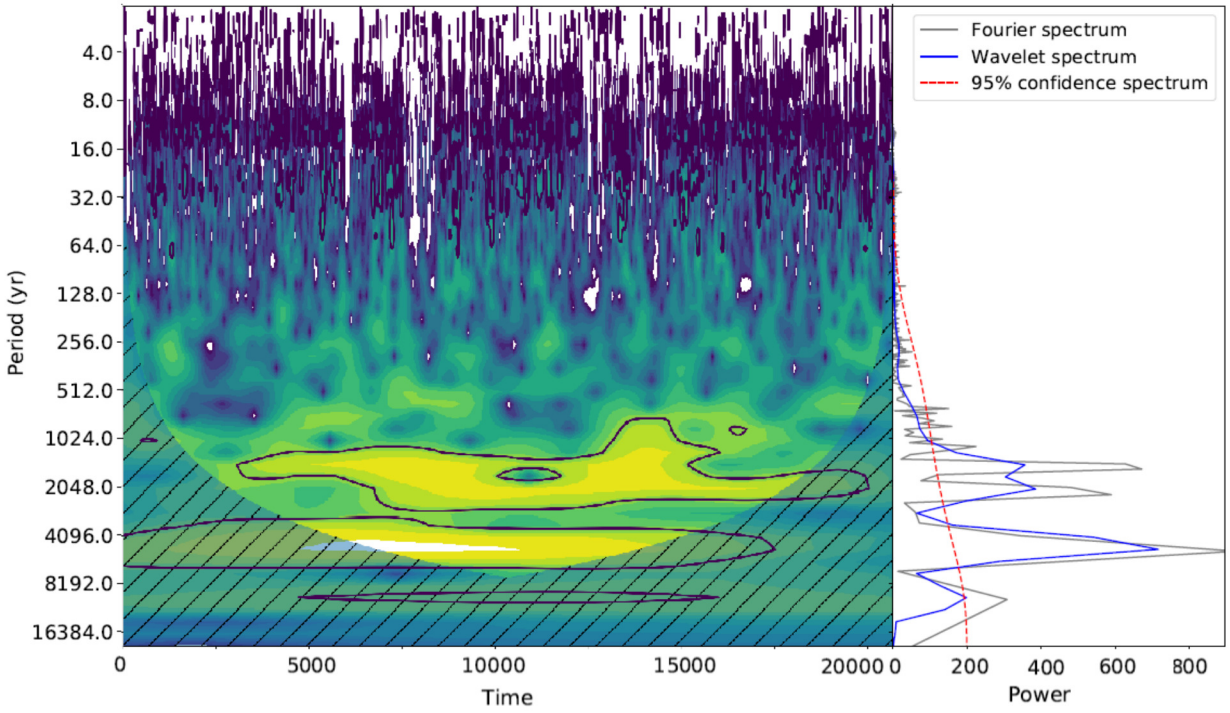

FIG. A.40. *Left*: Period as a function of power. *Right*: Global wavelet spectrum showing both Morlet(blue), Fourier(grey) power spectra and 95% significance level(red) for the Morlet wavelet spectrum. A 20,000 years simulation has a higher η_c compared to the case in §2.3 while other parameters are kept fixed ($K = 0.32$, $\alpha_0 = -12$ cm s^{-1}, $B_Q = 120$ G, $B_0 = 210$ G, $\eta_c = 10^9$ cm^{2}s^{-1}, $\eta_t = 10^{11.8}$ cm^{2}s^{-1}). Here, higher η_c results in slightly shorter super-secular quasi-periodicities.

Bibliography

Augustson, K., Brun, A.S., Miesch, M., Toomre, J.: 2015, Grand Minima and Equatorward Propagation in a Cycling Stellar Convective Dynamo. **809**, 149. DOI. ADS.

Babcock, H.W.: 1961, The Topology of the Sun's Magnetic Field and the 22-YEAR Cycle. **133**, 572. DOI. ADS.

Babcock, H.W., Babcock, H.D.: 1955, The Sun's Magnetic Field, 1952-1954. **121**, 349. DOI. ADS.

Bard, E., Raisbeck, G.M., Yiou, F., Jouzel, J.: 1997, Solar modulation of cosmogenic nuclide production over the last millennium: comparison between ^{14}C and ^{10}Be records. *Earth and Planetary Science Letters* **150**, 453. DOI. ADS.

Barekat, A., Schou, J., Gizon, L.: 2014, The radial gradient of the near-surface shear layer of the Sun. **570**, L12. DOI. ADS.

Barnard, L., Lockwood, M., Hapgood, M.A., Owens, M.J., Davis, C.J., Steinhilber, F.: 2011, Predicting space climate change. **38**, L16103. DOI. ADS.

Baumann, I., Schmitt, D., Schüssler, M., Solanki, S.K.: 2004, Evolution of the large-scale magnetic field on the solar surface: A parameter study. **426**, 1075. DOI. ADS.

Beer, J.: 2000, Long-term indirect indices of solar variability. **94**, 53. ADS.

Beer, J., McCracken, K., von Steiger, R.: 2012, *Cosmogenic Radionuclides*. DOI. ADS.

Beer, J., Tobias, S., Weiss, N.: 1998, An Active Sun Throughout the Maunder Minimum. **181**, 237. DOI. ADS.

Beer, J., Tobias, S.M., Weiss, N.O.: 2018, On long-term modulation of the Sun's magnetic cycle. **473**, 1596. DOI. ADS.

Beer, J., Blinov, A., Bonani, G., Finkel, R.C., Hofmann, H.J., Lehmann, B., Oeschger, H., Sigg, A., Schwander, J., Staffelbach, T., Stauffer, B., Suter, M., Wötfli, W.: 1990, Use of Be-10 in polar ice to trace the 11-year cycle of solar activity. **347**, 164. DOI. ADS.

Belucz, B., Dikpati, M., Forgács-Dajka, E.: 2015, A Babcock-Leighton Solar Dynamo Model with Multi-cellular Meridional Circulation in Advection- and Diffusion-dominated Regimes. **806**, 169. DOI. ADS.

Berggren, A.-M., Beer, J., Possnert, G., Aldahan, A., Kubik, P., Christl, M., Johnsen, S.J., Abreu, J., Vinther, B.M.: 2009, A 600-year annual ^{10}Be record from the NGRIP ice core,

Greenland. **36**, L11801. DOI. ADS.

Bonanno, A., Elstner, D., Rüdiger, G., Belvedere, G.: 2002, Parity properties of an advection-dominated solar alpha ^{2} Omega-dynamo. **390**, 673. DOI. ADS.

Brandenburg, A.: 2005, The Case for a Distributed Solar Dynamo Shaped by Near-Surface Shear. **625**, 539. DOI. ADS.

Brandenburg, A., Krause, F., Meinel, R., Moss, D., Tuominen, I.: 1989, The stability of nonlinear dynamos and the limited role of kinematic growth rates. **213**, 411. ADS.

Brooke, J., Moss, D., Phillips, A.: 2002, Deep minima in stellar dynamos. **395**, 1013. DOI. ADS.

Bushby, P.J.: 2006, Zonal flows and grand minima in a solar dynamo model. **371**, 772. DOI. ADS.

Caligari, P., Moreno-Insertis, F., Schussler, M.: 1995, Emerging flux tubes in the solar convection zone. 1: Asymmetry, tilt, and emergence latitude. **441**, 886. DOI. ADS.

Cameron, R.: 2016, The global solar dynamo. In: *41st COSPAR Scientific Assembly*, *COSPAR Meeting* **41**. ADS.

Cameron, R., Schüssler, M.: 2015, The crucial role of surface magnetic fields for the solar dynamo. *Science* **347**, 1333. DOI. ADS.

Cameron, R.H., Schüssler, M.: 2012, Are the strengths of solar cycles determined by converging flows towards the activity belts? **548**, A57. DOI. ADS.

Cameron, R.H., Schüssler, M.: 2016, The turbulent diffusion of toroidal magnetic flux as inferred from properties of the sunspot butterfly diagram. **591**, A46. DOI. ADS.

Cameron, R.H., Schüssler, M.: 2017, Understanding Solar Cycle Variability. **843**, 111. DOI. ADS.

Cameron, R.H., Jiang, J., Schmitt, D., Schüssler, M.: 2010, Surface Flux Transport Modeling for Solar Cycles 15-21: Effects of Cycle-Dependent Tilt Angles of Sunspot Groups. **719**, 264. DOI. ADS.

Charbonneau, P.: 2001, Multiperiodicity, Chaos, and Intermittency in a Reduced Model of the Solar Cycle. **199**, 385. DOI. ADS.

Charbonneau, P.: 2005, Dynamo Models of the Solar Cycle. *Living Reviews in Solar Physics* **2**, 2. DOI. ADS.

Charbonneau, P.: 2010, Dynamo Models of the Solar Cycle. *Living Reviews in Solar Physics* **7**, 3. DOI. ADS.

Charbonneau, P.: 2013, Solar and Stellar Dynamos. *Solar and Stellar Dynamos: Saas-Fee Advanced Course 39 Swiss Society for Astrophysics and Astronomy, Saas-Fee Advanced Courses, Volume 39. ISBN 978-3-642-32092-7. Springer-Verlag Berlin Heidelberg, 2013* **39**. DOI. ADS.

Charbonneau, P.: 2014, Solar Dynamo Theory. **52**, 251. DOI. ADS.

Charbonneau, P., Dikpati, M.: 2000, Stochastic Fluctuations in a Babcock-Leighton Model

of the Solar Cycle. **543**, 1027. DOI. ADS.

Charbonneau, P., Blais-Laurier, G., St-Jean, C.: 2004, Intermittency and Phase Persistence in a Babcock-Leighton Model of the Solar Cycle. **616**, L183. DOI. ADS.

Chatterjee, P., Nandy, D., Choudhuri, A.R.: 2004, Full-sphere simulations of a circulation-dominated solar dynamo: Exploring the parity issue. **427**, 1019. DOI. ADS.

Choudhuri, A.R.: 2015, A Critical Assessment of the Flux Transport Dynamo. *Journal of Astrophysics and Astronomy* **36**, 5. DOI. ADS.

Choudhuri, A.R., Karak, B.B.: 2012, Origin of Grand Minima in Sunspot Cycles. *Physical Review Letters* **109**(17), 171103. DOI. ADS.

Choudhuri, A.R., Schussler, M., Dikpati, M.: 1995, The solar dynamo with meridional circulation. **303**, L29. ADS.

Clauset, A., Shalizi, C.R., Newman, M.E.J.: 2009, Power-Law Distributions in Empirical Data. *SIAM Review* **51**, 661. DOI. ADS.

Clette, F., Svalgaard, L., Vaquero, J.M., Cliver, E.W.: 2014, Revisiting the Sunspot Number. A 400-Year Perspective on the Solar Cycle. **186**, 35. DOI. ADS.

Cowling, T.G.: 1933, The magnetic field of sunspots. **94**, 39. DOI. ADS.

Dasi-Espuig, M., Solanki, S.K., Krivova, N.A., Cameron, R., Peñuela, T.: 2010, Sunspot group tilt angles and the strength of the solar cycle. **518**, A7. DOI. ADS.

Devaney, R.: 1989, *An Introduction to Chaotic Dynamical Systems*. ADS.

Dikpati, M., Charbonneau, P.: 1999, A Babcock-Leighton Flux Transport Dynamo with Solar-like Differential Rotation. **518**, 508. DOI. ADS.

Dikpati, M., Gilman, P.A.: 2001a, Flux-transport Dynamos Driven by a Tachocline α - effect; a Solution to Magnetic Parity Selection in the Sun. *AGU Spring Meeting Abstracts*, SP31A. ADS.

Dikpati, M., Gilman, P.A.: 2001b, Symmetry Selection in Solar Cycle Dynamo Models. In: Mathys, G., Solanki, S.K., Wickramasinghe, D.T. (eds.) *Magnetic Fields Across the Hertzsprung-Russell Diagram*, *Astronomical Society of the Pacific Conference Series* **248**, 125. ADS.

Dikpati, M., Rempel, M., Gilman, P.A., MacGregor, K.B.: 2005, Comments on "Full-sphere simulations of circulation-dominated solar dynamo: Exploring the parity issue". **437**, 699. DOI. ADS.

D'Silva, S., Howard, R.F.: 1993, Limits on the magnetic field strength at the base of the solar convection zone. **148**, 1. DOI. ADS.

Durney, B.R.: 1995, On a Babcock-Leighton dynamo model with a deep-seated generating layer for the toroidal magnetic field. **160**, 213. DOI. ADS.

Eddy, J.A.: 1976, The Maunder Minimum. *Science* **192**, 1189. DOI. ADS.

Egeland, R.: 2017, Long-Term Variability of the Sun in the Context of Solar-Analog Stars. PhD thesis, Montana State University, Bozeman, Montana, USA

<EMAIL>ricky.egeland@montana.edu</EMAIL>. ADS.

Egeland, R., Soon, W., Baliunas, S., Hall, J.C., Pevtsov, A.A., Bertello, L.: 2017, The Mount Wilson Observatory S-index of the Sun. **835**, 25. DOI. ADS.

Fan, Y.: 2009, The Emergence of a Twisted Flux Tube into the Solar Atmosphere: Sunspot Rotations and the Formation of a Coronal Flux Rope. **697**, 1529. DOI. ADS.

Fligge, M., Solanki, S.K., Beer, J.: 1999, Determination of solar cycle length variations using the continuous wavelet transform. **346**, 313. ADS.

Frick, P., Galyagin, D., Hoyt, D.V., Nesme-Ribes, E., Schatten, K.H., Sokoloff, D., Zakharov, V.: 1997, Wavelet analysis of solar activity recorded by sunspot groups. **328**, 670. ADS.

Gibson, S.E., Zhao, L., Fisk, L.A.: 2011, The solar wind structure and heliospheric magnetic field in the solar Cycle 23-24 minimum and in the increasing phase of Cycle 24. *AGU Fall Meeting Abstracts*, SH31D. ADS.

Gleissberg, W.: 1939, A long-periodic fluctuation of the sun-spot numbers. *The Observatory* **62**, 158. ADS.

Gleissberg, W.: 1944, A secular change in the shape of the spot-frequency curve. *The Observatory* **65**, 244. ADS.

Guerrero, G.A., Muñoz, J.D.: 2004, Kinematic solar dynamo models with a deep meridional flow. **350**.

Guerrero, G., Smolarkiewicz, P.K., de Gouveia Dal Pino, E.M., Kosovichev, A.G., Mansour, N.N.: 2016, On the Role of Tachoclines in Solar and Stellar Dynamos. **819**, 104. DOI. ADS.

Hale, G.E.: 1919, On the Nature of Sun-Spots. *Proceedings of the Royal Society of London Series A* **95**, 234. DOI. ADS.

Hathaway, D.H.: 2009, Solar Cycle Forecasting. **144**, 401. DOI. ADS.

Hathaway, D.H.: 2015, The Solar Cycle. *Living Reviews in Solar Physics* **12**, 4. DOI. ADS.

Hathaway, D.H., Upton, L.: 2014, The solar meridional circulation and sunspot cycle variability. *Journal of Geophysical Research (Space Physics)* **119**, 3316. DOI. ADS.

Hathaway, D.H., Gilman, P.A., Harvey, J.W., Hill, F., Howard, R.F., Jones, H.P., Kasher, J.C., Leibacher, J.W., Pintar, J.A., Simon, G.W.: 1996, GONG Observations of Solar Surface Flows. *Science* **272**, 1306. DOI. ADS.

Hazra, S., Passos, D., Nandy, D.: 2014, A Stochastically Forced Time Delay Solar Dynamo Model: Self-consistent Recovery from a Maunder-like Grand Minimum Necessitates a Mean-field Alpha Effect. **789**, 5. DOI. ADS.

Hood, A.W., Hughes, D.W.: 2011, Solar magnetic fields. *Physics of the Earth and Planetary Interiors* **187**, 78. DOI. ADS.

Hotta, H., Yokoyama, T.: 2010, Solar Parity Issue with Flux-transport Dynamo. **714**, L308. DOI. ADS.

Howard, R.F.: 1991, Axial tilt angles of sunspot groups. **136**, 251. DOI. ADS.

Howe, R., Christensen-Dalsgaard, J., Hill, F., Komm, R.W., Larsen, R.M., Schou, J., Thompson, M.J., Toomre, J.: 2000, Deeply Penetrating Banded Zonal Flows in the Solar Convection Zone. **533**, L163. DOI. ADS.

Inceoglu, F., Arlt, R., Rempel, M.: 2017, The Nature of Grand Minima and Maxima from Fully Nonlinear Flux Transport Dynamos. **848**, 93. DOI. ADS.

Inceoglu, F., Simoniello, R., Knudsen, M.F., Karoff, C., Olsen, J., Turck-Chiéze, S., Jacobsen, B.H.: 2015, Grand solar minima and maxima deduced from ^{10}Be and ^{14}C: magnetic dynamo configuration and polarity reversal. **577**, A20. DOI. ADS.

Jennings, R.L., Weiss, N.O.: 1991, Symmetry breaking in stellar dynamos. **252**, 249. DOI. ADS.

Jiang, J., Hathaway, D.H., Cameron, R.H., Solanki, S.K., Gizon, L., Upton, L.: 2014, Magnetic Flux Transport at the Solar Surface. **186**, 491. DOI. ADS.

Käpylä, M.J., Käpylä, P.J., Olspert, N., Brandenburg, A., Warnecke, J., Karak, B.B., Pelt, J.: 2016, Multiple dynamo modes as a mechanism for long-term solar activity variations. **589**, A56. DOI. ADS.

Karak, B.B., Cameron, R.: 2016, Babcock-Leighton Solar Dynamo: The Role of Downward Pumping and the Equatorward Propagation of Activity. **832**, 94. DOI. ADS.

Karak, B.B., Choudhuri, A.R.: 2011, Possible explanations of the Maunder minimum from a flux transport dynamo model. In: Prasad Choudhary, D., Strassmeier, K.G. (eds.) *Physics of Sun and Star Spots*, *IAU Symposium* **273**, 430. DOI. ADS.

Karak, B.B., Jiang, J., Miesch, M.S., Charbonneau, P., Choudhuri, A.R.: 2015, In: Balogh, A., Hudson, H., Petrovay, K., von Steiger, R. (eds.) *Flux Transport Dynamos: From Kinematics to Dynamics*, 561. DOI. ADS.

Kitchatinov, L.L.: 2002, The Direction of Propagation of the Solar Dynamo Wave. *Astronomy Letters* **28**, 626. DOI. ADS.

Kitchatinov, L.L., Olemskoy, S.V.: 2012, Solar Dynamo Model with Diamagnetic Pumping and Nonlocal α-Effect. **276**, 3. DOI. ADS.

Kitchatinov, L.L., Olemskoy, S.V.: 2013, Solar dynamo model with nonlocal alpha-effect and diamagnetic pumping. In: Kosovichev, A.G., de Gouveia Dal Pino, E., Yan, Y. (eds.) *Solar and Astrophysical Dynamos and Magnetic Activity*, *IAU Symposium* **294**, 429. DOI. ADS.

Kitchatinov, L.L., Olemskoy, S.V.: 2016, Dynamo model for grand maxima of solar activity: can superflares occur on the Sun? **459**, 4353. DOI. ADS.

Kitchatinov, L.L., Pipin, V.V., Makarov, V.I., Tlatov, A.G.: 1999, Solar torsional oscillations and the grand activity cycle. **189**, 227. DOI. ADS.

Knudsen, M.F., Riisager, P., Jacobsen, B.H., Muscheler, R., Snowball, I., Seidenkrantz, M.-S.: 2009, Taking the pulse of the Sun during the Holocene by joint analysis of ^{14}C and ^{10}Be. **36**, L16701. DOI. ADS.

Krause, F., Raedler, K.-H.: 1980, *Mean-field magnetohydrodynamics and dynamo theory*. ADS.

Küker, M., Arlt, R., Rüdiger, G.: 1999, The Maunder minimum as due to magnetic Lambda -quenching. **343**, 977. ADS.

Küker, M., Rüdiger, G., Schultz, M.: 2001, Circulation-dominated solar shell dynamo models with positive alpha-effect. **374**, 301. DOI. ADS.

Leighton, R.B.: 1969, A Magneto-Kinematic Model of the Solar Cycle. **156**, 1. DOI. ADS.

Lemerle, A., Charbonneau, P.: 2017, A Coupled 2×2D Babcock-Leighton Solar Dynamo Model. II. Reference Dynamo Solutions. **834**, 133. DOI. ADS.

Lemerle, A., Charbonneau, P., Carignan-Dugas, A.: 2015, A Coupled 2×2D Babcock-Leighton Solar Dynamo Model. I. Surface Magnetic Flux Evolution. **810**, 78. DOI. ADS.

Lepreti, F., Carbone, V., Veltri, P.: 2001, Solar Flare Waiting Time Distribution: Varying-Rate Poisson or Lévy Function? **555**, L133. DOI. ADS.

McClintock, B.H., Norton, A.A.: 2013, Recovering Joy's Law as a Function of Solar Cycle, Hemisphere, and Longitude. **287**, 215. DOI. ADS.

McCracken, K.: 2013, The variable nature of the cosmic ray intensity over the past 10,000 years. In: Ormes, J.F. (ed.) *American Institute of Physics Conference Series*, *American Institute of Physics Conference Series* **1516**, 141. DOI. ADS.

Miesch, M.S., Dikpati, M.: 2014, A Three-dimensional Babcock-Leighton Solar Dynamo Model. **785**, L8. DOI. ADS.

Miyahara, H., Masuda, K., Muraki, Y., Kitagawa, H., Nakamura, T.: 2006, Variation of solar cyclicity during the Spoerer Minimum. *Journal of Geophysical Research (Space Physics)* **111**, A03103. DOI. ADS.

Moss, D., Brooke, J.: 2000, Towards a model for the solar dynamo. **315**, 521. DOI. ADS.

Moss, D., Sokoloff, D., Usoskin, I., Tutubalin, V.: 2008, Solar Grand Minima and Random Fluctuations in Dynamo Parameters. **250**, 221. DOI. ADS.

Muñoz-Jaramillo, A., Balmaceda, L.A., DeLuca, E.E.: 2013, Using the Dipolar and Quadrupolar Moments to Improve Solar-Cycle Predictions Based on the Polar Magnetic Fields. *Physical Review Letters* **111**(4), 041106. DOI. ADS.

Mursula, K., Ulich, T.: 1998, A new method to determine the solar cycle length. **25**, 1837. DOI. ADS.

Muscheler, R., Heikkilä, U.: 2011, Constraints on long-term changes in solar activity from the range of variability of cosmogenic radionuclide records. *Astrophysics and Space Sciences Transactions* **7**, 355. DOI. ADS.

Nagy, M., Lemerle, A., Labonville, F., Petrovay, K., Charbonneau, P.: 2017, The Effect of "Rogue" Active Regions on the Solar Cycle. **292**, 167. DOI. ADS.

Nandy, D., Choudhuri, A.R.: 2001, Toward a Mean Field Formulation of the Babcock-Leighton Type Solar Dynamo. I. α-Coefficient versus Durney's Double-Ring Approach.

551, 576. DOI. ADS.

Nandy, D., Choudhuri, A.R.: 2002, Explaining the Latitudinal Distribution of Sunspots with Deep Meridional Flow. *Science* **296**, 1671. DOI. ADS.

Olemskoy, S.V., Kitchatinov, L.L.: 2013, Grand Minima and North-South Asymmetry of Solar Activity. **777**, 71. DOI. ADS.

Olemskoy, S.V., Choudhuri, A.R., Kitchatinov, L.L.: 2013, Fluctuations in the alpha-effect and grand solar minima. *Astronomy Reports* **57**, 458. DOI. ADS.

Ossendrijver, A.J.H., Hoyng, P.: 1996, Stochastic and nonlinear fluctuations in a mean field dynamo. **313**, 959. ADS.

Ossendrijver, M.: 2005, The dynamo layer in solar-type stars. *Astronomische Nachrichten* **326**, 166. DOI. ADS.

Ossendrijver, M., Covas, E.: 2003, Crisis-induced intermittency due to attractor-widening in a buoyancy-driven solar dynamo. *International Journal of Bifurcation and Chaos* **8**. ADS.

Ossendrijver, M.A.J.H.: 2000, Grand minima in a buoyancy-driven solar dynamo. **359**, 364. ADS.

Owens, M.J., Usoskin, I., Lockwood, M.: 2012, Heliospheric modulation of galactic cosmic rays during grand solar minima: Past and future variations. **39**, L19102. DOI. ADS.

Parker, E.N.: 1955, Hydromagnetic Dynamo Models. **122**, 293. DOI. ADS.

Passos, D., Lopes, I.: 2012, Effects of cyclic fluctuations in meridional circulation using a low-order dynamo model. **422**, 1709. DOI. ADS.

Passos, D., Nandy, D., Hazra, S., Lopes, I.: 2014, A solar dynamo model driven by mean-field alpha and Babcock-Leighton sources: fluctuations, grand-minima-maxima, and hemispheric asymmetry in sunspot cycles. **563**, A18. DOI. ADS.

Petrovay, K.: 2010, Solar Cycle Prediction. *Living Reviews in Solar Physics* **7**, 6. DOI. ADS.

Pipin, V.V.: 1999, The Gleissberg cycle by a nonlinear alpha L\ dynamo. **346**, 295. ADS.

Pipin, V.V., Kosovichev, A.G.: 2011, Mean-field Solar Dynamo Models with a Strong Meridional Flow at the Bottom of the Convection Zone. **738**, 104. DOI. ADS.

Platt, N., Spiegel, E.A., Tresser, C.: 1993, On-off intermittency - A mechanism for bursting. *Physical Review Letters* **70**, 279. DOI. ADS.

Poluianov, S.V., Usoskin, I.G., Kovaltsov, G.A.: 2014, Cosmogenic Isotope Variability During the Maunder Minimum: Normal 11-year Cycles Are Expected. **289**, 4701. DOI. ADS.

Raisbeck, G.M., Yiou, F., Jouzel, J., Petit, J.R.: 1990, ^{10}Be and δ ^{2}H in Polar Ice Cores as a Probe of the Solar Variability's Influence on Climate. *Philosophical Transactions of the Royal Society of London Series A* **330**, 463. DOI. ADS.

Ribes, J.C., Nesme-Ribes, E.: 1993, The solar sunspot cycle in the Maunder minimum AD1645 to AD1715. **276**, 549. ADS.

Roy, J.-R.: 1977, The north-south distribution of major solar flare events, sunspot magnetic classes and sunspot areas /1955-1974/. **52**, 53. DOI. ADS.

Rüdiger, G., Hollerbach, R.: 2004, *The magnetic universe : geophysical and astrophysical dynamo theory*, 343. ADS.

Sanchez, S., Fournier, A., Aubert, J.: 2014, The Predictability of Advection-dominated Flux-transport Solar Dynamo Models. **781**, 8. DOI. ADS.

Schmitt, D.: 1987, An alpha-omega-dynamo with an alpha-effect due to magnetostrophic waves. **174**, 281. ADS.

Schmitt, D., Schuessler, M., Ferriz-Mas, A.: 1996, Intermittent solar activity by an on-off dynamo. **311**, L1. ADS.

Schou, J., Howe, R., Basu, S., Christensen-Dalsgaard, J., Corbard, T., Hill, F., Komm, R., Larsen, R.M., Rabello-Soares, M.C., Thompson, M.J.: 2002, A Comparison of Solar p-Mode Parameters from the Michelson Doppler Imager and the Global Oscillation Network Group: Splitting Coefficients and Rotation Inversions. **567**, 1234. DOI. ADS.

Schrijver, C.J., Siscoe, G.L.: 2010, *Heliophysics: Evolving Solar Activity and the Climates of Space and Earth*. ADS.

Schüssler, M., Schmitt, D.: 2004, Does the butterfly diagram indicate a solar flux-transport dynamo? **421**, 349. DOI. ADS.

Sokoloff, D., Nesme-Ribes, E.: 1994, The Maunder minimum: A mixed-parity dynamo mode? **288**, 293. ADS.

Solanki, S.K., Inhester, B., Schüssler, M.: 2006, The solar magnetic field. *Reports on Progress in Physics* **69**, 563. DOI. ADS.

Solanki, S.K., Usoskin, I.G., Kromer, B., Schüssler, M., Beer, J.: 2004, Unusual activity of the Sun during recent decades compared to the previous 11,000 years. **431**, 1084. DOI. ADS.

Solov'ev, A., Kirichek, E.: 2014, Basic properties of sunspots: equilibrium, stability and long-term eigen oscillations. **352**, 23. DOI. ADS.

Steenbeck, M., Krause, F.: 1966, Erklärung stellarer und planetarer Magnetfelder durch einen turbulenzbedingten Dynamomechanismus. *Zeitschrift Naturforschung Teil A* **21**, 1285. DOI. ADS.

Steinhilber, F., Abreu, J.A., Beer, J., Brunner, I., Christl, M., Fischer, H., Heikkila, U., Kubik, P.W., Mann, M., McCracken, K.G., Miller, H., Miyahara, H., Oerter, H., Wilhelms, F.: 2012, 9,400 years of cosmic radiation and solar activity from ice cores and tree rings. *Proceedings of the National Academy of Science* **109**, 5967. DOI. ADS.

Strugarek, A., Beaudoin, P., Brun, A.S., Charbonneau, P., Mathis, S., Smolarkiewicz, P.K.: 2016, Modeling turbulent stellar convection zones: Sub-grid scales effects. *Advances in Space Research* **58**, 1538. DOI. ADS.

Stuiver, M.: 1994, Atmospheric ^{14}C as a proxy of solar and climatic change. In: Nesme-Ribes, E. (ed.) *The Solar Engine and its Influence on Terrestrial Atmosphere and Climate*, 203. ADS.

Stuiver, M., Braziunas, T.F.: 1989, Atmospheric C-14 and century-scale solar oscillations. **338**, 405. DOI. ADS.

Suess, H.E.: 1980, The radiocarbon record in tree rings of the last 8000 years. *Radiocarbon* **22**(2), 200–209. DOI.

Svalgaard, L., Cliver, E.W., Kamide, Y.: 2005, Sunspot cycle 24: Smallest cycle in 100 years? **32**, L01104. DOI. ADS.

Thompson, M.J., Toomre, J., Anderson, E.R., Antia, H.M., Berthomieu, G., Burtonclay, D., Chitre, S.M., Christensen-Dalsgaard, J., Corbard, T., De Rosa, M., Genovese, C.R., Gough, D.O., Haber, D.A., Harvey, J.W., Hill, F., Howe, R., Korzennik, S.G., Kosovichev, A.G., Leibacher, J.W., Pijpers, F.P., Provost, J., Rhodes, E.J. Jr., Schou, J., Sekii, T., Stark, P.B., Wilson, P.R.: 1996, Differential Rotation and Dynamics of the Solar Interior. *Science* **272**, 1300. DOI. ADS.

Thompson, M.J., Christensen-Dalsgaard, J., Miesch, M.S., Toomre, J.: 2003, The Internal Rotation of the Sun. **41**, 599. DOI. ADS.

Tobias, S.M.: 1997, The solar cycle: parity interactions and amplitude modulation. **322**, 1007. ADS.

Tobias, S.M.: 2002, Modulation of solar and stellar dynamos. *Astronomische Nachrichten* **323**, 417. DOI. ADS.

Tobias, S.M., Weiss, N.O., Kirk, V.: 1995, Chaotically modulated stellar dynamos. **273**, 1150. DOI. ADS.

Usoskin, I.G.: 2008, A History of Solar Activity over Millennia. *Living Reviews in Solar Physics* **5**, 3. DOI. ADS.

Usoskin, I.G.: 2013, A History of Solar Activity over Millennia. *Living Reviews in Solar Physics* **10**, 1. DOI. ADS.

Usoskin, I.G.: 2017, A history of solar activity over millennia. *Living Reviews in Solar Physics* **14**, 3. DOI. ADS.

Usoskin, I.G., Mursula, K., Kovaltsov, G.A.: 2000, Regular and Random Components of Sunspot Activity during Active Sun and Great Minima: Model Simulation. In: Wilson, A. (ed.) *The Solar Cycle and Terrestrial Climate, Solar and Space weather*, *ESA Special Publication* **463**, 447. ADS.

Usoskin, I.G., Mursula, K., Kovaltsov, G.A.: 2001, Heliospheric modulation of cosmic rays and solar activity during the Maunder minimum. **106**, 16039. DOI. ADS.

Usoskin, I.G., Mursula, K., Kovaltsov, G.A.: 2003, Reconstruction of Monthly and Yearly Group Sunspot Numbers From Sparse Daily Observations. **218**, 295. DOI. ADS.

Usoskin, I.G., Sokoloff, D., Moss, D.: 2009, Grand Minima of Solar Activity and the Mean-Field Dynamo. **254**, 345. DOI. ADS.

Usoskin, I.G., Solanki, S.K., Kovaltsov, G.A.: 2007, Grand minima and maxima of solar activity: new observational constraints. **471**, 301. DOI. ADS.

Usoskin, I.G., Solanki, S.K., Taricco, C., Bhandari, N., Kovaltsov, G.A.: 2006, Long-term solar activity reconstructions: direct test by cosmogenic ^{44}Ti in meteorites. **457**, L25. DOI. ADS.

Usoskin, I.G., Hulot, G., Gallet, Y., Roth, R., Licht, A., Joos, F., Kovaltsov, G.A., Thébault, E., Khokhlov, A.: 2014, Evidence for distinct modes of solar activity. **562**, L10. DOI. ADS.

Usoskin, I.G., Arlt, R., Asvestari, E., Hawkins, E., Käpylä, M., Kovaltsov, G.A., Krivova, N., Lockwood, M., Mursula, K., O'Reilly, J., Owens, M., Scott, C.J., Sokoloff, D.D., Solanki, S.K., Soon, W., Vaquero, J.M.: 2015, The Maunder minimum (1645-1715) was indeed a grand minimum: A reassessment of multiple datasets. **581**, A95. DOI. ADS.

Usoskin, I.G., Kovaltsov, G.A., Lockwood, M., Mursula, K., Owens, M., Solanki, S.K.: 2016a, A New Calibrated Sunspot Group Series Since 1749: Statistics of Active Day Fractions. **291**, 2685. DOI. ADS.

Usoskin, I.G., Gallet, Y., Lopes, F., Kovaltsov, G.A., Hulot, G.: 2016b, Solar activity during the Holocene: the Hallstatt cycle and its consequence for grand minima and maxima. **587**, A150. DOI. ADS.

Vasiliev, S.S., Dergachev, V.A.: 2002, The ˜ 2400-year cycle in atmospheric radiocarbon concentration: bispectrum of ^{14}C data over the last 8000 years. *Annales Geophysicae* **20**, 115. DOI. ADS.

Vecchio, A., Lepreti, F., Laurenza, M., Alberti, T., Carbone, V.: 2017, Connection between solar activity cycles and grand minima generation. **599**, A58. DOI. ADS.

Wagner, G., Beer, J., Masarik, J., Muscheler, R., Kubik, P.W., Mende, W., Laj, C., Raisbeck, G.M., Yiou, F.: 2001, Presence of the Solar de Vries Cycle $(\sim 205 years) during the Last Ice Age$. **28**, 303. DOI. ADS.

Wang, Y.-M., Sheeley, N.R.: 2009, Understanding the Geomagnetic Precursor of the Solar Cycle. **694**, L11. DOI. ADS.

Wang, Y.-M., Sheeley, N.R. Jr.: 1991, Magnetic flux transport and the sun's dipole moment - New twists to the Babcock-Leighton model. **375**, 761. DOI. ADS.

Wang, Y.-M., Sheeley, N.R. Jr.: 2013, The Solar Wind and Interplanetary Field during Very Low Amplitude Sunspot Cycles. **764**, 90. DOI. ADS.

Wang, Y.-M., Lean, J., Sheeley, N.R. Jr.: 2002, Role of a Variable Meridional Flow in the Secular Evolution of the Sun's Polar Fields and Open Flux. **577**, L53. DOI. ADS.

Wang, Y.-M., Nash, A.G., Sheeley, N.R. Jr.: 1989, Magnetic flux transport on the sun. *Science* **245**, 712. DOI. ADS.

Watari, S.: 1996, Separation of Periodic, Chaotic, and Random Components in Solar Activity. **168**, 413. DOI. ADS.

Wheatland, M.S.: 2000, The Origin of the Solar Flare Waiting-Time Distribution. **536**, L109. DOI. ADS.

Wheatland, M.S.: 2003, The Coronal Mass Ejection Waiting-Time Distribution. **214**, 361.

DOI. ADS.

Whitbread, T., Yeates, A.R., Muñoz-Jaramillo, A., Petrie, G.J.D.: 2017, Parameter optimization for surface flux transport models. **607**, A76. DOI. ADS.

Williams, D.R.: 2013, "Sun Fact Sheet". NASA Goddard Space Flight Center. **390**.

Yang, S., Odah, H., Shaw, J.: 2000, Variations in the geomagnetic dipole moment over the last 12000 years. *Geophysical Journal International* **140**, 158. DOI. ADS.

Yeates, A.R., Muñoz-Jaramillo, A.: 2013, Kinematic active region formation in a three-dimensional solar dynamo model. **436**, 3366. DOI. ADS.

Yeates, A.R., Baker, D., van Driel-Gesztelyi, L.: 2015, Source of a Prominent Poleward Surge During Solar Cycle 24. **290**, 3189. DOI. ADS.

Yiou, F., Raisbeck, G.M., Baumgartner, S., Beer, J., Hammer, C., Johnsen, S., Jouzel, J., Kubik, P.W., Lestringuez, J., StiéVenard, M., Suter, M., Yiou, P.: 1997, Beryllium 10 in the Greenland Ice Core Project ice core at Summit, Greenland. **102**, 26. DOI. ADS.

Yoshimura, H.: 1975, Solar-cycle dynamo wave propagation. **201**, 740. DOI. ADS.

Zhao, J., Bogart, R.S., Kosovichev, A.G., Duvall, T.L. Jr., Hartlep, T.: 2013, Detection of Equatorward Meridional Flow and Evidence of Double-cell Meridional Circulation inside the Sun. **774**, L29. DOI. ADS.

Zięba, S., Nieckarz, Z.: 2014, Sunspot Time Series: Passive and Active Intervals. **289**, 2705. DOI. ADS.